University of Groningen

Studies of generalized transverse momentum dependent gluon distributions in diffractive processes

Setyadi, Chalis

DOI:
10.33612/diss.839099302

IMPORTANT NOTE: You are advised to consult the publisher's version (publisher's PDF) if you wish to cite from it. Please check the document version below.

Document Version
Publisher's PDF, also known as Version of record

Publication date:
2023

Link to publication in University of Groningen/UMCG research database

Citation for published version (APA):
Setyadi, C. (2023). *Studies of generalized transverse momentum dependent gluon distributions in diffractive processes*. [Thesis fully internal (DIV), University of Groningen]. University of Groningen. https://doi.org/10.33612/diss.839099302

Copyright
Other than for strictly personal use, it is not permitted to download or to forward/distribute the text or part of it without the consent of the author(s) and/or copyright holder(s), unless the work is under an open content license (like Creative Commons).

The publication may also be distributed here under the terms of Article 25fa of the Dutch Copyright Act, indicated by the “Taverne” license. More information can be found on the University of Groningen website: https://www.rug.nl/library/open-access/self-archiving-pure/taverne-amendment.

Take-down policy
If you believe that this document breaches copyright please contact us providing details, and we will remove access to the work immediately and investigate your claim.

Downloaded from the University of Groningen/UMCG research database (Pure): http://www.rug.nl/research/portal. For technical reasons the number of authors shown on this cover page is limited to 10 maximum.

Download date: 13-01-2024

Studies of Generalized Transverse Momentum Dependent gluon distributions in diffractive processes

Chalis Setyadi

This research was conducted at the Van Swinderen Institute for Particle Physics and Gravity, University of Groningen. Chalis Setyadi received a PhD scholarship from the Indonesia Endowment Fund for Education (LPDP).

ISBN: 978-94-6469-704-9
Printed by: ProefschriftMaken | www.proefschriftmaken.nl
Layout: Chalis Setyadi
Cover design: Chalis Setyadi

university of
groningen

Studies of Generalized Transverse Momentum Dependent Gluon Distributions in Diffractive Processes

PhD thesis

to obtain the degree of PhD of the
University of Groningen
on the authority of the
Rector Magnificus Prof. J.M.A. Scherpen
and in accordance with
the decision by the College of Deans.

This thesis will be defended in public on

Thursday 21 December 2023 at 09:00 hours

by

Chalis Setyadi

born on 25 February 1989

Supervisors
Prof. D. Boer
Prof. P.J.G. Mulders

Assessment Committee
Prof. C.J.G. Onderwater
Prof. B. Pasquini
Prof. R.G.E Timmermans

Contents

List of Tables

List of Figures

1

Introduction

As the quantum theory developed, researchers began to investigate the characteristics of subatomic particles in the search for the fundamental building blocks of matter. The discovery of the electron is considered the starting point of this journey. In 1897, J.J. Thomson identified negatively charged particles emitted from cathode ray tubes as electrons. Later Rutherford conducted a well-known gold foil experiment a few years later and observed that some of the alpha particles were deflected. He deduced that atoms were mostly empty space and had a small, dense nucleus made up of positively charged particles, called protons (1919). In 1932 Chadwick discovered neutral particles within the nucleus, referred to as neutrons.

In the 1960s, Gell-Mann and Zweig introduced the quark model [1, 2]. According to this theory, protons and neutrons were not elementary particles. They are proposed to be composed of more fundamental particles called quarks, the building blocks of all visible matter. Quarks and antiquarks are held together by gluons, the interaction mediator, forming protons and neutrons in the nucleus. The interactions between quarks, antiquarks, and gluons, known as partons [3], are described by the quantum field theory of the strong force, Quantum Chromodynamics (QCD), first proposed in 1972 [4]. The term ”chromo” in QCD refers to the color charge of the partons, named red, blue, green, or their counterparts. The color charge does not reflect the colors we see in everyday life, but it behaves like real colors in the sense that three different colors or a pair of a certain color and its counterpart can create a color-neutral particle. Quarks also come in six different flavors, distinguished by their mass and charge: up, down, charm, strange, top, and bottom. The lightest quarks, the up and down quark, play a major role in the structure of atomic nuclei and have a mass less than 6 MeV, while the top quark, which has a mass of approximately 173 GeV [5] was the last of the six to be discovered [6, 7].

The groundbreaking discoveries in the field of particle physics are closely related to the development of accelerator and detector technologies worldwide. For instance, the existence of quarks was first verified through inelastic electron-nucleon scattering experiments conducted at the Stanford Linear Accelerator Center (SLAC) in 1968 [8, 9]. The existence of gluons was confirmed at Deutsches Elektronen-Synchrotron (DESY) in 1979 [10–13]. The heaviest known quark, the top quark, was finally observed at the Tevatron at the Fermi National Accelerator Laboratory (Fermilab) in 1995 [6], completing the third generation of quarks, which is 40 times more massive than its pair, the bottom quark. After being proposed more than 50 years earlier, the Higgs particle was finally detected at the Large Hadron Collider (LHC) at CERN in 2012 [14, 15]. Despite these achievements, there are still many fundamental questions that cannot be addressed by existing accelerators. This has led to the requirement for the development of new accelerators. One of the candidates is the Electron Ion Collider (EIC) [16, 17] currently being constructed in the United States, as of the time this thesis is written, as the successor of the Relativistic Heavy Ion Collider (RHIC) which aims to provide high-resolution information about the internal structure of hadrons.

At particle colliders, QCD plays a crucial role in describing the interactions of high energy partons. QCD has two key features that are very important in high energy scattering analysis: color confinement [18] and asymptotic freedom [19, 20]. Color confinement arises from the non-Abelian nature of QCD, where the interaction mediator (gluon) carries a color charge. As a result, gluons interact with each other and the interaction between quarks becomes stronger as the distance between them increases. At a certain point, the amount of energy needed to separate two quarks becomes so large that it creates other quark-antiquark pairs. Hence, quarks have never been observed as single particles. The second key feature of QCD, asymptotic freedom, states that the effective coupling of QCD becomes asymptotically smaller at high energies (short distances), allowing us to treat quarks as (almost) free particles when the coupling is small. This makes QCD amenable to perturbative analysis at high energies, while the low energy regime remains non-perturbative and must be studied through experiments.

Deep Inelastic Scattering (DIS) is a widely-used technique in experiments, such as those conducted at SLAC, HERA, and the upcoming EIC. DIS is a collision between leptons (such as electrons, muons, and neutrinos) and hadrons (typically protons or heavier nuclei). The theoretical analysis is based on the factorization framework, in which the cross section can be divided into two components: the hard part and the soft part. The hard part of the process involves the interaction between a virtual photon, emitted by the incoming high-energy electron, and the partons within the proton. This part can be analyzed using perturbative methods. Alternatively, in the dipole picture that is valid at high energies, the emitted photon splits into a quark-antiquark pair (dipole) that interacts with partons within the hadron via two-gluon exchanges, referred to as the pomeron. The soft part of the process involves the interactions between partons within the hadron, described by Parton Distribution Functions (PDFs). These functions are uncalculable and must be measured through experiments. Fortunately, there is a universal PDF that is independent of the process, known as the collinear PDF [21]. This one-dimensional PDF only depends on the collinear momentum of the parent hadron and is the simplest form of PDF. The collinear PDF $f_q(x)$ describes the probability density of finding a parton q in a hadron with a longitudinal momentum fraction x.

Collinear PDF gives a fundamental understanding of the proton structure in terms of the variable x, but it is limited in providing a comprehensive picture. To gain a deeper understanding of the proton's content, it is important to consider multidimensional PDFs such as the three-dimensional Transverse Momentum Dependent (TMD) PDFs. These PDFs take into account the transverse momentum distribution of partons $\boldsymbol{k}_\perp$, which refers to the momentum direction perpendicular to the direction of the parent hadron's motion. This provides a more comprehensive description of the partonic structure of the hadron compared to the one-dimensional PDF by incorporating a greater number of observables into the cross-section that can be observed in experiments. However, the Wilson line/loop structures in TMDs which represent the resummation of infinite gluon interactions, lead to a process dependence. This means that each event requires a separate calculation, making TMDs a non-universal object. Despite the difficulties in extracting TMDs from experimental data, the study of TMDs remains a highly sought-after area of research in particle physics due to its potential to capture some interesting phenomena, such as single-spin asymmetries, investigation of the origin of the proton spin, and the intrinsic transverse momentum of quarks and gluons. The complexity of the calculation process has motivated scientists to develop advanced techniques for more efficient extraction of TMDs. In this thesis, we will only cover the basics of TMDs and not go into the details of TMD factorization and TMD evolution.

To gain deeper insights into the internal structure of hadrons, one can turn to the Wigner distribution [22], sometimes referred to as the "mother distribution". Compared to three-dimensional TMDs, the five-dimensional Wigner distribution provides a more comprehensive view of the phase-space distribution and dynamics of the partons within a hadron. The Wigner distribution is a function of parton's light cone momentum fraction x, the parton's transverse momentum $\boldsymbol{k}_\perp$, and the impact parameter $\boldsymbol{b}_\perp$. Upon taking the Fourier transform of the Wigner distribution in the $\boldsymbol{b}_\perp$ space, we can obtain the five-dimensional Generalized Transverse Momentum Dependent (GTMD) distributions, which are functions of x, $\boldsymbol{k}_\perp$, and the transverse off-forwardness $\boldsymbol{\Delta}_\perp$. These GTMDs provide information on the orbital angular momentum of quarks and gluons, not captured by the TMDs. The main focus of this thesis will be to examine the consistency of the GTMD picture in describing diffractive processes.

There is a growing interest among researchers to find ways to measure the GTMD experimentally. One proposed method involves observing diffractive dijet production in electron-proton collisions, where in the small x limit the cross section will be proportional to the gluon GTMD [23]. It is worth noting that approximately 10% of DIS events observed at HERA at small values of x are diffractive events, where the incoming proton remains intact while losing only a small fraction of its initial momentum. In this thesis, we focus on the gluon GTMD, since the density of gluons grows quickly as we move to high energy ($x \lesssim 0.01$ region), making the quark contribution negligible. The expected exponential growth of the gluon density is believed to slow down, leading to the phenomenon of gluon saturation which can only be described through non-linear QCD. Models that incorporate the saturation effect have been successful in describing inclusive and diffractive DIS at HERA and heavy ion collisions at RHIC and LHC. We aim to include this effect in our model of the gluon GTMD. We restrict our discussion to the unpolarized distribution of gluons within an unpolarized hadron.

This thesis focuses on exploring how a GTMD model, which incorporates the saturation effect, can describe various diffractive processes and provide predictions for future experiments, particularly at the EIC. The thesis begins with a brief overview of QCD and DIS in Chapter 2, followed by an in-depth examination of the non-linear QCD framework, in particular, the Color Glass Condensate (CGC), in Chapter 3. The CGC describes that in high-energy heavy-ion collisions, a large number of gluons are generated and become so dense that they form a disordered frozen state, similar to glass, see e.g. [24, 25]. The CGC is then the resulting state of gluon saturation. The Golec-Biernat-Wüsthof (GBW) model was developed to effectively describe the saturation regime observed in the HERA data [26, 27]. We will incorporate the GBW parametrization into our GTMD model.

In Chapter 4, we introduce multidimensional PDFs and provide definitions of GTMDs from two different perspectives. In Chapter 5, we construct a gluon GTMD model to describe the transverse off-forwardness squared t, the transverse momentum of the jets $K_\perp$, and the photon virtuality Q^2 dependence data from HERA-H1 on diffractive dijet production. At first, we used a small average x value to describe the Q^2 data, but we found that an x-dependent saturation scale was necessary to improve the description. By incorporating an x-dependence through adopting the GBW parameterization, we improved the description of the Q^2 data. In Chapter 6, we then extend the model to describe diffractive J/ψ production and argue that both diffractive dijet and J/ψ production should be described by the same underlying picture. However, there is some tension in the parameters we use in diffractive J/ψ production, which may only be resolved with more data from higher precision experiments at the EIC, but also from Ultra-peripheral Collisions (UPCs) at RHIC and LHC. We provide predictions for both diffractive dijet and J/ψ production with optimal parameterizations for each process as a test of the underlying model. In Chapter 7, we discuss the future prospects of GTMD studies and summarize the important points.

2

QCD in high energy collisions

This chapter is dedicated to giving a brief overview of the fundamental concepts of QCD and high-energy collisions. In Sec. 2.1, we examine the behavior of the running strong coupling as a result of QCD's non-Abelian symmetry. The section also delves into two important QCD phenomena: confinement and asymptotic freedom, which stem from the non-Abelian gauge theory. Sec. 2.2 explores high-energy Deep Inelastic Scattering (DIS) as a tool to study the internal structure of the proton. We then discuss collinear Parton Distribution Functions (PDFs) in Sec. 2.3, which serve as the foundation for further analysis of the proton's internal structure in subsequent chapters. We also emphasize the importance of Wilson lines and the gauge invariance of correlation functions.

2.1 The running strong coupling

One of the objectives in the study of QCD is to provide theoretical descriptions of the strong interaction in high-energy scattering processes. To achieve this, we need an expression for the cross section that includes observables and parameters that can be tested in experiments. In a field theory, these ingredients can be obtained by requiring invariance under gauge transformations in the Lagrangian which outlines all possible interactions between the fields. We can then construct the scattering amplitude for the process using Feynman diagrams, which are graphical representations of the propagation and interactions of the fields in the Lagrangian.

The general Lagrangian density for QCD which is invariant under SU(3) transformations, can be expressed as[1]

$$\mathcal{L}_{\text{QCD}} = \sum_f \bar{\psi}_f \left(i\not{D} - m_f I \right) \psi_f - \frac{1}{4} F^a_{\mu\nu} F^{a\mu\nu} + \mathcal{L}_{\text{GF}} + \mathcal{L}_{\text{FPG}}. \tag{2.1}$$

The first term of the Dirac Lagrangian describes the quark propagators, where the quark field is represented by ψ with mass m_f, and the sum runs over all six quark flavors f. Here, I represents the identity matrix and D_μ denotes the covariant derivative defined as

$$D_\mu \equiv I\partial_\mu + igt^a A^a_\mu, \tag{2.2}$$

with g determines both the coupling between the quark and gluon fields and the coupling between the gluons themselves. The color matrices t^a act as generators of the SU(3) color group. In the fundamental representation the color matrices can be related to the Gell-Mann matrices $t^a = \frac{\lambda^a}{2}$ [28] which satisfy

$$[t^a, t^b] = if^{abc}t^c \qquad \text{Tr}\left(t^a t^b\right) = \frac{1}{2}\delta^{ab} \tag{2.3}$$

where $a, b, c = 1, 2, ...8$ representing the eight generators $(3^2 - 1)$ of the SU(3) group. The real valued structure constants f^{abc} are antisymmetric under the exchange of any two indices, i.e., $f^{abc} = -f^{bac}$ and satisfy the Jacobi identity

$$f^{ade}f^{bcd} + f^{bde}f^{cad} + f^{cde}f^{abd} = 0. \tag{2.4}$$

The field strength tensor in the second term, which represents the interactions between gluon fields A^a_μ, is defined by

$$F^a_{\mu\nu} \equiv \partial_\mu A^a_\nu - \partial_\nu A^a_\mu + gf^{abc}A^b_\mu A^c_\nu. \tag{2.5}$$

The non-Abelian term $gf^{abc}A^b_\mu A^c_\nu$ gives rise to gluon self-interactions, distinguishing QCD from QED. The last two terms of Eq. (2.1), the gauge-fixing term (GF) and the Faddeev-Popov ghost term (FPG), will not play an important role in this thesis.

In the Abelian theory of Quantum Electrodynamics (QED), opposite charges attract each other through the electromagnetic force. This interaction strength decreases rapidly with distance, making it easy to separate two oppositely charged particles over long distances. In contrast, the strong interaction of quarks governed by the non-Abelian theory of QCD behaves differently. The self-interacting gluons create a flux tube between two quarks, as depicted in Fig. 2.1. As the two interacting quarks approach each other, the interaction weakens. Conversely, as the distance between the quarks increases, the interaction becomes stronger and at sufficiently large distance, it is energetically more favorable to create another pair of quarks than separating those quarks as free particles. Therefore, it is impossible to isolate a quark as a color-charged particle, and a single free quark has never been observed. This property is referred to as *confinement*.

---

[1] We use the standard Feynman-slash notation $\not{D} = \gamma^\mu D_\mu$.

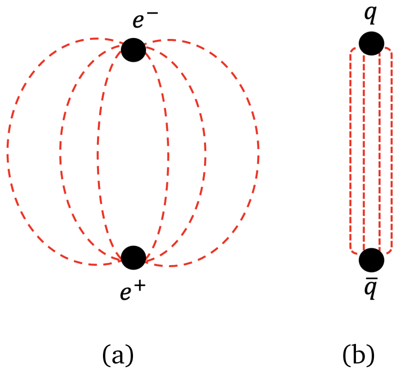

Figure 2.1: (a) Interaction of two electrostatic charged particles (e^+ and e^-) in QED. (b) Interaction of two color charged particles in QCD. The flux tube that connects the quark (q) and antiquark ($\bar{q}$) emerges because the gluons are confined by a force that is even stronger than the confinement between quarks.

Another consequence of the gluon's self-interacting behavior is the anti-screening of charges. In QED, an electron is surrounded by a cloud of virtual photons and e^+e^- pairs, and the fluctuating e^+e^- pairs will arrange themselves in such a way that the e^+ cloud is closer to the electron and screens the electron charge. This screening effect results in a smaller effective charge for the electron. As a result, the running QED coupling α decreases with increasing distance.

On the other hand, in QCD, a quark with a certain color charge is not only surrounded by $q\bar{q}$ pairs that cause a screening effect, but also by gluon pairs that result in an anti-screening effect. Eventually, the anti-screening effect from the gluons wins. As a result, unlike the QED's coupling behavior which is stronger at small distances, the running strong coupling $\alpha_s = g^2/4\pi$ is weaker at short distances and grows with increasing distance. Due to the strong coupling's decreasing asymptotic behavior with increasing energy, at small distances (high energy), quarks can be considered as free particles. This phenomenon, known as *asymptotic freedom*, was predicted by Politzer [20], Gross, and Wilczek [29, 30]. This powerful feature of QCD allows us to describe high energy collisions (small distances) using perturbative methods. However, in the non-perturbative regime where the strong coupling is large at large distances, perturbative QCD (pQCD) methods are not applicable. Perturbative QCD makes use of a small running coupling constant expansion for which the first order expansion in α_s is known as the leading order (LO), while the next power is called the next-to-leading order (NLO), and so on. The higher order terms in the expansion are considered to give a smaller contribution due to the larger powers of α_s. In this thesis we will mostly discuss the leading order in perturbation theory, focusing primarily on the nonperturbative aspects.

Effectively, the running of the coupling is derived from the renormalization group equations (RGE) [31], which follow from the requirement that the observables associated with the Lagrangian density in Eq. (2.1) should not depend on a renormalization scale

μ. Thus the RGE for QCD can be expressed as

$$\left[\mu^2 \frac{\partial}{\partial \mu^2} + \beta(\alpha_s)\right] \mathcal{O}(\alpha_s) = 0 \tag{2.6}$$

with $\alpha_s = g^2/4\pi$, g is the strength of the interaction, while the so-called β function is defined as

$$\beta(\alpha_s) \equiv \frac{\mathrm{d}\alpha_s(\mu^2)}{\mathrm{d}\ln(\mu^2)} = -\left(\beta_0 \alpha_s^2 + \beta_1 \alpha_s^3 + \beta_2 \alpha_s^4 + ...\right). \tag{2.7}$$

We will only consider the first order expansion (one-loop) where [19,20]

$$\beta_0 = \frac{11N_c - 2N_f}{12\pi}. \tag{2.8}$$

Here, N_c and N_f represent the number of colors and active flavors at a given energy scale μ, respectively. The higher order expansion (more loops) of the β–function — as has been calculated in for example [32–34] — will be ignored in our discussion. Taking the first order expansion of Eq. (2.7), the QCD running coupling reads

$$\alpha_s(\mu^2) = \frac{\alpha_s(\mu_0^2)}{1 + \alpha_s(\mu_0^2)\beta_0 \ln\left[\frac{\mu^2}{\mu_0^2}\right]}, \tag{2.9}$$

where μ_0 is a constant of integration which has dimension of energy and should be fixed experimentally.

The strong coupling can be predicted at any perturbative energy scale μ by fixing the renormalized coupling $\alpha_s(\mu_0^2)$ at a given scale μ_0 through the β-function (the RGE). The reference scale μ_0 is commonly defined as Λ. At one loop order, Λ represents the scale where the running strong coupling becomes infinite, as determined by the vanishing of the first order expansion of the β-function (the Landau pole)

$$\beta_0 \ln\left[\frac{\mu^2}{\Lambda^2}\right] \equiv \frac{1}{\alpha_s(\mu^2)} = \frac{1}{\alpha_s(\mu_0^2)} + \beta_0 \ln\left[\frac{\mu^2}{\mu_0^2}\right]. \tag{2.10}$$

Therefore, by setting the renormalization scale to the physical energy scale of the process $\mu^2 = Q^2$, the QCD running coupling can be expressed in a simpler form at one loop order

$$\alpha_s(Q^2) = \frac{1}{\beta_0 \ln\left[Q^2/\Lambda^2\right]}. \tag{2.11}$$

For three active flavors, the value of the reference scale Λ, also commonly referred to as Λ_{QCD}, to be in the range of $200 - 300$ MeV, indicating that QCD becomes strongly coupled when Q becomes smaller than approximately 1 GeV (infinitely large at $Q = \Lambda_{\text{QCD}}$), or equivalently at distances greater than 0.2 fm ($1/\Lambda_{\text{QCD}} \simeq 0.8 - 1$ fm), beyond which perturbative QCD is not applicable. In practice, the standard reference scale used in experiments is the mass of the Z boson, M_Z, determined by the experimental measurements of α_s shown in Fig. 2.2.

The strong coupling behavior around Λ_{QCD} and the rapid growth of α_s at low values of Q (less than 1 GeV) have led to the commonly accepted practice of applying a scale of 1 GeV or higher when using perturbation theory. This serves as a separation between the perturbative and non-perturbative regimes. Predictions of the running coupling behavior as a function of Q by pQCD can be compared to experimental data, as shown in Fig. 2.2(b). This comparison shows that pQCD provides very accurate predictions for the strong coupling behavior of QCD up to the NNLO and N^{3}LO, indicating that pQCD is a valid method for QCD calculations for energies above 1 GeV.

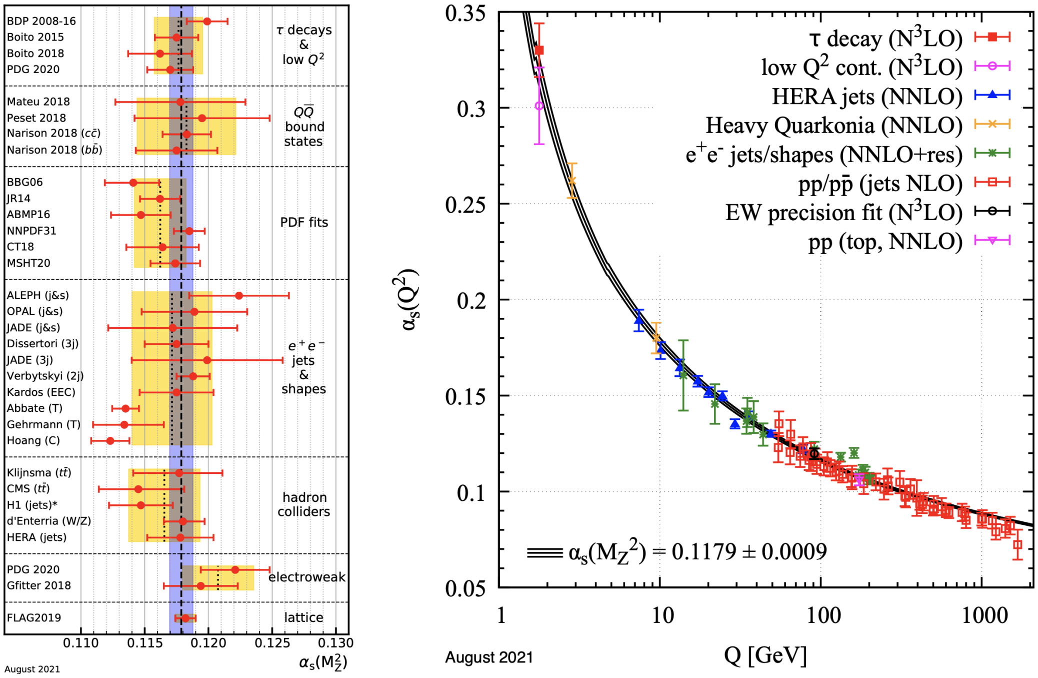

(a) (b)

Figure 2.2: (a) A collection of $\alpha_s(M_Z^2)$ measurements from seven distinct types of data. Here, M_Z represents the mass of the Z^0 gauge boson. The world average of $\alpha_s(M_Z^2)$ is depicted by the dashed line and dark shaded magenta band in the center. (b) A fit to $\alpha_s(Q^2)$ measurements from experiments using QCD perturbation theory. These figures are taken from [35].

Let us return to the examination of the screening and antiscreening effects in relation to the behavior of the running QCD coupling. To gain a deeper understanding of the contribution of these effects, we can analyze the β_0 term in Equation (2.8). The first term in β_0, $11N_c/12\pi$, arises from gluon loops (gluon self-interactions, antiscreening), while the second term, $-2N_f/12\pi$, is a result of quark loops (screening). For the Standard Model where $N_c = 3$ and $N_f = 6$ (in general $N_f \leq 16$), the antiscreening effect dominates, leading to $\beta(\alpha_s) = -\beta_0\alpha_s^2 < 0$ and $\beta_0 > 0$. This behavior illustrates the asymptotic freedom of QCD, where $\alpha_s(Q^2)$ decreases and approaches zero as Q^2 increases to infinity, as depicted in Fig. 2.2(b). It is important to note that the sign of the

β-function changes when $N_f > 16$. In the study of the conformal window, it is indicated that the nature of the theory changes even before $N_f = 16$, see for example [36, 37]. The discussion of large N_f falls outside the scope of this thesis, where in most of the discussions presented here, we will assume $N_f = 4$.

2.2 Deep inelastic scattering (DIS)

The existence of quarks can be detected through DIS of electrons off protons, where an incoming electron emits a virtual photon that collides with the proton target. In contrast to elastic scattering, where the electron scatters without breaking up the proton and no additional hadrons are produced in the final state, high energy virtual photons in DIS can penetrate the internal structure of the proton, resulting in the production of other hadrons in the final state. These observations, which demonstrate consistency between theoretical predictions and experimental measurements from many particle accelerators, provide strong evidence for the presence of quarks inside protons.

The Parton Model (PM) is a commonly used approach in the analysis of DIS experiments. This model, first introduced by Feynman [21], defines partons as the constituents of a hadron, which include quarks, antiquarks, and gluons. In the PM, it is assumed that partons are moving in the same direction as the parent proton, with each parton carrying a fraction x of the proton's momentum. The proton also contains a sea of gluons and quark-antiquark pairs, which fluctuate and interact with each other over time scales much longer than the interaction time between the partons and the virtual photon. Because the interaction between the partons and the virtual photon is short-lived, the virtual photon views the partons as a frozen state. As a result, the PM focuses only on the electromagnetic interaction between the partons and the virtual photon, ignoring any other particle interactions. For a comprehensive review of the Parton Model, see for example [38].

One advantage of using DIS to study the internal structure of a proton is because the DIS cross section can be factorized into two parts: soft and hard part. The *hard* process is the electromagnetic interaction between the virtual photon and the parton. This part is perturbatively calculable in QED. Whereas the parton-parton interactions inside the hadron which is called the *soft* process is not perturbatively calculable process and encoded by the PDFs.

Consider a high energy DIS collision as illustrated in Fig. 2.3

$$e(\ell) + H(P) \to e(\ell') + X(p_X) \tag{2.12}$$

where the electron with momentum ℓ emits a virtual photon and collides with a hadron H (a proton in this case) with momentum P. The collision results in a final state with momentum p_X and mass M_X. After the collision, the final momentum of the electron is ℓ'. In experiments, the virtual photon source can come from any type of lepton, such as electrons, muons, or (anti)-neutrinos, while the target can be any type of hadron, heavy nuclei in addition to a proton. Lead (Pb) and Gold (Au) are the heavy nuclei that are widely used in DIS experiments, particularly at LHC and RHIC.

The interaction between the virtual photon and the proton in DIS depends on the momentum transfer $q = \ell - \ell'$ and the incoming proton momentum P. We can build two important scalar kinematic variables that are Lorentz invariant from these two observables to characterize the DIS

$$x_B = Q^2/\left(2P \cdot q\right) \qquad \text{and} \qquad Q^2 = -q^2. \tag{2.13}$$

Here, x_B is commonly referred to as the Bjorken variable, which in DIS (PM) can be identified with the longitudinal momentum fraction carried by the parton struck by the virtual photon, while Q^2 represents the hard scale at which the proton is probed, also known as the photon virtuality. This Q^2 is a measure of the magnitude of the momentum transferred between the electron and the proton during the scattering process, where the interaction is mediated by a (virtual) photon. As a result, Q^2 characterizes the resolution with which the partons inside the proton can be probed. A high value of Q^2 indicates that the scattering process occurs at a small distance scale, which allows for a more detailed exploration of the internal structure of the proton. Conversely, a low value of Q^2 corresponds to a larger distance scale, leading to the observation of the proton as a more extended object.

In addition to these variables, there are several other kinematic variables that are often used to describe DIS, and will appear frequently throughout this thesis:

$y = (P \cdot q)/(P \cdot \ell)$	*inelasticity,*
$s = (P + \ell)^2$	*electron-proton centre of mass energy,*
$W^2 = (P + q)^2 \simeq ys - Q^2$	*invariant mass; photon-proton centre of mass energy,*
$m^2 = P^2$	*proton mass squared,*
$\nu = (P \cdot q)/m$	*energy transfer.*

In the lab frame y defines the fractional electron energy loss by the incoming particle $y = \frac{E-E'}{E}$, with $\ell^0 = E$ and $\ell'^0 = E'$ indicate the initial and final energy of the electron respectively. When the center-of-mass energy of a collision is much larger than the mass of the target particle, i.e. $s \gg m^2$, we can approximate $Q^2 \simeq xys$, where the dimensionless variables x and y satisfy $0 \leq x \leq 1$ and $0 \leq y \leq 1$.

The cross section of the DIS lepton-proton scattering will be comprised of two key elements, the leptonic term $L_{\mu\nu}$ and the hadronic term $W^{\mu\nu}$

$$\frac{d\sigma}{dxdy} \propto L_{\mu\nu} W^{\mu\nu}. \tag{2.14}$$

The leptonic tensor is determined through perturbative calculations in QED and represents the virtual photon emission from the electron. On the other hand, the hadronic tensor, which characterizes the virtual photon-parton interaction, involves both hard and soft components. The hard part can be evaluated through perturbative methods to yield coefficient functions, while the soft part, a non-perturbative quantity, gives rise to PDFs. The most general form of Lorentz structures will be used to parameterize the hadronic

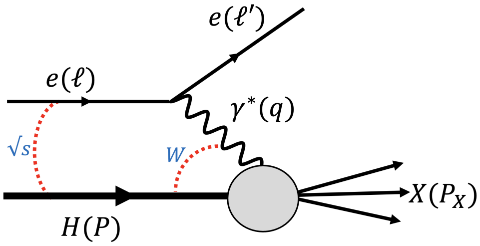

Figure 2.3: The leading order (lowest order in α) diagram of DIS illustrates a high energy electron e which emits a virtual photon γ^* and then interacts with a hadron H, represented as a gray blob. The electron transfers energy ν to the proton through the virtual photon with off-shellness $Q^2 = -q^2$. The momentum of the final state electron, ℓ', is detected, while the momentum of the final state X is integrated over as it is unspecified.

tensor and extract the PDFs from the structure functions. For a polarized proton, we can decompose $W^{\mu\nu}$ into tensor terms times scalar functions

$$\begin{aligned} W^{\mu\nu} = \left(-g^{\mu\nu} + \frac{q^\mu q^\nu}{q^2}\right) F_1(x,Q^2) + \frac{\left(P^\mu - \frac{q^\mu P\cdot q}{q^2}\right)\left(P^\nu - \frac{q^\nu P\cdot q}{q^2}\right)}{P\cdot q} F_2(x,Q^2) \\ + i\epsilon^{\mu\nu\alpha\beta}\frac{q_\alpha S_\beta}{P\cdot q} g_1(x,Q^2) + i\epsilon^{\mu\nu\alpha\beta}\frac{q_\alpha\left(S_\beta - P_\beta\frac{S\cdot q}{P\cdot q}\right)}{P\cdot q} g_2(x,Q^2) \end{aligned} \tag{2.15}$$

with F_1, F_2, g_1 and g_2 the structure functions which encode the non-perturbative information of the structure of the proton. In the unpolarized scattering process, which is the focus of this thesis, the last two terms are zero, leaving only F_1 and F_2. The structure function $F_1(x,Q^2)$ describes the longitudinal polarization of the virtual photon, while $F_2(x,Q^2)$ describes the transverse polarization. Both of these structure functions can be measured in experiments, and they are related to the PDFs in a nontrivial way.

2.3 Parton distribution functions

In the previous discussion, we stated an idea of factorisation where the hard and the soft part in DIS can be separated. While the hard part can be analysed using the perturbative method, the soft part that is described by the PDFs is non-perturbative and should be extracted from experiments. In case PDFs depend only on the longitudinal momentum fraction of a parton of the parent hadron x, the factorisation in hard and soft parts is called collinear factorisation and hence the PDF will be called collinear PDF. If the transverse momentum of the parton $\boldsymbol{k}_\perp$ is considered, we will encounter a transverse momentum dependent (TMD) factorisation where the PDF is known as the TMD PDF or simply TMD. The collinear PDF will be discussed in this chapter, while the TMD PDF will be discussed in chapter 4.

2.3.1 Operator definition of PDFs

To simplify calculations, we will often use light-cone coordinates, which are widely used in the discussion of high-energy scattering. The details of these coordinates can be found in Appendix A. In addition, We will be working in the Breit frame, where the momentum of the proton, photon, and quark, respectively, can be expressed as follows:

$$P^\mu = \left(P^+, P^-, \mathbf{0}_\perp\right) \qquad q^\mu = \left(-\frac{Q}{\sqrt{2}}, \frac{Q}{\sqrt{2}}, \mathbf{0}_\perp\right) \qquad k^\mu = \left(k^+, k^-, \mathbf{0}_\perp\right), \tag{2.16}$$

with $P^+ \gg P^-$ and $k^+ \gg k^-$. However, we will only use this frame as long as $Q^2 > 0$ (for electroproduction). When $Q^2 \to 0$, we will switch to the dipole frame, which is more appropriate for this case, especially when $x_B \to 0$. Further details about these reference frames can be found in Appendix B.

In order to obtain the operator definition of PDFs for the hadronic tensor $W^{\mu\nu}$, we need the help of the so-called handbag diagram. The operator definition of the process shown in the handbag diagram in Fig. 2.4 can be written as

$$\sim \left(\gamma^\mu \not{k} \gamma^\nu\right)^{\beta\alpha} \langle P|\bar{\psi}_\beta(0)|X\rangle\langle X|\psi_\alpha(0)|P\rangle. \tag{2.17}$$

In the leading twist approximation which is valid up to $\mathcal{O}(1/Q)$, the hadronic tensor $W^{\mu\nu}$ can be expressed as

$$W^{\mu\nu} \approx \frac{1}{4}\sum_q e_q^2 \,\mathrm{Tr}\left(\Phi^q(x)\gamma^\mu\gamma^+\gamma^\nu\right) \tag{2.18}$$

where we have ignored the quark mass. Here e_q denotes the electric charge of the parton, and γ^+ is one of the Dirac gamma matrices in light cone coordinates discussed in Appendix A.

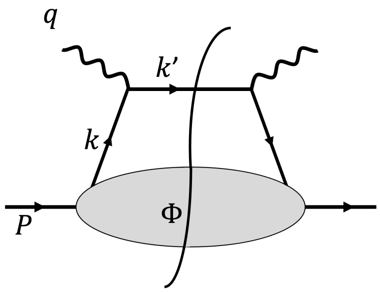

Figure 2.4: The handbag diagram showing a virtual photon scattering off a quark with momentum k inside a proton with momentum P and the momentum of the struck quark is denoted by k'. The blob represents a quark-quark correlator Φ. The wavy vertical line is a final-state cut, which represents the separation between the amplitude (to the left of the line) and its conjugate (to the right of the line).

In the Breit frame, it is assumed that the outgoing quark momentum moves in the minus direction after the collision, with $k'^{\mu} = k^{\mu} + q^{\mu} \approx (-k^{+}, k^{+}, 0)$, see Appendix B. As a result, the Bjorken variable can be approximated as

$$x_B = \frac{Q^2}{2P \cdot q} \simeq x = \frac{k^+}{P^+} \tag{2.19}$$

where we have used the fact that the momentum of the proton and the quark are dominated by the plus component. Here, x denotes the light cone momentum fraction carried by the struck quark. In this way, we will only discuss the collinear PDF, which solely depends on x. We have also introduced the integrated quark correlation function (correlator) $\Phi(x)$, which is defined as follows

$$\Phi(x)_{\alpha\beta} \equiv \int \frac{dz^-}{2\pi} \mathrm{e}^{ixP^+z^-} \langle P|\bar{\psi}_\beta(0^+, 0^-, \mathbf{0}_\perp)\psi_\alpha(0^+, z^-, \mathbf{0}_\perp)|P\rangle, \tag{2.20}$$

The integrated correlator is derived from the unintegrated quark-quark correlator, which is defined as follows

$$\Phi_{\alpha\beta}(k) \equiv \int \frac{d^4z}{(2\pi)^4} \mathrm{e}^{ik\cdot z} \langle P|\bar{\psi}_\beta(0)\psi_\alpha(z)|P\rangle. \tag{2.21}$$

The correlator mentioned above is called the unintegrated correlator because it depends on the full quark four-momentum. The relation between the collinear integrated correlator $\Phi(x)$ and the unintegrated correlator is the following

$$\Phi(x) = \int dk^- d^2\boldsymbol{k}_\perp \Phi(x, k^-, \boldsymbol{k}_\perp). \tag{2.22}$$

We should note that this is a naive relation. When this relation is used to define TMDs, as seen in, for example, [39], there may be issues with its convergence. This topic will be discussed further in Chapter 6.

The collinear PDF is constructed from the expansion of the integrated quark correlator (in the leading twist), which is similar to the parametrization method used for the structure function in Eq. (2.15). By applying this parametrization method, the unpolarized collinear PDF is defined by projecting the integrated correlator on the corresponding gamma matrices, see for example [39, 40]

$$f_q(x) = \frac{1}{2}\mathrm{Tr}\left(\Phi(x)\gamma^+\right). \tag{2.23}$$

We will revisit this PDF later after discussing the gauge invariance of the correlator.

Upon examining the unintegrated correlator in Eq. (2.21), it becomes clear that the expression for the unintegrated quark-quark correlator must be incomplete. This is because this type of two-point correlation function, which contains two quark fields at two different spacetime points, is not gauge invariant and therefore violates the (gauge) symmetry of the theory. In order to address this issue, we will investigate the problem further and show that the solution will lead to the introduction of the Wilson line.

First, we recall that under a non-Abelian gauge transformation, a Dirac field will transform as

$$\psi(x) \to V(x)\psi(x) \qquad\qquad \bar{\psi}(x) \to \bar{\psi}(x)V^\dagger(x) \tag{2.24}$$

with

$$V(x) = \mathrm{e}^{i\alpha_a(x)t_a}. \tag{2.25}$$

Applying this transformation to the unintegrated correlator we see that the correlator transforms as

$$\Phi(k) \to \int \frac{d^4z}{(2\pi)^4}\mathrm{e}^{ik\cdot z}\langle P|\bar{\psi}_\beta(0)V^\dagger(0)V(z)\psi_\alpha(z)|P\rangle, \tag{2.26}$$

which is clearly not gauge invariant. However, the gauge invariance of the quark correlator (or any two-point function in general) can be maintained by inserting an object that connects those two different spacetime points. Under a local SU(3) transformation, this object should transform as

$$\mathcal{U}_{[0,z]} \to V(0)\mathcal{U}_{[0,z]}V^\dagger(z). \tag{2.27}$$

This object is called a *Wilson line* — also called a *gauge link*— which in the fundamental representation takes the form

$$\mathcal{U}_{[x,y]} \equiv \mathcal{P}\exp\left[ig\int_x^y A_\mu^a(z)t^a dz_\mu\right] \tag{2.28}$$

with $\mathcal{P}$ is a path ordering operator and defined as

$$\mathcal{P}A(x)B(y) \equiv \theta(x-y)A(x)B(y) + \theta(y-x)B(y)A(x), \tag{2.29}$$

with θ is the Heaviside step function, which takes the value 0 when $x < y$, and 1 when $x \geq y$. The path ordering operator plays an important role for the non-Abelian case, because unlike in the Abelian case, the gauge fields A_μ at different points along the path do not necessarily commute. In Eq. (2.28), t^a are generators of SU(3) (in the fundamental representation) indicating that the Wilson line can be viewed as a rotation of the color state of the particle.

Finally, the gauge invariant unintegrated quark-quark correlator is obtained by inserting the Wilson line to the correlator given by

$$\Phi_{\alpha\beta}(k) \equiv \int \frac{d^4z}{(2\pi)^4}\mathrm{e}^{ik\cdot z}\langle P|\bar{\psi}_\beta(0)\,\mathcal{U}_{[0,z]}\,\psi_\alpha(z)|P\rangle. \tag{2.30}$$

We note that in the light-cone gauge, where $A^+ = 0$, the Wilson line becomes unity and can be omitted from the definition of the collinear PDF.

In the above the Wilson line is inserted into the correlator by hand and seems arbitrary without any physical justification. However, it turns out that the Wilson line is a resummation of an infinite number of gluons emitted by the struck quark, thus it has a physical basis. This resummation can be related to the eikonal approximation, which describes the interaction of a high-energy quark with the target and will be further discussed in the next section.

2.3.2 Wilson line and eikonal approximation

In high-energy DIS, a virtual photon collides with a quark. The struck quark, moving with very high momentum, can emit and absorb many soft gluons without any change in its initial momentum. This picture is known as the *eikonal approximation*. In this approximation, the infinite gluons emitted by the struck quark would be resummed as a Wilson line, which was previously encountered in the discussion of PDFs. The eikonal approximation is valid in the high-energy limit where the coupling constant is small, and the typical momentum transfer of the gluons is much smaller than the energy of the parent hadron. In this limit, the probability for multiple gluon emission is large. We will discuss how the Wilson line arises from resumming the infinite soft gluon exchanges in the eikonal approximation.

Consider a high-energy quark with momentum $k' = (k'^{+}, k'^{-}, \mathbf{0}_{\perp})$, which emits a soft gluon with momentum l as shown in Fig. 2.5(a). We are working in the Breit frame, where the quark momentum is highly boosted in the direction of its motion such that the momentum of the quark is dominated by the plus component, i.e., $k'^{+} \gg k'^{-}$. Following the Feynman rules described in Appendix C, the soft gluon emission process shown in Fig. 2.5(a) can be written as

$$\frac{i(\not{k}' + \not{l})}{(k'+l)^2 + i\epsilon} \left(-igt^a\gamma^u\right) u(k'), \tag{2.31}$$

where $u(k')$ is the quark spinor. In the eikonal approximation, where the momentum of the quark is much larger than that of the soft gluon, which is equal to neglecting l with respect to k' and using $k'^{+} \gg k'^{-}$, Eq. (2.31) can be approximated as

$$\frac{i(\not{k}' + \not{l})}{(k'+l)^2 + i\epsilon} \left(-igt^a\gamma^u\right) u(k') \quad \approx \quad \frac{in^{\mu}}{n \cdot l + i\epsilon} \left(-igt^a\right) u(k'), \tag{2.32}$$

where n^{μ} is a light like vector defined in Appendix A that can be used to express the light-like momentum such that $k'^{\mu} = |k'|n^{\mu}$. In obtaining Eq. (2.32), we used the fact that $\not{k}' u(k') = 0$, the anticommutation relation $\{\gamma^{\mu}, \gamma^{\nu}\} = 2g^{\mu\nu}$, and rewrote the quark momentum in terms of the directional vector n^{μ}. This equation shows that applying the eikonal approximation to the soft gluon emission process is equivalent to replacing the Dirac propagator with the Wilson line propagator

$$\frac{i(\not{k}' + \not{l})}{(k'+l)^2 + i\epsilon} \xrightarrow{\text{eikonal appr.}} \frac{in^{\mu}}{n \cdot l + i\epsilon} \tag{2.33}$$

This procedure can be extended to include infinite gluon emission, which is then represented by a Wilson line which runs from $-\infty$ to 0, see, for example [40]

$$\mathcal{U}_{[-\infty,0]} = \sum_{n=0}^{\infty} (ig)^n \int \frac{d^4 l_n}{16\pi^4}\, n\cdot A(l_n)\ldots n\cdot A(l_1) \prod_{j=1}^{n} \frac{-i}{n\cdot \sum_{k=1}^{j} l_k + i\epsilon}. \tag{2.34}$$

In this case, a high-energy quark that emits an infinite number of soft gluons can be approximated as a bare quark times a Wilson line running from $-\infty$ to 0, as illustrated in Fig. 2.5.

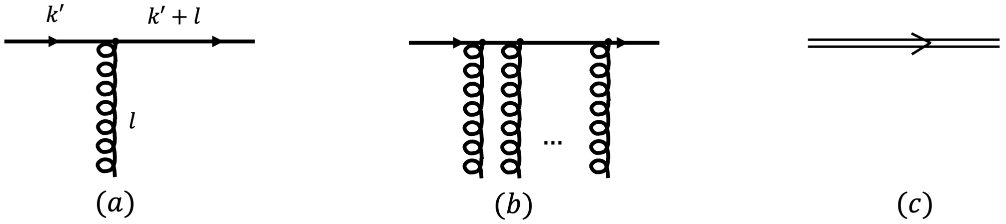

Figure 2.5: (a) A bare quark with momentum k' emits a soft gluon with momentum l. (b) A bare quark emits an infinite number of gluons. (c) In the eikonal approximation, resummation of infinite soft gluon emissions leads to a Wilson line (represented by the double line).

2.3.3 Collinear PDFs

We will now utilize the eikonal approximation discussed earlier to analyze the correlator $\Phi(x)$. This will allow us to demonstrate that the Wilson line arises from a physical phenomenon, specifically a resummation of infinitely many soft gluon exchange during the process. At the same time, the Wilson line also serves as an object that ensures the gauge invariance of the correlator. We begin by considering a first-order correction of the PDF, in which one soft gluon connects the struck quark with a blob, as shown in the handbag diagram in Fig. 2.6(a). This diagram contributes to the hadronic tensor as [40]

$$W^{\mu\nu} \sim \sum_q e_q^2 \frac{1}{2} \mathrm{Tr}\left[\Phi_\rho(k)\gamma^\mu\gamma^+\gamma^\rho \frac{\slashed{k}' - l}{(k'-l)^2 + i\epsilon}\gamma^\nu\right]. \tag{2.35}$$

Here, Φ_ρ is the quark-quark-gluon correlator

$$\Phi_\rho(k) \equiv \frac{1}{2}\int \frac{d^4 z}{(2\pi)^4}\frac{d^4 u}{(2\pi)^4} \mathrm{e}^{ik\cdot z}\mathrm{e}^{il\cdot(u-z)} \langle P|\bar{\psi}_\beta(0) g A_\rho(u)\psi_\alpha(z)|P\rangle. \tag{2.36}$$

Following the previous procedure of applying the eikonal approximation to the high energy quark, the Dirac propagator term can then be approximated as

$$\gamma^+\gamma^\rho \frac{\slashed{k}' - l}{(k'-l)^2 + i\epsilon} \approx \gamma^+\gamma^\rho \frac{\slashed{k}'}{-2k'\cdot l + i\epsilon} = \frac{-\gamma^+ n_\rho}{n\cdot l - i\epsilon} \tag{2.37}$$

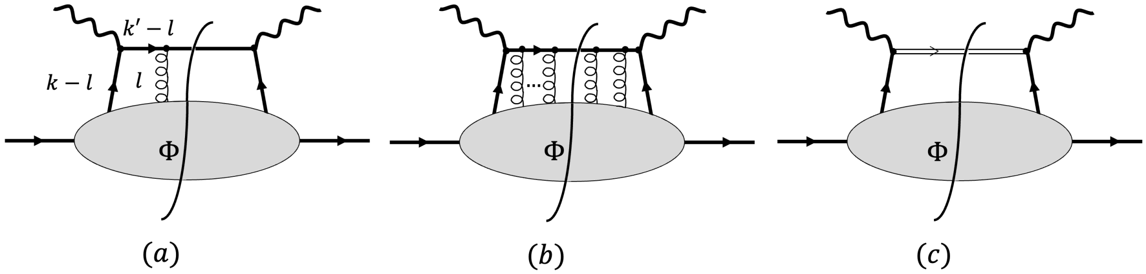

Figure 2.6: (a) A soft gluon exchange connects the struck quark and the blob, which represents the quark-quark-gluon correlator. Infinite soft gluon exchanges (b) can be resummed as a Wilson line represented by the double lines (c). Reproduced from Ref. [40].

which is a Wilson line propagator, see Appendix D.2. In this approximation, we utilize the fact that the quark is predominantly moving in the positive direction, leading to the suppression of the negative component with respect to the positive component. As previously mentioned, the Wilson line propagator replaces the Dirac propagator.

By using the perturbative expansion of the Wilson line in the momentum space

$$\mathcal{U}_{[z,+\infty]} = \sum_{n=0}^{\infty}(ig)^n \int \frac{d^4 l_n}{16\pi^4} n\cdot A(l_n)\ldots n\cdot A(l_1)\mathrm{e}^{iz\sum_n l_j}\prod_{j=1}^{n}\frac{-i}{n\cdot\sum_{k=1}^{j} l_{n-k+1} - i\epsilon} \tag{2.38}$$

and the Wilson line property

$$\mathcal{U}_{[x,y]} = \mathcal{U}^{\dagger}_{[y,x]}, \tag{2.39}$$

the single soft gluon emission in Equation 2.37 can be extended to include many soft gluon emissions, which are then absorbed in the definition of the quark-quark-gluon correlator as a Wilson line running from 0 to z^-

$$\mathcal{U}^{-}_{[0,z^-;\mathbf{0}_\perp]} \equiv \mathcal{P}\mathrm{e}^{ig\int_0^{z^-} d\lambda\ n\cdot A(0^+,\lambda^-,\mathbf{0}_\perp)}, \tag{2.40}$$

upon integrating over l. The correlator, as defined by Eq. (2.22), should be integrated over k^- and $\boldsymbol{k}_\perp$. Since we are discussing the collinear PDF, the correlator is evaluated at $z^+ = \boldsymbol{z}_\perp = 0$ or equivalently $z^2 = 0$. Thus, the quark-quark-gluon correlator can be expressed as follows:

$$\Phi_{\alpha\beta}(x) = \int \frac{dz^-}{2\pi}\mathrm{e}^{ixP^+z^-}\langle P|\bar{\psi}_\beta(0^+,0^-,\mathbf{0}_\perp)\mathcal{U}^{-}_{[0^-,z^-;\mathbf{0}_\perp]}\psi_\alpha(0^+,z^-,\mathbf{0}_\perp)|P\rangle, \tag{2.41}$$

where the hadronic tensor now reads

$$W^{\mu\nu} \approx \frac{1}{2}\sum_q e_q^2 \mathrm{Tr}\left[\Phi(x)\gamma^\mu\gamma^+\gamma^\nu\right]. \tag{2.42}$$

Another useful property of the Wilson line is that it can be decomposed into two lines such that

$$\mathcal{U}^{-}_{[0^-,z^-;\mathbf{0}_\perp]} = \mathcal{U}^{-}_{[0^-,+\infty;\mathbf{0}_\perp]}\mathcal{U}^{-}_{[+\infty,z^-;\mathbf{0}_\perp]}. \tag{2.43}$$

This property allows us to associate a separate line with the quark on each side of the cut, which is important when discussing the Wilson line in TMD PDFs that depend on more variables. It should be noted that this decomposition only applies when the path does not involve a transverse direction. In the case of TMD PDFs, the Wilson line does involve a transverse component (at lightcone infinity), so a decomposition in the transverse direction must also be considered which will be discussed in Chapter 4. The Wilson lines and a gauge invariant two-point function and its properties is discussed in Appendix D.2. We should also note that the introduction of the Wilson line to the correlator can result in path-dependent results, which in turn leads to process-dependent PDFs. Consequently, the same hadron may have different PDFs in different processes, depending on the specific path taken by the Wilson line, where in the context of the collinear PDF, the path will be in the plus or minus direction. In general we can only predict processes that involve the same path or a path that can be related to it.

From the definition of the PDF in Eq. (2.23) the operator definition of the integrated unpolarized collinear quark PDF for a quark with flavor q at leading twist approximation can be constructed as

$$f_q(x) = \int \frac{dz^-}{4\pi} \mathrm{e}^{ixP^+z^-} \langle P|\bar{\psi}(0^+,0^-,\mathbf{0}_\perp)\mathcal{U}^{-}_{[0^-,+\infty;\mathbf{0}_\perp]}\gamma^+\mathcal{U}^{-}_{[+\infty,z^-;\mathbf{0}_\perp]}\psi(0^+,z^-,\mathbf{0}_\perp)|P\rangle. \tag{2.44}$$

The anti-quark PDF has the same form as the quark PDF, but the direction of the Wilson line is reversed. Using a similar procedure, the integrated gluon PDF can also be obtained as

$$f_g(x) = \int \frac{dz^-}{2\pi}\frac{1}{xP^+} \mathrm{e}^{ixP^+z^-} \langle P|F^{+j\,a}(0^+,0^-,\mathbf{0}_\perp)\, U^{-\,ab}_{[0^-,z^-;\mathbf{0}_\perp]}\, F^{+j\,b}(0^+,z^-,\mathbf{0}_\perp)|P\rangle, \tag{2.45}$$

Since we are discussing gluons, we require the adjoint Wilson line, denoted as $U^{ab}_{[x,y]}$, which connects two gluons at different spacetime points

$$U^{ab}_{[x,y]} \equiv \mathcal{P}\exp\left[ig\int_x^y A^c_\mu(z)T^c_{ab}dz_\mu\right] \tag{2.46}$$

where T^a represents the generators of the QCD gauge group in the adjoint representation which obey relations

$$[T^a,T^b] = if^{abc}T^c \qquad \mathrm{Tr}\left(T^aT^b\right) = 3\delta^{ab}. \tag{2.47}$$

where the first relation (the Lie algebra commutation relations) is satisfied by the generators in any representation, thus also in the fundamental representation t^a, cf. Eq. (2.3), while the second relation (the trace) has a representation dependent prefactor.

In the collinear factorization framework, the quark PDFs enter the deep inelastic scattering (DIS) cross section as:

$$\frac{d\sigma}{dx} \sim H(x, \mu^2)\ f_q(x, \mu^2), \tag{2.48}$$

where $H(x, \mu^2)$ represents the hard part that depends on Q^2 and also on the type of parton (q), which is summed over. The variable μ denotes the energy of the factorization scale. The soft part, described by the PDFs $f_q(x, \mu^2)$, captures the probability of finding a parton of type q inside a proton. The PDFs obey the DGLAP (Dokshitzer-Gribov-Lipatov-Altarelli-Parisi) evolution equations [41–43], which allow them to be evolved from one energy scale to another. The DGLAP equations are a set of linear evolution equations that describe the behavior of PDFs as a function of energy, i.e. their μ dependence, enabling us to make predictions for experiments performed at different energies.

By studying the behavior of the PDFs as a function of x and μ, we can gain insight into the parton distribution inside the proton. The extraction of PDFs and their fits have been studied by many research groups, such as NNPDF [44], CT [45], MSTW [46], CTEQ [47], HERAPDF [48], and ABMP [49]. These groups use different methods and assumptions in their PDF fits, providing different sets of PDFs. Significant progress has been made in the extraction and understanding of PDFs. One of the intriguing results of these PDF fits is that they confirm that gluons dominate the proton content in the small x region (high energy), as seen in Fig. 2.7. This result has prompted the study of small x physics, which focuses on the gluon content of the proton, where the quark PDFs can be neglected with respect to the gluon PDFs.

At small values of x, the probability of finding a parton carrying a certain fraction of the proton's momentum increases significantly. This also follows from the fact that the DGLAP splitting function, which defines the probability of a gluon splitting into another gluon with a fraction of its momentum x, behaves like $P_{gg} \propto 1/x$ in the limit $x \to 0$. Perturbative corrections contain logarithms in $1/x$ that become large at small x and which become very relevant because of the large gluon distribution. These large logarithms need to be resummed to all orders in perturbation theory, and the BFKL (Balitsky-Fadin-Kuraev-Lipatov) equation [51–53] was developed to achieve this. Similar to the DGLAP equation, which describes the collinear evolution of the parton distributions, the BFKL equation is linear in the gluon distribution. However, at even smaller values of x, the gluon density in the proton becomes so high that the nonlinear effects become important, leading to a moderation of the growth of the gluon density. This phenomenon is known as gluon saturation. In this regime, single-gluon scatterings are unlikely, and instead, it is necessary to consider multi-gluon distributions as function of x and transverse momentum or its Fourier conjugate $\boldsymbol{r}_\perp$. Therefore, the Color Glass Condensate framework, which describes the proton as a collection of densely packed interacting gluons, cannot simply be described by the gluon PDF $f_g(x)$ with modified x behavior. The saturation regime and how it can be described is the main topic of the next chapter.

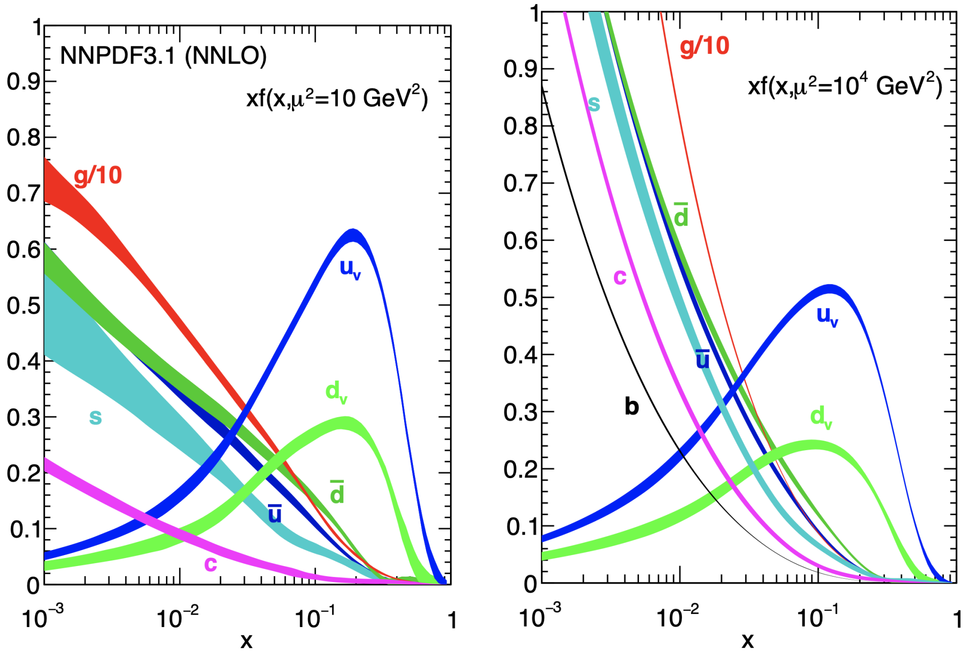

(a) (b)

Figure 2.7: Collinear (unpolarized) parton distribution functions $f(x, \mu^2)$ times x, evaluated at two different energy scales (a) $\mu^2 = 10$ GeV^2 and (b) $\mu^2 = 10^4$ GeV^2 obtained from NNLO NNPDF3.1 global analysis [50]. Here f of different parton types (u_v, d_v, $\bar{u}$, $\bar{d}$, $s \simeq \bar{s}$, $c \simeq \bar{c}$, $b \simeq b$, g) are indicated by different color with v meaning valence quark. Both plots show that at $x \lesssim 10^{-2}$ the proton content is dominated by the gluon (red) where the gluon PDF is divided by 10. In fact, the gluons exceed the quark distributions already at $x = 0.1$.

3

The Color Glass Condensate

The Color Glass Condensate (CGC) framework is an effective field theory that describes high-energy scattering processes ($s \gg Q^2$, i.e. small x) where the partonic content of a fast-moving hadron is dominated by gluons, as discussed previously. At high energies, gluon densities rapidly increase and their occupation numbers become large enough to be treated classically. This rapid increase in density leads to non-linear phenomena and results in gluon saturation. The CGC framework proposes that the higher momentum fraction partons are the source of the partons with smaller momentum fraction. The name CGC derives from the fact that it is a state of frozen disorder (like a glass), in this case frozen color charges, which has high occupation number (like a condensate). It is approximately frozen, in the sense that as a whole it evolves slowly compared to the time scale of the gluonic interactions. A detailed overview of the CGC can be found in e.g. [25, 54].

In this chapter, we provide a brief overview of the CGC framework in Sec. 3.1, which will be used to study high energy DIS. We then discuss the dipole picture description of DIS in Sec. 3.2. In Sec. 3.3, we investigate the widely used Gaussian weight function proposed by McLerran-Venugopalan (MV). The original MV model does not incorporate the dependence on either x or the impact parameter $\boldsymbol{b}_\perp$, both of which are expected to be necessary to accurately represent the phenomena observed in accelerators. To address this issue, several models have been proposed, including the Golec-Biernat-Wusthoff (GBW) model, which captures the saturation effect and successfully describes small x and small Q^2 data at HERA. We discuss the GBW model in Sec. 3.4. In Sec. 3.5, we explore the concept of geometric scaling as a possible indication of the saturation phenomenon.

3.1 A Brief Overview of the CGC Framework

In the CGC framework, at high energies, the partonic content of a hadron with large P^+ momentum can be described in terms of small-x partons (gluons essentially) that are emitted from partons with large x values (quarks essentially) that have high momentum xP^+. In a high-energy collision, these emitted small-x gluons form a classical strong gluon field which replaces the usual partonic description. In this scheme, the partons with large xP^+ momentum are treated as static color sources ρ. For the probe, due to time dilation, these sources are frozen in time. Because the gluon density is high or in other words, the occupation number of gluons is very large, these sources can be treated classically. These sources generate a current that is assumed to move in the z^+ direction (the dipole which scatters off the hadron is assumed to move in the z^- direction) [55]

$$J^\mu(z) = \delta^{\mu +}\rho(z^-, \boldsymbol{z}_\perp) \tag{3.1}$$

with $\rho = \rho_a T^a$. The colour field can be obtained by solving the classical Yang-Mills equations

$$[D_\mu, F^{\mu\nu}] = J^\nu \tag{3.2}$$

with $D_\mu = \partial_\mu - igA_\mu$ and $F^{\mu\nu}$ is the the colour field strength tensor. This equation should fulfil the conservation equation $[D_\mu, J^\mu] = 0$.

In the CGC framework, the distribution of color sources present in high-energy hadrons must be calculated by taking the average over all possible distributions of sources. The expectation value of an observable, represented by the classical color field $\mathcal{O}(\rho)$, for a particular source distribution ρ can be obtained through a path integral, see e.g. [25, 56]

$$\langle O \rangle = \int [\mathcal{D}\rho]\, \mathcal{W}[\rho]\, \mathcal{O}[\rho]. \tag{3.3}$$

The weight function $\mathcal{W}[\rho]$ is related to the color source distribution and is model dependent. In Sec. 3.3, we will provide the description of the weight function when discussing the MV model.

3.2 DIS in the dipole picture

When the density of gluons is very high, the probability that gluons interact will approach 1. At this point, instead of the scattering of the virtual photon off a single gluon from the target, scattering off multiple gluons simultaneously should be taken into account. This is expected to lead to moderation of the growth of the gluon distribution, which means saturation is expected to occur. Therefore, a new description of DIS is required at small values of x that incorporates the possibility of multiple scattering. In this regime, the dipole picture [57, 58] is frequently employed to describe DIS.

Within the framework of the dipole picture, DIS ep collisions can be thought of as a two-step process. First, the incoming electron emits a virtual photon that does not carry a color charge and fluctuates into a quark-antiquark pair (a color dipole). During the second step, the dipole interacts with the target through vacuum quantum number exchange, known as the pomeron which is typically represented by two gluons [59–61]. This interaction is illustrated in Figure 3.1. The former step is calculable in perturbative QED and can be described by the lightcone wave function Ψ of the virtual photon splitting into a $q\bar{q}$, while the latter is encoded by the dipole scattering amplitude, which incorporates both perturbative and non-perturbative factors in the leading order. For the next-to-leading-order corrections, the dipole factorization has been calculated in e.g. [62] and has been fitted to HERA data in e.g. [63]. In this thesis, we will only discuss the leading order, but for processes beyond DIS.

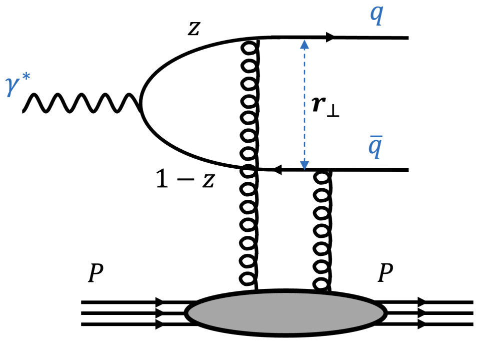

Figure 3.1: A lowest order diagram of DIS ep scattering. The virtual photon γ^* emitted by the electron splits into quark-antiquark pair (dipole) which scatters off the proton target P via two-gluon exchanges.

.

The cross section for $\gamma^* p$ scattering can be obtained using the optical theorem and taking the imaginary part of the forward dipole scattering amplitude $\mathcal{N}(x, \boldsymbol{r}_\perp, \boldsymbol{b}_\perp)$ convoluted with Ψ, which then takes the form:

$$\sigma_{T,L}^{\gamma^* p}(x, Q^2) = 2 \int dz\, d^2\boldsymbol{r}_\perp\, d^2\boldsymbol{b}_\perp \left|\Psi_{T,L}(z, \boldsymbol{r}_\perp, Q^2)\right|^2 \mathcal{N}(x, \boldsymbol{r}_\perp, \boldsymbol{b}_\perp), \tag{3.4}$$

where the indices T and L denote the transverse and longitudinal polarisation of the photon, respectively. Here, $z = k^+/q^+$ represents the longitudinal momentum fraction of the quark with respect to the photon q, where k denotes the quark momentum after the interaction. In this equation, $\boldsymbol{r}_\perp = \boldsymbol{x}_{1\perp} - \boldsymbol{x}_{2\perp}$ represents the transverse separation between the quark and the antiquark or the dipole size, where $\boldsymbol{x}_{1\perp}$ and $\boldsymbol{x}_{2\perp}$ are the quark and the antiquark transverse positions, respectively. Here we use an explicit expression that depends on the impact parameter $\boldsymbol{b}_\perp$ which is given by the average of the transverse positions of the quark and the antiquark, i.e., $\boldsymbol{b}_\perp = (\boldsymbol{x}_{1\perp} + \boldsymbol{x}_{2\perp})/2$. In a model where the impact paramater is not considered, the integration over $\boldsymbol{b}_\perp$ would be replaced by a constant $\sim \sigma_0$.

In the leading order, the photon lightcone wave functions can be written as [62, 64]

$$\Psi(\boldsymbol{r}_\perp, z) = (2\pi)^2\, 2ee_f\, \sqrt{z(1-z)}\Phi_{T,L}(\boldsymbol{r}_\perp, z)\delta_{h_q,h_{\bar{q}}} \tag{3.5}$$

with ee_f denotes the electric charge of a quark with flavor f, while h_q and $h_{\bar{q}}$ are the helicity of the quark and antiquark, respectively. The one loop corrections of the photon wave function has been calculated in e.g. [65] which will not be considered in this thesis. For the leading order, the scalar function $\Phi_{T,L}(\boldsymbol{r}_\perp, z)$ are defined as

$$\begin{aligned} \Phi_T(\boldsymbol{r}_\perp, z) &\equiv i\,(1-2z-2h_1\lambda)\,\frac{\epsilon_\lambda \cdot \boldsymbol{r}_\perp}{r_\perp^2} Q\sqrt{z(1-z)r_\perp^2} K_1\left(Q\sqrt{z(1-z)r_\perp^2}\right) \\ \Phi_L(\boldsymbol{r}_\perp, z) &\equiv -2z(1-z)QK_0\left(Q\sqrt{z(1-z)r_\perp^2}\right) \end{aligned} \tag{3.6}$$

with λ denotes the polarisation of the photon and $K_{0,1}(x)$ are the modified Bessel function of the second kind which decay rapidly when the argument increases. Explicitly, the squared photon wave functions can be expressed as

$$\begin{aligned} |\Psi_T(z, \boldsymbol{r}_\perp)|^2 &= \frac{6\alpha_{\text{em}}}{4\pi^2} \sum_f e_f^2 \left(\left[z^2 + (1-z)^2\right] \varepsilon_f^2 K_1^2(\varepsilon_f r_\perp) + m_f^2 K_0^2(\varepsilon_f r_\perp)\right) \\ |\Psi_L(z, \boldsymbol{r}_\perp)|^2 &= \frac{6\alpha_{\text{em}}}{4\pi^2} \sum_f e_f^2 \left(4Q^2 z^2 (1-z)^2 K_0^2(\varepsilon_f r_\perp)\right). \end{aligned} \tag{3.7}$$

The sum runs over the quark flavor f, while e_f is the quark charge, and $\varepsilon_f^2 \equiv z(1-z)Q^2 + m_f^2$ with m_f denotes the quark mass which will be neglected in most of our calculation.

The final ingredient of the cross section is the dipole scattering amplitude, which is defined as

$$\mathcal{N}(x, \boldsymbol{r}_\perp, \boldsymbol{b}_\perp) \equiv 1 - S(x, \boldsymbol{r}_\perp, \boldsymbol{b}_\perp), \tag{3.8}$$

where 1 represents the non-interacting term. As discussed in the previous chapter 2.3.2, the collinear quark PDFs require gauge invariance. Similarly, the S-matrix representing the probability amplitude for the dipole with size $\boldsymbol{r}_\perp$ to scatter off the hadron with impact parameter $\boldsymbol{b}_\perp$ should also be a gauge invariant expression. At small x, the S-matrix can be related to a two-point function of the Wilson lines that result from the summation of all gluon exchanges of the quark and antiquark of the dipole with the target during the scattering process, see e.g. [66, 67]. This two-point function can be defined as:

$$S(x, \boldsymbol{r}_\perp, \boldsymbol{b}_\perp) \equiv \left\langle \frac{1}{N_c} \text{Tr}\left[\mathcal{U}^\dagger(\boldsymbol{b}_\perp - \frac{\boldsymbol{r}_\perp}{2})\mathcal{U}(\boldsymbol{b}_\perp + \frac{\boldsymbol{r}_\perp}{2})\right]\right\rangle_C, \tag{3.9}$$

where $N_c = 3$ denotes the number of color and C indicates an average over the target color charge configurations. In Chapter 4 on GTMDs, the average $\langle \mathcal{O}(\boldsymbol{r}_\perp, \boldsymbol{b}_\perp)\rangle_C$ will be related at small x (following [68]) to off-forward matrix elements of the form

$\langle P'|\mathcal{O}(\boldsymbol{r}_\perp, \boldsymbol{b}_\perp)|P\rangle / \langle P|P\rangle$ or equivalently, $\langle P^+, \boldsymbol{R}_\perp = 0|\mathcal{O}(\boldsymbol{r}_\perp, \boldsymbol{b}_\perp)|P^+, \boldsymbol{R}_\perp = 0\rangle$ where $\boldsymbol{R}_\perp$ is the transverse center of longitudinal momentum.

In the definition of the S-matrix in Eq. (3.9), we use the Wilson line in the fundamental representation, which contains the transverse direction and is given by

$$\mathcal{U}(\boldsymbol{x}_\perp) \equiv \mathcal{P} \exp\left[ig \int A_a^+(0^+, z^-, \boldsymbol{x}_\perp) t^a dz^-\right]. \tag{3.10}$$

The Wilson line that goes in the transverse direction is a crucial component of the TMD PDFs, which will be discussed further in Chapter 4. This transverse piece that appears at lightcone infinity arises due to the inclusion of gluon exchanges [69–71]. In the Feynman gauge, it is often ignored, but in the lightcone gauge $A^+ = 0$, it must be included due to gauge invariance. The expression given by Eq. (3.9) should be closed as a (rectangular) loop at infinity with the inclusion of the transverse piece, hence it is usually referred to as the Wilson loop operator [72].

At high energy, the interaction between the dipole and the target is eikonal, meaning that the quark transverse position $\boldsymbol{x}_{1\perp} = \boldsymbol{b}_\perp + \frac{\boldsymbol{r}_\perp}{2}$ and the antiquark transverse position $\boldsymbol{x}_{2\perp} = \boldsymbol{b}_\perp - \frac{\boldsymbol{r}_\perp}{2}$ do not change during the process. However, the quark (as does the antiquark) undergoes a color rotation in the target color field, picking up a Wilson line $\mathcal{U}(\boldsymbol{b}_\perp + \frac{\boldsymbol{r}_\perp}{2})$, while the antiquark picks up a conjugate Wilson line $\mathcal{U}^\dagger(\boldsymbol{b}_\perp - \frac{\boldsymbol{r}_\perp}{2})$. The S-matrix encodes all the information about the hadronic scattering and can depend on x, $\boldsymbol{r}_\perp$, and $\boldsymbol{b}_\perp$. It cannot be calculated in perturbation theory, even though the coupling constant turns out to be small (large logarithms in $1/x$ necessitate resummation). An all-order expression for it was obtained by assuming a Gaussian distribution of colour sources, which is the widely-used model proposed by McLerran and Venugopalan that will be discussed in the following section.

3.3 The McLerran-Venugopalan Model

In the McLerran-Venugopalan (MV) model [55,73,74], the weight function $\mathcal{W}[\rho]$ appearing in Eq. (3.3) is assumed to be Gaussian which takes the form

$$\mathcal{W}[\rho] = \exp\left[-\frac{1}{2}\int dx^- d^2\boldsymbol{x}_\perp \frac{\rho_a(x^-, \boldsymbol{x}_\perp)\rho^a(x^-, \boldsymbol{x}_\perp)}{\mu^2(x^-)}\right] \tag{3.11}$$

where μ^2 is the average charge density squared per unit of transverse area. The distribution of the color sources $\rho_a(x^-, \boldsymbol{x}_\perp)$ in the nucleus will take the form [56]

$$\langle \rho_a(x_1^-, \boldsymbol{x}_{1\perp})\rho_b(x_2^-, \boldsymbol{x}_{2\perp})\rangle = \delta_{ab}\mu^2(x^-)\delta(x_1^- - x_2^-)\delta(\boldsymbol{x}_{1\perp} - \boldsymbol{x}_{2\perp}), \tag{3.12}$$

where in the original MV model the density of partons per unit area N per unit rapidity y for a large nucleus with radius R is defined as [73]

$$\rho = \frac{1}{\pi R^2}\frac{dN}{dy} \tag{3.13}$$

which is assumed to be large $\rho \gg \Lambda_{\text{QCD}}$

The distribution of the color sources μ^2 can be related to the saturation scale Q_s, which marks the energy scale at which the density of gluons inside a nucleus becomes so high that nonlinear QCD effects start to play a role and the exponential growth of the gluon distribution is stopped [56]. This phenomenon is described by nonlinear evolution equations such as the Balitsky-Kovchegov (BK) and Jalilian-Marian, Iancu, McLerran, Weigert, Leonidov, Kovner (JIMWLK) equations, which are necessary to account for the saturation effects and the nonlinearity of the gluon dynamics. In contrast, linear evolution equations such as DGLAP and BFKL are insufficient to describe the saturation regime.

The distribution of the colour sources μ^2 can be related to the saturation scale Q_s which corresponds to the energy scale at which the density of gluons inside a nucleus becomes so high that they start saturate, i.e. where nonlinear QCD effects start to play a role as [56]

$$Q_s^2 \equiv \frac{g^4}{2} t^a t_a \int dz^- \mu^2 (x^-)^2 \tag{3.14}$$

with g is the strong coupling constant.

The expected behavior of the saturation scale is to increase with the size of the nucleus, following roughly a $\sim A^{1/3}$ dependence, where A is the atomic mass number. At RHIC, the saturation scale is estimated to be around 1 GeV, while at LHC it is anticipated to be 2-3 GeV [56]. At these energies, the coupling constant $\alpha_s(Q_s)$ is expected to be small, such that $\alpha_s(Q_s) \ll 1$, indicating that we are in a regime where perturbation theory is applicable. However, the phenomenon of saturation is actually a nonperturbative effect. This is because the saturation scale itself is a nonperturbative quantity, and the behavior of the gluon distribution at small x requires resummation of large logarithms in $1/x$.

In the original formulation of the MV model, the average charge density squared μ^2 was assumed to be constant with a value of $\mu^2 = 1.1\, A^3\,\text{fm}^{-2}$ [55, 73]. Consequently, the saturation scale Q_s was also assumed to be constant. However, it is generally expected that the saturation scale will have a more complex dependence on both the nuclear size and x. This motivates other model proposals that include the x and also impact parameter $\boldsymbol{b}_\perp$ dependence on the saturation scale, based on the MV model.

In the MV model, the dipole correlator in Eq. (3.9) is related to the saturation scale, which is given by [56]:

$$S(r_\perp) = \exp\left[-\frac{r_\perp^2 Q_s^2}{4} \ln\left(\frac{1}{r_\perp^2 \Lambda^2} + \mathrm{e}\right)\right], \tag{3.15}$$

where Λ is an infrared cutoff that can be associated with confinement, and hence it is usually taken to be Λ_{QCD}. The Euler's number e is included to regulate the divergence for dipoles larger than $1/\Lambda$. Following the unitarity property of the Wilson line, if we insert $r_\perp = 0$ into Eq. (3.9), the dipole correlator will give $S = 1$ as it should also be fulfilled by Eq. (3.15). This describes the event of no scattering. However, for large dipole sizes, the dipole correlator vanishes, and the scattering amplitude will approach unity, as expected by the black-disk limit of the hadron. In this limit, the high gluon density in the hadron effectively screens out any incoming probe and absorbs all incoming particles, resulting in no scattering. Thus, in this limit, a hadron appears completely black to a probing particle and behaves like a perfect absorber that absorbs any interacting parton without scattering [75, 76].

In attempts to incorporate the impact parameter $\boldsymbol{b}_\perp$ into the saturation scale, several models have been proposed, such as the IPSat [77] and the bCGC [78] models. Another phenomenological model discussed in Ref. [79] modifies the MV model to include the impact-parameter dependence of the saturation scale inspired by fits to the HERA data. In this model, the impact parameter enters the dipole amplitude via the saturation scale and factorizes such that

$$Q_s^2(b_\perp) = Q_{0s}^2 T(b_\perp), \tag{3.16}$$

where $T(b_\perp)$ is the target profile in impact parameter (transverse) space, $b_\perp = |\boldsymbol{b}_\perp|$, and Q_{0s}^2 is a free parameter related to the saturation scale. The simplest profile for the proton is a Gaussian profile, while for heavier nuclei, the Woods-Saxon distribution is typically used. Here, we will follow the idea of Ref. [79] of including the impact parameter dependence to the saturation scale based on the MV model which will be explicitly discussed in Chapter 5. The model developed by Ref. [79] also discusses angular correlations, which will not be considered in this thesis.

3.4 The Golec-Biernat Wüsthoff Model

In order to capture the dynamics of saturation in $\gamma^* p$ DIS, Golec-Biernat and Wüsthoff (GBW) developed a dipole scattering amplitude model $\mathcal{N}$ that includes x dependence [26, 27]

$$\mathcal{N}(x, \boldsymbol{r}_\perp) = \sigma_0 \left[1 - \exp\left(-\frac{r_\perp^2}{4R_0^2(x)}\right)\right] \tag{3.17}$$

where $R_0(x)$ is the saturation radius which decreases with decreasing x and defined by

$$R_0(x) \equiv \frac{1}{Q_0}\left(\frac{x}{x_0}\right)^{\lambda/2} \tag{3.18}$$

with $Q_0 = 1$ GeV and $x = Q^2/(Q^2 + W^2)$. Therefore, the model contains three free parameters: σ_0, x_0, and λ, which are fitted to HERA data for $x \leq 0.01$. The key feature of the model is the Gaussian dependence on the quark-antiquark separation $r_\perp$ over $R_0(x)$, where $r_\perp = |\boldsymbol{r}_\perp|$, which for small $r_\perp$ implies

$$\mathcal{N} \propto \left(\frac{r_\perp}{2R_0(x)}\right)^2, \tag{3.19}$$

which means $\mathcal{N}$ rises quadratically at small $r_\perp$ and flattens off at large $r_\perp$. This flattening is expected as a sign of saturation, which occurs when the photon wavelength $1/Q$ is on the order of the proton size. Explicitly, if we insert Eq. (3.17) into the DIS cross section in Eq. (3.4) such that [26]

$$\sigma_{T,L}(x,Q^2) = \int_0^1 dz \int d^2\boldsymbol{r}_\perp |\Psi_{T,L}(z,Q^2,\boldsymbol{r}_\perp)|^2 \mathcal{N}(x,\boldsymbol{r}_\perp), \tag{3.20}$$

the cross section will be governed by $\mathcal{N}(x,r_\perp)$ which provides saturation of the cross section. We can observe the expected flattening behavior of the dipole scattering amplitude, which captures the saturation effect, as illustrated in Figure 3.2. At small Q^2, the total $\gamma^* p$ DIS cross section $\sigma^{\gamma^* p}$, where most of the contribution comes from σ_T, is constant and dominated by the saturation region $r_\perp \sim 2R_0$. This expression also reflects that for large Q^2, the dominant contribution comes from small dipoles, known as color transparency, which leads to a faster rise of the cross section as a function of energy. This effect arises due to the fact that at high energies, the quarks in a hadron can be thought of as nearly-free particles that move independently of one another. As a result, the hadron becomes more transparent to the probe as the energy of the probe increases.

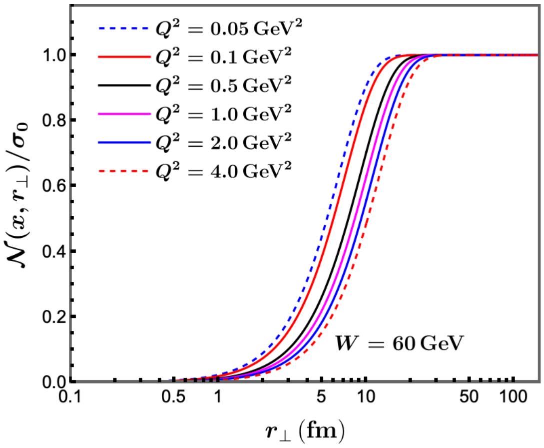

Figure 3.2: The behavior of the dipole cross section $\mathcal{N}(x,r_\perp)/\sigma_0$ as a function of the dipole size $r_\perp$ of the GBW model [26] at small x for different values of Q^2 with fixed $W = 60$ GeV. Larger Q^2 corresponds to larger x.

.

As depicted in Fig. 3.3(a), the GBW model provides an good description of the H1 [80, 81] and ZEUS [82, 83] data at $x \leq 0.01$, with the normalization found to be $\sigma_0 = 23.03$ mb, while the other two free parameters yield the best fit at $\lambda = 0.288$ and $x_0 = 3.04 \times 10^{-4}$. These fit parameters are obtained by assuming that the three light quark flavors involved (excluding charm) have a common mass of 140 MeV. However, assuming a different quark mass resulted in different parameter values, as the cross section increases logarithmically with decreasing quark mass and then diverges when the quark mass approaches zero, which serves as a regulator. Including charm, which has a significantly larger mass than the three light quark flavors, alters the parameters to different values: $\sigma_0 = 29.12$ mb, $\lambda = 0.277$, and $x_0 = 0.41 \times 10^{-4}$, as shown in Fig. 3.3(b) [26].

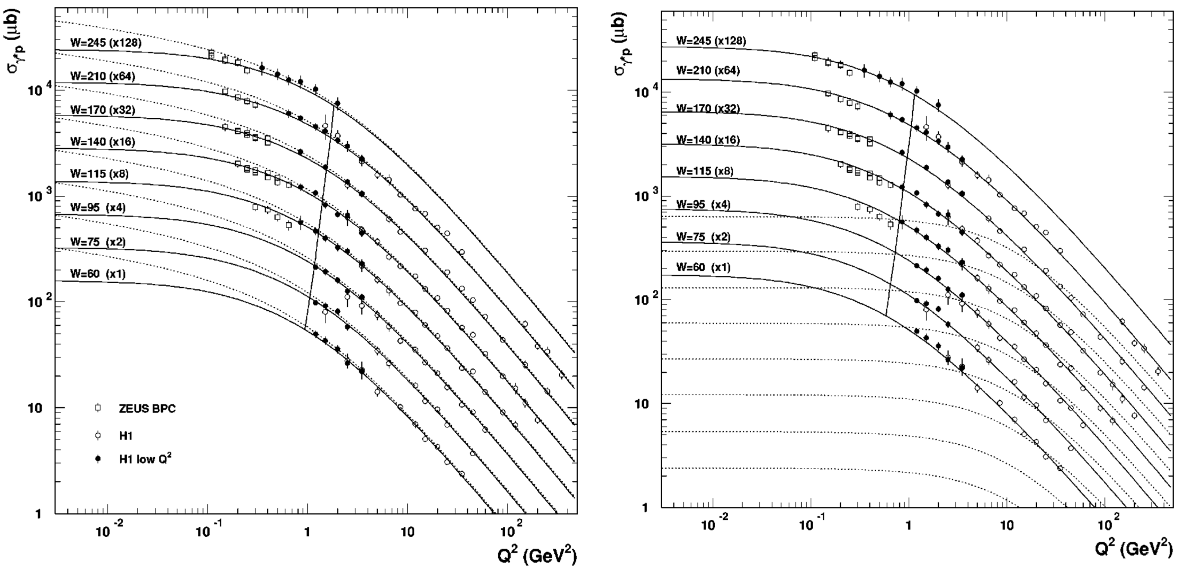

(a) (b)

Figure 3.3: (a) The GBW model, which exhibits a logarithmic Q^2 dependence, was fitted to HERA data at $x < 0.01$ for three light quarks with a common mass of 140 MeV (solid lines) and zero quark mass (dotted lines). The line across the curves indicates the critical line at $Q^2 = R_0^{-2}(x)$, which characterizes the transition to the nonlinear/saturation region In (b), the same behavior is shown, but with the inclusion of charm with different free parameters. The dotted lines in (b) show the charm contribution itself. The figures are taken from [26].

The GBW model not only provides a good description of HERA data but also makes predictions for saturation at low x and its dependence on perturbative Q^2. Specifically, the model predicts that saturation occurs at low $x \sim 10^{-4}$ at perturbative scales of $Q^2 \sim 1 - 2$ GeV^2 and that this saturation scale increases with increasing energy. This is significant because it suggests that saturation effects in high-energy collisions at small x, such as those at the LHC and future EIC, can be fully probed in the small coupling regime of QCD.

3.5 Geometric Scaling

In the limit of very small x, the linear BFKL equation predicts that the gluon density grows rapidly and eventually violates the unitarity of the scattering amplitude. Therefore, it is expected that the gluon density should saturate and the rapid growth of the gluon density should be tempered, leading to the non-linear Balitsky-Kovchegov (BK) equation [84–87] or more generally Jalilian-Marian-Iancu-McLerran-Weigert-Leonidov-Kovner (JIMWLK) equations [88–90], which form an infinite set of coupled equations. Because of the lack of an analytical solution to the non-linear BK and JIMWLK equations, phenomenological models have been proposed to include the small-x evolution incorporating the saturation phenomenon.

The saturation phenomenon is often associated with geometric scaling, which refers to the dependence of the cross section only on Q^2 and x through the dependence on $Q^2/Q_s^2(x)$, where $Q_s(x)$ denotes the saturation scale. There is strong evidence that geometric scaling is indeed a manifestation of saturation and can be related to the asymptotic properties of the BK equation [91,92], although it can also be accommodated by the DGLAP equation [93]. However, it has been shown that establishing geometric scaling for certain processes is experimentally challenging, particularly at RHIC and LHC, where a much wider range of transverse momentum and rapidity must be probed [94,95]. It should also be noted that the MV model does not have the geometric scaling property.

As discussed in the previous section, one of the well-known phenomenological models for the dipole scattering amplitude is the GBW model which incorporates the saturation scale that depends on x. This model describes the HERA data well and demonstrates the feature of geometric scaling in the DIS total cross section at small x. The model is characterized by the dipole scattering amplitude depending only on x and $r_\perp$ through the combination $r_\perp/R_0(x)$, which directly determines its dependence on energy via $x = Q^2/(W^2 + Q^2)$. In the GBW model, the geometric ratio is then translated into the scaling variable $\tau = Q^2/Q_s^2(x) \sim (R_0(x)/r_\perp)^2$. In the beginning, the geometric scaling behavior captured by the GBW model was observed in the total DIS cross section at HERA for small values of x and Q^2. However, this feature was later confirmed in the total DIS cross section over a relatively wide range of energies $0.045 < Q^2 < 450$ GeV^2 at $x \leq 0.01$ [96], as shown in Fig. 3.4, where the data are taken from more experiments: H1 [80,81], ZEUS [97–101], NMC [102], E665 [103], SLAC [104], BCDMS [105], and EMC [106]. Geometric scaling has also been confirmed in DIS on nuclei [107,108], as well as in other diffractive processes such as Deeply Virtual Compton Scattering (DVCS) and vector meson production [109].

In Fig. 3.4(a), the occurrence of geometric scaling is clearly shown at $x < 0.01$, while in Fig. 3.4(b), this property is not observed for $x > 0.01$. The scaling behavior, which is observed only at small values of x, is believed to be evidence of the saturation phenomenon in QCD at these small x values. Even if the geometric scaling observed at small x is not due to saturation (or its onset), the saturation phenomenon is still expected to exist on theoretical grounds, although probably at even smaller values of x in that case. In this respect it is promising that evidence for BFKL evolution, which is linear but does indicate the presence of large logarithms in $1/x$, has been seen in PDF fits [110].

Although the geometric scaling feature depends on the proposed saturation scale $Q_s^2(x)$, it is still unclear whether it indicates the existence of saturation phenomena. Therefore, it should be further tested in more processes. To understand the saturation phenomena, further studies are needed, particularly with the possibility of deeper investigation at the future EIC.

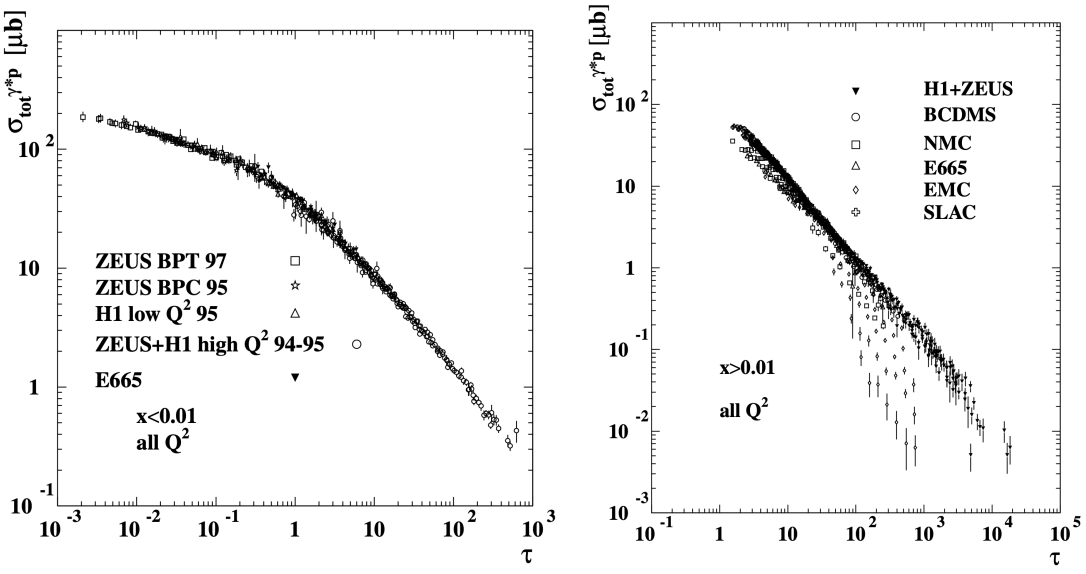

(a) (b)

Figure 3.4: (a) The total DIS $\gamma^* p$ cross section as a function of the scaling variable $\tau = Q^2/Q_s^2$ over a large range of Q^2: $0.045 < Q^2 < 450$ GeV^2 at $x < 0.01$ exhibits geometric scaling, while (b) at $x > 0.01$, it does not. The figures are taken from [96].

4

Multidimensional PDFs

The partons in a hadron are typically not collinear to the parent nucleon, which for certain scattering processes necessitates consideration of their transverse momentum $\boldsymbol{k}_\perp$. This, in turn, leads to the study of PDFs that depend on $\boldsymbol{k}_\perp$ in addition to x. The purpose of this chapter is to present various PDFs that depend on more variables than the one-dimensional collinear PDFs. Generally, PDFs that depend on more variables provide more information about the internal structure of hadrons.

Two closely related generalizations of the one-dimensional PDFs are the transverse momentum dependent PDFs (TMDs) and the generalized parton distributions (GPDs). The TMDs depend on both the longitudinal momentum fraction x and the transverse momentum of the partons $\boldsymbol{k}_\perp$. On the other hand, GPDs in general are four-dimensional objects that depend on the one-dimensional longitudinal momentum fraction x, the two-dimensional off-forwardness in the transverse direction $\boldsymbol{\Delta}_\perp$ (which is defined as $\Delta \equiv P' - P$), and the one-dimensional momentum fraction related to the longitudinal off-forwardness $\xi = -\Delta^+/(P^+ + P'^+)$ (known as the "skewness" parameter). Here, P and P' denote the proton momentum before and after interaction, respectively. However, if one sets $\xi = 0$ or ignores the direction of $\boldsymbol{\Delta}_\perp$ (and uses $t = -\boldsymbol{\Delta}_\perp^2$ instead, the GPDs become three-dimensional. In addition to the TMDs and GPDs, the generalized transverse momentum dependent PDFs (GTMDs) provide even more information by being six-dimensional functions when including the skewness parameter. However, in this chapter, we will only focus on the zero skewness case, i.e. on five-dimensional GTMDs. The Fourier transform of GTMDs in impact parameter space yields the Wigner distribution, also known as the “mother distribution.” All of the aforementioned PDFs are related to each other, as shown in Fig. 4.1.

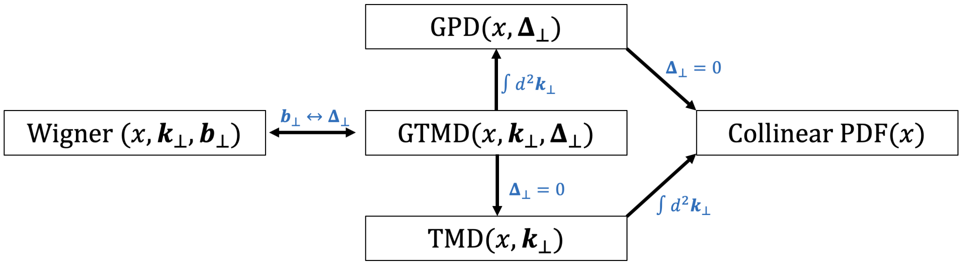

Figure 4.1: Relation between Wigner distribution, GTMD, TMD, GPD, and collinear PDF in the zero skewness case. We note that the integral $\int d^2\boldsymbol{k}_\perp$ cannot be literally taken since it requires a specific regularization method to be applied, see Eq. (4.30) and the discussion following it.

We begin this chapter by the discussion of TMDs in Sec. 4.1, followed by a discussion on GPDs in Sec. 4.2. In Sec. 4.3, we will demonstrate how the definition of GTMDs can be obtained from both TMDs and GPDs, along with the issues involved. Since we are interested in the small-x limit, we will restrict our discussion to the unpolarized gluon GTMD. Our final expression of the gluon GTMD will be utilized in the cross section of both diffractive dijet production in Chapter 5 and diffractive coherent J/ψ production in Chapter 6.

4.1 TMDs

Unlike collinear PDFs, which depend only on the longitudinal momentum fraction of partons, TMDs also depend on the transverse momentum of the partons with respect to the direction of the parent hadron’s momentum, providing information on the three-dimensional momentum structure of hadrons at the partonic level. TMDs are relevant in a variety of processes, such as Semi-Inclusive DIS (SIDIS), Drell-Yan (DY), and proton-proton collisions at the LHC.

The study of TMDs faces several challenges. TMDs are nonperturbative quantities and therefore, their computation requires the use of lattice QCD techniques. These techniques, in turn, demand a significant amount of computational resources. For further details, one may refer to [111,112] and the references therein. On the experimental side, TMDs can be extracted from fits to data, but also that is challenging because it requires less inclusive processes for which more than one particle in the final state has to be detected in order to become sensitive to the transverse momentum flow in the process. In such multiple particle production processes, one has to isolate the contributions from different particles and accurately determine the kinematics of the scattering process, but also the number of events is lower compared to the more inclusive processes, leading to less statistics and resulting in larger errors in the measurements. Nevertheless, for

SIDIS, DY and a few other processes sufficient data has been accumulated in recent years that quark TMDs have been extracted with reasonable precision, see e.g. [113–116] These are also the processes for which TMD factorization has been proven [39, 117, 118]. About gluon TMDs much less is known yet, but some first studies have been made recently [119, 120].

To obtain an expression for the quark TMDs, one can begin with the correlator described in Chapter 2. By integrating the unintegrated correlator in Eq. (2.30) over k^-, the quark-quark TMD correlator can be obtained:

$$\Phi_{\alpha\beta}(x, \boldsymbol{k}_\perp) = \int \frac{dz^- d^2\boldsymbol{z}_\perp}{(2\pi)^3} \mathrm{e}^{ixP^+z^- + i\boldsymbol{k}_\perp\cdot\boldsymbol{z}_\perp} \langle P|\bar{\psi}_\alpha(0^+, 0^-, \boldsymbol{0}_\perp)\,\mathcal{U}_{[0,z]}\,\psi_\beta(0^+, z^-, \boldsymbol{z}_\perp)|P\rangle \tag{4.1}$$

where the Wilson line that maintains the gauge invariance of the correlator is already included. However, unlike the collinear case, the Wilson line now connects the quark field at point $(0^+, 0^-, \boldsymbol{0}_\perp)$ with the quark field at point $(0^+, z^-, \boldsymbol{z}_\perp)$ which requires a piece of Wilson which runs through the transverse direction. The path connecting those fields depends on the process being considered. One of the most well-known Wilson line paths is the so called staple-like path, which commonly appears in high-energy collision processes. The staple-like path consists of three Wilson lines: one that runs from the origin $(0^+, 0^-, \boldsymbol{0}_\perp)$ to either plus or minus infinity in the minus direction $(0^+, \pm\infty^-, \boldsymbol{0}_\perp)$, another that runs along the transverse direction from $(0^+, \pm\infty^-, \boldsymbol{0}_\perp)$ to $(0^+, \pm\infty^-, \boldsymbol{z}_\perp)$, and the last one that runs from $(0^+, \pm\infty^-, \boldsymbol{z}_\perp)$ to $(0^+, z^-, \boldsymbol{z}_\perp)$. This path is explicitly written as:

$$\mathcal{U}^{[\pm]}_{[0,z]} = \mathcal{U}^{-}_{[0^-,\pm\infty^-;\boldsymbol{0}_\perp]}\,\mathcal{U}^{\perp}_{[\pm\infty^-;\boldsymbol{0}_\perp,\boldsymbol{z}_\perp]}\,\mathcal{U}^{-}_{[\pm\infty^-,z^-;\boldsymbol{z}_\perp]}. \tag{4.2}$$

The minus sign indicates the Wilson line which run along the minus direction which has been discussed when considering the collinear PDFs, while the Wilson which runs along the transverse direction is defined as (in the fundamental representation):

$$\mathcal{U}^{\perp}_{[\pm\infty;\boldsymbol{0}_\perp,\boldsymbol{z}_\perp]} \equiv \mathcal{P}\exp\left[ig\int_{\boldsymbol{0}_\perp}^{\boldsymbol{z}_\perp} d\boldsymbol{\lambda}_\perp A^a(0, \lambda^- = \pm\infty, \boldsymbol{\lambda}_\perp)t_a\right]. \tag{4.3}$$

The choice of either future $[+]$ or past $[-]$ pointing Wilson lines is dependent on the specific process being studied [69, 71, 121] For instance, in the case of SIDIS, a future pointing Wilson line is necessary, which runs along plus light-cone infinity, and represents the gluon interactions occurring after the quark is struck by the photon, a process known as final-state interaction. Conversely, in DY, a past pointing Wilson line is required, which runs along minus light-cone infinity, and describes the gluon interactions occurring before the quarks are annihilated which is referred to as initial-state interaction.

Under time-reversal projections, TMDs can be divided into two types: time-reversal odd (T-odd), which flip their sign under time reversal, and time-reversal even (T-even), which do not. Both T-even and T-odd TMD correlators can be constructed from the $[+]$ and $[-]$ Wilson lines in the definition of the quark correlator [71]

$$\begin{aligned} \Phi^{\text{T-even}}(x, \boldsymbol{k}_\perp) &= \frac{1}{2}\left(\Phi^{[+]}(x, \boldsymbol{k}_\perp) + \Phi^{[-]}(x, \boldsymbol{k}_\perp)\right) \\ \Phi^{\text{T-odd}}(x, \boldsymbol{k}_\perp) &= \frac{1}{2}\left(\Phi^{[+]}(x, \boldsymbol{k}_\perp) - \Phi^{[-]}(x, \boldsymbol{k}_\perp)\right). \end{aligned} \tag{4.4}$$

In the unpolarized spin-1/2 hadron case, the TMD quark correlator is T-even. However, in the polarized case, certain TMD correlators can be T-odd. The Sivers effect [122], which describes the correlation between the transverse spin of a polarized hadron and the transverse momentum of a struck parton, can induce a T-odd TMD. The predicted sign change of the T-odd Sivers function between SIDIS and DY processes is an important feature that can be experimentally verified to validate the predictions of the TMD formalism in polarized scattering. In these cases, under time reversal, the initial state interactions in DY represented by the past pointing Wilson lines are replaced by final state interactions in SIDIS represented by the future pointing Wilson lines [123]. We note that upon (formally) integrating the TMD correlator over the transverse momentum $\int d^2\boldsymbol{k}_\perp$ (using an appropriate method of regularization, see the discussion below Eq. (4.30), the TMD correlator will reduce to the collinear correlator, where the staple-like Wilson lines reduce to the one that runs along the straight line. In this case, all T-odd functions vanish, which means that the collinear correlator should be T-even.

To obtain TMD expressions, one needs to parameterize the quark correlator in terms of Dirac matrices that characterize the polarization of the quark: unpolarized (U), vector polarized (longitudinally (L) or transversely (T)), or tensor polarized. However, the parameterization for tensor polarization will not be considered here, as we restrict to protons. For a complete description of the tensor polarized parameterization, see e.g. [124, 125].

In practice, one usually starts by parameterizing the unintegrated correlator and then integrates each parameterized correlator term over k^-. At leading twist the resulting TMDs from the parameterization can be divided into eight types, depending on the type of hadron polarization, as shown in Table 4.1. Out of these eight types, only two are T-odd: the Sivers $f_{1T}^\perp$ [122, 126] and Boer-Mulders $h_1^\perp$ [127] functions. The former encodes the correlation between the transverse momentum of an unpolarized quark in a transversely polarized hadron, while the latter encodes the correlation between the transverse momentum and the transverse polarization of a quark inside an unpolarized hadron. The worm-gear function g_{1T} [128] describes the distribution of longitudinally polarized quarks inside a transversely polarized hadron, while the other worm-gear function $h_{1L}^\perp$ describes the distribution of transversely polarized quarks in a longitudinally polarized hadron. The pretzelosity $h_{1T}^\perp$ [129] is related to the shape of the nucleon and can provide information on its deviation from sphericity. Out of the eight types of TMDs, only three survive the integration upon the parton transverse momentum $\int d^2\boldsymbol{k}_\perp$: number density f_1, helicity g_1 and transversity h_1. In recent years, significant progress has been made in extracting TMDs from data, particularly in determining the number density f_1 and the Sivers function $f_{1T}^\perp$, both of which have been observed to be non-zero [130–132]. Additionally, for the first time the extraction of the worm-gear function g_{1T} from SIDIS has been made [133] and attempts to extract the pretzelosity function $h_{1T}^\perp$ [134].

		Parent hadron polarization		
		U	L	T
Quark polarization	U	f_1 (number density)		$h_1^\perp$ (Boer-Mulders)
	L		g_1 (helicity)	$h_{1L}^\perp$ (worm-gear L)
	T	$f_{1T}^\perp$ (Sivers)	g_{1T} (worm-gear T)	h_1 (transversity) $h_{1T}^\perp$ (pretzelosity)

Table 4.1: The eight leading-twist TMDs based on the polarization of the parent hadron and the quark. Here, U, L, and T refer to the unpolarized, longitudinally polarized, and transversely polarized, respectively.

Similar to TMD PDFs, there exist eight independent TMD fragmentation functions (FFs) at leading twist, which describe the probability distribution of producing a hadron with a certain momentum fraction of the initial parton. A detailed review of this topic is available in e.g. [135].

Analogous to the quark TMDs, the gluon correlator can be obtained from the unintergrated gluon correlator for the unpolarized case

$$\Gamma^{UU'\mu\nu;\rho\sigma}(k) = \int \frac{d^4z}{(2\pi)^4} \mathrm{e}^{ik\cdot z} \langle P| \mathrm{Tr}\left[F^{\mu\nu}(0) U_{[0,z]} F^{\rho\sigma}(z) U'_{[z,0]}\right] |P\rangle \tag{4.5}$$

where the Wilson lines are now in the adjoint representation, but they have the same properties as in Eq. (4.2). The trace (Tr) indicates a trace over the color indices of the two gluon fields. After integrating over k^-, the gluon-gluon TMD correlator can be obtained as

$$\begin{aligned}\Gamma^{UU'\mu\nu;\rho\sigma}(x, \boldsymbol{k}_\perp) = \quad & \frac{2}{P^+} \int \frac{dz^- d^2\boldsymbol{z}_\perp}{(2\pi)^3} \mathrm{e}^{ixP^+z^- - i\boldsymbol{k}_\perp\cdot\boldsymbol{z}_\perp} \\ & \times \langle P| \mathrm{Tr}\left[F^{\mu\nu}(0) U_{[0,z]} F^{\rho\sigma}(z) U'_{[z,0]}\right] |P\rangle \Big|_{z^+=0} .\end{aligned} \tag{4.6}$$

In fact, there are multiple ways to obtain a gauge-invariant definition of the gluon-gluon TMD correlators, each of which may arise in different physical processes. It has been shown that there are three different types of Wilson line structures related to the gluon that can be used to obtain a gauge-invariant quantity. The structure shown in the above equation is the simplest of these structures and is referred to as the type-1 structure [136]. In subsequent chapters, we will focus only on this structure, as it is directly relevant to the diffractive processes that we are concerned with.

The parameterization of the gluon TMD correlator is similar to that of the quark TMD, with leading-twist gluon TMD correlator being parameterized in terms of unpolarized, vector polarized, and tensor polarized. For more details on the parameterization of the gluon TMD correlator, see [125]. Also as in the quark case, under time reversal, the gluon TMD correlator can be divided into T-even and T-odd. For the unpolarized case, the T-even function f_1 possesses the following properties:

$$f_1^{[+,+]} = f_1^{[-,-]} \qquad f_1^{[+,-]} = f_1^{[-,+]}. \tag{4.7}$$

The $+$ and $-$ symbols represent the future- and past-pointing Wilson lines, respectively, similar to the quark case. However, there are two Wilson lines involved in each gluon TMD. In the small-x limit, these two structures are related to the two fundamental gluon distributions: the former is the unintegrated Weizsäcker-Williams (WW) distribution, while the latter is the dipole distribution. The dipole distribution appears in a wide range of processes, such as inclusive DIS, SIDIS, DY, and dijet production in pA collisions. On the other hand, the WW distribution is involved in fewer processes, such as quark-antiquark dijet correlation in DIS. However, a direct-photon jet correlation process in pA collisions has been identified as a potential probe to separately study these two-gluon distributions [67]. The dipole distribution will be an important ingredient of the gluon GTMDs in the small-x region, which will be discussed in Sec. 4.3.

4.2 GPDs

GPDs are a complementary source of transverse distribution information to TMDs. While TMDs describe the momentum-space distribution of partons in a nucleon, GPDs provide information on the spatial distribution of partons. GPDs are also known as “off-diagonal," “off-forward," “nondiagonal," “nonforward," or “skewed" parton distributions [137], as they involve matrix elements of proton states with different momenta P and P': $\langle P'|...|P\rangle$. The off-forwardness is then given by $P' - P$, with the $+$ component referred to as “skewness”. GPDs can be probed in some exclusive processes, such as exclusive deeply virtual production of photons (DVCS) or mesons (DVMP). Comprehensive references on these GPDs can be found in [137–143].

Generally, GPDs depend on variables x, ξ, and t. Like TMDs, they can be described in terms of matrix elements of nonlocal operators with light-cone separated quark or gluon fields. In the lightcone gauge, where the Wilson lines that maintain the gauge invariance of the two-point functions become unity, quark GPDs in the unpolarized case can be expressed as follows [137, 144]:

$$\begin{aligned}\mathcal{H}_q(x,\xi,t) &= \frac{1}{2}\int \frac{dz^-}{2\pi}\mathrm{e}^{ixP^+z^-}\langle P'|\bar{\psi}(-z^-/2)\gamma^+\psi(z^-/2)|P\rangle \\ &= \frac{1}{2P^+}\left[H_q(x,\xi,t)\bar{u}(P')\gamma^+u(P) + E_q(x,\xi,t)\bar{u}(P')\frac{i\sigma^{+\nu}\Delta_\nu}{2M}u(P)\right],\end{aligned} \tag{4.8}$$

while for gluons

$$\begin{aligned}\mathcal{H}_g(x,\xi,t) &= \frac{1}{2}\int\frac{dz^-}{2\pi}\mathrm{e}^{ixP^+z^-}\langle P'|F^{+\mu}(-z^-/2)F_\mu{}^+(z^-/2)|P\rangle \\ &= \frac{1}{2P^+}\left[H_g(x,\xi,t)\bar{u}(P')\gamma^+u(P)+E_g(x,\xi,t)\bar{u}(P')\frac{i\sigma^{+\nu}\Delta_\nu}{2M}u(P)\right].\end{aligned} \tag{4.9}$$

In the above equations ψ is the quark field and $F^{\mu\nu}$ is the gluon field strength tensor Here, $\Delta = P' - P$ denotes the momentum transfer or the so-called off-forwardness, while $t = \Delta^2$. The skewness parameter is given by $\xi = -\Delta^+/(P'^+ + P^+)$. In a covariant gauge, Wilson lines need to be inserted as in the collinear PDF case. For the polarized case of GPDs, one can refer to [137] which will not be discussed here. We should note that the definition of GPDs may vary among different authors, with some differing by a factor of $2x$ or 2.

GPDs are dependent on two lightcone momentum fractions: x and ξ, which must satisfy the condition $(x,\xi) \in [-1,1]^2$ [145]. This dependence leads to different regions, each with three possible values of ξ corresponding to different values of x, as depicted in Fig. 4.2. The applicability of the evolution equations governing GPDs: DGLAP and ERBL (Efremov–Radyushkin–Brodsky–Lepage) [146], is also subject to the specific values of x and ξ. The evolution of GPDs in the range $-1 \le x \le -\xi$ and $\xi \le x \le 1$ is governed by the DGLAP equation (which is referred to as the DGLAP region), while in the range $-\xi \le x \le \xi$, the ERBL equation is applied (the ERBL region), as illustrated in Fig. 4.3. At the transition region where $x = \xi$, the GPDs are expected to be continuous but not necessarily smooth [147, 148].

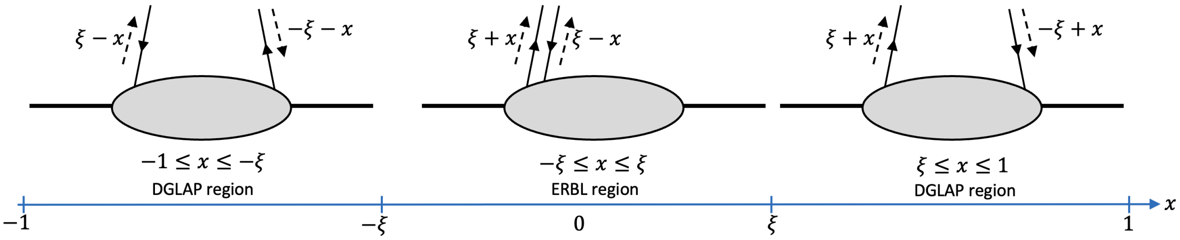

Figure 4.2: Different regions probed by GPDs for $\xi > 0$: (left) $x \in [-1,-\xi]$: emission of an antiquark with momentum $\xi - x$ and reabsorption of an antiquark with momentum $-\xi - x$, (middle) $x \in [-\xi,\xi]$: emission of quarks and antiquarks with momentum fractions $\xi - x$ and (right) $\xi + x$, $x \in [\xi, 1]$: emission and reabsorption of a quark with momentum $x - \xi$. Reproduced from [137].

4.3 GTMDs

The most general GTMDs are 6-dimensional parton distributions that depend on the skewness parameter ξ, the parton's lightcone momentum fraction x, the parton's transverse momentum $\boldsymbol{k}_\perp$, and transverse off-forwardness $\boldsymbol{\Delta}_\perp$ which describes how the

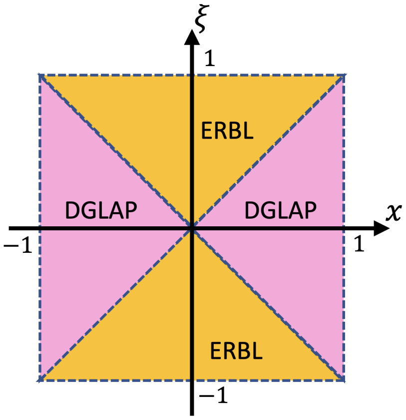

Figure 4.3: The regions probed by the two different evolution equations: DGLAP and ERBL, are determined by the values of x and ξ. Reproduced from [144].

incoming hadron momentum is modified. In the subsequent discussion, we will focus on the zero skewness case ($\xi = 0$), where the GTMDs reduce to 5-dimensional objects. The associated Wigner distribution parton is a function of x, $\boldsymbol{k}_\perp$, and the impact parameter $\boldsymbol{b}_\perp$ which is the Fourier conjugate of $\boldsymbol{\Delta}_\perp$. GTMDs can be viewed as off-forward extensions of TMDs or as transverse momentum dependent extensions of GPDs. As a consequence, the GTMDs inherit properties of both TMDs and GPDs and any subtle issues related to them. In this section we will go into some of these matters, restricting the discussion to the distribution of unpolarized quarks inside an unpolarized hadron, for which we take a proton for definiteness.

GTMDs and the associated Wigner parton distributions were first considered in [149,150] and analyzed further in e.g. [151–154] for quarks and in [154,155] for gluons, while the classification of gluon GTMDs was first introduced in [157]. In [149, 150], the relation between the Wigner distribution and the 6-dimensional GTMDs relies on nonrelativistic approximations, while the relation between the Wigner distribution and the 5-dimensional GTMDs ($\xi = 0$) in the infinite momentum frame was first introduced in [156]. The first suggestion to access GTMDs experimentally was put forward in [23]. In that paper the process of diffractive dijet production in electron-proton collisions was considered to probe gluon GTMDs. Diffractive dijet production was earlier suggested as a way to probe gluon GPDs [158] and considered at small x in [64]. Diffractive single jet production was studied in [159]. In this thesis, we will build upon these ideas and develop a model for the unpolarized gluon GTMD, similar to the one proposed in [23]. The analysis of diffractive processes that we will be discussing in Chapters 5 and 6 will be based on this model. Models for quark GTMDs have been considered in e.g. [160–162]. For gluon GTMDs the models are so-far based on the small-x MV model [55, 73, 74] and related CGC descriptions. In the subsequent chapters, we will also use the MV model as our starting point but introduce a few free parameters to be fitted to the available data from H1, ZEUS, and LHC. This will enable us to make predictions for the EIC, RHIC, and LHC, which will hopefully help to further test the underlying GTMD description.

4.3.1 Two definitions of GTMD

As shown in Fig. 4.1, GTMD can be obtained from either the TMD or GPD extensions. In light of these relations, we will discuss several issues related to obtaining GTMD from both the TMD and GPD. First of all, the quark GTMD $q(x, \boldsymbol{k}_\perp, \boldsymbol{\Delta}_\perp)$ can be defined as the off-forward generalization of the quark TMD $q(x, \boldsymbol{k}_\perp)$:

$$q(x, \boldsymbol{k}_\perp, \boldsymbol{\Delta}_\perp) \equiv \int \frac{d\lambda}{2\pi P^+}\, d^2\boldsymbol{r}_\perp\, e^{i\lambda x} e^{i\boldsymbol{k}_\perp\cdot\boldsymbol{r}_\perp}\, \langle P'|\, \overline{\psi}(-\frac{\lambda}{2}n - \frac{\boldsymbol{r}_\perp}{2})\, \gamma^+ \mathcal{U}\; \psi(\frac{\lambda}{2}n + \frac{\boldsymbol{r}_\perp}{2})\, |P\rangle, \tag{4.10}$$

where the lightlike vector n specifies the $-$ direction, whereas the proton momentum P specifies the $+$ direction: $P \cdot n = P^+$. In the above expression $\Delta = P' - P$ denotes the off-forwardness considered here for zero skewness, i.e. $\xi = -\Delta^+/(P'^+ + P^+) = 0$, such that $\Delta = \Delta_\perp$. The Wilson line $\mathcal{U}$ is one of the staple-like lines discussed in Sec. 4.1 which does not play an important role here and will be left unspecified.

Alternatively, the quark GTMD can be defined as the Fourier transform of the Wigner quark distribution $W(x, \boldsymbol{k}_\perp, \boldsymbol{b}_\perp)$, which itself can be defined as the transverse momentum dependent generalization of the impact parameter dependent GPD $q(x, \boldsymbol{b}_\perp)$ [139, 163–166]:

$$q(x, \boldsymbol{b}_\perp) = \int \frac{d\lambda}{2\pi P^+}\, e^{i\lambda x}\, \langle P^+, \boldsymbol{R}_\perp = 0|\, \overline{\psi}(-\frac{\lambda}{2}n + \boldsymbol{b}_\perp)\, \gamma^+ \mathcal{U}\, \psi(\frac{\lambda}{2}n + \boldsymbol{b}_\perp)\, |P^+, \boldsymbol{R}_\perp = 0\rangle, \tag{4.11}$$

where the impact parameter $\boldsymbol{b}_\perp$ is measured with respect to the transverse center of longitudinal momentum $\boldsymbol{R}_\perp^{CM} \equiv \sum_i x_i \boldsymbol{r}_{\perp i}$ of the system and $|P^+, \boldsymbol{R}_\perp = 0\rangle$ is the normalized proton state localized in the spatial $\perp$ direction [139, 166]:

$$|P^+, \boldsymbol{R}_\perp = 0\rangle = \mathcal{N} \int \frac{d^2\boldsymbol{P}_\perp}{(2\pi)^2} \Phi(\boldsymbol{P}_\perp) |P^+, \boldsymbol{P}_\perp\rangle, \tag{4.12}$$

for some wave packet $\Phi(\boldsymbol{P}_\perp)$. This expression for $q(x, \boldsymbol{b}_\perp)$ thus depends on the wave packet considered. If this wave packet is sufficiently localized in transverse position space, such that $\Phi(\boldsymbol{P}_\perp + \boldsymbol{\Delta}_\perp) \approx \Phi(\boldsymbol{P}_\perp)$, meaning it is slowly varying on the scale of the off-forwardness, one can relate it to the standard GPD H [139, 164–166]:

$$\begin{aligned} q(x, \boldsymbol{b}_\perp) &= |\mathcal{N}|^2 \int \frac{d\lambda}{2\pi P^+}\, e^{i\lambda x} \int \frac{d^2\boldsymbol{P}_\perp}{(2\pi)^2}\frac{d^2\boldsymbol{P}'_\perp}{(2\pi)^2}\, \Phi^*(\boldsymbol{P}'_\perp)\Phi(\boldsymbol{P}_\perp) \\ &\qquad\qquad \times \langle P^+, \boldsymbol{P}'_\perp|\, \overline{\psi}(-\frac{\lambda}{2}n + \boldsymbol{b}_\perp)\, \gamma^+ \mathcal{U}\, \psi(\frac{\lambda}{2}n + \boldsymbol{b}_\perp)\, |P^+, \boldsymbol{P}_\perp\rangle \\ &= |\mathcal{N}|^2 \int \frac{d\lambda}{2\pi P^+}\, e^{i\lambda x} \int \frac{d^2\boldsymbol{P}_\perp}{(2\pi)^2}\frac{d^2\boldsymbol{P}'_\perp}{(2\pi)^2}\, \Phi^*(\boldsymbol{P}'_\perp)\Phi(\boldsymbol{P}_\perp) e^{-i\boldsymbol{b}_\perp\cdot\boldsymbol{\Delta}_\perp} \\ &\qquad\qquad \times \langle P^+, \boldsymbol{P}'_\perp|\, \overline{\psi}(-\frac{\lambda}{2}n)\, \gamma^+ \mathcal{U}\, \psi(\frac{\lambda}{2}n)\, |P^+, \boldsymbol{P}_\perp\rangle \\ &\approx |\mathcal{N}|^2 \int \frac{d^2\boldsymbol{P}_\perp}{(2\pi)^2} |\Phi(\boldsymbol{P}_\perp)|^2 \frac{d^2\boldsymbol{\Delta}_\perp}{(2\pi)^2}\, e^{-i\boldsymbol{b}_\perp\cdot\boldsymbol{\Delta}_\perp} H(x, 0, -\boldsymbol{\Delta}_\perp^2) \\ &= \int \frac{d^2\boldsymbol{\Delta}_\perp}{(2\pi)^2}\, e^{-i\boldsymbol{b}_\perp\cdot\boldsymbol{\Delta}_\perp} H(x, 0, -\boldsymbol{\Delta}_\perp^2). \end{aligned} \tag{4.13}$$

In the second step we used that, unlike forward matrix elements, off-forward matrix elements of the form $\langle P^+, \boldsymbol{P}'_\perp|\, O(\boldsymbol{b}_\perp)\, |P^+, \boldsymbol{P}_\perp\rangle$ are not translation invariant, but pick up a phase when translating the operator $O(\boldsymbol{b}_\perp)$ to $O(\boldsymbol{0}_\perp)$. In the above derivation it was also used that $\langle P^+, \boldsymbol{P}'_\perp|\, O(\boldsymbol{0}_\perp)\, |P^+, \boldsymbol{P}_\perp\rangle$ only depends on the difference of $\boldsymbol{P}'_\perp$ and $\boldsymbol{P}_\perp$, which is a consequence of invariance under transverse boosts, see [139], in particular its Eq. (5).

One observes that only in the case that $\Phi(\boldsymbol{P}_\perp)$ is a constant, the relation between $q(x, \boldsymbol{b}_\perp)$ and $H(x, 0, -\boldsymbol{\Delta}_\perp^2)$ is exact. When viewing $q(x, \boldsymbol{b}_\perp)$ as the Fourier transform of the GPD $H(x, 0, -\boldsymbol{\Delta}_\perp^2)$ it is thus understood that one considers a wave packet that is sufficiently localized in coordinate space and hence sufficiently delocalized in momentum space. This then raises the question of how to reconcile such a very delocalized state in transverse momentum space with a state that has a specific z-momentum and energy, which are related by $P^- = (M^2 + P_\perp^2)/(2P^+)$, which means that large uncertainty in $P_\perp^2$ generally translates into large uncertainty in $P^- \propto P^0 - P^3$ and hence in P^0 and/or P^3. This issue is known to pose a problem for 3D spatial distributions, where a state cannot be simultaneously in a definite eigenstate of position and momentum and frame and wave packet dependence enters[1]. For the 2D charge distribution and analogously for $q(x, \boldsymbol{b}_\perp)$ one can avoid this issue by boosting to a frame in which P^+ is much larger than the typical $P_\perp$ values. This allows to maintain $P^- = (M^2 + P_\perp^2)/(2P^+) \ll P^+$ in the wave packet, such that the state has sufficiently definite P^0 and P^3 components even if the $P_\perp$ distribution is very broad, cf. [139] for further discussion.

Starting from the impact parameter dependent GPD $q(x, \boldsymbol{b}_\perp)$ one obtains a definition

---

[1] This issue received renewed attention recently in the context of defining the 3D charge radius for the nucleon [167, 168]. For nucleons (as opposed to heavy nuclei) the system size is not sufficiently large with respect to the Compton wavelength to allow for an unambiguous, wave packet independent, definition of the charge distribution and hence of the charge radius [168].

of the Wigner parton distribution $W(x, \boldsymbol{k}_\perp, \boldsymbol{b}_\perp)$ defined as[2]

$$W(x, \boldsymbol{k}_\perp, \boldsymbol{b}_\perp) \equiv \int \frac{d\lambda}{2\pi P^+}\, d^2\boldsymbol{r}_\perp\, e^{i\lambda x} e^{i\boldsymbol{k}_\perp\cdot\boldsymbol{r}_\perp} \\ \times \langle P^+, \boldsymbol{R}_\perp = 0|\, \overline{\psi}(-\frac{\lambda}{2}n + \boldsymbol{b}_\perp - \frac{\boldsymbol{r}_\perp}{2})\, \gamma^+ \mathcal{U}\, \psi(\frac{\lambda}{2}n + \boldsymbol{b}_\perp + \frac{\boldsymbol{r}_\perp}{2})\, |P^+, \boldsymbol{R}_\perp = 0\rangle. \tag{4.14}$$

The GTMD can then be obtained by Fourier transforming the Wigner distribution from $\boldsymbol{b}_\perp$ space to the $\boldsymbol{\Delta}_\perp$ space, which takes the following form:

$$q_W(x, \boldsymbol{k}_\perp, \boldsymbol{\Delta}_\perp) \equiv \int \frac{d^2\boldsymbol{b}_\perp}{(2\pi)^2}\, e^{i\boldsymbol{b}_\perp\cdot\boldsymbol{\Delta}_\perp} W(x, \boldsymbol{k}_\perp, \boldsymbol{b}_\perp). \tag{4.15}$$

Just like for the Fourier transform of $q(x, \boldsymbol{b}_\perp)$ and the GPD $H(x, 0, -\boldsymbol{\Delta}_\perp^2)$, one can equate the two GTMD definitions $q(x, \boldsymbol{k}_\perp, \boldsymbol{\Delta}_\perp)$ in Eq. (4.10) and $q_W(x, \boldsymbol{k}_\perp, \boldsymbol{\Delta}_\perp)$ in Eq. (4.15) for a sufficiently narrow state $|P^+, \boldsymbol{R}_\perp = 0\rangle$ in coordinate space, for which, as we discussed above, one has to consider a frame in which P^+ is much larger than the typical $P_\perp$ values. The assumptions under which q and q_W can be considered equivalent GTMD definitions are usually left implicit. We emphasize that the sufficiently narrow state refers to the wave packet in which the state is prepared, not to the nucleon or nucleus which itself will have some profile in transverse coordinate space that may be considerably less narrow. Assuming for illustration purposes a ball-shaped object, the wave packet around $\boldsymbol{R}_\perp = 0$ characterizes the distribution of the center of the ball, accounting for any uncertainty in its position, rather than describing the shape of the ball itself. It is to be expected that the center of a ball can be located with much greater precision than the size of the ball. However, for subatomic particles this is not necessarily the case, but, as explained, for the two-dimensional momentum distribution of the proton in the Infinite Momentum Frame it is.[3]

4.3.2 Gluon GTMD at small x

Since gluons constitute the dominant part of the hadron content at small values of x, it is justifiable to concentrate on the gluon distributions and ignore the contributions from quarks. In particular, it has been proposed that in the small-x limit the dipole gluon GTMD can be probed in the process of electron-proton or electron-nucleus collisions in DIS where the dipole gluon GTMD, for zero skewness and for the unpolarized case, is defined as [23, 72]:

$$G^{[+,-]}(x, \boldsymbol{k}_\perp, \boldsymbol{\Delta}_\perp) = \frac{2}{P^+} \int \frac{dz^-}{2\pi} \frac{d^2\boldsymbol{z}_\perp}{(2\pi)^2}\, e^{ik\cdot z}\, \langle P'|\, \mathrm{Tr}\left[F^{+i}\left(-\frac{z}{2}\right) U^{[+]} F^{+i}\left(\frac{z}{2}\right) U^{[-]}\right]\, |P\rangle\Big|_{z^+=0}. \tag{4.16}$$

---

[2] In [149, 150] the Wigner quark distribution was defined as a generalization of the 3D charge density in the Breit frame (for a brief discussion of that see [169]), which inherits the mentioned wave packet dependence issue for the nucleon.

[3] We thank Markus Diehl for this insight.

Here i is a transverse index that is summed over in this case of unpolarized gluons and $U^{[\pm]}$ are the standard staple-like Wilson lines in the forward $(+)$ and backward $(-)$ lightcone directions, also simply referred to as $+$ and $-$ links. In discussing GTMDs, Ref. [23] introduces a function $xG_{\mathrm{DP}}(x, \boldsymbol{q}_\perp, \boldsymbol{\Delta}_\perp)$ which corresponds to $G^{[+,-]}(x, \boldsymbol{q}_\perp, \boldsymbol{\Delta}_\perp)$ in our notation. This function is represented as a blob with two gluons attached to it as shown in Fig. 4.4. While this is a simplified representation, it is important to note that an infinite number of eikonal gluon exchanges are present, which lead to the Wilson line in the correlator expression, even if they are not explicitly depicted.

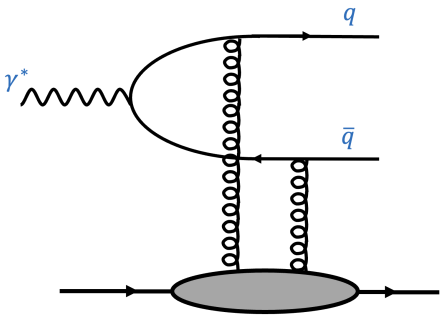

Figure 4.4: An illustration of the GTMD in a diffractive process which is represented by a blob with two gluons attached to it. For simplicity, the infinite number of eikonal gluon exchanges are not shown.

Since we are interested in the small-x region, we can approximate Eq. (4.16) in the limit of $x \to 0$ for which one can show to arrive at [72]

$$\begin{aligned} G^{[+,-]}(\boldsymbol{k}_\perp, \boldsymbol{\Delta}_\perp) &= \frac{4}{g^2\langle P|P\rangle} \int \frac{d^2\boldsymbol{x}_\perp d^2\boldsymbol{y}_\perp}{(2\pi)^3}\, e^{-i\boldsymbol{k}_\perp\cdot(\boldsymbol{x}_\perp-\boldsymbol{y}_\perp)} e^{i\boldsymbol{\Delta}_\perp\cdot(\boldsymbol{x}_\perp+\boldsymbol{y}_\perp)/2} \\ &\qquad\qquad\times \langle P'|\, \partial_x^i \partial_y^i \mathrm{Tr}\left[U^{[\Box]}(\boldsymbol{y}_\perp, \boldsymbol{x}_\perp)\right]\, |P\rangle \\ &\equiv \frac{1}{2\pi g^2}\left[\boldsymbol{k}_\perp^2 - \frac{\boldsymbol{\Delta}_\perp^2}{4}\right] G^{[\Box]}(\boldsymbol{k}_\perp, \boldsymbol{\Delta}_\perp), \end{aligned} \tag{4.17}$$

where

$$U^{[\Box]}(\boldsymbol{y}_\perp, \boldsymbol{x}_\perp) = U^{[+]}(\boldsymbol{y}_\perp, \boldsymbol{x}_\perp) U^{[-]}(\boldsymbol{x}_\perp, \boldsymbol{y}_\perp) \tag{4.18}$$

will be referred to as the Wilson loop and

$$\langle P'|P\rangle = (2\pi)^3 2P^+ \delta(\Delta^+)\delta^{(2)}(\Delta_\perp) \tag{4.19}$$

yielding the divergent factor

$$\langle P|P\rangle = 2P^+ \int db^- d^2\boldsymbol{b}_\perp, \tag{4.20}$$

which is assumed to be regularized, e.g. by considering a finite volume. In this way one finds that

$$G^{[\square]}(\boldsymbol{k}_\perp,\boldsymbol{\Delta}_\perp)=\frac{4N_c}{\langle P|P\rangle}\int\frac{d^2\boldsymbol{x}_\perp d^2\boldsymbol{y}_\perp}{(2\pi)^2}\,e^{-ik\cdot(\boldsymbol{x}_\perp-\boldsymbol{y}_\perp)}e^{i\Delta\cdot(\boldsymbol{x}_\perp+\boldsymbol{y}_\perp)/2}\langle P'|\;S^{[\square]}(\boldsymbol{x}_\perp,\boldsymbol{y}_\perp)\;|P\rangle$$
$$=\frac{4N_c}{\langle P|P\rangle}\int\frac{d^2\boldsymbol{r}_\perp d^2\boldsymbol{b}_\perp}{(2\pi)^2}\,e^{-i\boldsymbol{k}_\perp\cdot\boldsymbol{r}_\perp}e^{i\boldsymbol{\Delta}_\perp\cdot\boldsymbol{b}_\perp}\langle P'|\;S^{[\square]}(\boldsymbol{b}_\perp-\frac{\boldsymbol{r}_\perp}{2},\boldsymbol{b}_\perp+\frac{\boldsymbol{r}_\perp}{2})\;|P\rangle \tag{4.21}$$

where

$$S^{[\square]}(\boldsymbol{x}_\perp,\boldsymbol{y}_\perp)\equiv\frac{1}{N_c}\mathrm{Tr}\left[U^{[\square]}(\boldsymbol{y}_\perp,\boldsymbol{x}_\perp)\right],\qquad \boldsymbol{r}_\perp=\boldsymbol{y}_\perp-\boldsymbol{x}_\perp,\qquad \boldsymbol{b}_\perp=\frac{(\boldsymbol{x}_\perp+\boldsymbol{y}_\perp)}{2}. \tag{4.22}$$

Comparing again to the notation of [23] we see that

$$\mathcal{F}_x=G^{[\square]}/((4\pi)^2N_c) \tag{4.23}$$

where $\mathcal{F}_x$ satisfies the normalization condition

$$\int d^2\boldsymbol{k}_\perp\,d^2\boldsymbol{\Delta}_\perp\,e^{-i\boldsymbol{\Delta}_\perp\cdot\boldsymbol{b}_\perp}\,\mathcal{F}_x(\boldsymbol{k}_\perp,\boldsymbol{\Delta}_\perp)=1. \tag{4.24}$$

In Eq. (4.21) $\boldsymbol{b}_\perp$ is defined with respect to some unspecified reference point, so one may wonder what determines this position? In fact, in the derivation of Eq. (4.17) the following step is performed:

$$\langle P+\Delta_\perp|O(\boldsymbol{0}_\perp,\boldsymbol{r}_\perp)|P\rangle=e^{i\boldsymbol{b}_\perp\cdot\boldsymbol{\Delta}_\perp}\langle P+\Delta_\perp|O(\boldsymbol{b}_\perp,\boldsymbol{r}_\perp)|P\rangle$$
$$=\frac{\int d^2\boldsymbol{b}_\perp e^{i\boldsymbol{b}_\perp\cdot\boldsymbol{\Delta}_\perp}\langle P+\Delta_\perp|O(\boldsymbol{b}_\perp,\boldsymbol{r}_\perp)|P\rangle}{\int d^2\boldsymbol{b}_\perp}, \tag{4.25}$$

where the last step is formally exact, but as mentioned, the normalization factor $\int d^2\boldsymbol{b}_\perp$ (which is part of $\langle P|P\rangle$, cf. Eq. (4.20)) is actually divergent and requires consideration of a regulator. In the derivation it is used that although matrix elements of the form $\langle P+\Delta_\perp|O(\boldsymbol{b}_\perp)|P\rangle$ are both $\boldsymbol{b}_\perp$ and $\boldsymbol{\Delta}_\perp$ dependent, despite $\boldsymbol{b}_\perp$ and $\boldsymbol{\Delta}_\perp$ being each other's Fourier conjugates, the $\boldsymbol{b}_\perp$ dependence enters just through a phase. As a result, the integrand is actually $\boldsymbol{b}_\perp$ independent and any reference point will do. However, the analysis in the previous subsection suggests that it is better to replace Eq. (4.25) by

$$\langle P+\Delta_\perp|O(\boldsymbol{0}_\perp,\boldsymbol{r}_\perp)|P\rangle=\int\frac{d^2\boldsymbol{b}_\perp}{(2\pi)^2}\,e^{i\boldsymbol{b}_\perp\cdot\boldsymbol{\Delta}_\perp}\langle P^+,\boldsymbol{R}_\perp=0|O(\boldsymbol{b}_\perp,\boldsymbol{r}_\perp)|P^+,\boldsymbol{R}_\perp=0\rangle, \tag{4.26}$$

where $\boldsymbol{b}_\perp$ is considered with respect to $\boldsymbol{R}_\perp=0$ and a large P^+ momentum frame and a spatially localized wave packet are implicitly considered. It is also implicitly used that $\langle P^+,\boldsymbol{P}'_\perp|\;O(\boldsymbol{0}_\perp,\boldsymbol{r}_\perp)\;|P^+,\boldsymbol{P}_\perp\rangle$ only depends on the difference of $\boldsymbol{P}'_\perp$ and $\boldsymbol{P}_\perp$, just like for $\boldsymbol{r}_\perp=0$ in the GPD case ($\boldsymbol{r}_\perp$ is not affected by the required transverse boosts, since the corresponding $r^+ = 0$). It is furthermore interesting to note that Eq. (4.26) relates an off-forward matrix element to an integral over diagonal matrix elements.

Following the above replacement, matrix elements of the form

$$\langle P'|O(\boldsymbol{b}_\perp, \boldsymbol{r}_\perp)|P\rangle / \langle P|P\rangle \tag{4.27}$$

are to be interpreted as

$$\langle P^+, \boldsymbol{R}_\perp = 0|O(\boldsymbol{b}_\perp, \boldsymbol{r}_\perp)|P^+, \boldsymbol{R}_\perp = 0\rangle \tag{4.28}$$

in the expression for $G^{[\Box]}$ and, similarly, for $\mathcal{F}^{[\Box]}$ which follows from $G^{[\Box]}$ by the replacement $S^{[\Box]}(\boldsymbol{x}_\perp, \boldsymbol{y}_\perp) \to 1 - S^{[\Box]}(\boldsymbol{x}_\perp, \boldsymbol{y}_\perp)$:

$$\begin{aligned}\mathcal{F}^{[\Box]}(\boldsymbol{k}_\perp, \boldsymbol{\Delta}_\perp) &= \frac{4N_c}{\langle P|P\rangle} \int \frac{d^2\boldsymbol{x}_\perp d^2\boldsymbol{y}_\perp}{(2\pi)^2}\, e^{-ik\cdot(\boldsymbol{x}_\perp - \boldsymbol{y}_\perp)} e^{i\Delta\cdot(\boldsymbol{x}_\perp + \boldsymbol{y}_\perp)/2} \langle P'|\, 1 - S^{[\Box]}(\boldsymbol{x}_\perp, \boldsymbol{y}_\perp)\, |P\rangle \\ &= \frac{4N_c}{\langle P|P\rangle} \int \frac{d^2\boldsymbol{r}_\perp d^2\boldsymbol{b}_\perp}{(2\pi)^2}\, e^{-i\boldsymbol{k}_\perp\cdot\boldsymbol{r}_\perp} e^{i\boldsymbol{\Delta}_\perp\cdot\boldsymbol{b}_\perp} \langle P'|\, 1 - S^{[\Box]}(\boldsymbol{b}_\perp - \frac{\boldsymbol{r}_\perp}{2}, \boldsymbol{b}_\perp + \frac{\boldsymbol{r}_\perp}{2})\, |P\rangle .\end{aligned} \tag{4.29}$$

The function $\mathcal{F}^{[\Box]}$, which is associated with $G^{[\Box]}$ in the small-x limit of the gluon GTMD definition of Eq. (4.17), will be extensively used in the analysis of diffractive dijet production and diffractive J/ψ production in the subsequent chapters.

Once the gluon GTMD is extracted from data one may wonder if it can be used to obtain the gluon GPD by integration, as suggested by Fig. 4.1. In [170] it was pointed out that the gluon GPD H_g at small x can be expressed in terms of the small-x gluon GTMD through the following integral[4]:

$$xH_g(x, \Delta_\perp) = \frac{1}{(4\pi)^2\alpha_s} \int d^2\boldsymbol{q}_\perp \boldsymbol{q}_\perp^2 \mathcal{F}_0^{[\Box]}(x, q_\perp, \Delta_\perp). \tag{4.30}$$

This relation is derived using the operator definitions of the functions, not taking into account renormalization. However, this relation suffers from the same problems as its forward limit, where the collinear PDF $f(x)$ is viewed as the integral of a TMD [39]:

$$f(x) \overset{?}{=} \int d^2\boldsymbol{q}_\perp f(x, q_\perp^2). \tag{4.31}$$

Since the large transverse momentum tail of the TMD $f(x, q_\perp^2)$ behaves as $1/q_\perp^2$, the integral will diverge logarithmically and requires some form of regularization. More formally, beyond tree level TMD factorization implies that the TMD depends on two scales, the rapidity scale ζ and the renormalization scale μ, satisfying two coupled evolution equations, whereas the collinear PDF only depends on the scale μ and satisfies just one evolution equation. It is thus not straightforward how to relate them beyond

---

[4] Taking into account that the definition of $\mathcal{F}_0^{[\Box]}$ differs from that of F_0 in [170], Eq. (4.30) differs by a factor 2 from the one given in [170].

tree level, and it will be scale and scheme dependent. Clearly, Eq. (4.30) suffers from the same problems. Because of this, here we do not provide curves for GPDs based on the GTMDs we obtain, as they would unavoidably depend on the adopted procedure of how to regulate the large transverse momentum behavior to make the integral in Eq. (4.30) converge. Rather than expecting that the TMD determines the collinear PDF through an integral relation, one can instead consider the unambiguous relation in which the collinear PDF determines the large transverse momentum dependence of the TMD:

$$f(x, q_\perp^2) \propto \alpha_s \frac{1}{q_\perp^2} \int \frac{dy}{y} P\left(\frac{x}{y}\right) f(y), \tag{4.32}$$

where P denotes a splitting function (ignoring for simplicity the possibility of mixing among various PDFs). Similar expressions hold for the perturbative large transverse momentum tails of GTMDs in terms of GPDs, as recently studied at the one loop level in [171]. So rather than using fits of GTMDs to obtain results for GPDs, it is better to use models, lattice determinations, or fits of GPDs to predict the tails of the GTMDs and compare those to GTMD fits. This we do not attempt here, as we are primarily concerned with the small transverse momentum region in the discussion. In the analyses in the next two chapters we will emphasize which information on GTMDs one can obtain that go beyond the GPDs in terms of integrals of GTMDs other than the one in Eq. (4.30).

5

Probing gluon GTMD in diffractive dijet production

As discussed earlier, diffractive dijet production at small x is proposed as a potential probe of the gluon GTMD. In this chapter, we will discuss how a gluon GTMD model, based on the MV model with a minimum number of free parameters, can describe the available data from the H1 experiment at the HERA collider and provide predictions as a test for future experiments, especially at the future EIC. First, we will consider the general expression of the cross section in Sec. 5.1, then show how the GTMD enters the cross section in Sec. 5.2. Next, we will introduce an x independent model based on the impact parameter-dependent MV model in Sec. 5.3, and fit it to the HERA data. We will also provide predictions based on this model. In Sec. 5.4, we improve the model by incorporating the x dependent GBW parameterization, resulting in an improvement in the fit to the H1 data, especially the Q^2 dependence. Lastly, we also discuss how this diffractive dijet production process probes information about the GTMD that goes beyond the GPD description of it that has been considered in e.g. [158].[1]

---

[1] Most of the results in this chapter are published in [68] and [172].

5.1 Diffractive dijet production cross section

According to the dipole framework, the production of a quark-antiquark pair $q\bar{q}$ (a dipole) from a photon can be obtained by applying the quark and anti-quark creation operators to the vacuum state, represented in mixed momentum-coordinate space, see e.g. [64, 65]:

$$|q(p_1^+, \boldsymbol{x}_{1\perp}, \alpha_1, h_1)\,\bar{q}(p_2^+, \boldsymbol{x}_{2\perp}, \alpha_2, h_2)\rangle = b^\dagger(p_1^+, \boldsymbol{x}_{1\perp}, \alpha_1, h_1)\, d^\dagger(p_2^+, \boldsymbol{x}_{2\perp}, \alpha_2, h_2)|0\rangle. \tag{5.1}$$

Here, $\boldsymbol{x}_{i\perp}$ denotes the transverse position of the quark/anti-quark when interacting with the target, $h_i = \pm 1/2$ denotes their helicity, while p_i and k_i represent their momentum before and after interacting with the target, respectively. The index $i = 1, 2$ refers to the quark and antiquark, respectively. The quark/anti-quark color indices before and after the interaction with the target are indicated by α_i and β_i, respectively. The momentum space $(p^+, \boldsymbol{p}_\perp)$ and the mixed space $(p^+, \boldsymbol{x}_\perp)$ representation of the creation operator for quark (antiquark) $b^\dagger$ ($d^\dagger$) are related by the Fourier transform of the transverse part

$$b^\dagger(p^+, \boldsymbol{p}_\perp) = \int \frac{d^2\boldsymbol{x}_\perp}{2\pi} e^{i\boldsymbol{p}_\perp\cdot\boldsymbol{x}_\perp} b^\dagger(p^+, \boldsymbol{x}_\perp), \tag{5.2}$$

where the creation operators in the mixed space representation follow the anti-commutation relation [62, 65]:

$$\begin{aligned}\{b(p'^+, \boldsymbol{x}'_\perp, \alpha', h'), b^\dagger(p^+, \boldsymbol{x}_\perp, \alpha, h)\} &= \{d(p'^+, \boldsymbol{x}'_\perp, \alpha', h'), d^\dagger(p^+, \boldsymbol{x}_\perp, \alpha, h)\} \\ &= (2\pi)2p^+\delta(p'^+ - p^+)\delta^{(2)}(\boldsymbol{x}'_\perp - \boldsymbol{x}_\perp)\delta_{\alpha'\alpha}\delta_{h'h}.\end{aligned} \tag{5.3}$$

Following the definition of the $q\bar{q}$ states in the mixed space representation given by Eq. (5.1), we can define the splitting of the incoming virtual photon into the dipole as:

$$|\gamma^*(z_i, \boldsymbol{x}_{i\perp})\rangle = \sum_{q\bar{q}\,\text{states}} \Psi_{q\bar{q}}(z_i, \boldsymbol{x}_{i\perp})|q(z_1, \boldsymbol{x}_{1\perp})\bar{q}(z_2, \boldsymbol{x}_{2\perp})\rangle \tag{5.4}$$

where $\Psi_{q\bar{q}}$ is the incoming virtual photon lightcone wave function defined in Eq. (3.5). However, here we use a different notation, where $z_1 = z$ for the quark and $z_2 = 1 - z$ for the antiquark. We will use z_i instead of k_i^+ to define the longitudinal component of the quark/anti-quark momentum.

Within the eikonal approximation, the dipole interacts with an infinite number of gluon exchanges, which can be expressed in terms of Wilson lines $\mathcal{U}(\boldsymbol{x}_{i\perp})$. Since the interaction takes a very short time, the transverse position of the quark and antiquark, denoted by $\boldsymbol{x}_{i\perp}$, remains constant. Therefore, the outgoing wave function after the interaction can be expressed as follows

$$\hat{S}|\gamma^*\rangle = \sum_{q\bar{q}\,\text{states}} \left[\mathcal{U}(\boldsymbol{x}_{1\perp})\mathcal{U}^\dagger(\boldsymbol{x}_{2\perp})\right]_{\beta_1\beta_2} \Psi_{q\bar{q}}(z_i, \boldsymbol{x}_{i\perp})\, |q(z_1, \boldsymbol{x}_{1\perp}, \beta_1)\bar{q}(z_2, \boldsymbol{x}_{2\perp}, \beta_2)\rangle \tag{5.5}$$

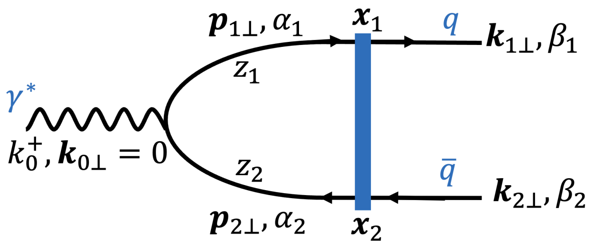

Figure 5.1: Diagram of diffractive DIS $\gamma^* p$ at the leading order. A virtual photon which splits into a dipole ($q\bar{q}$ pair) interacts with the target. The bold blue vertical line indicates the interaction position of the dipole with the target.

with $\mathcal{U}(\boldsymbol{x}_{1\perp})$ is the Wilson line in the fundamental representation defined in Eq. (3.10). The overlap of the incoming and outgoing wave functions, which defines the dipole scattering amplitude or the S-matrix, now reads:

$$S_{q\bar{q}}(\boldsymbol{x}_{1\perp}, \boldsymbol{x}_{2\perp}) = \langle \bar{q}(k_1^+, \boldsymbol{x}_{1\perp})\, q(k_2^+, \boldsymbol{x}_{2\perp}) | \hat{S} | \gamma^*(z_i, \boldsymbol{x}_{i\perp}) \rangle \tag{5.6}$$

As we are working in the momentum representation, we should perform a Fourier transform of the mixed-space representation to obtain the momentum-space representation

$$S_{q\bar{q}}(\boldsymbol{k}_{1\perp}, \boldsymbol{k}_{2\perp}) = \int \frac{d^2\boldsymbol{x}_{1\perp}}{2\pi} \int \frac{d^2\boldsymbol{x}_{2\perp}}{2\pi} \mathrm{e}^{-i\boldsymbol{k}_{1\perp}\cdot\boldsymbol{x}_{1\perp} - i\boldsymbol{k}_{2\perp}\cdot\boldsymbol{x}_{2\perp}} \left[\mathcal{U}(\boldsymbol{x}_{1\perp})\mathcal{U}^\dagger(\boldsymbol{x}_{2\perp})\right] \Psi_{q\bar{q}}(z_i, \boldsymbol{x}_{i\perp}). \tag{5.7}$$

Using the optical theorem

$$\sigma^{\gamma^* p(A)} = \frac{2}{2q^+(2\pi)\delta(k_1^+ + k_2^+ - q^+)} \mathrm{Re}\left[\langle \bar{q}(k_1^+, \boldsymbol{k}_{1\perp})\, q(k_2^+, \boldsymbol{k}_{2\perp}) | I - \hat{S} | \gamma^*(z_i, \boldsymbol{k}_{i\perp}) \rangle\right] \tag{5.8}$$

the scattering amplitude can be obtained as

$$\begin{aligned} \langle \mathcal{M}_{q\bar{q}} \rangle_C = {} & \frac{1}{2(2\pi)\delta(z_1 + z_2 - 1)} \int \frac{d^2\boldsymbol{x}_{1\perp}}{2\pi} \int \frac{d^2\boldsymbol{x}_{2\perp}}{2\pi} \mathrm{e}^{-i\boldsymbol{k}_{1\perp}\cdot\boldsymbol{x}_{1\perp} - i\boldsymbol{k}_{2\perp}\cdot\boldsymbol{x}_{2\perp}} \\ & \times \left[I - S(\boldsymbol{x}_{1\perp}, \boldsymbol{x}_{2\perp})\right] \Psi_{q\bar{q}}(z_i, \boldsymbol{x}_{i\perp}). \end{aligned} \tag{5.9}$$

The scattering amplitude will enter the diffractive dijet DIS cross section, which is defined as:

$$\begin{aligned} 2k_1^+ 2k_2^+ \frac{d\sigma^{\gamma^* p(A)}}{dk_1^+ dk_2^+ d^2\boldsymbol{k}_{1\perp} d^2\boldsymbol{k}_{2\perp}} &= \sum_{\beta_i h_i} \frac{(2q^+)\,\delta(k_1^+ + k_2^+ - q^+)}{(2\pi)^5} \left|\langle \mathcal{M}_{q\bar{q}} \rangle_C\right|^2 \\ \frac{d\sigma^{\gamma^* p(A)}}{dz_1 dz_2 d^2\boldsymbol{k}_{1\perp} d^2\boldsymbol{k}_{2\perp}} &= \sum_{\beta_i h_i} \frac{\delta(z_1 + z_2 - 1)}{2z_1 z_2\,(2\pi)^5} \left|\langle \mathcal{M}_{q\bar{q}} \rangle_C\right|^2 \end{aligned} \tag{5.10}$$

with C indicates an average over the color of the target. In the expression of the cross section, one usually utilizes $\boldsymbol{K}_\perp$ and $\boldsymbol{\Delta}_\perp$ instead of $\boldsymbol{k}_{i\perp}$, which are the Fourier conjugates of $\boldsymbol{b}_\perp$ and $\boldsymbol{r}_\perp$, respectively. They can be related as follows:

$$\begin{aligned} \boldsymbol{b}_\perp &= \frac{\boldsymbol{x}_{1\perp}+\boldsymbol{x}_{2\perp}}{2} \quad &\leftrightarrow \quad \boldsymbol{\Delta}_\perp &= \boldsymbol{k}_{1\perp}+\boldsymbol{k}_{2\perp} \\ \boldsymbol{r}_\perp &= \boldsymbol{x}_{1\perp}-\boldsymbol{x}_{2\perp} \quad &\leftrightarrow \quad \boldsymbol{K}_\perp &= \frac{\boldsymbol{k}_{1\perp}-\boldsymbol{k}_{2\perp}}{2}. \end{aligned} \tag{5.11}$$

We will discuss the cross section further in Sec. 5.3.1 after introducing the explicit form of the dipole scattering amplitude.

5.2 Diffractive dijet production cross sections in terms of GTMD

The GTMD enters the diffractive dijet cross section via $\mathcal{F}^{[\square]}$, which is defined in Eq. (4.29) and related to the GTMD $G^{[\square]}$. As emphasized before, we will only consider unpolarized gluons, particularly because the azimuthal modulations in the diffractive dijet cross section arising from the elliptic GTMD [23, 173] are expected to be much smaller than the present cross section uncertainties. In the model studies of [174–178] and in the CMS data [179] the azimuthal asymmetries are found to be at the 10-30% level or (much) smaller. As a first step it would be important to check whether the GTMD description of diffractive dijet production is consistent with cross section measurements in various kinematic variables and various kinematic regions. With the presented results we hope to facilitate such a study.

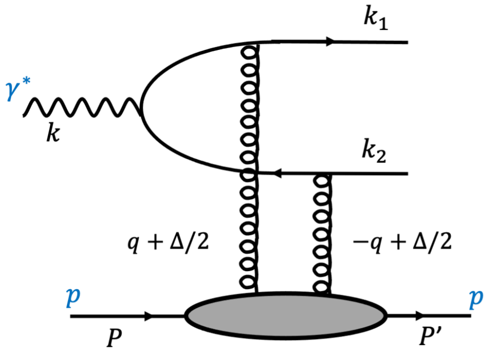

Figure 5.2: One of the leading order diagrams of diffractive dijet production in ep collisions.

Following Ref. [23] the cross section of diffractive dijet production in electron-proton collisions is expressed in terms of $\mathcal{F}^{[\Box]}$ cf. Eq. (4.29) as

$$\frac{d\sigma}{dy_1 dy_2 d^2\boldsymbol{k}_{1\perp} d^2\boldsymbol{k}_{2\perp}} \propto \int d^2\boldsymbol{q}_\perp d^2\boldsymbol{q}'_\perp \mathcal{F}^{[\Box]}(\boldsymbol{q}_\perp, \boldsymbol{\Delta}_\perp)\mathcal{F}^{[\Box]}(\boldsymbol{q}'_\perp, \boldsymbol{\Delta}_\perp)\mathcal{A}(\boldsymbol{K}_\perp, \boldsymbol{q}_\perp, \boldsymbol{q}'_\perp, \epsilon_f^2), \quad (5.12)$$

for a particular amplitude function $\mathcal{A}$, with $\boldsymbol{q}_\perp^{(\prime)}$ related to the transverse momentum of the gluons as depicted in Fig. 5.2. Here $K_\perp$ is the transverse part of $K = (k_1 - k_2)/2$, where k_i denotes the momentum of jet i, $\Delta_\perp$ is the transverse part of $\Delta = k_1 + k_2$, y_i is the rapidity of jet i, and $\epsilon_f^2 = z(1-z)Q^2$ (ignoring the quark mass), with z is the momentum fraction of one of the two jets. One considers this process in the so-called correlation limit: $\Delta_\perp \ll K_\perp$, where $K_\perp$ sets the hard scale, allowing to also consider the photoproduction ($Q^2 = 0$) case. One of the leading order diagrams of diffractive dijet production in ep collisions in this kinematic regime is shown in Fig. 5.2. In this exclusive process the transverse momentum of the jet pair gives a handle on the $\boldsymbol{\Delta}_\perp$ momentum, even if the off-forwardness of the struck nucleon or nucleus itself is not measured. More details of the cross section calculation will be given below, but first we will discuss the model for the Wilson loop GTMD $G^{[\Box]}$ and the corresponding $\mathcal{F}^{[\Box]}$.

In the process considered the incoming virtual photon splits into a quark-antiquark dipole pair that interacts with the proton or nucleus.[2]

The large jet transverse momentum, or equivalently large $K_\perp$, the typical size $r_\perp$ of the dipole will be small. At small enough x even small dipoles will have multiple interactions with the target. In the saturation regime at small x one often employs the MV model for the dipole scattering amplitude [25, 55, 56, 73, 74]:

$$\left\langle \frac{S^{[\Box]}(\boldsymbol{x}_\perp, \boldsymbol{y}_\perp) + S^{[\Box]\dagger}(\boldsymbol{x}_\perp, \boldsymbol{y}_\perp)}{2} \right\rangle_C = \exp\left(-\frac{1}{4} r_\perp^2 Q_s^2 \ln\left[\frac{1}{r_\perp^2 \Lambda^2} + e\right]\right), \quad (5.13)$$

where the subscript C indicates that an average over the color configuration of the target is taken, Λ denotes the QCD scale, and e is the natural number that is introduced as an infrared regulator, see [88]. For an infinitely large nuclear target the saturation scale Q_s is only a function of x. As a consequence, in that case the MV model expression applies to the forward scattering case and it is only a function of $\boldsymbol{r}_\perp = \boldsymbol{y}_\perp - \boldsymbol{x}_\perp$ due to translational invariance ($r_\perp^2 = |\boldsymbol{r}_\perp^2|$). For finite nuclei at small x, a dependence of Q_s on impact parameter is often considered, see e.g. [58, 79, 182]. The $b_\perp (= |\boldsymbol{b}_\perp|)$ dependence of Q_s is usually implemented as $Q_s^2(x, b_\perp) \equiv Q_s^2(x) T_A(b_\perp)$, where $T_A(b_\perp)$ is the nuclear

---

[2] Note that for sufficiently high center of mass energy of the scattering this dipole picture can be reconciled with the target having a large P^+ momentum which, as we discussed, was required to consider the impact parameter dependence with respect to a sufficiently well determined center $R_\perp = 0$ of the target. The appropriate frame is referred to as the dipole frame [180] which is discussed in Appendix B. In addition, for large dipole sizes the impact parameter should also be defined with respect to the center of momentum of the dipole [181], but that is not relevant for the small dipole sizes considered here. The impact parameter definition actually depends on what one considers the centers of the two extended objects: the proton/nucleus and the dipole. One can consider the center of the dipole or the transverse center of longitudinal momentum. The former definition is used here, while the latter, which is typically applied to the proton/nucleus state [139, 165], could also be adopted for the dipole as done in Chapter 6.

profile function or nuclear thickness function that describes the distribution of nuclear matter inside a nucleus integrated over the z component of $\boldsymbol{b}$ [79]. Here $T_A(b_\perp)$ scales with $A^{1/3}$. For scattering off a proton at very small x that is described by the CGC, one can similarly introduce a profile function. To be specific, we will consider

$$Q_s^2(b_\perp) = \frac{4\pi\alpha_s^2 C_F}{N_c} T_p(b_\perp), \tag{5.14}$$

with a Gaussian $b_\perp$ profile [177]:

$$T_p(b_\perp) = \exp\left(-b_\perp^2/(2R_p^2)\right), \tag{5.15}$$

where R_p is the gluonic radius of the proton for which we will take the value $R_p = 0.5$ fm, such that $1/R_p \approx 0.4$ GeV.

Using Eq. (5.13) with this $Q_s^2(b_\perp)$ implies automatically nonzero off-forwardness, even if one is considering only diagonal expectation values. Furthermore, by identifying (and implicitly absorbing the lightcone volume factor $2P^+ \int db^-$ of $\langle P|P\rangle$ in the process, see the discussion around Eqs. (4.26) - (4.28))

$$\langle S^{[\Box]}(\boldsymbol{b}_\perp, \boldsymbol{r}_\perp)\rangle_C = \langle P^+, \boldsymbol{R}_\perp = 0|S^{[\Box]}(\boldsymbol{b}_\perp, \boldsymbol{r}_\perp)|P^+, \boldsymbol{R}_\perp = 0\rangle, \tag{5.16}$$

we arrive at the following expression for the GTMD:

$$G^{[\Box]}(\boldsymbol{k}_\perp, \boldsymbol{\Delta}_\perp) = 4N_c \int \frac{d^2\boldsymbol{r}_\perp d^2\boldsymbol{b}_\perp}{(2\pi)^2}\, e^{-i\boldsymbol{k}_\perp\cdot\boldsymbol{r}_\perp} e^{i\boldsymbol{\Delta}_\perp\cdot\boldsymbol{b}_\perp} \exp\left(-\frac{1}{4} r_\perp^2 Q_s^2(b_\perp) \ln\left[\frac{1}{r_\perp^2\Lambda^2} + e\right]\right). \tag{5.17}$$

This becomes the standard MV model expression for the gluon TMD in the limit $R_p \to \infty$ and $\Delta_\perp \to 0$. We expect this model expression to be applicable as long as the typical $b_\perp$ values probed are larger than the typical dipole sizes. Therefore, we will restrict application of the model to the region $\Delta_\perp \lesssim 1$ GeV, which is consistent with the correlation limit, because well-defined jets will have transverse momenta of at least a few GeV. In practice, higher $\Delta_\perp$ will hardly matter, as will be seen (cf. Fig. 5.4).

In [174, 175] Gaussian weighting factors $e^{-\epsilon_r r_\perp^2}$ and $e^{-\epsilon_b b_\perp^2}$ are introduced as cut offs. This will cut out the regions where the $q\bar{q}$ dipole does not overlap with the target or its size becomes large compared to the target size, where the model should not be applicable. Here we will only introduce $e^{-\epsilon_r r_\perp^2}$, as we found that there is actually no need for $e^{-\epsilon_b b_\perp^2}$ when considering $\mathcal{F}^{[\Box]}$.

5.3 An x independent model

To develop a realistic yet simple GTMD model, we will introduce a model with a minimal number of free parameters and investigate whether it can adequately describe the available data, or if further improvements are necessary. To be specific, in order to fit the model to H1 data, we will introduce two free parameters $\{\epsilon_r, \chi\}$ in the model in the following way:

$$\mathcal{F}^{[\Box]}(\boldsymbol{k}_\perp, \boldsymbol{\Delta}_\perp) = 4N_c \int \frac{d^2\boldsymbol{r}_\perp d^2\boldsymbol{b}_\perp}{(2\pi)^2}\, e^{-i\boldsymbol{k}_\perp\cdot\boldsymbol{r}_\perp} e^{i\boldsymbol{\Delta}_\perp\cdot\boldsymbol{b}_\perp}\, e^{-\epsilon_r r_\perp^2} \\ \times \quad \left[1 - \exp\left(-\frac{1}{4} r_\perp^2 \chi Q_s^2(b_\perp) \ln\left[\frac{1}{r_\perp^2\Lambda^2} + e\right]\right)\right]. \tag{5.18}$$

These parameters introduced here are chosen based on physical considerations. The parameter ϵ_r serves as the dipole size cutoff to ensure that the dipole sizes contributing are restricted to the perturbative region, since we expect the dipole sizes that contribute to the cross section to be small. This Gaussian weight factor was also introduced in the Wigner, Husimi and GTMD distributions of [174, 175]. In practice the dipole size restriction should result from the kinematics of the process, i.e. by the large transverse momentum of the jets (recall that $\boldsymbol{K}_\perp$ is the Fourier conjugate of $\boldsymbol{r}_\perp$) or the large mass of the produced quarkonium, but by enforcing it explicitly in the model, we can obtain convergent integrals of the GTMD without reference to a process. The other free parameter χ allows to change the overall magnitude of the saturation scale, which is expected to be close to 1 if the estimates of the saturation scale in DIS are also applicable in this diffractive process. In the numerical calculation, we will use $\epsilon_r = (0.5\,\mathrm{fm})^{-2}$ and $\chi = 1.25$, which were obtained from fitting to the H1 data, as will be explained in Sec. 5.3.4. We will consider a fixed value $\Lambda = 0.24\,\mathrm{GeV}$ and consider $N_f = 4$ for the number of active flavors. In the context of photoproduction for the EIC prediction, we consider $K_\perp$ to set the hard scale. Therefore, it is necessary to have $K_\perp > 2m_c$. The fitted χ value can be viewed as determining the (average) x value of the model through the x dependence of the saturation scale. In applications of the MV model the saturation scale is usually taken to be $Q_s^2(x) = A^{1/3}(3\cdot 10^{-4}/x)^{0.3}$ $[\mathrm{GeV}^2]$, that stems from the GBW (geometric scaling) description of the inclusive DIS data from HERA [183]. Equating this expression with $\chi Q_s^2(b_\perp = 0_\perp) = 0.5\chi A^{1/3}$ $[\mathrm{GeV}^2]$, one finds $\chi = 2(3\cdot 10^{-4}/x)^{0.3}$.

Expanding Equation (5.18) in the Fourier mode decomposition yields:

$$\mathcal{F}^{[\Box]}(\boldsymbol{k}_\perp, \boldsymbol{\Delta}_\perp) = \mathcal{F}_0^{[\Box]}(k_\perp, \Delta_\perp) + 2\mathcal{F}_2^{[\Box]}(k_\perp, \Delta_\perp)\cos 2\theta_{k\Delta} + ..., \tag{5.19}$$

where $\theta_{k\Delta}$ denotes the angle between $\boldsymbol{k}_\perp$ and $\boldsymbol{\Delta}_\perp$. The contribution of the elliptic part $\mathcal{F}_2^{[\Box]}$, and even more so of the higher order harmonics, to the cross section will be small compared to the angular independent part $\mathcal{F}_0^{[\Box]}$. Therefore, we will only retain the latter.

In Fig. 5.3, we show the function $\mathcal{F}_0^{[\Box]}$ for various parameter choices and ranges that we will consider for the model. This figure indicates that the contribution to the cross section comes from small values of $\Delta_\perp$, where $\Delta_\perp > 1$ GeV provides hardly any contribution. This justifies the requirement that the process we consider should be in the correlation limit. We note that the associated function of $\mathcal{F}_0^{[\Box]}$ has also been studied in [184], but we obtain a different result.

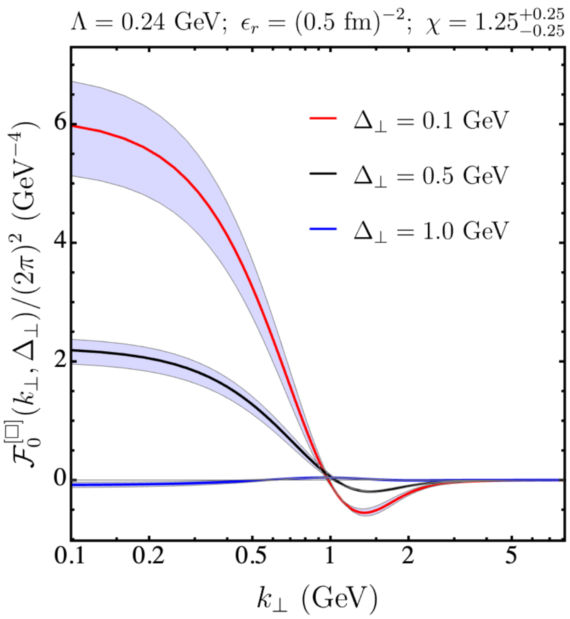

Figure 5.3: The function $\mathcal{F}_0^{[\square]}/(2\pi)^2$ as a function of the transverse momentum $k_\perp$ for three different values of $\Delta_\perp$ for the choice $\epsilon_r = (0.5\,\text{fm})^{-2}$. The curves are for $\chi = 1.25$ and the bands around them correspond to χ in the range from 1.0 to 1.5, where larger χ yields larger results.

5.3.1 The cross section

As discussed earlier, the cross section for the diffractive dijet production process $\gamma^* p(A) \to q\bar{q}p(A)$ can be calculated at leading order (LO) by combining two steps: 1) the incoming virtual photon which splits into a quark-antiquark dipole pair and 2) the interaction of the pair with the proton or nucleus via two-gluon exchange. The LO of the virtual photon light cone wave function with virtuality Q described in Eq. (3.5) is discussed in many papers, such as [62, 64, 65]. Following Eq. (5.10), the diffractive dijet production cross section differential in z_i, $\boldsymbol{K}_\perp$ and $\boldsymbol{\Delta}_\perp$ can be expressed as:

$$\frac{d\sigma_{T,L}^{\gamma^* p}}{dz_1 dz_2 d^2\boldsymbol{K}_\perp d^2\boldsymbol{\Delta}_\perp} = \frac{1}{2(2\pi)^5 z_1 z_2}\delta(z_1 + z_2 - 1)\sum_{\beta_i h_i}\left|\langle \mathcal{M}_{q\bar{q}}\rangle_C\right|^2, \tag{5.20}$$

where $\mathcal{M}_{q\bar{q}}$ denotes the amplitude of this process defined in Eq. (5.9), $z_{1,2} = k_{1,2}^+/k^+$ are the outgoing quark and antiquark longitudinal momentum fraction with respect to the virtual photon longitudinal momentum, and the sum is over color indices β_i and quark helicities h_i. For the case of a transverse photon the amplitude is given by:

$$\begin{aligned}\mathcal{M}_{q\bar{q}}^T \;&=\; ee_f\sqrt{z_1 z_2}\,[z_2 - z_1 - 2h_1\lambda]\,\delta_{h_1,-h_2}\int d^2\boldsymbol{q}_\perp \int \frac{d^2\boldsymbol{r}_\perp\, d^2\boldsymbol{b}_\perp}{(2\pi)^2} e^{-i\boldsymbol{b}_\perp\cdot\boldsymbol{\Delta}_\perp} e^{-i\boldsymbol{r}_\perp\cdot\boldsymbol{q}_\perp} \\ &\times \left[\mathcal{U}_{\beta_1\beta_2}^{[\square]}(\boldsymbol{b}_\perp - \frac{\boldsymbol{r}_\perp}{2}, \boldsymbol{b}_\perp + \frac{\boldsymbol{r}_\perp}{2}) - \delta_{\beta_1\beta_2}\right]\frac{\boldsymbol{\epsilon}_\lambda\cdot(\boldsymbol{K}_\perp - \boldsymbol{q}_\perp)}{z_1 z_2 Q^2 + (\boldsymbol{K}_\perp - \boldsymbol{q}_\perp)^2},\end{aligned} \tag{5.21}$$

and for a longitudinal photon by:

$$\begin{aligned}\mathcal{M}^L_{q\bar{q}} &= -2ee_f\sqrt{z_1z_2}\,\delta_{h_1,-h_2}\int d^2\boldsymbol{q}_\perp \int \frac{d^2\boldsymbol{r}_\perp\, d^2\boldsymbol{b}_\perp}{(2\pi)^2} e^{-i\boldsymbol{b}_\perp\cdot\boldsymbol{\Delta}_\perp} e^{-i\boldsymbol{r}_\perp\cdot\boldsymbol{q}_\perp} \\ &\times \left[\mathcal{U}^{[\Box]}_{\beta_1\beta_2}(\boldsymbol{b}_\perp - \frac{\boldsymbol{r}_\perp}{2}, \boldsymbol{b}_\perp+\frac{\boldsymbol{r}_\perp}{2}) - \delta_{\beta_1\beta_2}\right]\frac{z_1z_2Q}{z_1z_2Q^2+(\boldsymbol{K}_\perp-\boldsymbol{q}_\perp)^2},\end{aligned} \tag{5.22}$$

where $\boldsymbol{\epsilon}_\lambda$ denotes the polarization vector of a photon with helicity λ. In the above expressions, we used the integral form of the modified Bessel functions $K_{0,1}$ in the photon wave functions in Eq. (3.5) using

$$\begin{aligned}\int d^2\boldsymbol{k}\frac{e^{i\boldsymbol{k}\cdot\boldsymbol{x}}}{\varepsilon_f^2+\boldsymbol{k}^2} &= 2\pi K_0\left(|\boldsymbol{x}|\varepsilon_f\right) \\ \int d^2\boldsymbol{k}\frac{e^{i\boldsymbol{k}_{1\perp}\cdot\boldsymbol{x}}}{\varepsilon_f^2+\boldsymbol{k}^2}\boldsymbol{k}^j &= 2\pi i\frac{\boldsymbol{x}^j}{|\boldsymbol{x}|}\varepsilon_f K_1\left(|\boldsymbol{x}|\varepsilon_f\right).\end{aligned} \tag{5.23}$$

We also assumed that in the dipole frame the incoming photon has zero transverse momentum, such that the quark and antiquark momenta are related as $\boldsymbol{p}_{1\perp} = -\boldsymbol{p}_{2\perp}$ (see Fig. 5.1).

After averaging over color and photon polarization, and after summing over quark helicities [64], we arrive at

$$\begin{aligned}\frac{d\sigma_T^{\gamma^*p}}{dz_1dz_2d^2\boldsymbol{K}_\perp d^2\boldsymbol{\Delta}_\perp} &= \frac{\alpha_{em}}{8(2\pi)^4N_c}\sum_f e_f^2\,\delta(z_1+z_2-1)\left[z_1^2+z_2^2\right] \\ &\times \int d^2\boldsymbol{q}_\perp \int d^2\boldsymbol{q}'_\perp\, \mathcal{F}^{[\Box]}(\boldsymbol{q}_\perp,\boldsymbol{\Delta}_\perp)\mathcal{F}^{[\Box]}(\boldsymbol{q}'_\perp,\boldsymbol{\Delta}_\perp) \\ &\times \left[\frac{(\boldsymbol{K}_\perp-\boldsymbol{q}_\perp)}{z_1z_2Q^2+(\boldsymbol{K}_\perp-\boldsymbol{q}_\perp)^2}\right]\cdot\left[\frac{(\boldsymbol{K}_\perp-\boldsymbol{q}'_\perp)}{z_1z_2Q^2+(\boldsymbol{K}_\perp-\boldsymbol{q}'_\perp)^2}\right],\end{aligned} \tag{5.24}$$

and

$$\begin{aligned}\frac{d\sigma_L^{\gamma^*p}}{dz_1dz_2d^2\boldsymbol{K}_\perp d^2\boldsymbol{\Delta}_\perp} &= \frac{\alpha_{em}}{2(2\pi)^4N_c}\sum_f e_f^2\,\delta(z_1+z_2-1)\;z_1^2z_2^2Q^2\int d^2\boldsymbol{q}_\perp \int d^2\boldsymbol{q}'_\perp \\ &\times \mathcal{F}^{[\Box]}(\boldsymbol{q}_\perp,\boldsymbol{\Delta}_\perp)\mathcal{F}^{[\Box]}(\boldsymbol{q}'_\perp,\boldsymbol{\Delta}_\perp) \\ &\times \frac{1}{z_1z_2Q^2+(\boldsymbol{K}_\perp-\boldsymbol{q}_\perp)^2}\frac{1}{z_1z_2Q^2+(\boldsymbol{K}_\perp-\boldsymbol{q}'_\perp)^2}.\end{aligned} \tag{5.25}$$

As discussed earlier we will only consider the angular independent part $\mathcal{F}_0^{[\Box]}$.

We note that since there is an average over the color configurations of the target, the cross section will scale as N_c, the sum over colors of the quark-antiquark pair. Since we express the cross section in terms of GTMDs that themselves scale as N_c, the above expressions have an overall $1/N_c$ factor, rather than N_c like in e.g. [64]. But the results are consistent with each other.

In order to relate $\sigma^{\gamma^* p}$ to the diffractive dijet cross section σ^{ep} for electron-proton collisions in DIS in HERA experiments, one can use [64]

$$\frac{d\sigma^{ep}}{dx\, dQ^2} = \frac{\alpha_{em}}{\pi x Q^2} \left[\left(1 - y + \frac{y^2}{2}\right) \sigma_T^{\gamma^* p} + (1-y)\, \sigma_L^{\gamma^* p} \right], \tag{5.26}$$

with $y = Q^2/sx$ and $\sqrt{s}$ is the center of mass energy of ep collision, which for the H1 data to be discussed was 319 GeV. We will fit the resulting expression to the high Q^2 electroproduction data of H1 and make predictions for high Q^2 electroproduction at EIC. We will also make predictions for photoproduction, which we now discuss.

5.3.2 Photoproduction: $Q^2 = 0$

For the case of $Q^2 = 0$ the expression for $d\sigma_T^{\gamma^* p}$ can be used to arrive at:

$$\begin{aligned} \frac{d\sigma^{\gamma p}}{dz_1 dz_2 d^2\boldsymbol{K}_\perp d^2\boldsymbol{\Delta}_\perp} &= \frac{\alpha_{em}}{8(2\pi)^4 N_c} \sum_f e_f^2\, \delta(z_1 + z_2 - 1) \left[z_1^2 + z_2^2\right] \\ &\times \int d^2\boldsymbol{q}_\perp \int d^2\boldsymbol{q}'_\perp \mathcal{F}^{[\Box]}(\boldsymbol{q}_\perp, \boldsymbol{\Delta}_\perp)\mathcal{F}^{[\Box]}(\boldsymbol{q}'_\perp, \boldsymbol{\Delta}_\perp) \\ &\times \left[\frac{(\boldsymbol{K}_\perp - \boldsymbol{q}_\perp)}{(\boldsymbol{K}_\perp - \boldsymbol{q}_\perp)^2}\right] \cdot \left[\frac{(\boldsymbol{K}_\perp - \boldsymbol{q}'_\perp)}{(\boldsymbol{K}_\perp - \boldsymbol{q}'_\perp)^2}\right]. \end{aligned} \tag{5.27}$$

The integrations over the angles of $\boldsymbol{q}_\perp$ and $\boldsymbol{q}'_\perp$ can be calculated analytically to arrive at [175, 185]

$$\int d^2\boldsymbol{q}_\perp \frac{\mathcal{F}_0^{[\Box]}(q_\perp, \Delta_\perp)\,(\boldsymbol{K}_\perp - \boldsymbol{q}_\perp)}{(\boldsymbol{K}_\perp - \boldsymbol{q}_\perp)^2} = \frac{(2\pi)^3 \boldsymbol{K}_\perp}{K_\perp^2} A_T(K_\perp, \Delta_\perp), \tag{5.28}$$

with

$$A_T(K_\perp, \Delta_\perp) = \frac{1}{(2\pi)^2} \int_0^{K_\perp} dq_\perp\, q_\perp\, \mathcal{F}_0^{[\Box]}(q_\perp, \Delta_\perp). \tag{5.29}$$

In Fig. 5.4 we show the function $A_T(K_\perp, \Delta_\perp)$ as a function of $K_\perp$ for the same parameters choices and ranges as in Fig. 5.3. It shows that the function is already very small when $\Delta_\perp = 1$ GeV.

The γp differential cross section can thus be written as:

$$\frac{d\sigma^{\gamma p}}{dz_1 dz_2 dK_\perp d\Delta_\perp^2} = \frac{(2\pi)^4 \alpha_{em}}{16 N_c} \sum_f e_f^2\, \delta(z_1 + z_2 - 1) \left[z_1^2 + z_2^2\right] \frac{A_T^2(K_\perp, \Delta_\perp)}{K_\perp}. \tag{5.30}$$

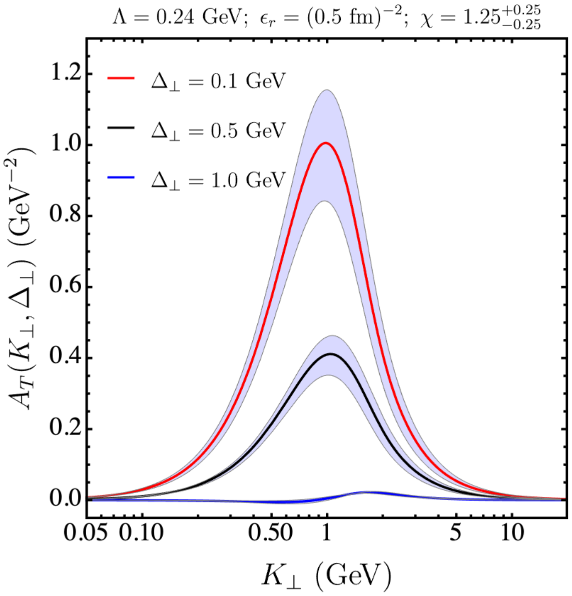

Figure 5.4: The function $A_T(K_\perp, \Delta_\perp)$ as a function of $K_\perp$ for three different values of $\Delta_\perp$.

5.3.3 Electroproduction: $Q^2 > 0$

For the case of $Q^2 > 0$ the cross section receives contributions from both the transverse and the longitudinal polarization states of the photon. The integrations over the angles of $\boldsymbol{q}_\perp$ and $\boldsymbol{q}'_\perp$ can again be calculated analytically to arrive for the transverse part in Eq. (5.24) at

$$\int d^2\boldsymbol{q}_\perp \mathcal{F}_0^{[\Box]}(q_\perp, \Delta_\perp) \left[\frac{(\boldsymbol{K}_\perp - \boldsymbol{q}_\perp)}{z_1 z_2 Q^2 + (\boldsymbol{K}_\perp - \boldsymbol{q}_\perp)^2}\right] = \frac{(2\pi)^3 \boldsymbol{K}_\perp}{K_\perp^2} \mathcal{A}_{\mathrm{T}}(K_\perp, \Delta_\perp, z_i, Q) \tag{5.31}$$

with

$$\mathcal{A}_{\mathrm{T}}(K_\perp, \Delta_\perp, z_i, Q) = \frac{1}{(2\pi)^2} \int_0^\infty dq_\perp \, \frac{q_\perp \, \mathcal{F}_0^{[\Box]}(q_\perp, \Delta_\perp)}{2} \left[1 + \frac{K_\perp^2 - q_\perp^2 - z_1 z_2 Q^2}{\sqrt{(K_\perp^2 + q_\perp^2 + z_1 z_2 Q^2)^2 - (2K_\perp q_\perp)^2}}\right], \tag{5.32}$$

while for the longitudinal part in Eq. (5.25) can be evaluated to be

$$\int d^2\boldsymbol{q}_\perp \mathcal{F}_0^{[\Box]}(q_\perp, \Delta_\perp) \left[\frac{Q}{z_1 z_2 Q^2 + (\boldsymbol{K}_\perp - \boldsymbol{q}_\perp)^2}\right] = \frac{(2\pi)^3 K_\perp}{K_\perp^2} \mathcal{A}_{\mathrm{L}}(K_\perp, \Delta_\perp, z_i, Q) \tag{5.33}$$

with

$$\mathcal{A}_{\mathrm{L}}(K_\perp, \Delta_\perp, z_i, Q) = \int_0^\infty \frac{dq_\perp}{(2\pi)^2} \; q_\perp \mathcal{F}_0^{[\Box]}(q_\perp, \Delta_\perp) \left[\frac{K_\perp Q}{\sqrt{(K_\perp^2 + q_\perp^2 + z_1 z_2 Q^2)^2 - (2K_\perp q_\perp)^2}}\right]. \tag{5.34}$$

Therefore, the $\gamma^* p$ differential cross section for $Q^2 > 0$ can be expressed in terms of $\mathcal{A}_\mathrm{T}$ and $\mathcal{A}_\mathrm{L}$ as

$$\frac{d\sigma_L^{\gamma^* p}}{dz_1 dz_2 dK_\perp d\Delta_\perp^2} = \frac{(2\pi)^4 \alpha_{em}}{16 N_c} \sum_f e_f^2 \, \delta(z_1 + z_2 - 1) \left[z_1^2 + z_2^2\right] \frac{\mathcal{A}_\mathrm{T}^2(K_\perp, \Delta_\perp, z_i, Q)}{K_\perp} \tag{5.35}$$

and

$$\frac{d\sigma_L^{\gamma^* p}}{dz_1 dz_2 dK_\perp d\Delta_\perp^2} = \frac{(2\pi)^4 \alpha_{em}}{4 N_c} \sum_f e_f^2 \, \delta(z_1 + z_2 - 1) z_1^2 z_2^2 \frac{\mathcal{A}_\mathrm{L}^2(K_\perp, \Delta_\perp, z_i, Q)}{K_\perp}. \tag{5.36}$$

In Figs. 5.5 we show the functions $\mathcal{A}_\mathrm{T}$ and $\mathcal{A}_\mathrm{L}$ for the same parameter choices as in Fig. 5.3 and Fig. 5.4, and for $Q^2 = 4$ GeV^2 and $z_1 = z_2 = 0.5$. It can be seen that the magnitude of $\mathcal{A}_\mathrm{L}$ is comparable to that of $\mathcal{A}_\mathrm{T}$. However, the $z_1^2 z_2^2$ term in front of $\mathcal{A}_\mathrm{L}$ makes its contribution to the differential cross section much smaller as can be seen in the next section. In Figs. 5.6 we show $\mathcal{A}_\mathrm{T}$ and $\mathcal{A}_\mathrm{L}$ for different values of Q^2.

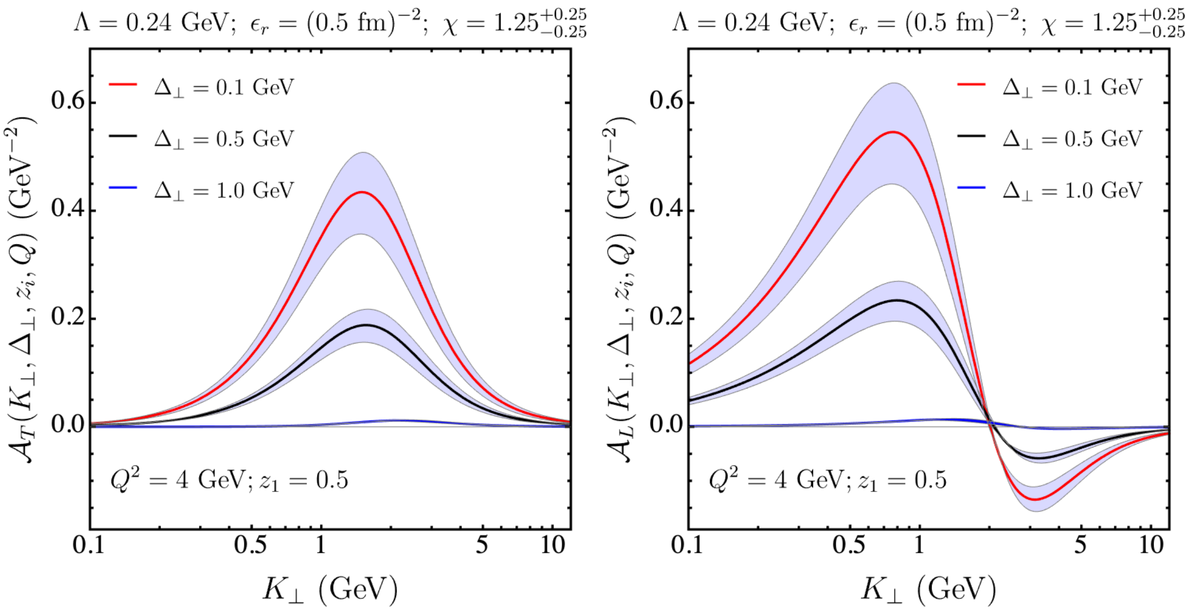

(a) (b)

Figure 5.5: (a) The functions $\mathcal{A}_\mathrm{T}$ from Eq. (5.32) and (b) $\mathcal{A}_\mathrm{L}$ from Eq. (5.34) as functions of $K_\perp$ for three different values of $\Delta_\perp$, $Q^2 = 4$ GeV^2, and $z_1 = z_2 = 0.5$.

The expressions of $\mathcal{A}_T$ in Eq. (5.32) and $\mathcal{A}_L$ in Eq. (5.34) show that exclusive coherent diffractive dijet production allows to obtain information on GTMDs even though the transverse momentum dependence is integrated over. The dependence on the external momenta of the weights inside the integrals can be used to study the transverse momentum dependence of the GTMDs. For photoproduction γp one can set $Q^2 = 0$ and drop the longitudinal part as it does not give any contribution.

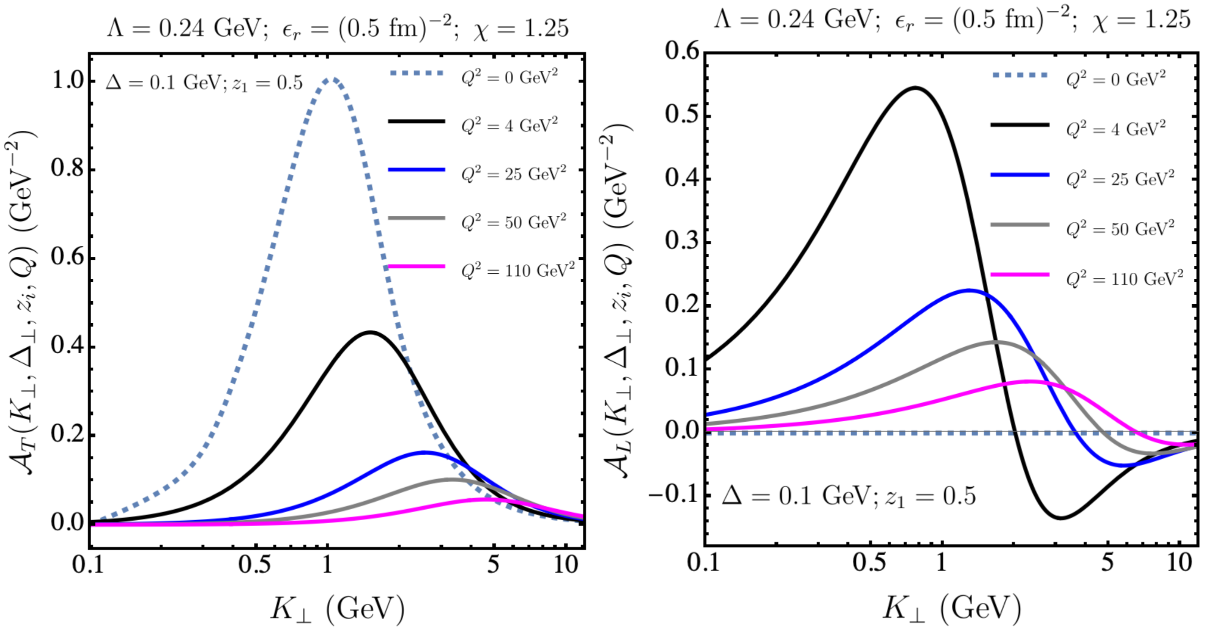

(a) (b)

Figure 5.6: (a) The functions $\mathcal{A}_\mathrm{T}$ from Eq. (5.32) and (b) $\mathcal{A}_\mathrm{L}$ from Eq. (5.34) as functions of $K_\perp$ for five different values of Q^2, $\Delta_\perp = 0.1$ GeV, and $z_1 = z_2 = 0.5$. We note that strictly speaking one can not simultaneously have small values of both Q^2 and $K_\perp$ due to the absence of a hard scale in such a scenario. Consequently, a factorized description becomes unfeasible in that case.

The expressions also show that exclusive coherent diffractive dijet production allows to obtain information on GTMDs that goes beyond the GPDs, in the sense that they probe integrals other than the one of [170] where the gluon GPD H_g at small x is expressed in terms the small-x gluon GTMD, cf. Eq. (4.30):

$$xH_g(x,\Delta_\perp) = \frac{1}{(4\pi)^2\alpha_s}\int d^2\boldsymbol{q}_\perp \boldsymbol{q}_\perp^2 \mathcal{F}_0^{[\Box]}(x,q_\perp,\Delta_\perp). \tag{5.37}$$

As pointed out in the previous chapter formally this relation requires specification of the scale and scheme dependences beyond tree level and also in the model the integral will not converge despite the fast fall-off for large transverse momenta as shown in Fig. 5.7. The important point here is that the expressions of $\mathcal{A}_T$ in Eq. (5.32) and $\mathcal{A}_L$ in Eq. (5.34) involve convergent integrals that moreover can be changed by varying Q and $K_\perp$. In that sense exclusive coherent diffractive dijet production allows to obtain information on GTMDs that goes beyond the GPDs.

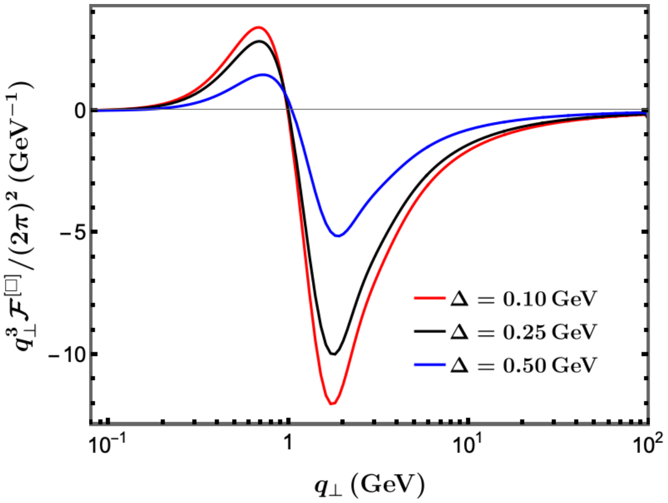

Figure 5.7: The function $q_\perp^3 \mathcal{F}_0^{[\Box]}/(2\pi)^2$ from Eq. (5.37).

5.3.4 Model fit of H1 data

The H1 and ZEUS experiments at HERA have studied the diffractive dijet process in a series of papers [186–188]. Here we focus on [187] where data in the Q^2 range of $4-110$ GeV^2 was presented, for $y \in [0.05, 0.7]$ and $t \leq 1$ GeV^2, that allows us to study the correlation limit region, where here we use $t = |\Delta_\perp|^2$.[3] Given this Q^2 range we consider the case of four flavors. In the case of photoproduction for the EIC prediction (cf. Fig. 5.12), we consider $K_\perp$ as the determining factor for the hard scale. Hence, we require $K_\perp > 2m_c$. The H1 cross sections for two central jets shown in Fig. 5.8 are

---

[3] Strictly speaking, this is $-t$ compared to the general definition $t = (P' - P)^2$ used in earlier chapters. We redefined this t for simplicity, in order to avoid minus sign mistakes or having to write $|t|$ everywhere.

obtained by extrapolation to the range $t_{\text{min}} \leq t \leq 1$ GeV^2 in order to compare to earlier results [186]. We fit our model to this extrapolation range. Here, t_{min} is the minimum kinematically accessible value of t.

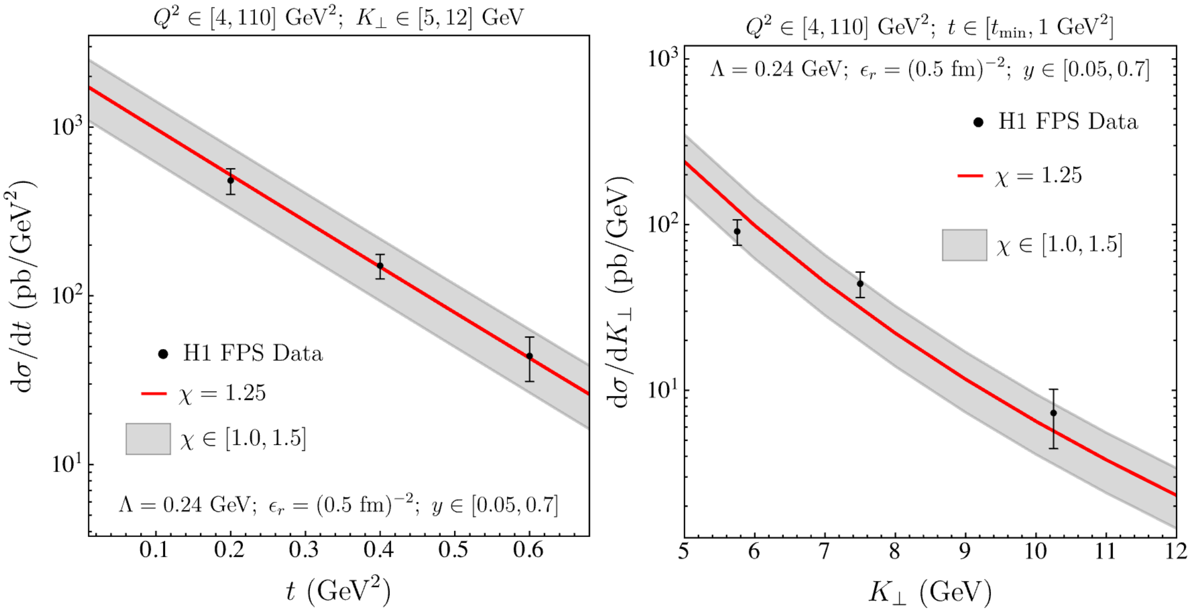

(a) (b)

Figure 5.8: Differential cross section as a function of (a) t and (b) $K_\perp \approx k_{1\perp}$ for the model for the indicated parameter choices and ranges, and for the H1 FPS data including the total uncertainties δ_{tot}. For the $K_\perp$ dependent, the ranges ($t_{\text{min}} \approx 0$).

We first consider the data for the t-dependence of the differential cross section based on Eqs. (5.35) and (5.36). We select $\epsilon_r = (0.5\,\text{fm})^{-2}$ and find that $\chi = 1.25$ can describe the data quite well, as shown in Fig. 5.8, which has a very clear e^{-bt} dependence, with $b \approx 6$ GeV^{-2}. The slope of the cross section as a function of t is controlled by the proton profile in Eq. (5.15). The H1 data description does not depend much on ϵ_r as shown in Fig. 5.9, where the two different values of ϵ_r give approximately the same result. Therefore, we have chosen $\epsilon_r = (0.5\ \text{fm})^{-2}$ which is the cutoff used in [174, 175, 189].

We also display a band corresponding to χ in the range from 1.0 to 1.5. This range is selected on the basis of the $K_\perp$-dependence of the differential cross section. The H1 data is actually presented as a function of the transverse momentum of one of the jets, which is large (in the range $5 - 12$ GeV) and almost back-to-back with the other jet in the transverse plane, such that one can expect that $q_\perp \ll K_\perp$, although the values of $q_\perp$ are not included in [187]. On the basis of this expectation we approximate $K_\perp = (k_{1\perp} - k_{2\perp})/2 = k_{1\perp} - q_\perp/2 \approx k_{1\perp}$. The result is shown in Fig. 5.8. As can be seen the transverse momentum dependence does not show as clear a power law fall-off as the model curves, hence, the considerable uncertainty in the χ value. The contribution of the longitudinal part to the cross section is not very large as shown in Fig. 5.10, where it

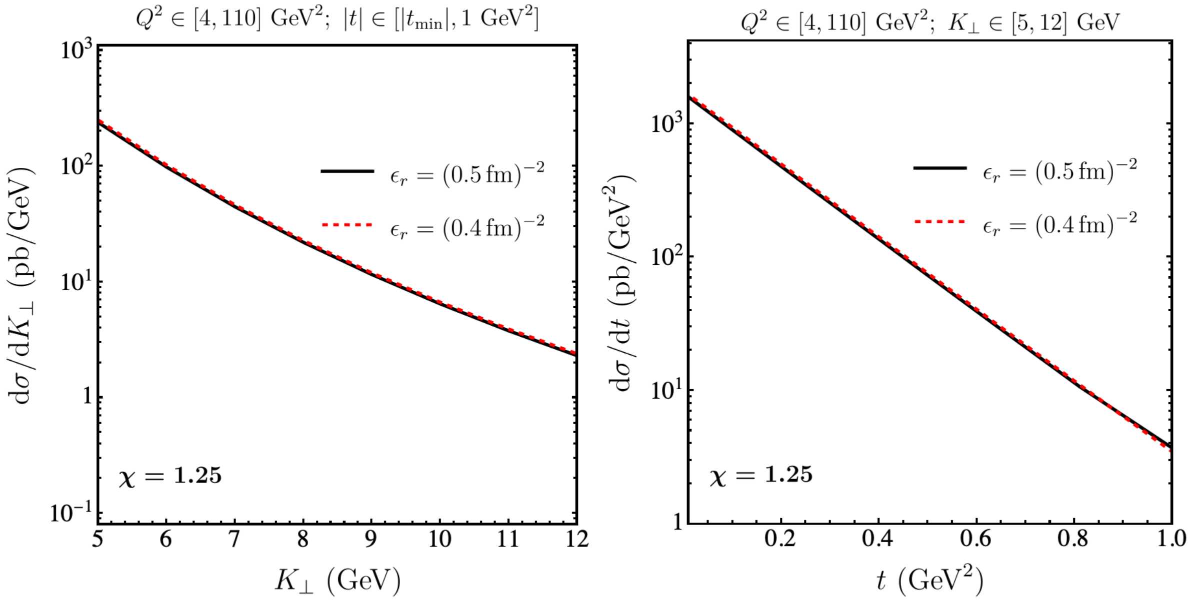

(a) (b)

Figure 5.9: Diffractive dijet production cross section for two different values of ϵ_r for (a) the $K_\perp$ distribution and (b) the t distribution.

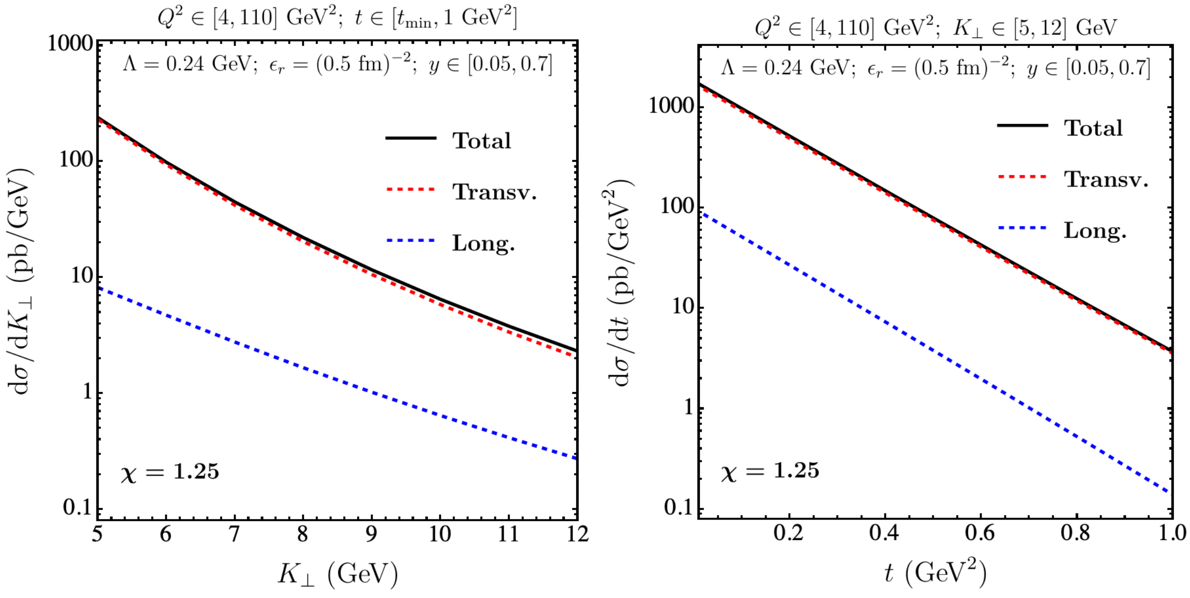

(a) (b)

Figure 5.10: Contribution from the longitudinal (Long.) and transverse (Transv.) parts to the diffractive dijet production cross section for (a) the $K_\perp$ distribution and (b) the t distribution.

is 12 % at $K_\perp = 12$ GeV and becomes smaller for smaller $K_\perp$, e.g. it is 3.5 % for $K_\perp = 5$ GeV.

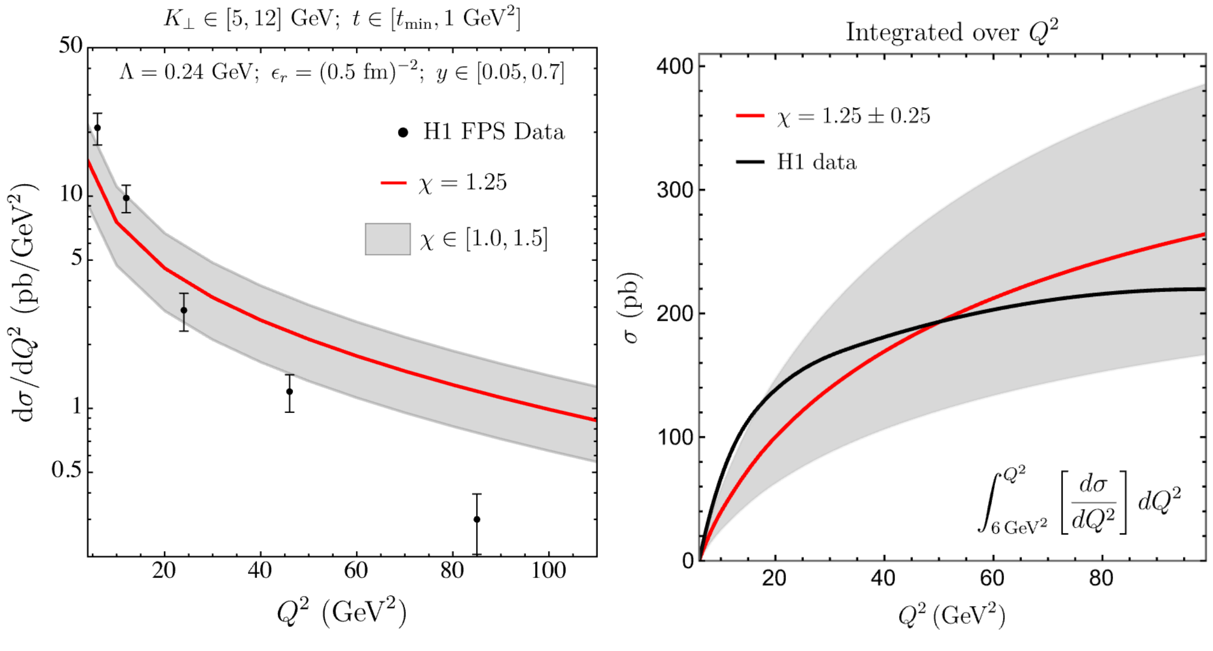

(a) (b)

Figure 5.11: (a) Differential cross section as a function of Q^2 for the model for the indicated parameter choices and ranges ($t_{\min} \approx 0$), and for the H1 FPS data including the total uncertainties δ_{tot}. (b) Demonstration that the central values of the H1 data as a function of Q^2 fall within the range of the Q^2 integral of the model.

For the description of the H1 data we selected values for χ in the range $1.0 - 1.5$ with a central value $\chi = 1.25$. One could relate these values using the GBW model expression for the saturation scale to corresponding x values: $\chi = 2(3 \cdot 10^{-4}/x)^{0.3}$, such that $\chi = 1.25 \pm 0.25$ corresponds to $x \sim (1-3) \cdot 10^{-3}$. We consider such χ values to be acceptable and consistent with the typical x values at which the MV model is generally considered to be applicable. Selecting a fixed χ value corresponds to selecting an average x value. In Fig. 5.11 we show the Q^2 dependence of the model in comparison to the H1 data. It shows that for smaller Q^2, which corresponds to smaller x values for given y and s, a larger χ value is needed, whereas at larger Q^2, a smaller χ value is needed. Clearly a better description of the Q^2 dependence of the data could be obtained with an x dependent χ. However, since the integral of a curve through the central values of the H1 data as function of Q^2 is found to fall within the range of the Q^2 integral of the model, we proceed with the model with a fixed χ, i.e. with an average x. We note that the H1 data spans an x range from $5 \cdot 10^{-5}$ to 0.02, giving a geometric mean of 10^{-3}, which corresponds well with the x values we obtain from the GBW model expression for the χ values considered.

All in all, we conclude that an x independent GTMD model allows for a fair description of the diffractive dijet production H1 data, for reasonable model parameters, in reasonable agreement with assumptions on the gluonic radius and the x values the model applies to. However, it is clear that this model needs to be improved in order to more accurately capture all features of the H1 data. The improved model will be discussed in Sec. 5.4.

5.3.5 Model predictions for EIC and LHC

Here we present predictions for diffractive dijet production at the EIC using our model. For leptoproduction we consider the range $3 \leq K_\perp \leq 9$ GeV, because the center of mass energy of EIC will be lower than at HERA. At even lower $K_\perp$ we expect that jets cannot be resolved anymore and by selecting this range, we can consider the fixed flavor case with $N_f = 4$. We consider $Q^2 \in [1 \text{ GeV}^2, K_\perp^2]$ rather than the fixed range $Q^2 \in [4, 110] \text{ GeV}^2$ of HERA and also show the cases for $Q^2 = K_\perp^2$ and $Q^2 = 4K_\perp^2$ (here we expect smaller Q^2 to be better described by larger χ and vice versa).

We also present model predictions for photoproduction. As expected, the cross section is much larger in this case. The photoproduction result can also be translated into predictions for Ultra-Peripheral Collisions (UPCs) in p-Pb and Pb-Pb collisions at the LHC upon folding in the appropriate photon distribution inside a Pb nucleus, cf. [175]. However, if in such collisions $K_\perp$ values are reached that are much larger than Q_s, then the saturation description may no longer be appropriate. Also it is important that the dijet pair has a rapidity gap in order to ensure a diffractive process. The only currently available UPC jet production data is by the ATLAS collaboration [190], where such a rapidity gap condition is not imposed however. The diffractive contribution was estimated to be at most at the 5% level for the small x part of the data [191] and it may thus not be surprising that our GTMD model cannot describe those ATLAS UPC data, underestimating the cross section by two or three orders of magnitude as shown in Fig. 5.13, where the cross section is highly sensitive to the values of χ that are chosen. In contrast, the collinear factorization description of [192] at NLO is able to describe the ATLAS data well. We expect that the LHC will provide more data on exclusive diffractive dijet UPCs in a region where $\Delta_\perp \ll K_\perp$ which is expected to be able to probe the GTMD.

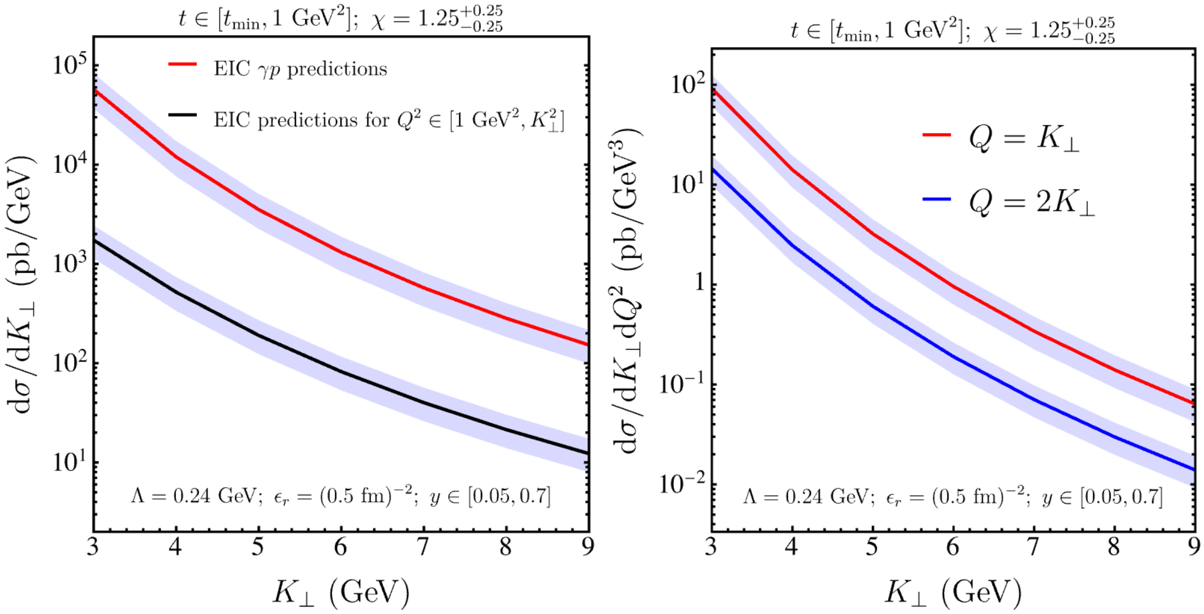

(a) (b)

Figure 5.12: (a) Predictions for diffractive dijet production in ep (black curve) and γp (red curve) collisions at the EIC. (b) Predictions for diffractive dijet production in ep collisions at the EIC for $Q = K_\perp$ and $Q = 2K_\perp$.

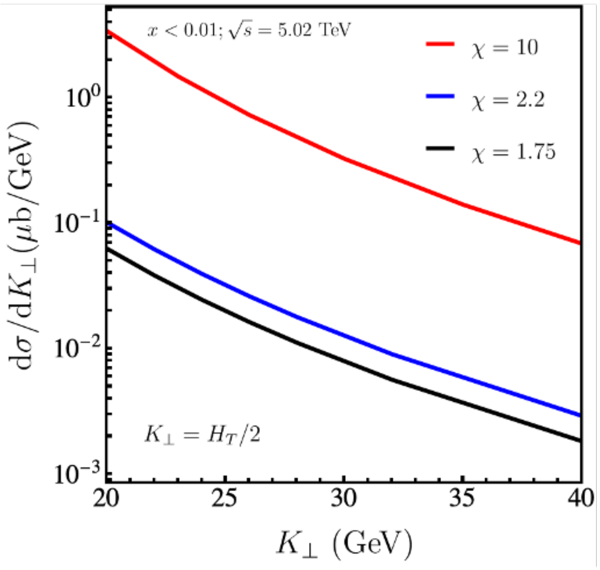

Figure 5.13: Predictions for exclusive diffractive dijet production in ultra-peripheral Pb-Pb collisions at the LHC in the small-x region associated with the kinematic regimes probed by ATLAS [190].

5.4 An x dependent model

In the previous section we used a small-x model without any x dependence, because the expressions in terms of the Wilson loop operator were obtained in the strict $x \to 0$ limit [67, 72, 193, 194]. The model was able to describe the H1 data on the differential cross sections as function of t and $K_\perp$ quite well, for which all data have the same small average x value. But the model did not describe well the data as a function of Q^2 for which the average x value is different for each data point or each bin, cf. Fig. 5.11. To improve on this we now incorporate an x dependence in the model by replacing the constant free model parameter χ (cf. Eq. (5.18)) by the following function of x and Q^2:

$$\chi(x) = \bar{\chi} \left(\frac{x_0}{x}\right)^{\lambda}, \tag{5.38}$$

with $x_0 = 3 \times 10^{-4}$ and $\lambda = 0.29$ based on the model by GBW for the saturation scale [26, 27]. This value of λ also turns out to allow for a reasonably good description of the Q^2 dependence of the H1 diffractive dijet electroproduction data (using $x = Q^2/(ys)$) for diffractive dijet production, but as we will see later J/ψ production prefers a somewhat smaller value $\lambda = 0.22$.

Our motivation to include this type of x dependence in our model is the observation of geometric scaling behaviour of DIS ep collisions data in the low x and low Q^2 region at HERA [26, 27]. This feature of the data was well-described by a saturation scale of the form $Q_s^2(x) \sim x^{-\lambda}$ with $\lambda \approx 0.29$. Later, it was shown that the total cross section of $\gamma^* p$ exhibited geometric scaling over a much wider range of Q^2 values (from 0.045 to $450\,\mathrm{GeV}^2$) in the $x < 0.01$ region of HERA data [96] (see also [92, 93]). Similar scaling was also observed in diffractive DIS with a specific parameterization [109] and in inclusive eA processes [107].

We note that apart from this new Q^2 dependence introduced through the kinematic relation between x and Q^2, we do not introduce any additional x and/or Q^2 dependence from QCD corrections. We also consider a fixed coupling constant. The reason for not including evolution is that the scale evolution of GTMDs has not been studied in full yet. Even for TMD evolution the interplay between the x and Q^2 evolution is not yet fully clear (the scale evolution of TMDs and Sudakov resummation for TMD processes at small x has been investigated in e.g. [195–198]). Since the kinematic range of EIC is not too different from the one of H1 and ZEUS, we expect evolution not to be essential for obtaining predictions. Given the large uncertainties in the model parameters we expect logarithmic corrections to be of minor importance at this stage. This also avoids the question of what precisely sets the hard scale in the various processes (dijet versus J/ψ, electroproduction versus photoproduction). But the kinematic relation between x and Q^2 for the J/ψ case is affected by the J/ψ mass, of course.

5.4.1 The model

With all the above considerations taken into account we arrive at the following McLerran-Venugopalan (MV) [55, 73, 74] like model for the dipole scattering amplitude (see Eq. (5.18):

$$1 - \langle S^{[\Box]}(\boldsymbol{b}_\perp, \boldsymbol{r}_\perp)\rangle_C = \left[1 - \exp\left(-\frac{1}{4} r_\perp^2 \chi(x) Q_s^2(b_\perp) \ln\left[\frac{1}{r_\perp^2 \Lambda^2} + e\right]\right)\right] e^{-\epsilon_r r_\perp^2}. \tag{5.39}$$

As in the previous case, here the factor $e^{-\epsilon_r r_\perp^2}$ in Eq. (5.39) is introduced to ensure that the dipole sizes contributing are restricted to the perturbative region. This Gaussian weight factor was also introduced in the Wigner, Husimi and GTMD distributions of [174, 175]. In practice the dipole size restriction should result from the kinematics of the process, i.e. by the large transverse momentum of the jets (recall that $\boldsymbol{K}_\perp$ is the Fourier conjugate of $\boldsymbol{r}_\perp$) or the large mass of the produced quarkonium, but by enforcing it explicitly in the model, we can obtain convergent integrals of the GTMD without reference to a process. In principle, ϵ_r is a free parameter of the model but we will use the fixed value $\epsilon_r = (0.4 \text{ fm})^{-2}$ for both diffractive dijet and J/ψ production discussed in Chapter 6, which corresponds to the gluonic radius of the proton used in [177]. The dependence of the model on ϵ_r will be further discussed in Sec. 6.4 after the discussion of the fit to J/ψ production data.

The above corresponds to a leading order description of a dipole interacting with a proton or nucleus through two-gluon exchange in the t-channel. The resulting $\langle S^{[\Box]}\rangle_C$, $\mathcal{N}$, and $\mathcal{F}_0^{[\Box]}$ are purely real. In principle GTMDs can be complex, with an imaginary part that is referred to as the odderon contribution. In the forward limit for unpolarized protons this contribution has to vanish for the dipole case since the odderon contribution will be T-odd, whereas there is no TMD corresponding to that case [72]. Odderon contributions may arise for nuclei or from quadrupoles or higher multipoles. Even when the odderon contribution is considered absent down to a certain small x value, nonlinear QCD evolution would generate a nonzero contribution for even smaller x values [199]. Therefore, in principle the imaginary part has to be included, but that has not been done in diffractive dijet production thus far. Later on we comment on the size of the expected correction from the imaginary part.

The saturation scale in the model will be taken as

$$Q_s^2(x, \boldsymbol{b}_\perp) \equiv \chi(x) Q_s^2(b_\perp) = \bar{\chi}\left(\frac{x_0}{x}\right)^\lambda \frac{4\pi\alpha_s^2 C_F}{N_c} Q_{0s}^2\, T(\boldsymbol{b}_\perp) \tag{5.40}$$

with $T(\boldsymbol{b}_\perp)$ is the profile of the proton or nucleus. For the proton we use a Gaussian profile

$$T_p(\boldsymbol{b}_\perp) = \exp\left(-\frac{\boldsymbol{b}_\perp^2}{2R_p^2}\right) \tag{5.41}$$

with R_p the gluonic radius of the proton [177]. For heavy nuclei the profile is described by the thickness function [79]

$$T_A(\boldsymbol{b}_\perp) = N_A \int dz \; \rho_A \left(\sqrt{\boldsymbol{b}_\perp^2 + z^2} \right) \tag{5.42}$$

which is obtained from the Woods-Saxon distribution

$$\rho_A(r) = \frac{1}{1 + \exp\left[\frac{r - R_A}{a_A}\right]}. \tag{5.43}$$

Here, N_A is a normalization factor such that $T_A(\boldsymbol{b}_\perp = 0) = 1$. For the numerical calculations we choose the nuclear radius $R_A = 1.12 A^{1/3}$ fm with A the mass number of the nucleus[4]. For lead ($A = 208$) we use $a_A = 0.546$ fm and for gold ($A = 197$) we use $a_A = 0.535$ fm. For the proton we use $Q^2_{0s,p} = 1$ GeV^2, while (similar to what was done in [177]) for the heavy nuclei $Q^2_{0s,\mathrm{A}}$ can be obtained from the relation

$$\int d^2\boldsymbol{b}_\perp \; Q^2_{0s,\mathrm{A}}(x, \boldsymbol{b}_\perp) = A^\eta \int d^2\boldsymbol{b}_\perp \; Q^2_{0s,p}(x, \boldsymbol{b}_\perp) \tag{5.44}$$

to be evaluated at the same value of x. Here η will be considered a free parameter to be fitted to the data. Explicitly, for heavy nuclei we have

$$Q^2_{0s,\mathrm{A}} = A^\eta Q^2_{0s,p} \frac{\int d^2\boldsymbol{b}_\perp T_p(\boldsymbol{b}_\perp)}{\int d^2\boldsymbol{b}_\perp T_A(\boldsymbol{b}_\perp)} \tag{5.45}$$

Requiring $\int d^2\boldsymbol{b}_\perp T_A(\boldsymbol{b}_\perp) \propto R_A^2 \propto A^{2/3}$ we obtain the following expression for the saturation scale

$$Q^2_{0s,\mathrm{A}} \propto A^{\eta - \frac{2}{3}} Q^2_{0s,p} \tag{5.46}$$

which will determine the saturation scale of the heavy nuclei. The general expectation is that η should have a value near 1.

In Figs. 5.14, we present the function A_T (cf. Eq. (5.29)) for the x-dependent model. The plot demonstrates that the model is suitable for the considered process, particularly in the correlation limit where the contribution from $\Delta > 1$ GeV is negligible (see also Fig. 5.4). The figures illustrate that the amplitude of the x-dependent model is smaller compared to the x-independent model. Additionally, they demonstrate that the amplitude increases as x decreases.

---

[4] Using a different nuclear radius will affect the t distribution of the cross section, as shown in [200], where a larger radius corresponds to a steeper slope.

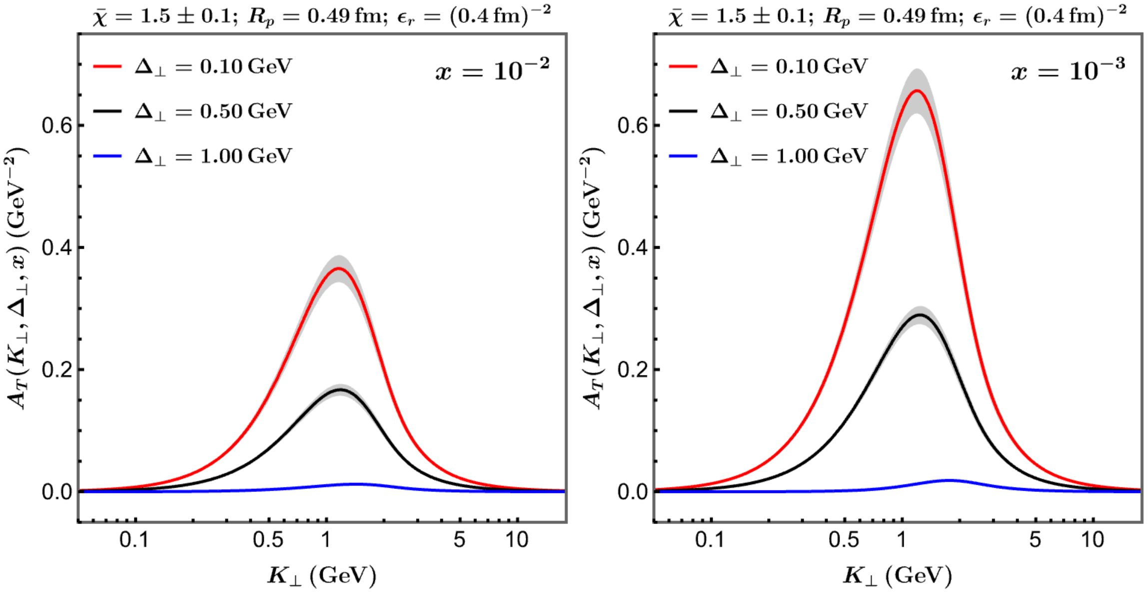

(a) (b)

Figure 5.14: The function $A_T(K_\perp, \Delta_\perp, x)$, as described in Eq. (5.29) for the x-dependent model for (a) $x = 10^{-2}$ and (b) $x = 10^{-3}$, considering three different values of $\Delta_\perp$.

5.4.2 Model fit of H1 data

With the above model and cross section expressions we fit the H1 data of [201]. Although the data is for the production of at least two jets and not fully exclusive, a leading order description in the measured kinematic regime will be dominated by the production of two jets in any case. Also the data is not fully for coherent diffraction, but the t values are so small and the kinematic cuts on the final state proton are such that the additional light hadrons that may be produced in the process are not expected to alter the process much compared to the coherent case. The data is consistent within errors with actual exclusive coherent diffractive dijet production data from ZEUS [188] (to be specific, this we checked for $d\sigma/d\beta$ at $\beta = x_B/x_{I\!P} = 0.1$). The ZEUS data is less differential however and therefore not used here. Finally, the H1 data do not have zero skewness, in fact, it may typically be larger than the x values (the average value for $x_{I\!P} \approx \xi$ is around 0.03-0.04 [201], whereas the geometric average of the upper and lower value of the x range is 10^{-3}), meaning that the ERBL region is probed rather than the DGLAP one, cf. e.g. [137]. These caveats concerning this data should be kept in mind, when we discuss the tension with the best GTMD model description of the J/ψ production case (for which ξ is also not exactly zero, of course). This is also one of the reasons why we do not attempt to find the best model fit that can describe both processes simultaneously. The purpose here is to demonstrate those features that the model fits have in common and those that are in tension, such that future experimental investigations can focus particular attention on these aspects.

The best fit to the t distribution of H1 data [201] is shown in Fig. 5.15. The t distribution is well described by an exponential fall-off, $d\sigma/dt \propto \exp(-bt)$, as also is the case for the t distribution for J/ψ production. The slope b is mainly determined by the gluonic radius of the proton R_p and we find that the model gives the best fit for $R_p = 0.49 \pm 0.02$ fm which leads to the slope $b = 6.0 \pm 0.5\,\text{GeV}^{-2}$ (in [201] $b = 5.89 \pm 0.50\,\text{GeV}^{-2}$ is given for the H1 data). Incorporating the statistical and systematic uncertainties of the data which are simply added in quadrature, we give a band around the best fit (central value) $\bar{\chi} = 1.5 \pm 0.1$.

Within errors, our model gives a reasonable description of the t, Q^2, $K_\perp$ and y distribution data, an improvement with respect to the x independent model of our previous study [68]. In Fig. 5.16, it is demonstrated how the Q^2 description of the data improves in the x dependent model. In determining the free parameters, we first determine R_p, which governs the slope of the t dependence and does not depend on $\bar{\chi}$. This is due to the clear exponential form e^{-bt} observed in the t dependence. Subsequently, we perform a χ^2/dof analysis (cf. Fig. 6.2) to determine the optimal value of $\bar{\chi}$, which governs the amplitude of the cross section. The number of degrees of freedom (dof) is 15, taking into account all available data (combined t, $K_\perp$, Q^2, and y), and it leads to the best fit value (the lowest χ^2/dof) at $\bar{\chi} = 1.5$. This is in contrast to the x independent model, where the best fit is obtained solely from the t dependence data. Consequently, the best fit of the $K_\perp$ distribution in the x dependent model exhibits a slightly lower magnitude compared to the x independent model, but still falls within the range of the band, which is constrained by $\bar{\chi}$. Bands around the central value are shown to reflect the 1σ error range for the t dependence data. The parameters obtained from fitting the H1 data for both the x independent and x dependent models are summarized in Table 5.1.

Parameters	
x independent model	x dependent model
$\chi = 1.25 \pm 0.25$ $R_p = 0.5\,\text{fm}$ $\epsilon_r = (0.5\,\text{fm})^{-2}$	$\bar{\chi} = 1.5 \pm 0.1$ $R_p = 0.49\,\text{fm}$ $\epsilon_r = (0.4\,\text{fm})^{-2}$ GBW parameterization: $(x_0/x)^\lambda$ $x_0 = 3 \times 10^{-4}$ $\lambda = 0.29$

Table 5.1: Parameters utilized for both the x independent and x dependent models. We note that in the x independent model, we take $\epsilon_r = R_p$, whereas in the x dependent model, we consider a fixed $\epsilon_r = (0.4\,\text{fm})^{-2}$ in line with the gluonic radius of the proton used in Ref. [177], which is also employed for the J/ψ production in Chapter 6. Furthermore, $R_p = 0.49\,\text{fm}$ is obtained from fitting the slope of the t-dependence data, see Fig. 5.15.

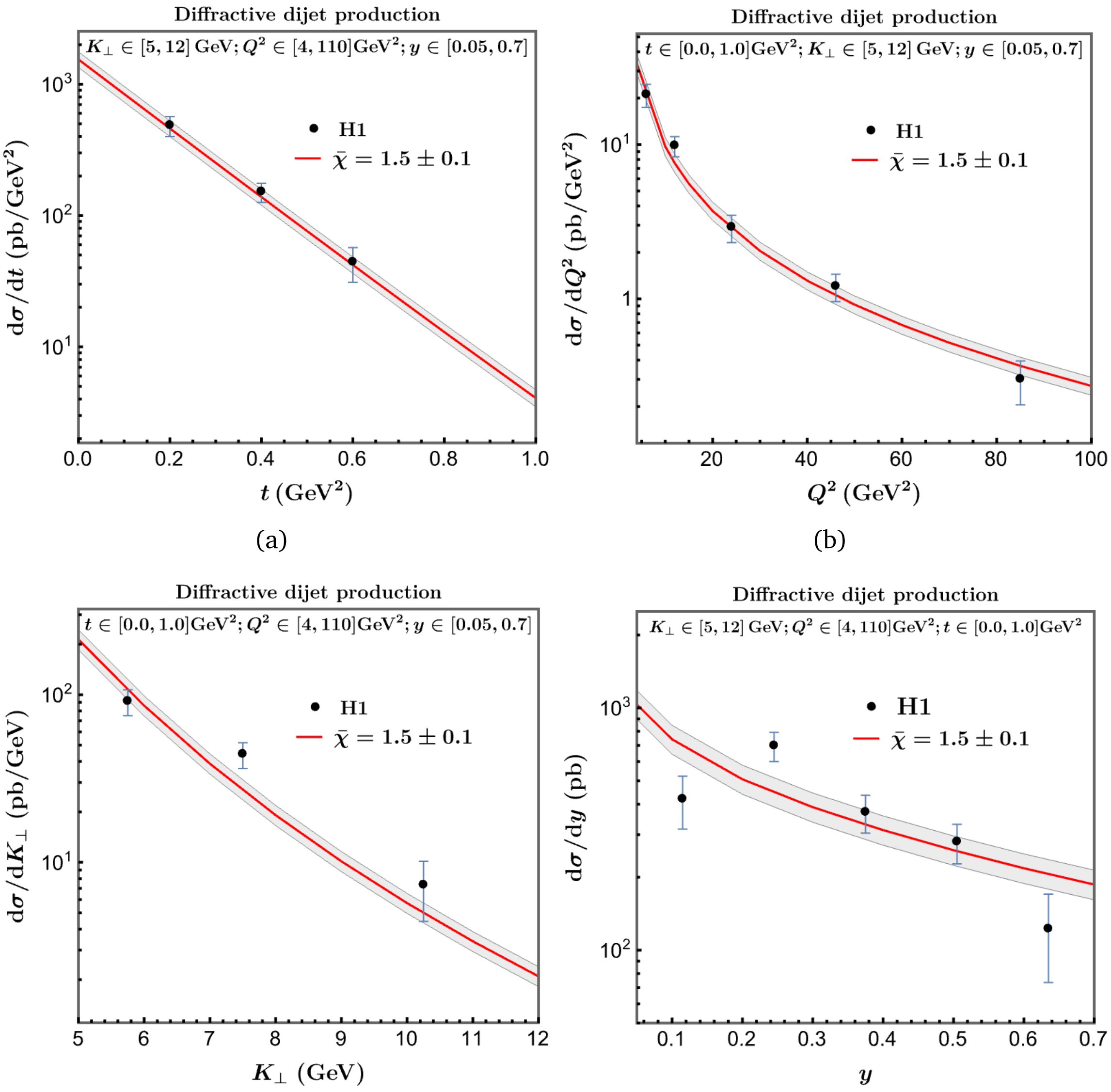

(a) (b)

(c) (d)

Figure 5.15: The best fit of diffractive dijet production to H1 data with $R_p = 0.49$ fm, $\lambda = 0.29$, and $\epsilon_r = (0.4 \text{ fm})^{-2}$. The central value corresponds to $\bar{\chi} = 1.5$ while the band correspond to $\bar{\chi} = 1.4$ and $\bar{\chi} = 1.6$ for the lower and upper band respectively. The systematic and statistical uncertainties are added in quadrature.

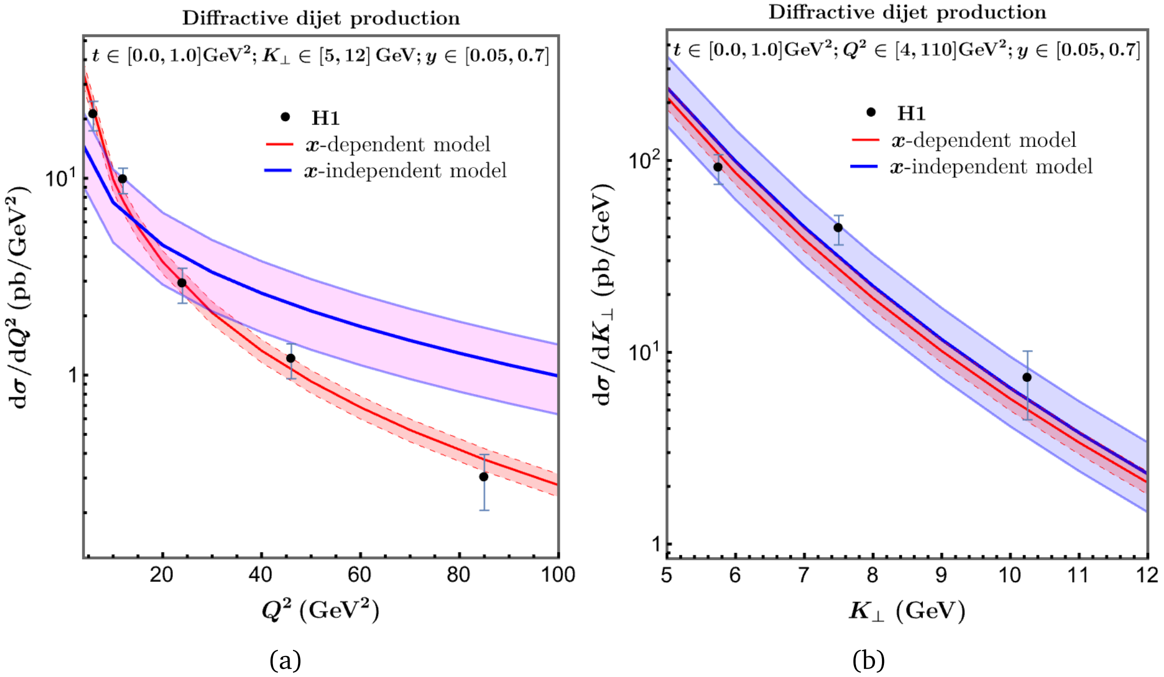

Figure 5.16: Comparison between the x dependent and x independent model fits of the Q^2 and $K_\perp$ distribution data.

5.4.3 Model predictions for EIC

Comparing Figs. 5.8 and 5.15, we observe a significant distinction between the x independent and x dependent models in terms of their capability to reproduce the slope of the Q^2-dependent data (see also Fig. 5.16). The x dependent model captures this aspect better than the x independent model, as it was intended to do. However, both models exhibit similar trends in the t and $K_\perp$ distributions. To show the differences between the x dependent model and the previous x independent model, we present predictions for diffractive dijet photo- and electroproduction at the EIC, utilizing the obtained fit parameter values (cf. Table 5.1) and considering the same range of $K_\perp$ values.

In contrast to the x independent model, here we should consider the center-of-mass energy s of the process. In this study, we focus on two specific EIC energies: $\sqrt{s} = 45$ GeV and $\sqrt{s} = 140$ GeV, see e.g. [16]. These energies will also be used to provide predictions for J/ψ production in Chapter 6. To investigate the small-x regime, we analyze for which values of y and Q^2 these energies probe $x < 0.01$. From Fig. 5.17 one can see that for $\sqrt{s} = 45$ GeV, only a limited range of Q^2 values probes $x < 0.01$.

In Fig. 5.18(a), we provide predictions for photoproduction ($Q^2 = 0.05\,\mathrm{GeV}^2$) at the EIC for these two center-of-mass energies. The range of y is chosen to be the same as in Fig. 5.12(a), which corresponds to the y ranges probed by H1. We observe that both the x-independent and x-dependent models yield predictions with the same slope for the

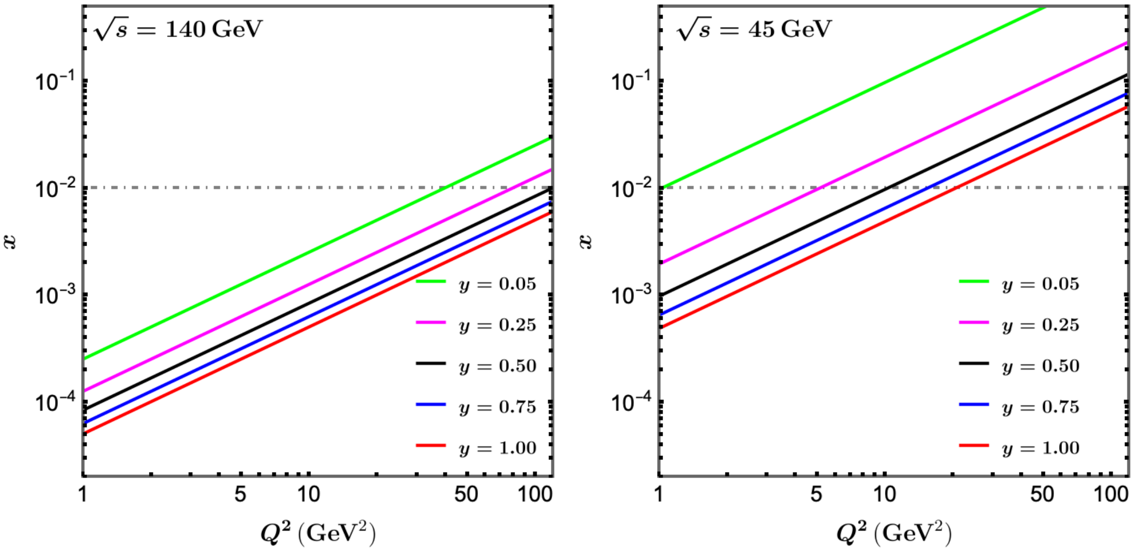

(a) (b)

Figure 5.17: The range of x values probed by (a) $\sqrt{s} = 140$ GeV and (b) $\sqrt{s} = 45$ GeV at the EIC for $Q^2 \in [1, 100]\,\text{GeV}^2$ and $y \in [0.05, 1.00]$. The dot-dashed line indicates $x = 0.01$.

$K_\perp$ dependent photoproduction cross section. This observation is expected because the $K_\perp$ distribution of the cross section probes a constant x value for both models (hence a constant Q^2). Consequently, for a given Q^2 value, $\sqrt{s} = 140$ GeV probe a smaller x (leading to a larger amplitude), while $\sqrt{s} = 45$ GeV probes larger x (resulting in a smaller amplitude). Thus, the $\sqrt{s} = 140$ GeV case demonstrates a larger amplitude compared to the x-independent model, whereas the $\sqrt{s} = 45$ GeV case shows a smaller amplitude. It is important to note that the x-independent model does not specify the value of s.

We also present predictions for electroproduction in Fig. 5.18(b), considering $Q = K_\perp$ as in Fig. 5.12(b) case. However, it is important to note that $\sqrt{s} = 45$ GeV only probes a very narrow range of Q^2, as depicted in Fig. 5.17(b). Therefore, we do not provide predictions for electroproduction at $\sqrt{s} = 45$ GeV. Two different ranges for y are considered: $y \in [0.05, 0.7]$, which corresponds to the H1 y range shown in Fig. 5.12(b), and $y \in [0.4, 0.99]$, which covers a range where all values of Q^2 in the predictions ($Q^2 \in [9, 81], \text{GeV}^2$) are fully within the desired small x limit. It is worth noting that the former choice of y range probes $0.083 < x < 0.0007$, which is not fully in the small x limit. Compared to the predictions of the x-independent model in Fig. 5.12(b), the x-dependent model shows a smaller amplitude but with a steeper slope. This observation is expected because the Q^2 dependence of the x-dependent model decreases more rapidly compared to the x-independent model, as demonstrated in Fig. 5.16(a).

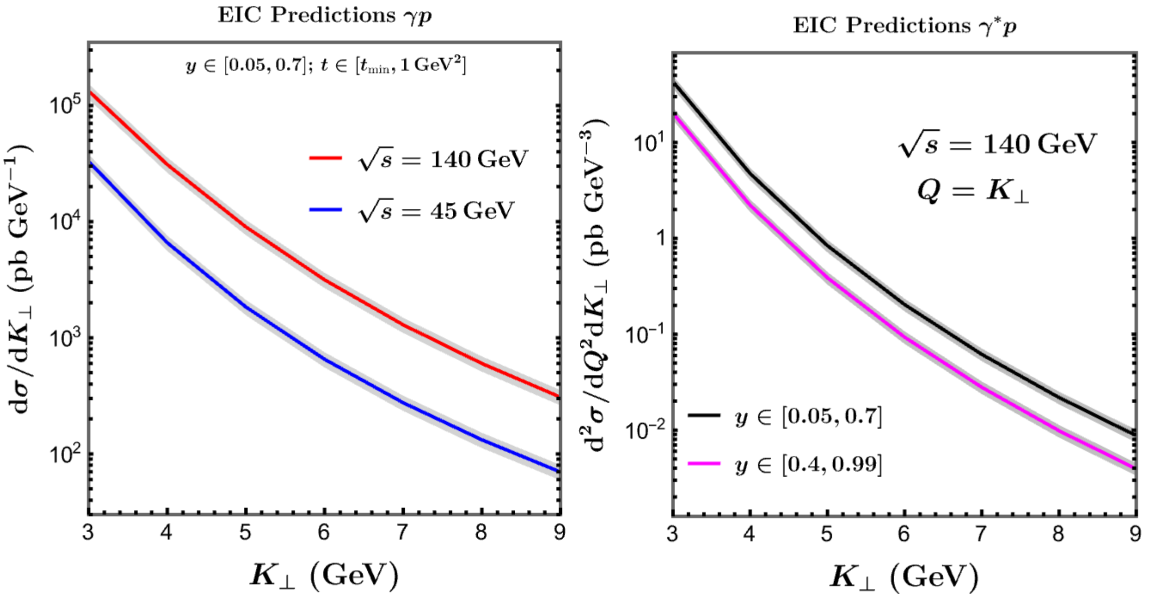

(a) (b)

Figure 5.18: (a) Predictions of the x-dependent model for photoproduction (γp) at two different EIC center-of-mass energies: $\sqrt{s} = 45$ GeV (blue line) and $\sqrt{s} = 140$ GeV (red line). (b) Predictions of the x-dependent model for electroproduction ($\gamma^* p$) with $Q_\perp = K_\perp$ at $\sqrt{s} = 140$ GeV for two different choices of y ranges. The bands correspond to the values of $\bar{\chi} = 1.5 \pm 0.1$.

6

Probing gluon GTMDs in exclusive coherent diffractive J/ψ production

Coherent diffractive processes form a promising way to probe GTMDs. For example, exclusive coherent diffractive dijet production in electron-proton collisions, which was the subject of the previous chapter, has been suggested as a probe of gluon GTMDs in [23] (see also [176]). By measuring the transverse momenta of the two jets one can access the off-forwardness as well as the transverse momentum distribution of gluons, albeit the latter only in an indirect way through a weighted integral where the weight is a function of the observed momenta (see Sec. 5.2). Exclusive coherent diffractive J/ψ production in electron-proton collisions can also be used [202, 203], but in this case the weight of the integral cannot be varied substantially (double J/ψ would be more suited for that), in that sense it is closer to processes like DVCS that probe GPDs, which are fixed integrals of GTMDs [170]. Nevertheless, if the underlying GTMD description is valid, then the various processes should be describable simultaneously by the same GTMDs. There is data from the H1 and ZEUS experiments of HERA, which can be used to check this to a certain extent. In this chapter we will attempt such a combined analysis and reach the conclusion that there is considerable tension between the optimal dijet and J/ψ descriptions. This tension can be due to the theoretical assumptions that go into the GTMD description, such as the selected GTMD model form or the model for the J/ψ wave function, but can also have an experimental origin. This offers an excellent opportunity for the future U.S.-based EIC as it can provide additional and more precise data on both processes in different kinematical regions. Other tests of the underlying GTMD description can come from UPC data of RHIC and/or LHC. Here it is important to ensure that the processes are exclusive and coherent diffractive which means the proton or nucleus has to remain intact.

In the previous chapter we have considered a MV based (small x) model in order to obtain a description of diffractive dijet production data of H1. Although the data is neither fully exclusive, nor fully coherent, the kinematics is such that in leading order a GTMD description is expected to be appropriate. The x-independent model was able to describe the t dependence and the transverse momentum of the jets, but the Q^2 and y dependence was not described very well. By incorporating an x dependence in the model following the GBW parameterization, a better description of the Q^2 and y dependence was obtained. In this chapter we will show that the x-dependent GTMD model can also provide a good description of the t dependence of the exclusive coherent diffractive J/ψ production data of H1 and ZEUS for different Q^2 values, including the photo-production case. However, it turns out there is no choice of parameters that leads a good description of the dijet and J/ψ data *simultaneously*. The tension is solely in the slope of the exponential fall-off in t, which in the model is entirely governed by the width of the proton profile. We do no intend to resolve this tension by adjusting the model, because there may be other reasons for the tension beyond the GTMD model and future data will be needed to confirm or refute the tension. We use the optimal model for the J/ψ data to obtain predictions for the EIC and for UPCs, rather than the model that has the minimal tension with the dijet data as it would not yield a satisfactory description of either process.

In this chapter, we will only discuss the J/ψ production case with the x-dependent model. Our aim is to use as much as possiblethe fit parameters obtained from the dijet case to also describe diffractive J/ψ production data at HERA and LHC. The diffractive J/ψ production cross section expression in terms of GTMDs is given in Sec. 6.1, followed by discussions about certain phenomenological corrections often considered. The fit results to H1 and ZEUS $\gamma^{(*)}p$ data are presented in Sec. 6.2 We additionally perform a fit of the model to the ALICE Run 2 data on mid-rapidity UPCs off Pb nuclei in order to incorporate the A dependence into the model. This analysis is presented in Sec. 6.5. Based on the obtained fits, we provide predictions for $\gamma^{(*)}p$ in Sec. 6.6 at the EIC and for UPCs at RHIC, LHC (at Run 1 center-of-mass energy), as well as the EIC with Au nuclei. [1]

---

[1] The results in this chapter are largely based on [172].

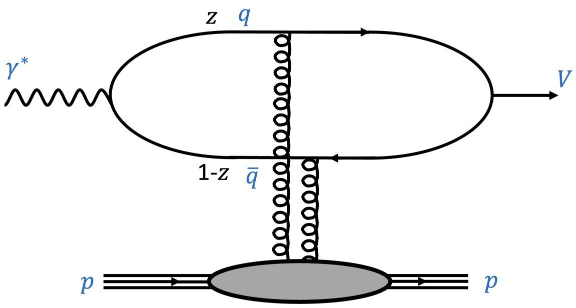

Figure 6.1: Vector meson production.

6.1 Exclusive coherent diffractive J/ψ production cross section

The differential cross section of exclusive coherent diffractive vector meson production as a function of momentum transfer squared $t = -\Delta_\perp^2$ (for $\xi = 0$) can be written as [78, 202]

$$\frac{d\sigma^{\gamma^*p\to Vp}_{T,L}}{dt} = \frac{1}{16\pi}\left|\mathcal{A}^{\gamma^*p\to Vp}_{T,L}\right|^2 \left(1+\beta^2_{T,L}\right) R_g^2, \tag{6.1}$$

expressed in terms of the elastic scattering amplitudes

$$\mathcal{A}^{\gamma^*p\to Vp}_{T,L} = 2i\int d^2\boldsymbol{r}_\perp \int d^2\boldsymbol{b}_\perp \int_0^1 \frac{dz}{4\pi} \left(\Psi_V^*\Psi_\gamma\right)_{T,L} \mathrm{e}^{-i\left[\boldsymbol{b}_\perp-(\frac{1}{2}-z)\boldsymbol{r}_\perp\right]\cdot\boldsymbol{\Delta}_\perp}\left[1-S(\boldsymbol{r}_\perp,\boldsymbol{b}_\perp)\right], \tag{6.2}$$

for the transverse/longitudinal polarization (T/L) of the virtual photon. Here $\boldsymbol{b}_\perp$ denotes the impact parameter, $S(\boldsymbol{r}_\perp, \boldsymbol{b}_\perp)$ is (the real part of) the dipole-proton scattering amplitude defined in Eq. (5.39), and $(\Psi_V^*\Psi)_{T,L}$ is the overlap between the photon and the vector meson wave functions which depends on the transverse dipole size $\boldsymbol{r}_\perp$, momentum fraction z carried by the quark, the quark mass m_f, the vector meson mass M_V, and the photon virtuality Q^2. We are working in a frame where the colliding virtual photon and proton have zero transverse momentum. We note that in Eq. (6.2) we use the phase factor $e^{i(\frac{1}{2}-z))\boldsymbol{r}_\perp\cdot\boldsymbol{\Delta}_\perp}$ as suggested in [170], rather than $e^{i(1-z))\boldsymbol{r}_\perp\cdot\boldsymbol{\Delta}_\perp}$ as used in [202]. In practice, it does not make much difference though. In models studied by [204], the cross section amplitude using the phase factor from [170] is only 3.5% larger than using the one from [202]. Note that the impact parameter $\boldsymbol{b}' \equiv \boldsymbol{b}_\perp - (\frac{1}{2}-z)\boldsymbol{r}_\perp$ corresponds to the distance between the transverse center of longitudinal momentum of the proton/nucleus ($R_\perp = 0$) and the transverse center of longitudinal momentum of the dipole ($z\boldsymbol{x}_\perp + (1-z)\boldsymbol{y}_\perp$), rather than simply the center of the dipole corresponding to $\boldsymbol{b}_\perp$ defined earlier, cf. [139, 166, 181].

The photon-vector meson wave functions overlaps are expressed as [202]

$$
\begin{aligned}
(\Psi_V^*\Psi)_T &= \hat{e}_f e \frac{N_c}{\pi z(1-z)} \left[m_f^2 K_0(\epsilon \boldsymbol{r}_\perp)\phi_T(\boldsymbol{r}_\perp, z) - \left(z^2 + (1-z)^2\right) \epsilon K_1(\epsilon \boldsymbol{r}_\perp)\partial_{\boldsymbol{r}_\perp}\phi_T(\boldsymbol{r}_\perp, z)\right] \\
(\Psi_V^*\Psi)_L &= \hat{e}_f e \frac{N_c}{\pi} 2z(1-z) Q K_0(\epsilon \boldsymbol{r}_\perp) \left[M_V \phi_L(\boldsymbol{r}_\perp, z) + \delta \frac{m_f^2 - \nabla^2_{\boldsymbol{r}_\perp}}{M_V z(1-z)} \phi_L(\boldsymbol{r}_\perp, z)\right] \qquad (6.3)
\end{aligned}
$$

where $\phi_{T,L}$ are model dependent scalar functions and δ is usually taken to be 0 or 1. Because the wave function overlap of the longitudinal part is linearly dependent on Q, the chosen value of δ does not affect photoproduction ($Q^2 \approx 0$). However, the chosen δ value significantly affects the large Q^2 cross section as the longitudinal part becomes a larger portion as Q^2 grows: the second term of $(\Psi_V^*\Psi)_L$ grows faster than the first term when $\delta = 1$. In this study, we will use the so-called Gaus-LC (GLC) and boosted Gaussian (BG) vector meson models [77, 202]. The GLC model is given by:

$$
\begin{aligned}
\phi_T(\boldsymbol{r}_\perp, z) &= N_T z^2 (1-z)^2 \exp\left[-\frac{\boldsymbol{r}_\perp^2}{2R_T^2}\right] \qquad (6.4) \\
\phi_L(\boldsymbol{r}_\perp, z) &= N_L z (1-z) \exp\left[-\frac{\boldsymbol{r}_\perp^2}{2R_L^2}\right]. \qquad (6.5)
\end{aligned}
$$

For $V = J/\psi$ the parameters are listed in [202]: $N_T = 1.23$, $N_L = 0.83$, $R_T^2 = 6.5\ \mathrm{GeV}^{-2}$, $R_L^2 = 3.0\ \mathrm{GeV}^{-2}$, with $m_f = 1.4\ \mathrm{GeV}$. The BG model is given by [205, 206]:

$$
\phi_{T,L}(\boldsymbol{r}_\perp, z) = \mathcal{N}_{T,L} z(1-z) \exp\left[a_1(z)\boldsymbol{r}_\perp^2 + a_2(z)\right] \qquad (6.6)
$$

with $a_1(z) = -\frac{2z(1-z)}{\mathcal{R}^2}$ and $a_2(z) = -\frac{m_f^2 \mathcal{R}^2}{8z(1-z)} + \frac{m_f^2 \mathcal{R}^2}{2}$. The parameters are listed in [202] (see also [207]): $\mathcal{N}_T = 0.578$, $\mathcal{N}_L = 0.575$, $\mathcal{R}^2 = 2.3\,\mathrm{GeV}^{-2}$, and $M_V = 3.097$ GeV. For both models the parameters are fixed by requiring that the wave function is normalized and that the decay widths are reproduced (for details on this we refer to [202]). We also note that other vector meson wave functions and potential models have been considered in order to describe diffractive production of J/ψ and other heavy quarkonia, see for example [77, 208–214]. These descriptions can in principle also be translated into GTMD model expressions, which possibly allows for a more direct comparison of models (rather than a comparison of how they describe the data), but that is not our objective here.

The objective of this study is to investigate a gluon GTMD description of diffractive processes. For this purpose we employ a relatively generic model for the gluon GTMD at small x values. Our primary goal is thus not the model itself. Rather, we aim to examine the feasibility of a unified GTMD description for both diffractive dijet and J/ψ production data, identify agreements, differences, and potential tensions, and provide predictions to help identify the underlying causes of any discrepancies, using a generic GTMD model. Additionally, we aim to highlight the unique insights that can be gained from these processes regarding GTMDs that go beyond the scope of GPDs. As far as we are aware, these aspects have not been previously examined in this manner, which enhances their significance, especially for the EIC community and for investigations related to UPC at LHC and RHIC.

Before moving on to the description of the data, we make some observations about whether this process probes a GPD rather than a GTMD. If we restrict to the angular independent part only, then we can express Eq. (6.2) as[2]

$$\mathcal{A}_{T,L} = \frac{\pi i}{2N_c}\int_0^1 dz \int d^2\boldsymbol{r}_\perp \left(\Psi_V^*\Psi_\gamma\right)_{T,L}(\boldsymbol{r}_\perp, z) \int d^2\boldsymbol{q}_\perp J_0\left(|q_\perp+\delta_\perp|\boldsymbol{r}_\perp\right)\mathcal{F}_0^{[\Box]}(x,q_\perp,\Delta_\perp), \tag{6.7}$$

with $\boldsymbol{\delta}_\perp = (\frac{1}{2}-z)\boldsymbol{\Delta}_\perp$. This expression shows that also in diffractive J/ψ production one probes an integral over a GTMD with an integrand that depends on the kinematic variables of the process (in this case z and $\Delta_\perp$) and hence different integrals of the GTMD can be obtained in this way, even though with less possibilities for varying the integrand than in the dijet case. This also means that the expression cannot be given in terms of a GPD (which does not depend on z), only in an approximation, as pointed out by [170]. As the weight of the integral over the GTMD depends on $\Delta_\perp$ through $\delta_\perp$ and $\Delta_\perp$ is generally small and only relevant in a small kinematic region (and the region around $z = 1/2$ contributes the most), this dependence may be ignored to good approximation leaving a fixed integral over the GTMD, which however still is not an expression in terms of the gluon GPD H_g through Eq. (4.30). This would require small $|q_\perp+\delta_\perp|$, for which we can consider the first order expansion of the Bessel function $J_0\left(|q_\perp+\delta_\perp|\boldsymbol{r}_\perp\right) \approx 1 - \frac{(q_\perp+\delta_\perp)^2 r_\perp^2}{4}$, and use the fact that $\int d^2\boldsymbol{q}_\perp \mathcal{F}_0^{[\Box]}(x,q_\perp,\Delta_\perp) = 0$ [170], to find that

$$\begin{aligned}\mathcal{A}_{T,L} &\approx \frac{\pi i}{8N_c}\int_0^1 dz \int d^2\boldsymbol{r}_\perp \boldsymbol{r}_\perp^2 \left(\Psi_V^*\Psi_\gamma\right)_{T,L}(\boldsymbol{r}_\perp, z) \int d^2\boldsymbol{q}_\perp \boldsymbol{q}_\perp^2 \mathcal{F}_0^{[\Box]}(x,q_\perp,\Delta_\perp)\\ &= \frac{\pi^3 i\alpha_s}{N_c}\int_0^1 dz \int d^2\boldsymbol{r}_\perp \boldsymbol{r}_\perp^2 \left(\Psi_V^*\Psi_\gamma\right)_{T,L}(\boldsymbol{r}_\perp, z)\, xH_g(x,\Delta_\perp),\end{aligned} \tag{6.8}$$

where in the last step we used Eq. (4.30). It should be stressed that this is an approximation that depends on the relevant range of the $q_\perp$ integration. Therefore, following the discussion at the end of chapter 4 we will consider the GTMD expression rather than the approximate one in terms of the GPD. Diffractive scattering in terms of GPDs has been studied in [158], where a different limit is considered though: $\Delta_\perp \to 0$ while $\xi \neq 0$.

6.2 Analysis of coherent diffractive J/ψ production data

The total $\gamma^* p$ cross section for J/ψ production studied by H1 [215] is defined as $\sigma_{\text{tot}} = \sigma_T + \varepsilon\sigma_L$ with $\varepsilon = (1-y)/(1-y+\frac{1}{2}y^2)$ (with $\langle\varepsilon\rangle = 0.99$ in [64,202]), while by ZEUS [216] it is defined as $\sigma_{\text{tot}} = \sigma_T + \sigma_L$. Here we will also use $\varepsilon = 0.99$, which corresponds to $\langle y\rangle \simeq 0.13$. This differs from the dijet case where a range of y values is considered and the x value depends on y. The x value used in the J/ψ production case is determined

---

[2] See the discussion in footnote 2.

by [78, 217]

$$x = x_B \left(1 + \frac{M_V^2}{Q^2}\right) = \frac{M_V^2 + Q^2}{W^2 + Q^2}. \tag{6.9}$$

We recall that $\sigma_L = 0$ for the photoproduction case.

Diffractive vector meson production at HERA and LHC has been studied extensively with various model approaches, such as [78, 204, 207, 218–224]. It has been shown in [202,203,225,226] that MV-like models can describe diffractive vector meson production well. In most model studies the dipole scattering amplitude is real and hence $\mathcal{A}_{T,L}^{\gamma^* p \to Vp}$ imaginary, but as mentioned in Sec. 5.4.1, in reality there will be an imaginary part. The phenomenological correction $1 + \beta^2$ is introduced to account for that contribution. Using dispersion relations an expression for β has been obtained [217, 227, 228]:

$$\beta_{T,L} = \tan\left[\frac{\pi \lambda_{T,L}}{2}\right], \qquad \lambda_{T,L} \equiv \frac{\partial \ln\left[\mathcal{A}_{T,L}^{\gamma^* p \to Vp}\right]}{\partial \ln\left[\frac{1}{x}\right]}. \tag{6.10}$$

This expression implies that only x dependent elastic scattering amplitudes yield nonzero β. Phenomenological studies of HERA data [217, 229, 230] find that the real part correction $(1 + \beta^2)$ is anywhere between 10% and 25%. Given the large uncertainty in the model fits that we obtain from these HERA data, this correction will not be of much importance. Therefore, we will first fit the data without this correction and then estimate the size of the correction for that fit afterwards. In this way we find that in our case $(1 + \beta^2)$ is in the 10-15% range. More details on this will be presented below.

Another correction often considered comes from taking into account nonzero skewness. The off-forwardness $\Delta = P' - P$ for zero skewness, i.e. $\xi = -\Delta^+/(P'^+ + P^+) = 0$, means $\Delta = \Delta_\perp$ and $t = -|\boldsymbol{\Delta}_\perp^2|$. In practice ξ will not be exactly zero. Therefore, in order to correct for this the factor R_g^2 is included, where R_g for gluons at small x and small ξ is given by [228]

$$R_g \equiv \frac{H_g(x = \xi, \xi)}{H_g(x = 2\xi, 0)} \approx \frac{2^{2\delta+3}}{\sqrt{\pi}} \frac{\Gamma(\lambda + \frac{5}{2})}{\Gamma(\lambda + 4)}, \tag{6.11}$$

where $H_g(x, \xi)$ is the standard (helicity non-flip) gluon GPD (now for nonzero skewness, unlike in Eq. (4.30)). This factor R_g^2 is a substantial correction for HERA kinematics, found to be in the order of 40-70% [217, 229, 230]. We note though that the value $H_g(x = \xi, \xi)$ is at the boundary of the ERBL and DGLAP regions, where the function is continuous but not differentiable, hence changing abruptly, so a slight change in x with respect to ξ or vice versa can matter considerably. This introduces an uncertainty regarding the actual correction that is needed, as the data span a range of x and ξ values. Furthermore, the specific value $x = 2\xi$, which is in the DGLAP region, stems from the GPD analysis of [231] for which the region around this value is found to make the dominant contribution. This is quite different from our GTMD approach for which $x = 2\xi$ plays no dominant role and the ratio $H_g(x, \xi)/H_g(x, 0)$ (i.e. with the same x value in numerator and denominator) for small nonzero ξ seems more appropriate to consider.

Moreover, the data are more likely in the ERBL region ($x < \xi$), like for the dijet data (see discussion in Sec. 5.4.2). However, strictly speaking we do not know exactly what is ξ in the J/ψ case, because that is not clearly specified in the experimental papers. Hence, given these considerations, here we do not include the R_g^2 correction factor in this paper and also not correct for nonzero skewness in another way. Given the large uncertainties in the model fits (due to the large uncertainties in the data), this is not expected to be essential.

6.3 Combined fit of diffractive dijet and J/ψ production

Having obtained the fit parameters for diffractive dijet production in Chapter 5, our next objective is to apply these parameter values to fitting the data for J/ψ production. Thus far, no previous phenomenological study has simultaneously investigated both types of processes, despite the potential for both to be described within the same GTMD-based approach. In this section, we will demonstrate our method for performing a combined fit of both processes using this model. Additionally, we will reveal the presence of tensions that arise and show that the model alone cannot resolve them. Our focus will be on identifying the specific areas where these tensions emerge and discussing the unresolved aspects within this particular context.

To begin with, our emphasis will be on the t slope of both processes, as they both exhibit a similar functional form of $d\sigma/dt \sim \exp[-bt]$. As in the dijet case, the model parameter R_p of the proton profile directly determines the t slope of the differential cross section for J/ψ production. However, it turns out that the latter is found to be quite different from that of the dijet case, with the J/ψ production slope substantially smaller. They are only compatible at the 3σ level, hence there is considerable tension. Due to this aspect of tension, the uncertainty in the model parameters is larger than what is suggested by studying only one of the two types of process. Future data is needed to resolve this issue.

In Fig. 6.2(a) the χ^2 per degree of freedom (dof) as a function of $\bar{\chi}$ is shown for the case that a fit is made to both the photo- and electroproduction data[3]. It can be seen that also in this case GLC gives a slightly better minimal χ^2/dof and prefers a $\bar{\chi}$ close to the one of the dijet case. Therefore, the GLC model seems to be preferred. However, when it comes to the t and W slope, all vector meson wave function models require $\bar{\chi}$, R_p and λ values that are smaller than those obtained from the dijet data. This is clearly visible in Fig. 6.2(b) where we show the value of b of $d^2\sigma/dt\, dQ^2 \propto e^{-bt}$ for ep collisions, where b is solely determined by R_p in Eq. (5.41).

The preferred proton profile for the dijet case is $R_p = 0.49$ fm. For the J/ψ case we choose two different values of R_p due to the fact that the photoproduction data exhibits a somewhat steeper slope ($R_p = 0.41$ fm) compared to the electroproduction data ($R_p = 0.40$ fm), although this difference is not statistically significant, see Fig. 6.2(b). Here it should be recalled that the J/ψ data is for fixed y ($\gamma^{(*)}p$) and the dijet data is y

---

[3] We thank Gerco Onderwater for useful discussions on the fits.

integrated (ep) (cf. Fig. 5.15(d) for the y dependence of the dijet data). The $d^2\sigma/dtdQ^2$ slope data points in Fig. 6.2(b) are only available for J/ψ production [216, 232, 233], while the Q^2 dependence of the dijet slope is extracted from the fit (see Fig. 5.15). The dijet slope data is given only for Q^2 and y integrated which is $b = 5.89 \pm 0.50\,\mathrm{GeV}^{-2}$. The bands of the t slope (b) for the J/ψ case shown in Fig. 6.2(b) reflect the aforementioned R_p values, while for the dijet case the bands correspond to the 1σ error in R_p, i.e. $R_p = 0.49 \pm 0.02$ fm, for which a larger R_p gives a larger b. The fact that the b slope of each process is not completely constant in the range of $(0.01\,\mathrm{GeV})^2 \leq t \leq 1\,\mathrm{GeV}^2$ has also been included in the bands, see Fig. 6.7 for the t dependence of the slope.

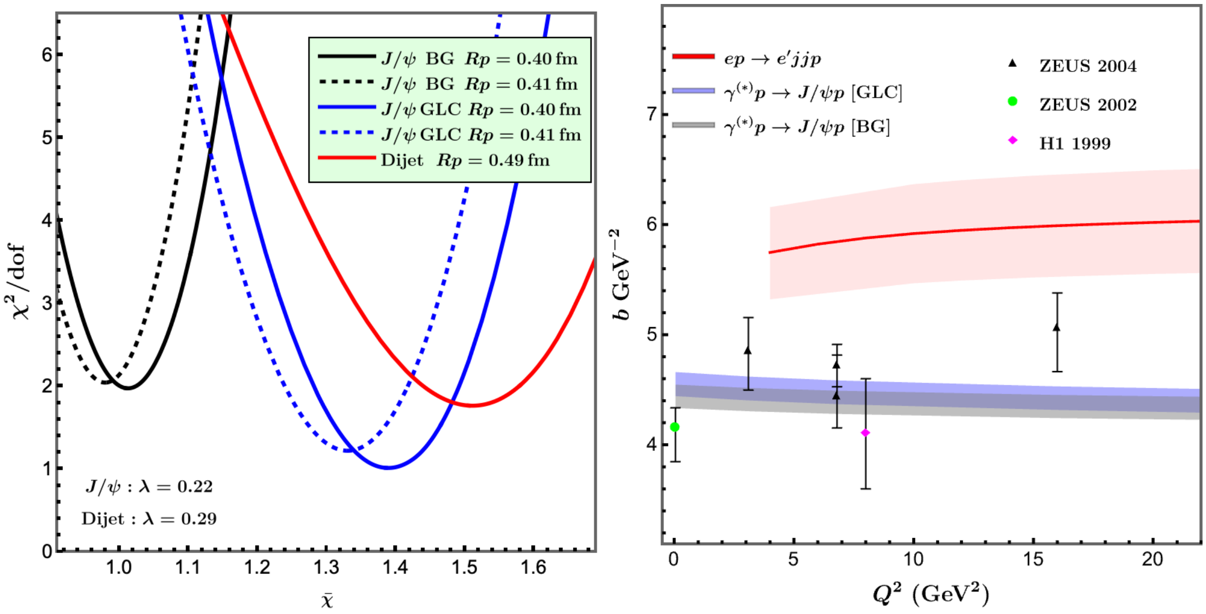

(a) (b)

Figure 6.2: (a) χ^2/dof vs $\bar{\chi}$ for dijet production (combined Q^2, t, $K_\perp$, and y dependence data [201] with dof=15) and J/ψ production (combined photo- and electroproduction data [215, 216] with dof=35) for two different possible values of R_p. (b) t slope (b) of the model as a function of Q^2 for the dijet and J/ψ cases. The J/ψ data are taken from [216, 232, 233]. Note that the diffractive dijet production case is y integrated, while the J/ψ case is evaluated at $W = 90\,\mathrm{GeV}$ and for fixed y. The slopes of both dijet and J/ψ cases are calculated in the range of $(0.01\,\mathrm{GeV}^2) \leq t \leq 1\,\mathrm{GeV}^2$.

Our model shows that the dijet slope is slowly increasing in Q^2 while for J/ψ it is steadily decreasing. This tension cannot be resolved with the present set of just three free parameters. It is also clear that it cannot be attributed to the vector meson wave function, but stems from the proton profile. Of course, it may be (in part) due to the aforementioned caveats about the dijet data, but without additional future data, that can likely not be clarified.

We also constrain the combined fit to the data on the W dependence of the photoproduction of J/ψ production. For both GLC and BG wave functions, the slope of the W dependence data is primarily governed by the λ parameter, as illustrated in Fig. 6.3 Therefore, the determination of the parameter λ relies on fitting the slope of the W dependence data of the total cross section for J/ψ photoproduction from HERA and LHC. Importantly, there exists a pivotal point where any chosen λ yields the same value. This point corresponds to $(x_0/x)^\lambda = 1$ in Eq. (5.38), and its location depends on the chosen value of x_0. In this analysis, we select $x_0 = 3 \times 10^{-4}$ obtained from the GBW parameterization, which corresponds to $W \simeq 178$ GeV for $M_{J/\psi} = 3.1$ GeV in this particular model. It turns out that unlike the dijet case, this data favors a smaller value of $\lambda = 0.22$ compared to λ_{GBW}. The fit result to the W dependence data is shown in Fig. 6.4(b). The complete parameter values for each wave function obtained by fitting the model to the t and W dependence data are summarized in Table 6.1.

Parameters	**Diffractive dijet**	J/ψ		
			GLC	**BG**
$\bar{X}$	1.5 ± 0.1	$R_p = 0.41$ fm	$1.40 - 1.45$	$1.05 - 1.10$
	$R_p = 0.49$ fm	$R_p = 0.40$ fm	$1.45 - 1.50$	$1.10 - 1.15$
λ	0.29	0.22		
ϵ_r	$(0.4\,\text{fm})^{-2}$			

Table 6.1: Parameters of the x-dependent model employed in diffractive dijet and J/ψ production.

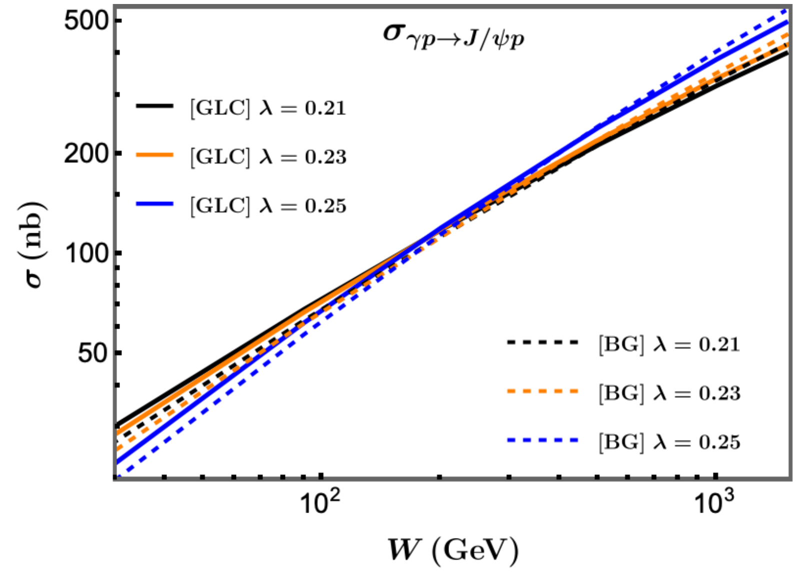

Figure 6.3: The slope of the total J/ψ photoproduction cross section as a function of W for each wave function: BG (dashed lines) and GLC (solid lines) for different values of λ.

We note that trying to obtain a better fit of the W dependence of the total cross section will lead to a less good description of the photoproduction differential cross section $d\sigma/dt$. As the model is probably less appropriate for the integral over all t, we have given preference to the latter. We refer to [200] for a combined description of H1 data of total photoproduction cross section and the differential cross section for both coherent and incoherent diffraction, taking into account proton shape fluctuations.

6.4 Model description for J/ψ production

In Fig. 6.4 we show that our MV-like model with optimum fit parameters $\bar{\chi}$, R_p and λ obtained from Sec. 6.3 and without the mentioned corrections (cf. Eq. (6.10)) can describe the t distribution data of HERA [215, 216] and of the data on the total cross section as a function of W from HERA (H1 [234] and ZEUS [233]) and LHC (ALICE [235] and LHCb [236, 237])[4], even though it is not optimal for the W dependence fit. As discussed in Sec. 6.3, the t dependence of the model is controlled by the proton profile R_p, the W slope by λ, while the amplitude of the cross section is $\bar{\chi}$ dependent where large $\bar{\chi}$ means a larger cross section. Here we give preference to the description of the photoproduction data, i.e. the parameters are obtained from a simultaneous description of the t and W dependence of the photoproduction data, where there is only a very narrow range of R_p and $\bar{\chi}$ values that describe those data simultaneously. If one would include electroproduction data, the parameters would change considerably (cf. Fig. 6.2(a) such that the photoproduction data would be described less well. In this case, we do not solely rely on the minimum χ^2/dof analysis. Instead, we consider the $\bar{\chi}$ value which is close to the minimum, and take a band around it to better describe the photoproduction data. As depicted in Fig. 6.4, if the electroproduction data is incorporated in the χ^2/dof analysis (cf. Fig. 6.2), it would favor smaller $\bar{\chi}$ values, because the electroproduction data presented in Fig. 6.4 indicates a preference for smaller $\bar{\chi}$ values. For instance, in the χ^2/dof analysis with $R_p = 0.41$ fm, the minimum value of $\bar{\chi}$ for GLC is 1.34, but in our final fit to the data, we utilize $\bar{\chi} = 1.40 - 1.45$ (see Table 6.1).

Here we note that the H1 and ZEUS data sometimes differ quite a bit from each other, when comparing data sets at the same or very similar values of Q^2. Therefore, we prefer to let the Q^2 dependence be determined by the model after the parameters are fixed at $Q^2 = 0.05\,\mathrm{GeV}^2$. It then turns out that the t dependence is well described using GLC for all values of Q^2 considered, while BG overestimates the data for large Q^2.

We show bands of values of $\bar{\chi}$ and R_p which describe the photoproduction data qualitatively equally well within the errors of the data points. However, they should not be interpreted as 1σ error bands, as they are not obtained from a fit to all data points through a minimization with respect to all parameters simultaneously. Instead, we determine R_p by adjusting it to match the slope of the t dependence observed in the photoproduction and electroproduction data from H1 and ZEUS, cf. Fig. 6.4(a). Similarly, we determine λ by tuning it to fit the slope of the W dependence observed

---

[4] We thank Cristina Sánchez Gras for helping us reproduce the LHCb data points.

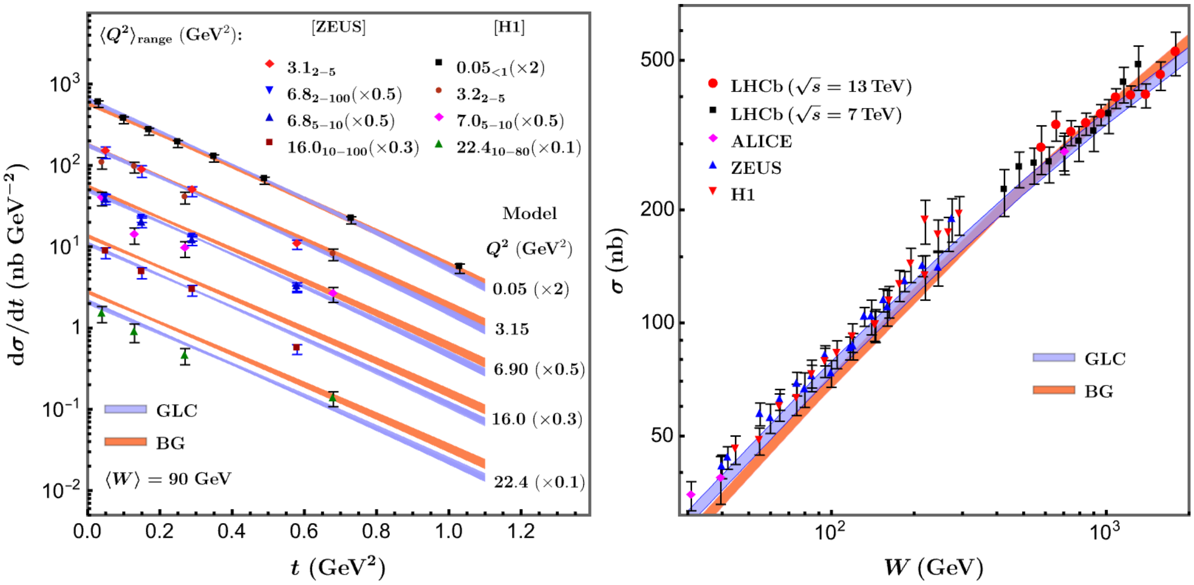

(a) (b)

Figure 6.4: Left: GTMD model fit of the t dependence of exclusive coherent diffractive J/ψ production data from H1 [215] and ZEUS [216], for two vector meson wave function models: GLC and BG. The systematic and statistical uncertainties are added in quadrature. The bands correspond to the ranges of values of $\bar{\chi}$ and R_p specified in the text. Right: Fit of the model to the W dependence of the total J/ψ photoproduction cross section at HERA and LHC [233–237]. The data are only shown for $x \lesssim 0.01$ which corresponds to $W > 30$ GeV ($\approx 10 M_{J/\psi}$).

in the total photoproduction data from LHC and HERA, as shown in cf. Fig. 6.4(b). Subsequently, we obtain $\bar{\chi}$ through a χ^2 analysis, as illustrated in Figure 6.2. Given the uncertainties in the data and the tension with the dijet data, a more sophisticated determination of the parameters and the error bands does not seem to be called for at this point. To be specific about the bands, for GLC we use $\bar{\chi} = 1.45 - 1.50$ for $R_p = 0.40$ fm and $\bar{\chi} = 1.40 - 1.45$ for $R_p = 0.41$ fm, while for BG we use $\bar{\chi} = 1.10 - 1.15$ for $R_p = 0.40$ fm and $\bar{\chi} = 1.05 - 1.10$ for $R_p = 0.41$ fm. We choose two different possible R_p because of the fact that the photoproduction data prefers a steeper slope ($R_p = 0.41$ fm) than the electroproduction data ($R_p = 0.40$ fm).

We emphasize that, unlike in the dijet case, for the J/ψ case, the cross section is more sensitive to the chosen value of ϵ_r, which means that the adopted wave function of the J/ψ is broader than the gluonic radius of the proton (to be specific, for the models used here, the GLC wave function is about twice as broad, while the BG wave function is 1.5 times broader, see Fig. 6.5). For the dijet case, changing ϵ_r from $(0.4\,\text{fm})^{-2}$ to $(0.5\,\text{fm})^{-2}$ results in a 4% decrease in the cross section at $t \simeq (0.01\,\text{GeV})^2$ and a 3% increase in the cross section at $t \simeq (1\,\text{GeV})^2$, indicating that $K_\perp$ is indeed large enough to ensure only contributions from small enough dipoles. In addition, the slope of the exponential fall-off in t remains almost independent of ϵ_r as shown in Fig. 6.6. As said, for the J/ψ case, the cross section is more sensitive to the chosen value of ϵ_r, where changing ϵ_r from $(0.4\,\text{fm})^{-2}$ to $(0.5\,\text{fm})^{-2}$ results in almost a 30% increase in the cross section. Fig. 6.7 demonstrates that even though GLC wave functions exhibit a larger change in slope compared to BG, it still remains relatively small. For instance, when changing from $\epsilon_r = (0.4, \text{fm})^{-2}$ to $\epsilon_r = (0.5, \text{fm})^{-2}$, the slope of the GLC changes by approximately 1% to 2%, whereas for the BG, it changes by less than 1%. For heavier quarkonia (which can be investigated at the EIC too) the adopted value of ϵ_r should matter less. We note that the change in amplitude due to a change in ϵ_r can be compensated for by a change in the free parameter $\bar{\chi}$ which makes the precise value of ϵ_r less relevant. Here we try to keep the values of ϵ_r and $\bar{\chi}$ as similar as possible to the dijet case. Since also for the J/ψ case the slope remains largely unchanged for different values of ϵ_r, we conclude that the damping factor is in any case not relevant to the problem of the tension between the slopes.

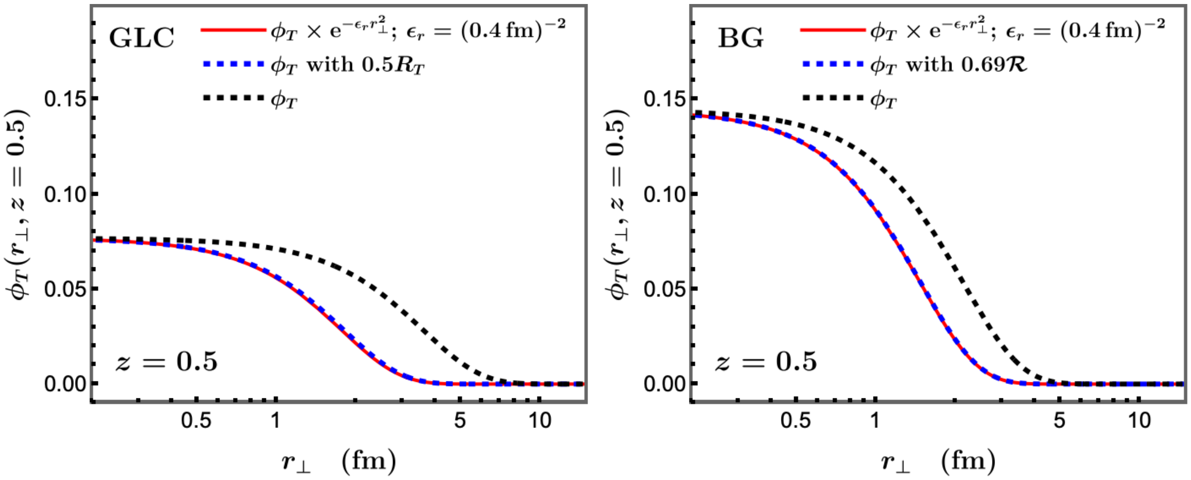

(a) (b)

Figure 6.5: The widths of the GLC and BG wave functions as a function of the dipole size $\boldsymbol{r}_\perp$ for $z = 0.5$, compared with the dipole size cutoff ϵ_r of the model. Here, R_T and $\mathcal{R}$ represent the free parameters of the GLC and BG wave functions, respectively, see Eqs. (6.4) and (6.6). The figures show that the width of the BG and GLC wave functions ϕ_T (black dashed lines) are equal to ϕ_T times the cutoff $\exp[-\epsilon_r r_\perp^2]$ (red lines) if the free parameters of each wave function are decreased to $0.5R_T$ for GLC and $0.69\mathcal{R}$ for BG (blue dashed lines).

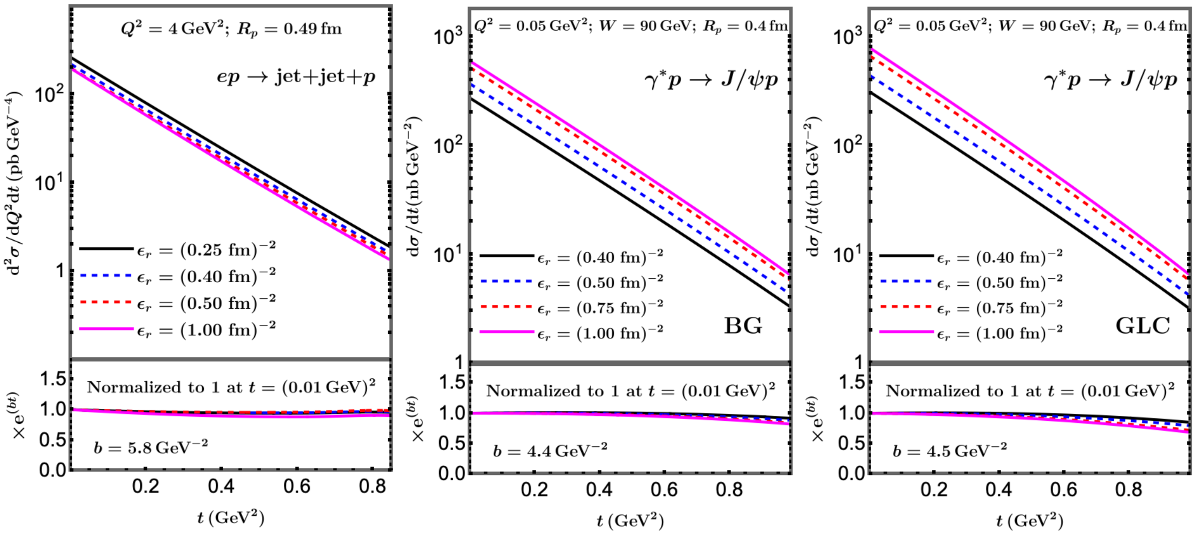

(a) (b) (c)

Figure 6.6: Sensitivity of the slope and amplitude of the cross-sections to changes in ϵ_r for (a) diffractive dijet and J/ψ production: (b) BG wave function, and (c) GLC wave function. The lower section of each figure displays the differential cross section multiplied by e^{bt} and normalized to 1 at $t = (0.01\ \mathrm{GeV})^2$. The lower sections show that the slopes of both dijet and J/ψ production hardly change with the variation in ϵ_r.

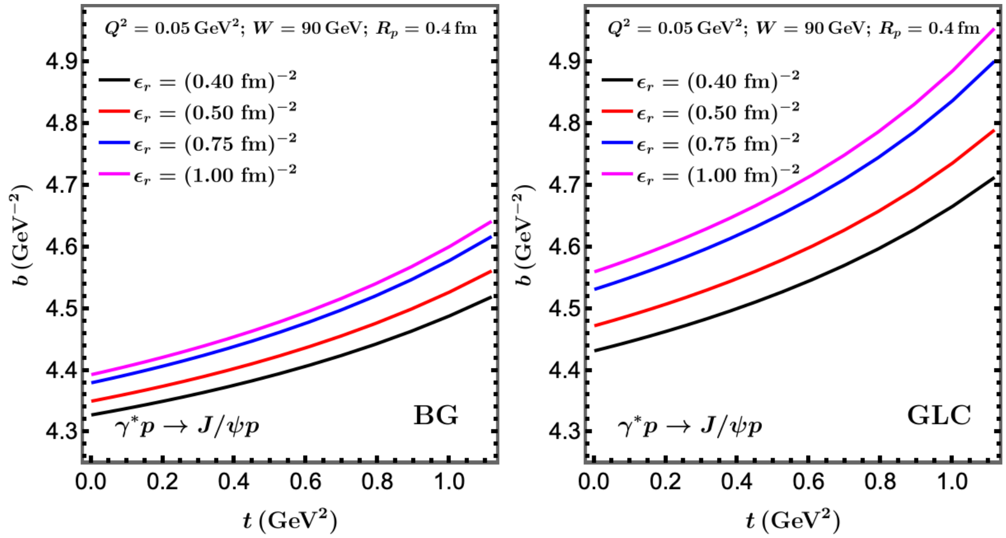

(a) (b)

Figure 6.7: The slope of the exponential fall-off of the cross section (b) for different values of ϵ_r in the case of (a) BG and (b) GLC wave functions. The slope, which is not completely constant, is calculated at a given value of t with respect to $t = (0.01\,\mathrm{GeV})^2$.

In Fig. 6.8, we present the model description of the combined W dependence data of the total J/ψ photoproduction and contrast it with the JMRT (Jones-Martin-Ryskin-Teubner) NLO [238, 239] and the power law fit to H1 [240]. The power-law function representing the photoproduction cross section, which was obtained through fitting the H1 data, can be expressed as follows:

$$\sigma_{\gamma p\to J/\psi p} = N\left(\frac{W}{90\,\text{GeV}}\right)^{\delta} \tag{6.12}$$

with $\delta = 0.67 \pm 0.03$ and $N = 81 \pm 3$ pb.

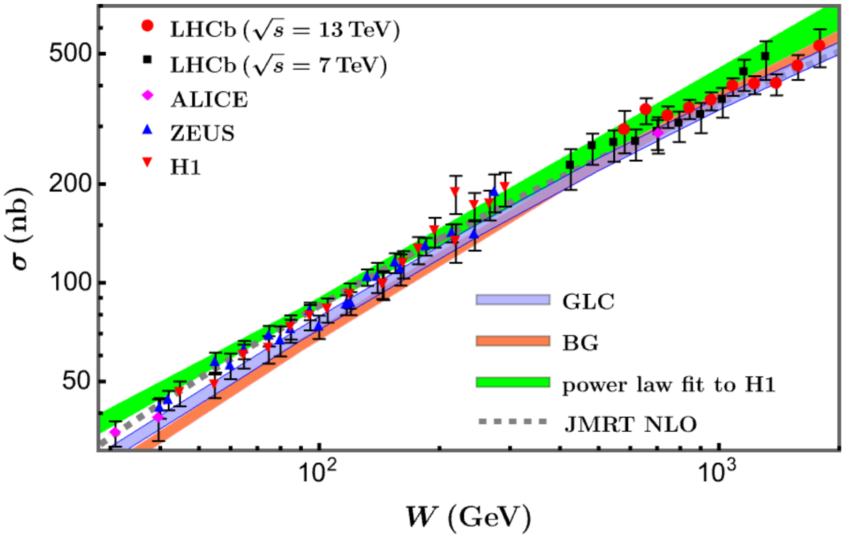

Figure 6.8: Comparison of the model description of the combined W dependence data to the JMRT NLO model [238] and the power law fit to H1 [240]. The data points are obtained from [236, 240].

We note that the total photoproduction cross section $\sigma_{\gamma p\to J/\psi p}$ as a function of W of LHCb for both $\sqrt{s} = 7$ TeV and $\sqrt{s} = 13$ TeV presented in Figs. 6.4 and 6.8 is derived from the central exclusive production (CEP) cross section of J/ψ in pp collisions $\sigma_{pp\to J/\psi p}$ (or any vector mesons ψ) which is related as [239]

$$\sigma_{pp\to\psi p} = r(W_+)k_+\frac{dn}{dk_+}\sigma_{\gamma p\to\psi p}(W_+) + r(W_-)k_-\frac{dn}{dk_-}\sigma_{\gamma p\to\psi p}(W_-), \tag{6.13}$$

where r, $k_\pm = M_\psi/2\exp[\pm Y]$, $dn/dk_\pm$, and $W_\pm^2 = 2k_\pm\sqrt{s}$ denote the gap survival factor, photon energy, photon flux, and the invariant mass of the photon-proton system, respectively. The necessary parameter values are listed in [236, 239], see also [241].

For our model, the total photoproduction cross section is obtained by integrating the differential cross section $d\sigma/dt$ in Eq. (6.1) up to $t = 1.2$ GeV^2 at $Q^2 = 0.05\,\text{GeV}^2$ which correspond to the kinematic regime probed by HERA [215], without considering the β and skewness corrections. As expected, the GLC model provides a better fit to the data compared to the BG wave function. However, at low W, the GLC model slightly underestimates the data and falls below the description provided by the JMRT, which incorporates NLO QCD effects. The JMRT NLO is shown to follow the trends of the data across the entire W range. Nevertheless, both BG and GLC wave functions still offer a better description of the data compared to the power law fit, which exhibits deviations from the data at both low and high W.

In Fig. 6.9 we show the W distribution resulting from the model fits to the t-dependence. Both models can describe well the small Q^2 data (photoproduction). For electroproduction GLC overestimates the data by at most 2σ, while BG shows a larger deviation from the data, as shown in Fig. 6.9(b).

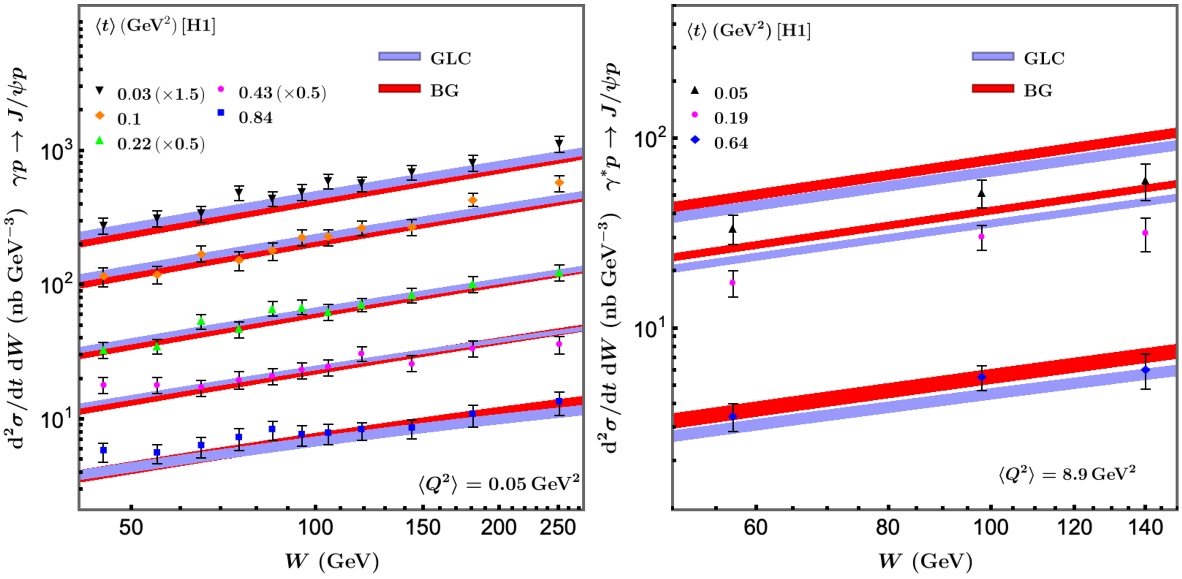

(a) (b)

Figure 6.9: W dependence of the model fits compared to the H1 data for (a) photoproduction and for (b) $\langle Q^2\rangle = 8.9$ GeV^2 for the two different wave function models and the same model parameters as in Fig. 6.4.

Using the obtained fit parameters, we also fit the model to the data of the total cross section of photo- and electroproduction from H1 [215] and ZEUS [216] experiments. The fit is performed for both GLC and BG wave functions, with a fixed center-of-mass energy $W_{\gamma p} = 90$ GeV. It is evident that the model effectively describes the data throughout the entire range of Q^2, as demonstrated in Figure 6.10. The cross section is determined by integrating up to $t = 1.2\,\text{GeV}^2$. In this analysis, we use $R_p = 0.4$ fm, which corresponds to $\bar{\chi} = 1.45 - 1.50$ for GLC and $\bar{\chi} = 1.10 - 1.15$ for BG, see Table 6.1.

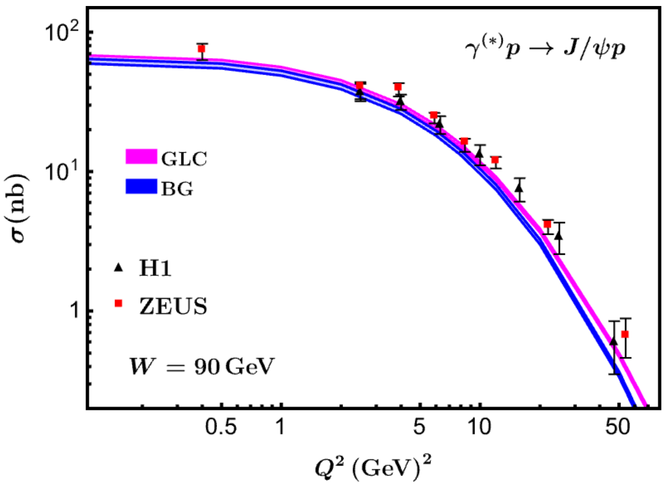

Figure 6.10: Fit of the model to the total cross section of $\gamma^{(*)}p \to J/\psi p$ as a function of Q^2 data from H1 [215] and ZEUS [216] for both GLC and BG wave functions.

6.5 Coherent Diffractive J/ψ Production in UPCs at midrapidity

Ultra-peripheral Heavy Ion Collisions at LHC and RHIC can be used to study photon-nucleus collisions. In order to make sure that one is dealing with exclusive coherent diffractive production of a J/ψ there need to be rapidity gaps between the J/ψ and both nuclei. We consider the J/ψ to be produced at mid-rapidity which is also known as CEP, characterized by the presence of two (pseudo)rapidity gaps, as depicted in Fig. 6.11. Note that a vector meson like the J/ψ cannot be produced from two photons. The central rapidity range of the LHC is $|Y| < 0.8$ and at RHIC $|Y| < 1$. Here we simply take $Y = 0$. In that case the colliding photon and gluon will both have an energy of $M_V/2$, which means that the gluon has a momentum fraction of $x_g = M_V/\sqrt{s_{NN}}$. For the LHC Pb-Pb UPC data [242] at $\sqrt{s_{NN}} = 5.02$ TeV (Run 2) this corresponds to $x_g = 6 \cdot 10^{-4}$ and at $\sqrt{s_{NN}} = 2.76$ TeV (Run 1) to $x_g = 0.001$. For the RHIC Au-Au UPC data at $\sqrt{s_{NN}} = 200$ GeV this corresponds to $x_g = 0.015$, which is at the edge of the range of applicability of the MV-like model that we are using. We will use the ALICE data to fit η and then obtain predictions for RHIC, keeping in mind this caveat.

The photoproduction cross section in A-A UPCs at midrapidity ($Y = 0$) can be related to the photonuclear γA cross section as [242]:

$$\frac{\mathrm{d}^2\sigma_{J/\psi}}{\mathrm{d}Y\,\mathrm{d}p_T^2}|_{Y=0} = 2n_{\gamma\mathrm{A}}(Y=0)\frac{\mathrm{d}\sigma_{\gamma\mathrm{A}}}{\mathrm{d}t} \tag{6.14}$$

with p_T is the transverse momentum of the J/ψ and $n_{\gamma\mathrm{A}}$ is the photon flux averaged over the impact parameter range corresponding to the UPC centralities. The factor 2 in front of $n_{\gamma\mathrm{A}}$ is to account for the fact that there are two possible photon sources [243]. The photon-nucleon center of mass energy squared $W_{\gamma\mathrm{N}}$ for A-A UPCs at mid-rapidity is

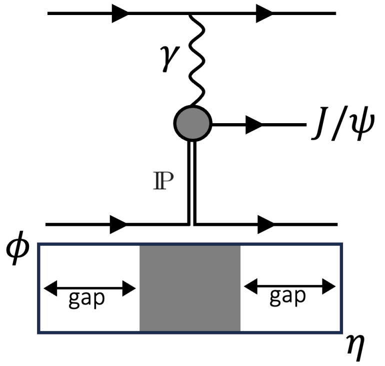

Figure 6.11: Diffractive J/ψ photoproduction at mid-rapidity (CEP) mediated by the pomeron $\mathbb{P}$. The plot under the diagram shows the distribution of particles in the azimuthal angle (ϕ) vs pseudorapidity (η) plane, revealing two gaps in (pseudo)rapidity for the final state particles. The shaded area represents the region of pseudorapidity of the produced particles. Reproduced from [241].

determined by $W_{\gamma\mathrm{N}}^2 = M_V\sqrt{s_{NN}}$ [239, 244]. For LHC Pb-Pb UPC data at $\sqrt{s_{NN}} = 5.02$ TeV this corresponds to $W_{\gamma\mathrm{N}} = 125$ GeV and at $\sqrt{s_{NN}} = 2.76$ TeV to $W_{\gamma\mathrm{N}} = 93$ GeV, while for RHIC Au-Au UPC data at $\sqrt{s_{NN}} = 200$ GeV this corresponds to $W_{\gamma\mathrm{N}} = 25$ GeV.

In Fig. 6.12 we provide a fit of our model to the t dependence of the differential cross section $d^2\sigma/dY dt$ [242] for coherent diffractive J/ψ production at $Y = 0$ in ultra-peripheral Pb-Pb collisions at $\sqrt{s_{NN}} = 5.02$ TeV. According to [242], various models can describe the ALICE data well. One such model is the leading-twist approximation (LTA) of nuclear shadowing [245, 246], which combines the Glauber-Gribov formalism with the phenomenology of photon diffraction from HERA. The lower bound of the GLC fit in our model is close to the LTA (low shadowing) model result with a slightly steeper slope, as shown in Fig. 6.12(b). Another model, the b-BK [204, 247, 248], was proposed based on the solution of the Balitsky-Kovchegov equation [84, 87] with an impact parameter dependence. Another study that incorporates nucleon shape fluctuations [200] also provides a good fit to the data, including the W dependence of the coherent J/ψ photoproduction total cross section and the t distribution of coherent and incoherent J/ψ photoproduction data from HERA. While the former two models utilize the BG wave function, our model provides a better description of the t and W dependence data using the GLC wave function. Another wave function model based on the Buchmüller-Tye potential [214] that uses $\vec{r}$-$\vec{b}$ correlation [249] with two different parameterizations: GBW [26, 27] and BGBK [250], also gives good agreement with the data [251]. Differences in the magnitude and slope of the cross section between other models and ours could also be due to the use of different nuclear radius parameters.

Extrapolating the fit gives a prediction of the first diffractive minimum (or dip) to be at $t \simeq 0.016\,\mathrm{GeV}^2$. We find that the dip position is determined by the target profile R_A, such that it will move towards a smaller t value for larger R_A. The fit turns out to be very sensitive not only to the value of R_A, but also to the power of A. With the fit of the

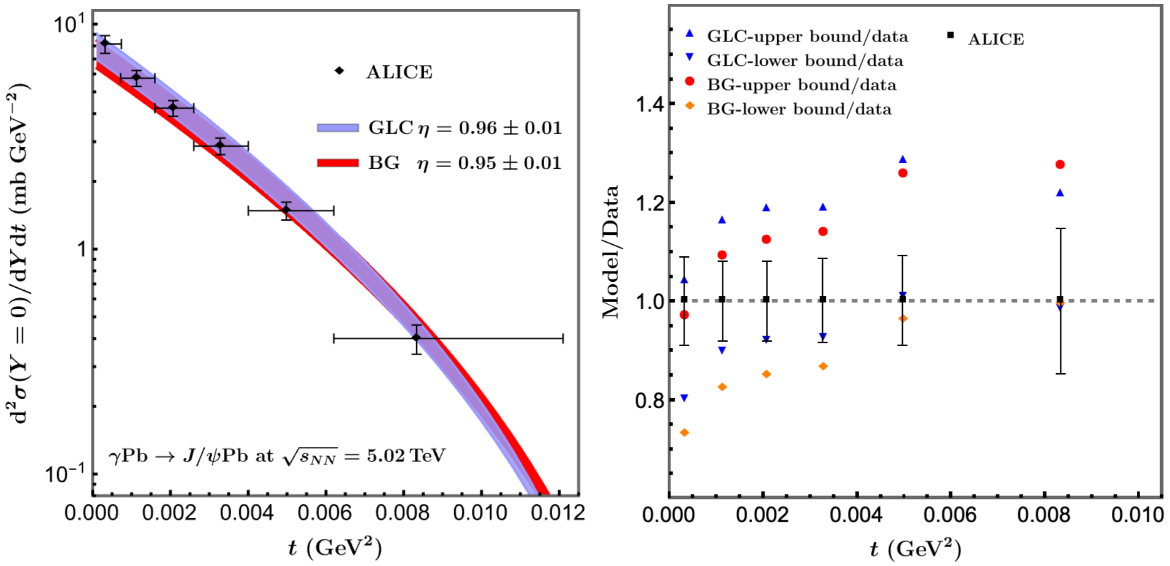

(a) (b)

Figure 6.12: (a) Fit of the model to ALICE (Run 2) data [242] of coherent diffractive J/ψ production at midrapidity in ultra-peripheral Pb-Pb collisions at $\sqrt{s_{NN}} = 5.02$ TeV. We use the same parameter values as in Fig. 6.4, but fit the additional parameter η that determines the saturation scale for nuclei. (b) Ratio of the model fit to the ALICE data for lower and upper bounds of each wave function.

model to the ALICE data, we find that $\eta = 0.96 \pm 0.01$ for GLC and $\eta = 0.95 \pm 0.01$ for BG give the best fit, see Fig. 6.12. The values of η for each wave function are determined through a χ^2/dof analysis, as shown in Fig. 6.13. Therefore, our model fit indicates that the saturation scale behaves like $Q_s^2 \propto A^{0.27-0.30}$, not $A^{1/3}$. The latter in fact does not provide a good fit. Following Eq. (5.46), the saturation scale $Q^2_{0s,\mathrm{A}}$ for the heavy nucleus A depends on η, R_A, and R_p, and is in all cases found to be between 1.5 and 1.9 GeV^2. The choice of proton and nuclear profile, particularly the Gaussian proton profile used in our study, can affect the fitted η value and may differ with different profiles. We did not attempt to find profiles that would lead to $\eta = 1$ and do not exclude that that is possible. To obtain the actual value of η, data for intermediate A values is needed. Here, we only use $A = 208$, which is insufficient to draw a definite conclusion about the A dependence. The saturation scales used for each η for Au and Pb nuclei obtained from Eq. (5.44) are summarized in Table 6.2.

A	R_p (fm)	η	$Q^2_{0s,\mathrm{Pb}}$ (GeV^2)
Pb	0.40	0.94	1.54
		0.95	1.63
		0.96	1.72
		0.97	1.81
Pb	0.41	0.94	1.62
		0.95	1.71
		0.96	1.80
		0.97	1.90

A	R_p (fm)	η	$Q^2_{0s,\mathrm{Au}}$ (GeV^2)
Au	0.40	0.94	1.52
		0.95	1.60
		0.96	1.69
		0.97	1.78
Au	0.41	0.94	1.60
		0.95	1.68
		0.96	1.78
		0.97	1.87

Table 6.2: Saturation scales for Pb and Au with their dependence on η.

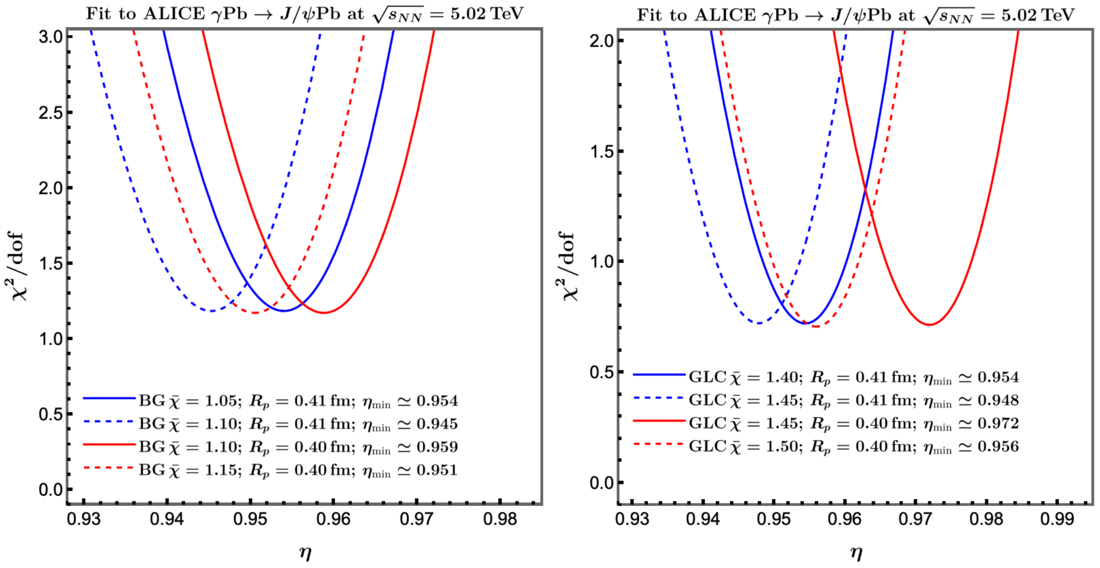

(a) (b)

Figure 6.13: Determination of η for the (a) BG and (b) GLC wave functions.

6.6 Predictions

We will present predictions for processes that are relevant at RHIC, LHC, and EIC, utilizing the parameters obtained from the previous analysis.

6.6.1 $\gamma^{(*)}p$ predictions for the EIC

With the obtained model fits to the H1 data of the electro- and photo-production processes in Sec. 6.2, we provide predictions for the same processes at EIC. The EIC will cover a different kinematic region, although not significantly different enough for evolution to play a significant role[5]. Fig. 6.14(a) shows the predictions without the phenomenological correction $1+\beta^2$ and Fig. 6.14(b) with. In Fig. 6.15 we show the correction by itself. The predictions presented in Fig. 6.14 pertain to two distinct center-of-mass energy values, specifically $\sqrt{s} = 45$ GeV and $\sqrt{s} = 140$ GeV, which are the standard values assumed for EIC predictions. For the inelasticity variable y, we have selected values of approximately 0.79 and 0.13, which fall within the range of y values investigated in the HERA experiments. To explore the small-x_g regime ($x_g \lesssim 0.01$), we have chosen $W = 40$ GeV and $W = 50$ GeV for each respective $\sqrt{s}$ value. The analysis outlining the selected values of y, W, and Q^2 for each $\sqrt{s}$ is presented in Fig. 6.16.

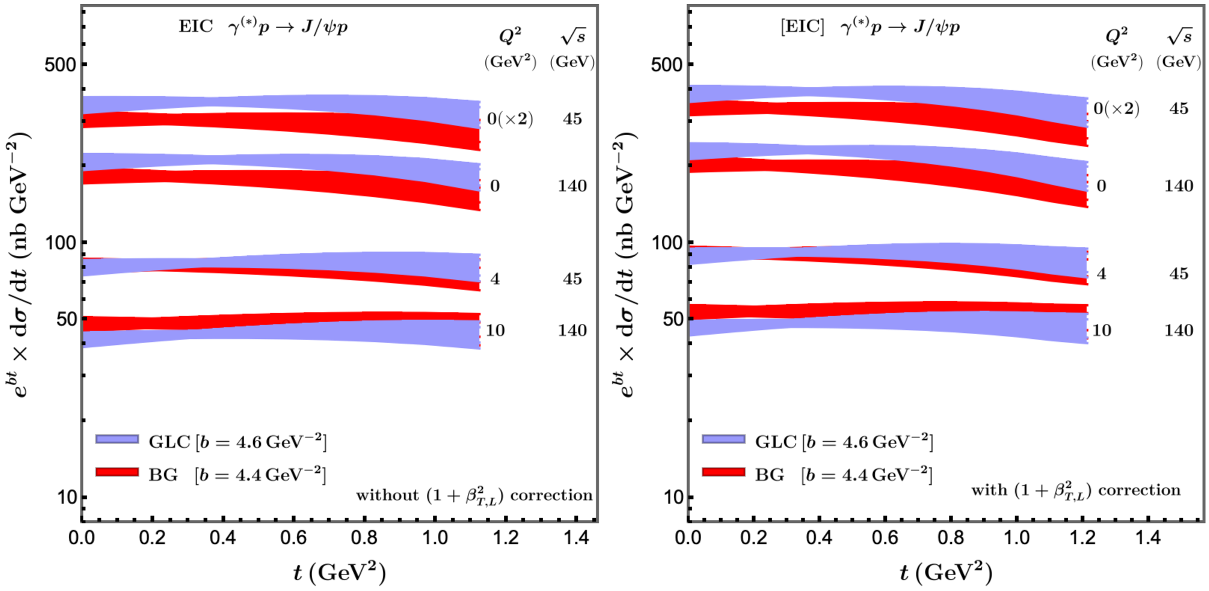

(a) (b)

Figure 6.14: Predictions of diffractive $\gamma^{(*)}p \to J/\psi\, p$ at the EIC for two different wave function models, (a) without β correction and (b) with β correction. We choose $W = 40$ GeV for $\sqrt{s} = 45$ GeV which will probe $y \approx 0.79$ while $W = 50$ GeV for $\sqrt{s} = 140$ GeV will probe $y \approx 0.13$, where we use $y = \left(Q^2 + W^2\right)/s$.

It is important to note that the EIC predictions displayed in Fig. 6.14 represent $e^{bt} d\sigma/dt$, where the parameter b characterizes the slope of each wave function. Specifically, we have chosen $b = 4.6$ GeV^2 for GLC and $b = 4.4$ GeV^2 for BG. These particular values of b have been selected to ensure that the predictions, along with their associated bands, roughly exhibit a linear trend. By presenting the predictions in this manner, we

---

[5] Here evolution in both x and Q is meant. As discussed in Sec. 5.4 GTMD evolution due to quantum corrections has not been studied yet, but it is expected to affect the predictions by much less than the current uncertainties of the data. A rough estimate of the impact of logarithmic quantum corrections is given by $\log\left(\sqrt{s_1}/\sqrt{s_2}\right)$. Assuming a coupling constant of order 1, we find that $\log(319/140) \approx 0.82$ and $\log(140/45) \approx 1.13$. However, when we extend the model to LHC energies, the evolution may become relevant. This is evident from $\log(5.02/0.319) = 2.76$, indicating that the probed x values at LHC Run2 are significantly smaller compared to those at HERA and EIC.

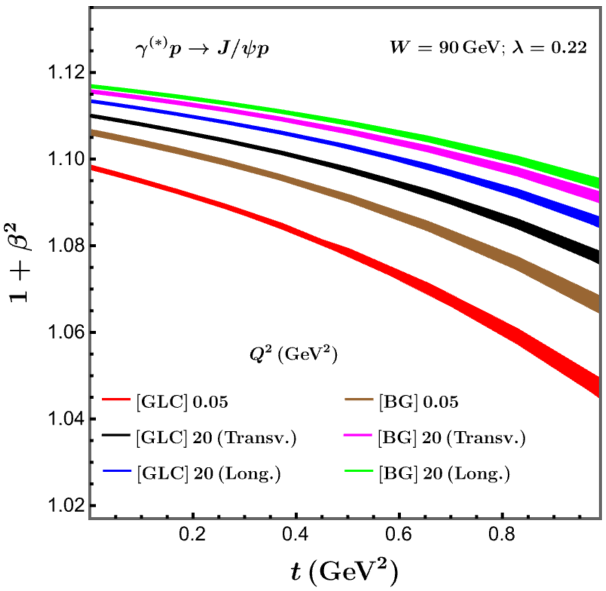

(a)

Figure 6.15: The phenomenological correction $1+\beta^2$ of the model for diffractive J/ψ production in $\gamma^{(*)}p$ for the EIC predictions in Fig. 6.14.

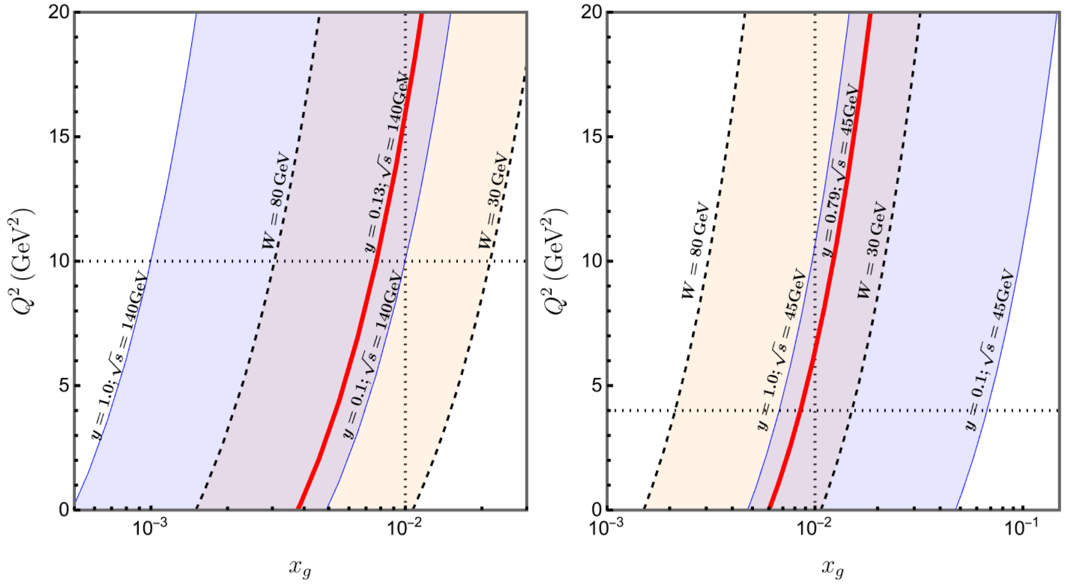

(a) (b)

Figure 6.16: Determination of the y, Q^2 and W range of the EIC predictions for which $x_g \lesssim 0.01$ for (a) $\sqrt{s} = 140$ GeV and (b) $\sqrt{s} = 45$ GeV. The horizontal dotted lines indicate the selected values of Q^2 for electroproduction: (a) $10\,\mathrm{GeV}^2$ and (b) $4\,\mathrm{GeV}^2$. The red lines correspond to the chosen inelasticity y values.

aim to facilitate the analysis of the slope behavior, which may not precisely follow the e^{bt} function. Notably, for $t > 0.5$ GeV^2, the majority of the bands in the plot exhibit a decreasing trend.

In Fig. 6.15 the correction obtained with the model is plotted for $\gamma^{(*)}p$ collisions as a function of t and found to be in the 10-15% range, a bit larger in the BG model than in the GLC model, and slowly increasing in Q^2. This is in agreement with other phenomenological studies [217, 229, 230]. For longitudinal photon polarization a similar size correction is obtained. Fig. 6.19 shows similar size corrections for UPCs to which we will turn next.

6.6.2 UPC predictions for RHIC, LHC and EIC

Using the parameterization for UPCs obtained in Sec. 6.5 by analyzing the ALICE data (LHC Run 2), we present predictions for RHIC and LHC (Run 1) at midrapidity in Fig. 6.17. In general, both wave function models give very similar results but GLC shows a somewhat larger band than BG as expected from the previous analysis on γp (see the χ^2/dof in Fig. 6.2). Fig. 6.17(a) is for Au-Au UPCs at $\sqrt{s_{NN}} = 200$ GeV. Fig. 6.17 shows that the first diffractive dip for Au-Au at RHIC is predicted to be around $t \simeq 0.017 \pm 0.001\,$GeV^2 which is close to its location in RHIC preliminary data [252] and other studies [219, 244], while for Pb-Pb at LHC Run 1 it is predicted to be around $t \simeq 0.015 \pm 0.001\,$GeV^2. Fig. 6.17(b) is for Pb-Pb UPCs at LHC Run 1 with $\sqrt{s_{NN}} = 2.76$ TeV. In Fig. 6.18, we provide predictions of e-Au collisions at the EIC for photoproduction ($Q^2 = 0\,$GeV^2) and electroproduction ($Q^2 = 10\,$GeV^2) for fixed $x_g = 0.01$ which corresponds to $W_{\gamma \mathrm{N}} = 31\,$GeV and $W_{\gamma \mathrm{N}} = 44\,$GeV, respectively. The bands for each wave function model reflect the uncertainties on R_p (which translates to η) and $\bar{\chi}$. As shown in Fig. 6.19, the β corrections are in the order of 6-10% for UPCs, which is small compared to the uncertainties, hence not included here.

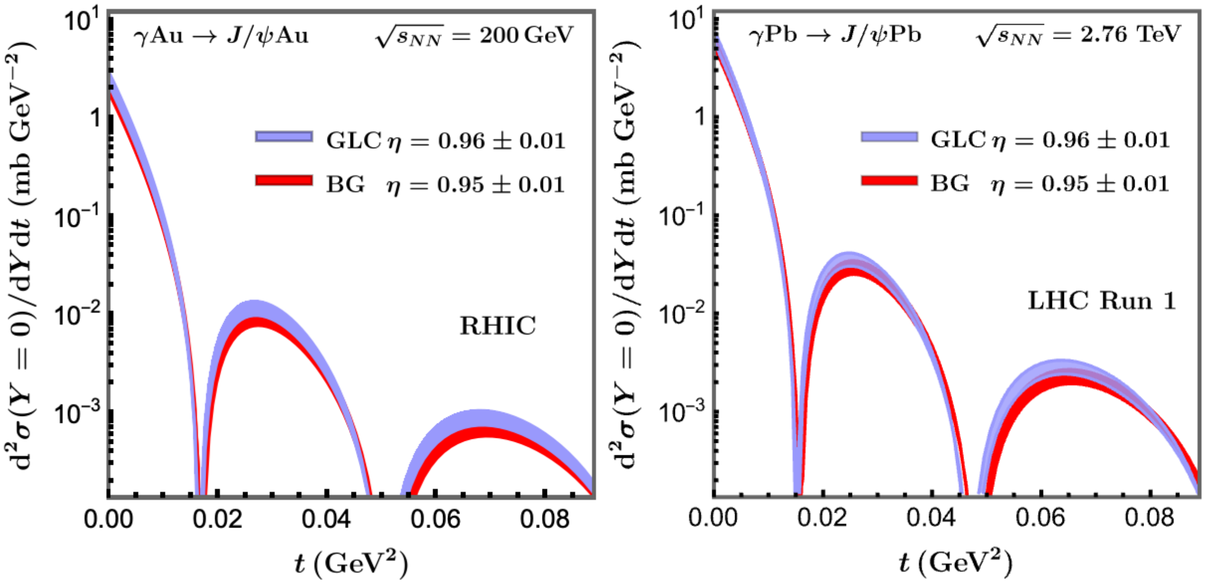

(a) (b)

Figure 6.17: Model predictions for coherent diffractive J/ψ production at midrapidity in ultra-peripheral (a) Au-Au collisions with $\sqrt{s_{NN}} = 200$ GeV at RHIC and (b) Pb-Pb collisions with $\sqrt{s_{NN}} = 2.76$ TeV at LHC.

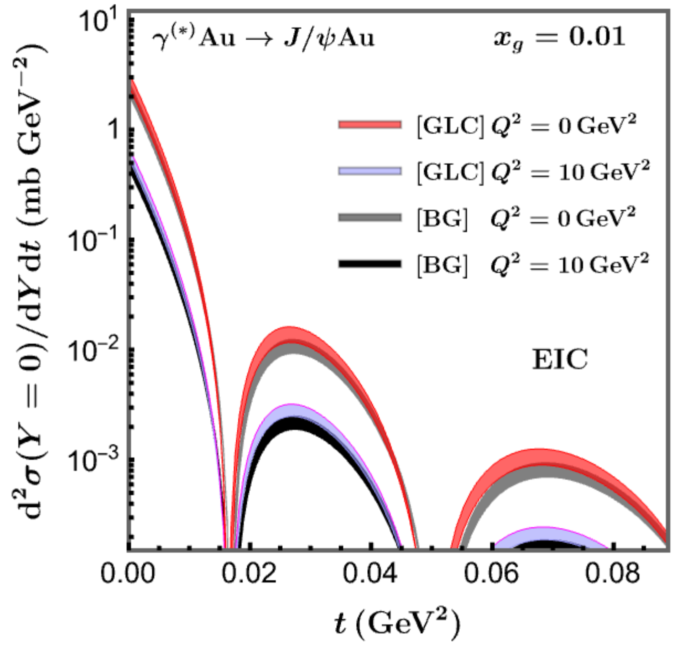

Figure 6.18: Model predictions for coherent diffractive J/ψ production in e-Au collisions at the EIC at fixed $x_g = 0.01$ at $Q^2 = 0\,\text{GeV}^2$ and $Q^2 = 10\,\text{GeV}^2$.

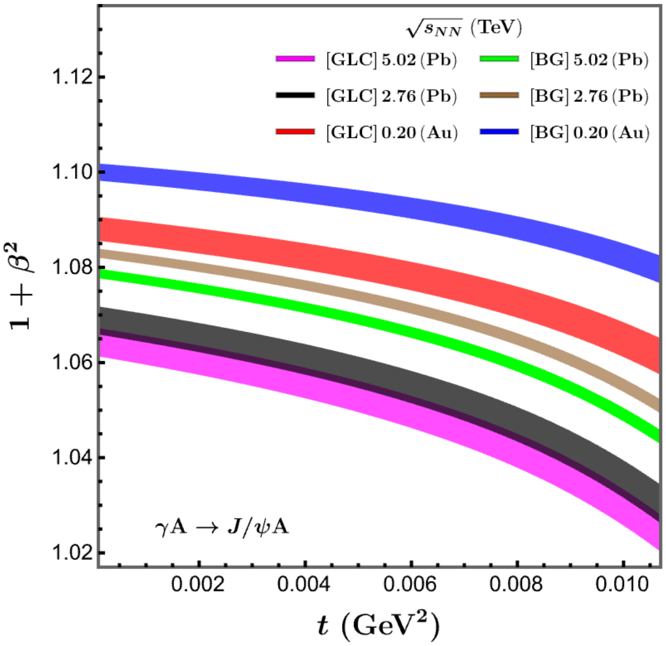

Figure 6.19: The phenomenological correction $1+\beta^2$ of the model for diffractive J/ψ production in γA in UPCs in Fig. 6.17. We show only small t for γA because the correction diverges at the diffractive dip.

7

Summary and outlook

We have investigated high-energy (small x) diffractive dijet production utilizing a multi-dimensional parton distribution function, the gluon GMTD, for which we considered a generic small-x model. To start we employed an x-independent, impact parameter-dependent MV model, along with two additional free parameters. After fitting the model to HERA data, we found that the model described the data quite well, although some improvements were still needed in order to capture all features of the data. To achieve this, we implemented an x-dependent saturation scale in the model, following the GBW approach. We applied the improved model to the description of the exclusive diffractive J/ψ production data from both HERA and LHC. A good description of the data were obtained, although a tension regarding the t dependence of the dijet case could not be resolved. With the obtained model we provided predictions for the EIC, LHC, and RHIC to assess the consistency of the model and of the unified GTMD description of the various processes. After this very brief overall summary, the contents of this PhD thesis will now be summarized in more detail.

After a general introduction in Chapter 1, in Chapter 2, we examined the DIS high-energy collision process, which is widely employed as a tool to investigate the internal structure of hadrons, for instance using accelerators such as the Stanford Linear Accelerator, HERA, the SPS at CERN and the future EIC. One important aspect of DIS is that its cross section can be factorized into soft and hard parts. The hard part can be calculated in perturbative QED, while the soft part contains non-perturbative QCD information encoded by the PDFs (Parton Distribution Functions), which can only be extracted from experiments or calculated using lattice QCD. The correlator in the definition of PDFs, which involves two fields at different space-time points, is not gauge invariant. However, it can be restored by introducing the Wilson line (gauge link). In the eikonal approximation, the Wilson line represents the resummation of an infinite number of gluon interactions during the process.

The simplest type of PDFs, the one-dimensional collinear PDFs, played a crucial role in confirming the dominance of gluons in the small x regime. This dominance formed the foundation for the analysis of high-energy collisions in this thesis, where we neglected the contribution from quarks in the proton or nucleus. Another important aspect of the PDFs was their predictive power on different energy scales, which is governed by the DGLAP equations. This allowed to make predictions for experiments performed at different energies. However, the one-dimensional collinear PDFs do not properly describe the behavior of the gluons in the small x limit. The collinear PDFs describing the gluon distribution exhibit rapid growth, eventually violating the unitarity of the scattering amplitude.

In order to analyze high-energy scattering properly, a suitable framework is required to define the distribution of partons and control the rapid growth of the gluon distribution, which requires inclusion of nonlinear QCD effects and transverse momentum dependence (through its Fourier conjugate). In Chapter 3, we discuss this within the CGC framework, that applies at small x where nonlinear phenomena become dominant. In this regime, the occupation number of gluons becomes extremely high, making single scattering events between the probe and a gluon unlikely to occur. Due to the high occupation number, the gluons can be described classically, where the expectation value of associated observables can be obtained through a path integral weighted by a weight function. The MV model utilizes a Gaussian weight function, which can be related to the saturation scale, i.e. the scale at which the non-linear QCD effects become significant, through the scattering amplitude. The latter is a matrix element of Wilson lines, that in addition to lines that runs along a straight line along the light-cone, also contains Wilson lines in the transverse direction at light-cone infinity, together forming a Wilson loop. This is an important ingredient of the higher-dimensional PDFs called GTMDs that play a main role in this thesis.

In Chapter 4, we investigated higher-dimensional PDFs that go beyond the one-dimensional collinear PDFs. Firstly, we discussed two such PDFs that probed distinct aspects of parton momentum: TMDs and GPDs. TMDs are three-dimensional and depend on x and $\boldsymbol{k}_\perp$, while GPDs are four-dimensional with dependencies on x, ξ, and $\boldsymbol{\Delta}_\perp$. To gain a more comprehensive insight into the internal structure of the hadron, we could utilize even higher-dimensional PDFs, the six-dimensional GTMDs. The Fourier transform counterparts of GTMDs known as the Wigner distributions, are often referred to as the "mother distributions". Although GTMDs can, in principle, be viewed as either the off-forward generalization of TMDs or transverse momentum-dependent GPDs, the generalization process requires the use of regularization techniques, making it not a straightforward step. It should also be emphasized that the description provided by GTMDs is more comprehensive than the combined information obtained from separate examinations of GPDs and TMDs.

It was proposed that the gluon GTMD could be probed through the diffractive dijet production process at small x and zero skewness. In this regime, the staple-like Wilson line structure inherent in the GTMD can be related to the Wilson loop matrix element of the dipole scattering amplitude. This motivated us to develop an MV-like CGC model for the gluon GTMD at small x that we introduce in Chapter 5. The small x gluon GTMD model was constructed by initially considering a simple x-independent model and fitting it to the available data of diffractive dijet production. Given the dominance of the gluon at small x, our primary focus was on the gluon GTMD. The main objective of this study was to demonstrate that a simple gluon GTMD model could effectively describe the available data of diffractive processes, especially diffractive dijet production, rather than aiming to provide a comprehensive model to describe general processes. We began our description of the gluon GTMD model by incorporating the impact parameter dependence into the saturation scale, building upon the MV model. This approach allowed us to minimize the number of parameters in our model that needed to be fitted to the data. Specifically, we introduced two physically motivated free parameters: ϵ_r and χ. The ϵ_r parameter limited the contribution of large dipole sizes, effectively restricting our model to probe dipole sizes on the order of the gluonic radius of the proton. On the other hand, the χ parameter served as a constant that adjusted the overall value of the saturation scale.

Fitting the model free parameters to the H1 data, we found that their values turned out to be reasonable from the physical interpretation point of view. With this we obtained a good description of the t dependence of the data and a reasonable description of the jet transverse momentum dependence. This provided confidence that the gluon GTMD description is appropriate for this process in the examined kinematic range. With this model we provided predictions for the EIC for both electroproduction in a somewhat different kinematic regime and for photoproduction which has a much higher cross section. Hopefully this will allow further tests of the underlying GTMD description.

By the fact that at least formally GPDs can be obtained from GTMDs, we also have addressed some theoretical issues known for GPDs and small x studies that are relevant for small-x gluon GTMD models with an impact parameter dependent saturation scale. First there is the issue that considering the impact parameter dependence requires the target (and the dipole) to be sufficiently localized in transverse coordinate space. This in turn requires consideration of the dipole frame with large P^+ and hence sufficiently large center of mass energy. Second, the dipole size has to be much smaller than the size of the impact parameter profile considered. This requires consideration of the correlation limit for dijet production, in which $\Delta_\perp = k_{1\perp} + k_{2\perp}$ is much smaller than $K_\perp = (k_{1\perp} - k_{2\perp})/2 \approx k_{1\perp} \approx k_{2\perp}$, where the latter scale determines the relevant dipole sizes. On the other hand, $K_\perp$ should not be so large that one is outside the saturation regime. Under these kinematic conditions the MV model with impact parameter dependent saturation scale is expected to be an appropriate model for the gluon GTMDs probed.

Analyzing the model description of the Q^2 dependence data, we observed that the model, which effectively concerns an average value of x only, should be improved. To enhance the agreement between the model and the data, we proposed incorporating an x dependence into our model, allowing it to probe different x values corresponding to various Q^2. By incorporating an x dependence into our previous (x independent) gluon GTMD model, following the approach of the GBW parameterization for the saturation scale, we were able to improve the description of the HERA-H1 diffractive dijet production data. Specifically, the model effectively captured the Q^2 dependence, as well as the t and $K_\perp$ distribution data. Additionally, considering that x is related to the inelasticity y, we were also able to describe the data's y dependence. Importantly, this improved description was achieved without introducing any new parameters but rather by defining the existing parameter χ as an x-dependent variable, denoted as $\chi(x)$. The good agreement with the H1 data provides support for the GTMD framework employed in this study. We anticipate that further scrutiny and validation of this framework will be possible with forthcoming data from the EIC and LHC experiments.

After having successfully described dijet production, we wanted to try to obtain a simultaneous description with diffractive J/ψ production. However, as outlined in Chapter 6, describing diffractive J/ψ production in the same way as the diffractive dijet production case leads to tension for the slope of the t dependence, which is quite distinct for the two processes, where dijet production requires a steeper slope than J/ψ production. In the model this slope is solely determined by the (Gaussian) proton profile and there appears to be no clear way to resolve the tension. A few other differences between the optimal parameter choices for dijet and J/ψ production are found but these can be reduced by adjusting the J/ψ wave function or by modifying the x dependence with respect to the GBW parameterization. For instance, dijet production can be described well by an x dependence of the saturation scale $Q_s \propto x^{-\lambda}$ with $\lambda = \lambda_{\text{GBW}} = 0.29$, while the W dependence of photoproduction of J/ψ's prefers a smaller $\lambda \approx 0.22$. A non-constant λ may be needed, but we did not explore that option, anticipating that future more precise data may shed new light on the differences between dijet and J/ψ production. Another distinction lies in the parameter $\bar{\chi}$, where diffractive dijet production tended to favor a larger value of $\bar{\chi}$, specifically $\bar{\chi} = 1.5 \pm 0.1$, compared to J/ψ production. However, this tension could be minimized by choosing the GLC wave function, which provided a generally good fit to the data with $\bar{\chi} = 1.4 - 1.5$, in contrast to the BG wave function, which preferred $\bar{\chi} = 1.05 - 1.15$. All in all, we thus expect that a common gluon GTMD model description of dijet and J/ψ production may be possible once the slope issue is clarified by new data.

With the best fit of our model to combined H1 and ZEUS data on J/ψ production, we have provided predictions for the diffractive J/ψ production in e-p collisions at the future EIC. We further fitted our model to UPC data from ALICE (Run 2) to determine the A dependence of the saturation scale. The fit turned out to be very sensitive to the power of A and the nuclear profile R_A, which suggests that also the profile function shape will matter considerably. We find an A dependence that is slightly less than the generally expected $A^{1/3}$, to be specific, $Q_s^2 \propto A^{0.27-0.30}$, but intermediate A values would be needed to reach a definite conclusion on the A dependence. With the obtained fit we provided predictions for UPCs at LHC (Run 1) and RHIC, and for e-Au collisions at EIC. We have also investigated a phenomenological correction commonly used for J/ψ production which comes from the odderon contribution, which is in the 10-15% range and thus unimportant given the present large uncertainties in the available data of electroproduction at HERA (H1 and ZEUS), and hence in the model. The larger correction from accounting for non-zero skewness that is often considered in GPD approaches in the DGLAP regime does not seem appropriate for our GTMD model and was thus not included. Moreover, a similar correction has not been applied in dijet production, which would affect the comparison. We have also pointed out that dijet and J/ψ production go beyond probing GPDs, rather they probe weighted integrals of GTMDs with weights that depend on external kinematical variables of the process that can be varied and exploited. A remaining open question is whether the used data is in the DGLAP or ERBL region. Hopefully future studies will report specifically which region is being probed, as the model may have to depend on that.

The predictions from the presented x-dependent gluon GTMD model for J/ψ production at EIC, LHC, and RHIC, and measurements for heavier quarkonia and different nuclei, will hopefully facilitate resolution of the t distribution tension with dijet production, clarify the dependence on the skewness probed in the process, and determine the x and A dependence of the saturation scale of heavy nuclei.

A
Light cone coordinates

Light-cone (light-front) coordinates are a very useful tool in the analysis of high-energy physics, especially in the study of DIS. They are constructed by taking the time axis x^0 and one space axis x^3 from the usual four-vector components (x^0, x^1, x^2, x^3) to create two new coordinates x^+ and x^-, while the remaining two space axes x^1 and x^2 are denoted by $\boldsymbol{x}_\perp$. In this way, the four-vector x^μ can be expressed as $x^\mu = (x^+, x^-, \boldsymbol{x}_\perp)$, where

$$x^\pm = \frac{x^0 \pm x^3}{\sqrt{2}} \qquad \boldsymbol{x}_\perp = (x^1, x^2). \tag{A.1}$$

It should be noted that some authors may not include the $1/\sqrt{2}$ factor when defining the light-cone coordinates. The volume element in these coordinates can be written as

$$d^4x = dx^+\, dx^-\, d^2\boldsymbol{x}_\perp. \tag{A.2}$$

The scalar products of two vectors also take a simplified form, given by

$$\begin{aligned} u \cdot v &= g_{\mu\nu} u^\mu v^\nu = u^+ v^- + u^- v^+ - \boldsymbol{u}_\perp \cdot \boldsymbol{v}_\perp \\ u \cdot u &= 2u^+ u^- - \boldsymbol{u}_\perp^2. \end{aligned} \tag{A.3}$$

where the light-cone Minkowski flat space metric is defined as

$$g_{\mu\nu} \equiv \begin{pmatrix} 0 & 1 & 0 & 0 \\ 1 & 0 & 0 & 0 \\ 0 & 0 & -1 & 0 \\ 0 & 0 & 0 & -1 \end{pmatrix} \tag{A.4}$$

In other words, the metric tensor $g_{\mu\nu}$ for this coordinate system has $g_{+-} = g_{-+} = 1$ while $g_{ij} = -\delta_{ij}$ for the transverse components (i and j). All other components of the metric tensor are zero. Note that g_{+-} and g_{-+} are the only non-zero off-diagonal elements, reflecting the correlation between the light cone components x^+ and x^-. It is also common to define light-like vectors $\bar{n}^\mu \equiv (1, 0, \mathbf{0}_\perp)$ and $n^\mu \equiv (0, 1, \mathbf{0}_\perp)$ satisfying $\bar{n} \cdot \bar{n} = n \cdot n = 0$ and $\bar{n} \cdot n = 1$, such that $u^\mu = u^+ \bar{n}^\mu + u^- n^\mu + u^\mu_\perp$, where u^+ and u^- are the light-cone components of the vector u^μ while $\boldsymbol{u}_\perp$ denotes its transverse component. In this expression we have promoted $\boldsymbol{u}_\perp$ to a four-vector $u^\mu_\perp \equiv (0, 0, \boldsymbol{u}_\perp)$.

The Dirac gamma matrices will take the form

$$\gamma^\pm = \frac{1}{\sqrt{2}} \left(\gamma^0 \pm \gamma^3 \right) \qquad \gamma^5 = \gamma^+ \gamma^- \gamma^\perp. \tag{A.5}$$

which satisfy anticommutation relations

$$\{\gamma^\mu, \gamma^\nu\} = 2 g^{\mu\nu}. \tag{A.6}$$

In the analysis of high energy DIS, rapidity is a frequently used variable to describe the longitudinal motion of particles in the center-of-mass frame, and is defined as the natural logarithm of the ratio of the energy and longitudinal momentum of a particle

$$y = \frac{1}{2} \ln \left(\frac{E + p_z}{E - p_z} \right) = \frac{1}{2} \ln \left(\frac{p^+}{p^-} \right), \tag{A.7}$$

where E and p_z represent the energy and momentum along the z-axis of the particle, respectively. The use of rapidity allows for a simpler representation of Lorentz boosts along the longitudinal direction (the z-axis in this case). In terms of rapidity, the Lorentz-invariant phase-space integration will be expressed as

$$\frac{\mathrm{d}^3 \boldsymbol{p}}{2E_p (2\pi)^3} = \frac{\mathrm{d}p^+ \, \mathrm{d}^2 \boldsymbol{p}_\perp}{2p^+ (2\pi)^3} = \frac{\mathrm{d}y \, \mathrm{d}^2 \boldsymbol{p}_\perp}{2(2\pi)^3}. \tag{A.8}$$

One advantage of using the light cone coordinates is the ability to separate a particle's momentum into longitudinal and transverse components, which is particularly relevant in DIS, where the momentum of the proton is dominated by the longitudinal component while the virtual photon's momentum is primarily in the transverse direction. By boosting the proton momentum along a specific direction, usually the beam direction axis, the z-axis, the large and small components of momentum can be separated into distinct components. This feature enables the use of various approximations, such as the eikonal approximation, to simplify calculations in high-energy physics.

B

Reference frames

Let us consider a four-vector with components $x^0 = t$ and $x^3 = z$. By performing a boost along the z-axis, we can obtain new components z' and t', given by

$$z' = \gamma\,(z + vt) \qquad t' = \gamma\left(t + \frac{vz}{c^2}\right) \tag{B.1}$$

where $\gamma = (1-\beta^2)^{-1/2}$ is the Lorentz factor, $\beta = v/c$ is the velocity of the inertial frame one moves to from the rest frame, and $c = 1$ for convenience. As discussed in the previous appendix, the t and z components of the four-vector are used to form the light-cone coordinates $x^{\pm} = (t \pm z)/\sqrt{2}$. Hence, applying a boost along the z-axis to these components yields

$$\begin{aligned} x'^{+} &= \frac{\gamma(t+z) + \gamma\beta(t+z)}{\sqrt{2}} = \gamma\,(1+\beta)\,x^{+} \\ x'^{-} &= \frac{\gamma(t-z) - \gamma\beta(t-z)}{\sqrt{2}} = \gamma\,(1-\beta)\,x^{-}. \end{aligned} \tag{B.2}$$

Defining $A \equiv \gamma(1+\beta)$ as the transformation coefficient and $B \equiv \gamma(1-\beta) = 1/A$, we will have $AB = 1$. Therefore, if we apply a boost in the z-direction to a vector P expressed in light-cone coordinates, we obtain

$$\left(P^{+}, P^{-}, P_{\perp}\right) \xrightarrow[\text{along } z]{\text{boost}} \left(AP^{+}, \frac{1}{A}P^{-}, P_{\perp}\right). \tag{B.3}$$

The boost formula will be frequently used in the following discussion to transform from one frame to another.

B.1 The quark Breit frame

The Breit frame is a commonly used reference frame in the analysis of high-energy DIS collisions which is obtained by boosting the photon in the direction of its propagation towards the proton, in such a way that the q^0 component of the photon momentum becomes zero. In this frame, the proton moves along the z direction, while the virtual photon moves in the $-z$ direction, with the photon transferring momentum but not energy. It is important to note that this is only true in the Breit frame. This frame is also referred to as the infinite momentum frame, since the proton moves with a very large momentum towards the virtual photon. It is also known as the brick wall frame, as the proton (quark in this case) appears to bounce off the virtual photon like a tennis ball off a brick wall, with its 3-momentum exactly reversing, as depicted in Figure B.1. Here we will be discussing the Breit frame for the quark, whereas the original Breit frame was considered for the proton.

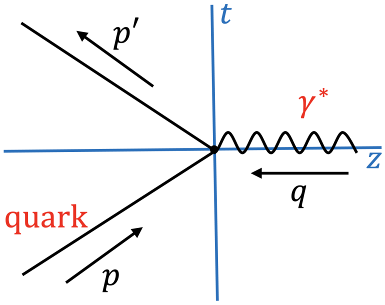

Figure B.1: An illustration of the quark Breit frame, where a quark with momentum $p^\mu = (p^+, p^-, \boldsymbol{p}_\perp)$ moves towards the virtual photon q, which acts as a "wall", and bounces back with a reversed momentum $p'^\mu = (p^-, p^+, \boldsymbol{p}_\perp)$.

Consider a quark with momentum, given in light cone coordinates, as $p = (p^+, p^-, \boldsymbol{p}_\perp)$ where $p \cdot p = 0$ and $p^- = p_\perp^2/(2p^+)$ with the condition $p^+ \gg p^-$. In the Breit frame, the incoming quark moves in the positive z direction with momentum

$$p^z = \frac{p^+ - p^-}{\sqrt{2}} = \frac{p^+}{\sqrt{2}} - \frac{p_\perp^2}{2p^+\sqrt{2}} \approx \frac{p^+}{\sqrt{2}}. \tag{B.4}$$

The struck quark p', moves in the negative z direction with $p'^z = -p^z$ and $p'^0 = p^0$. Thus, in light cone coordinates, it can be expressed as $p'^+ = p^-$ and $p'^- = p^+$, resulting in $p' = (p^-, p^+, \boldsymbol{p}_\perp)$. The photon momentum can be obtained as

$$q^\mu = p' - p = \left(p^- - p^+, p^+ - p^-, \boldsymbol{0}_\perp\right) \approx \left(-p^+, p^+, \boldsymbol{0}_\perp\right). \tag{B.5}$$

By using the relation[1] $(q^\mu)^2 = -Q^2$, we can express $p^+ = Q/\sqrt{2}$. Thus, the momentum

---

[1] In this Appendix we will use q and P as components in the four-vectors q^μ and P^μ. To avoid confusion, in this Appendix we use the notation $q^\mu q_\mu = q \cdot q = (q^\mu)^2$, and $(q^\mu)^2 \neq q^2$, where the latter q represents a component of the four-vector q^μ. We also use this notation for $P^\mu P_\mu = (P^\mu)^2 = P \cdot P$ and $(P^\mu)^2 \neq P^2$, where the latter P represents a component of the four-vector P^μ.

of the incoming quark, outgoing quark, and photon can be expressed in terms of Q as follows:

$$p^\mu \approx \left(\frac{Q}{\sqrt{2}}, 0, \boldsymbol{p}_\perp\right) \qquad p'^\mu \approx \left(0, \frac{Q}{\sqrt{2}}, \boldsymbol{p}_\perp\right) \qquad q^\mu = \left(-\frac{Q}{\sqrt{2}}, \frac{Q}{\sqrt{2}}, \mathbf{0}_\perp\right) \tag{B.6}$$

where the approximation $p^- = p_\perp^2/\left(2p^+\right) = p_\perp^2/\left(\sqrt{2}Q\right) \approx 0$ has been used. The momentum of the proton can be expressed as

$$P^\mu = \left(\frac{Q}{x_B\sqrt{2}}, \frac{x_B M^2}{Q\sqrt{2}}, \mathbf{0}_\perp\right), \tag{B.7}$$

where P and M represent the momentum and mass of the proton, respectively, and satisfy the relation $(P^\mu)^2 = M^2$. The Bjorken scaling variable is defined as $x_B = Q^2/(2P \cdot q)$, where the scalar product of the proton momentum P and the photon momentum q can be expressed as

$$P \cdot q = \frac{Q^2}{2x_B}\left(1 + \mathcal{O}\left(\frac{M^2}{Q^2}\right)\right). \tag{B.8}$$

In terms of the proton momentum P, the quark momentum can be estimated as $p \approx x_B P + p_\perp$. As can be seen in Eqs. B.6 and B.7, when $Q^2 = 0$, we obtain or the approximated momenta

$$q^\mu_{Q^2=0} = (0, 0, \mathbf{0}_\perp) \qquad P^\mu_{Q^2=0} = (0, \infty, \mathbf{0}_\perp), \tag{B.9}$$

which prevents us from using the quark Breit frame in the case of photoproduction.

B.2 The dipole frame

While the Breit frame is a powerful tool in analyzing DIS, the approximations become invalid in the case of photoproduction ($Q^2 \to 0$). This limitation can be avoided by considering the dipole frame [180]. The dipole frame remains valid even at low Q^2 values and enables the treatment of photoproduction without encountering singularities. Furthermore, it provides a clearer distinction between the hard and soft scales involved in the scattering process.

In the dipole frame, the proton and virtual photon momenta are given by (in four vector notation)

$$P^\mu = \left(P + \frac{M^2}{2P}, 0, 0, P\right) \qquad q^\mu = \left(\sqrt{q^2 - Q^2}, 0, 0, -q\right) \tag{B.10}$$

where $P \gg M$ implies $(P^\mu)^2 = M^2\left(1 + \frac{M^2}{4P^2}\right) \approx M^2$ and $(q^\mu)^2 = -Q^2$. In addition, $q \gg Q$ leads to the approximations

$$q^\mu \approx \left(q\left(1 - \frac{Q^2}{2q^2}\right), 0, 0, -q\right). \tag{B.11}$$

The plus and minus components of the light cone coordinates are then given by

$$q^- = \sqrt{2}q\left(1 + \mathcal{O}(Q^2/q^2)\right) \qquad q^+ \approx \frac{Q^2}{2\sqrt{2}q}. \tag{B.12}$$

It can be shown that the relation $(q^\mu)^2 = 2q^+q^- = -Q^2$ still holds even with these approximations.

To apply the dipole frame to the context of both small x_B and small Q^2, which is the focus of this thesis, slight adjustments must be made to the original dipole frame. These adjustments can be made as follows (in four vector notation):

$$P^\mu = \left(\sqrt{\frac{P^2}{2} + M^2}, 0, 0, \frac{P}{\sqrt{2}}\right) \qquad q^\mu = \left(\sqrt{\frac{q^2}{2} - Q^2}, 0, 0, -\frac{q}{\sqrt{2}}\right). \tag{B.13}$$

The modified expressions for P^μ and q^μ satisfy the conditions $(P^\mu)^2 = M^2$ and $(q^\mu)^2 = -Q^2$ within the dipole frame when $P \gg M$ and $q \gg Q$. We can then express them in light cone coordinates as:

$$\begin{aligned} P^\mu &\approx \left(\frac{P}{\sqrt{2}} + \frac{M^2}{\sqrt{2}P}, 0, 0, \frac{P}{\sqrt{2}}\right) \approx \left(P, \frac{M^2}{2P}, \mathbf{0}_\perp\right) \\ q^\mu &\approx \left(\frac{q}{\sqrt{2}} - \frac{Q^2}{\sqrt{2}q}, 0, 0, -\frac{q}{\sqrt{2}}\right) \approx \left(-\frac{Q^2}{2q}, q, \mathbf{0}_\perp\right). \end{aligned} \tag{B.14}$$

Using the fact that

$$P \cdot q = Pq - \frac{M^2Q^2}{4Pq} \approx Pq \qquad \text{with} \quad \frac{M^2Q^2}{4Pq} \ll 1, \tag{B.15}$$

we can express

$$\begin{aligned} s &= (P^\mu + q^\mu)^2 = 2P\cdot q + M^2 - Q^2 \approx 2Pq \\ x_B &= \frac{Q^2}{2P\cdot q} \approx \frac{Q^2}{2Pq} = \frac{Q^2}{s}. \end{aligned} \tag{B.16}$$

Therefore, in the regime where $s \gg Q^2$, we have $x_B \ll 1$, which is valid at high energies as the regime of our interest. In this regime, both s and $1/x_B$ become large with Q^2 fixed. Using this approximation, the scalar product of P and q reads

$$P \cdot q = \frac{Q^2}{2x_B} - M^2 x_B = \frac{Q^2}{2x_B}\left(1 - \frac{M^2}{Q^2}2x_B^2\right). \tag{B.17}$$

Thus, for $M^2/Q^2 \ll 1/x_B^2$ and $Q^2 \to 0$, this new dipole frame parameterization approximation is valid and can serve as an appropriate frame for both electroproduction ($Q^2 > 0$) and photoproduction ($Q^2 \to 0$). This can be seen by applying $Q^2 = 0$ to the momentum of the proton and photon in Eq. (B.14)

$$\begin{aligned} P^\mu_{Q^2=0} &= \left(P, \frac{M^2}{2P}, \mathbf{0}_\perp\right) \\ q^\mu_{Q^2=0} &= (0, q, \mathbf{0}_\perp) \\ s &= (P+q)^2 = M^2 + 2Pq \approx 2Pq \end{aligned} \tag{B.18}$$

which will result in $(P^\mu)^2 = M^2$ and $(q^\mu)^2 = 0$, while for $x_B \to 0$ we will have $s \gg M^2$. Therefore, in this thesis, we will discuss photoproduction in the dipole frame instead of the Breit frame.

To return from the dipole frame (DF) to the Breit frame (BF) for large enough Q, we can perform a boost. Using the prescription in Eq. (B.3) for the photon, we obtain

$$q^\mu_{\text{DF}} = \left(-\frac{Q^2}{2q}, q, \mathbf{0}_\perp\right) \xrightarrow{\text{boost}} q^\mu_{\text{BF}} = \left(-A_{\text{D}\to\text{B}}\frac{Q^2}{2q}, \frac{1}{A_{\text{D}\to\text{B}}}q, \mathbf{0}_\perp\right). \tag{B.19}$$

By comparing the photon momentum in the Breit frame given by Eq. (B.6) with the photon momentum in the dipole frame given by Eq. (B.14), we find the boost coefficient from the dipole frame to the Breit frame as

$$A_{\text{D}\to\text{B}} = \frac{\sqrt{2}q}{Q} \gg 1. \tag{B.20}$$

As a validation, we can use $A_{\text{D-B}}$ to find the corresponding expression for P^μ in the Breit frame after the boost from the dipole frame. This expression is given by

$$P^\mu_{\text{DF}} = \left(P, \frac{M^2}{2P}, \mathbf{0}_\perp\right) \xrightarrow{\text{boost}} P^\mu_{\text{BF}} = \left(A_{\text{D}\to\text{B}}P, \frac{1}{A_{\text{D}\to\text{B}}}\frac{M^2}{2P}, \mathbf{0}_\perp\right) \tag{B.21}$$

where we used $x_B \simeq Q^2/2Pq$ in Eq. (B.16). As a result, we find

$$P^\mu_{\text{BF}} = \left(\frac{Q}{x_B\sqrt{2}}, \frac{x_B M^2}{Q\sqrt{2}}, \mathbf{0}_\perp\right) \tag{B.22}$$

which is the expression for the proton momentum in the Breit frame given by Eq. (B.7).

B.3 The rest frame

Another useful frame for DIS, especially in a fixed target experiment, is the rest frame where the photon interacts with a proton at rest. In this frame, the proton's momentum is given by $P^\mu_{\text{RF}} = (M, 0, 0, 0) = \left(M/\sqrt{2}, M/\sqrt{2}, \mathbf{0}_\perp\right)$, where RF indicates the rest frame. By using the boost formula in Eq. (B.3), we can transform the rest frame of the proton to the Breit frame, which is only applicable for $Q^2 > 0$, as follows:

$$P^\mu_{\text{RF}} = \left(\frac{M}{\sqrt{2}}, \frac{M}{\sqrt{2}}, \mathbf{0}_\perp\right) \xrightarrow{\text{boost}} P^\mu_{\text{BF}} = \left(A_{\text{R}\to\text{B}}\frac{M}{\sqrt{2}}, \frac{1}{A_{\text{R}\to\text{B}}}\frac{M}{\sqrt{2}}, \mathbf{0}_\perp\right) \tag{B.23}$$

By comparing with the expression for the proton momentum in the Breit frame in Eq. (B.7), we find that $A_{\text{R}\to\text{B}} = Q/(x_B M)$, where $A_{\text{R}\to\text{B}} \gg 1$ if $Q^2 \gg M^2$.

We can also boost the rest frame to the dipole frame such that

$$P^\mu_{\text{RF}} = \left(\frac{M}{\sqrt{2}}, \frac{M}{\sqrt{2}}, \mathbf{0}_\perp\right) \xrightarrow{\text{boost}} P^\mu_{\text{DF}} = \left(A_{\text{R}\to\text{D}}\frac{M}{\sqrt{2}}, \frac{1}{A_{\text{R}\to\text{D}}}\frac{M}{\sqrt{2}}, \mathbf{0}_\perp\right). \tag{B.24}$$

By comparing this expression with the proton momentum in the dipole frame in Eq. (B.14), we find that $A_{\mathrm{R}\to\mathrm{D}} = \sqrt{2}P/M \gg 1$.

As a double check, if we move from the dipole frame to the Breit frame, we will have

$$\text{Dipole frame} \xrightarrow{A_{\mathrm{D}\to\mathrm{R}} = \frac{M}{\sqrt{2}P}} \text{Rest frame} \xrightarrow{A_{\mathrm{R}\to\mathrm{B}} = \frac{Q}{x_B M}} \text{Breit frame}$$

with

$$A_{\mathrm{D}\to\mathrm{B}} = A_{\mathrm{R}\to\mathrm{B}} A_{\mathrm{D}\to\mathrm{R}} = \frac{Q}{\sqrt{2}x_B P} = \frac{\sqrt{2}q}{Q}$$

which is the transformation coefficient we have found in Eq. (B.20). It is important to note that the boost $A_{\mathrm{D}\to\mathrm{B}}$ can be performed for $M = 0$, however, the boosts $A_{\mathrm{D}\to\mathrm{R}}$ and $A_{\mathrm{R}\to\mathrm{B}}$ cannot be performed for $M = 0$ as there is no rest frame for a massless particle. The transformations between frames are illustrated in Fig. B.2.

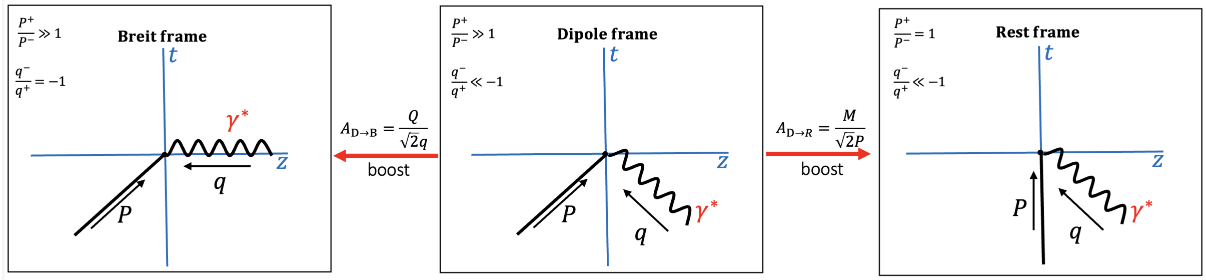

Figure B.2: The transformation relations between the dipole frame, the rest frame, and the (quark) Breit frame.

However, the rest frame also poses a problem when discussing photoproduction. To demonstrate this issue explicitly, we will examine the photon in the rest frame, which can be obtained by, for example, boosting the photon momentum from the dipole frame to the rest frame using $A_{\mathrm{D}\to\mathrm{R}}$. We will find that

$$q^\mu_{\mathrm{RF}} = \left(-\frac{x_B M}{\sqrt{2}}, \frac{Q^2}{x_B\sqrt{2}M}, \mathbf{0}_\perp\right) \tag{B.25}$$

Explicitly, this frame poses a problem when discussing photoproduction, as at $Q^2 = 0$ we will have

$$q^\mu_{\mathrm{RF},Q^2=0} = \left(-\frac{x_B M}{\sqrt{2}}, 0, \mathbf{0}_\perp\right) \tag{B.26}$$

which result in

$$\begin{gathered} q^- = 0 \leftrightarrow q^0 = q^3 \\ q^+ = \tfrac{q^0+q^3}{\sqrt{2}} = \sqrt{2}q^0 = -\tfrac{x_B M}{\sqrt{2}} \leftrightarrow q^0 < 0. \end{gathered} \tag{B.27}$$

To further compare the frames, we will look at how the following variables behave in each frame: P^+/P^- and q^-/q^+ which corresponds to the fraction of longitudinal momentum carried by the target nucleon and the fraction of longitudinal momentum carried by the struck quark in the virtual photon, respectively. As shown by the transformation formula in Eq. (B.3), under boost these variables will transform as

$$\frac{P^+}{P^-} \xrightarrow{\text{boost}} A^2 \frac{P^+}{P^-} \qquad \text{and} \qquad \frac{q^-}{q^+} \xrightarrow{\text{boost}} \frac{1}{A^2}\frac{q^-}{q^+}. \tag{B.28}$$

The values of these quantities, along with the light cone components for each frame, are presented in Table B.1.

	Breit frame	Dipole frame	Rest frame
P^μ	$\left(\frac{Q}{x_B\sqrt{2}}, \frac{x_B M^2}{Q\sqrt{2}}, \mathbf{0}_\perp\right)$	$\left(P, \frac{M^2}{2P}, \mathbf{0}_\perp\right)$	$\left(\frac{M}{\sqrt{2}}, \frac{M}{\sqrt{2}}, \mathbf{0}_\perp\right)$
q^μ	$\left(-\frac{Q}{\sqrt{2}}, \frac{Q}{\sqrt{2}}, \mathbf{0}_\perp\right)$	$\left(-\frac{Q^2}{2q}, q, \mathbf{0}_\perp\right)$	$\left(-\frac{x_B M}{\sqrt{2}}, \frac{Q^2}{x_B\sqrt{2}M}, \mathbf{0}_\perp\right)$
$\frac{P^+}{P^-}$	$\frac{Q^2}{x_B^2 M^2} \gg 1$	$\frac{2P^2}{M^2} \gg 1$	1
$\frac{q^-}{q^+}$	-1	$-\frac{2q^2}{Q^2} \ll -1$	$-\frac{Q^2}{2M^2} \ll -1$

Table B.1: List of momentum components, P^+/P^- and q^+/q^- values for Breit, dipole and rest frames, see also Fig. B.2 for a pictorial representation.

C

Feynman rules for Wilson lines

In Sect. 2.3.2, we discussed Wilson lines and the eikonal approximation. In order to calculate the contribution of the Wilson lines to the scattering process at high energies, it is necessary to employ the corresponding Feynman rules. We primarily employ the Feynman rules and notation outlined in [40].

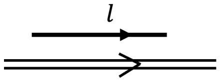	$\frac{i}{n \cdot l + i\epsilon}$	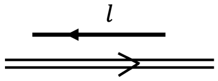	$-\frac{i}{n \cdot l + i\epsilon}$
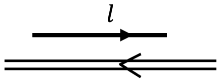	$-\frac{i}{n \cdot l + i\epsilon}$	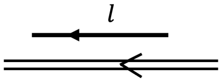	$\frac{i}{n \cdot l + i\epsilon}$
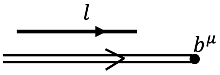	$\mathrm{e}^{-ib\cdot l}$	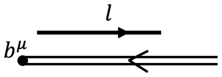	$\mathrm{e}^{ib\cdot l}$
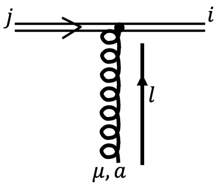	$-ign^\mu (t_a)_{ij}$	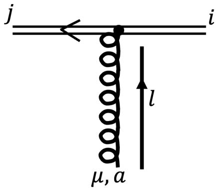	$ign^\mu (t_a)_{ij}$

Table C.1: Some relevant Feynman rules for Wilson lines. Here, n represents the vector defined in Appendix A, while the arrow on the Wilson line (represented by double lines) indicates the direction of the path.

D

Gauge invariance and Wilson lines

D.1 Wilson lines and a two-point function

In this section, our primary reference for the discussion of the Wilson line will be [40]. We will begin by demonstrating how the Wilson line preserves the gauge invariance of a two-point function. Consider a two-point correlation function $\Phi(y,x) = \bar{\psi}(y)\psi(x)$, where the wave functions are located at different positions. It is evident that $\Phi(y,x)$ is not gauge invariant under the transformation

$$\Phi(y,x) \rightarrow \bar{\psi}(y)U^{\dagger}(y)U(x)\psi(x). \tag{D.1}$$

Our objective is to identify an operator, denoted as $T_{[y,x]}$, that establishes a connection between the field $\psi(x)$ and another point in spacetime, $\psi(y)$. This operator will enable us to define a gauge-invariant two-point function

$$\bar{\psi}(y)T_{[y,x]}\psi(x) \rightarrow \bar{\psi}(y)U^{\dagger}(y)U(y)\left[T_{[y,x]}\psi(x)\right] = \bar{\psi}(y)T_{[y,x]}\psi(x). \tag{D.2}$$

Throughout the main discussion of this thesis, this operator will be encountered repeatedly.

Our primary focus is on identifying this type of operator within the non-Abelian case, specifically in QCD. We begin by considering the simpler scenario of the $U(1)$ Abelian gauge group, where

$$U(x) = e^{\pm ig\alpha(x)} \tag{D.3}$$

with $\alpha(x)$ is a scalar function. In this case, the gauge field will transform as

$$A_\mu(x) \to A_\mu(x) + \partial_\mu \alpha(x) \tag{D.4}$$

By comparing Eq. (D.2) and Eq. (D.4), we can deduce that in an Abelian theory, the required operator takes the form

$$T_{[y,x]} = e^{\pm ig \int_x^y dz^\mu A_\mu(z)}. \tag{D.5}$$

In order to generalize this operator, we must take into account that in a non-Abelian theory, the fields at different spacetime points, $A_\mu(z)$ and $A_\mu(z')$, do not commute. We need to revisit Eq. (D.2), where the gauge transporter must be in the form

$$\frac{d}{dt}T_{[y,x]} = \mathcal{A}_\gamma(t) T_{[y,x]} \quad \text{with} \quad \mathcal{A}_\mu(t) = \pm ig A_\mu[z(t)]\dot{z}_\mu(t). \tag{D.6}$$

Since the specific path along which the operator will "transport" the field $\psi(x)$ from point x to y is unknown, we introduce an arbitrary path denoted as γ. The assumption is made that γ can be parameterized as

$$z(0) = x, \qquad z(t) = y, \qquad dz_\mu = \dot{z}_\mu(t)dt; \qquad z \in \gamma.$$

Upon integrating Eq. (D.6), we obtain

$$T_{[y,x]} - T_{[x,x]} = T(t) - T(0) = \int_0^t ig \mathcal{A}_\gamma(t) T(t) dt. \tag{D.7}$$

Assuming that g is small, we can expand $T_{[y,x]}$ as

$$T_{[y,x]}(t) = T^{(0)} + T^{(1)} + T^{(2)} + ... + T^{(n)} + ... \tag{D.8}$$

In Eq. (D.8), the initial condition, represented by the first term $T(0) = T_{[x,x]} = T^{(0)}$, is independent of t_1. The second and third terms can be expressed in terms of $T(0)$

$$\begin{aligned} T^{(1)}(t) &= \int_0^t \mathcal{A}_\gamma(t_1) dt_1 T(0) \\ T^{(2)}(t) &= \int_0^t \mathcal{A}_\gamma(t_1) T(t_1) dt_1 = \int_0^t \mathcal{A}_\gamma(t_1) \int_0^{t_1} \mathcal{A}_\gamma(t_2) dt_1 dt_2 T(0) \end{aligned} \tag{D.9}$$

From this pattern, we can rewrite $T^{(2)}$ as [see e.g. Chapter 15 of [253]]

$$T^{(2)}(t) = \frac{1}{2}\left(\mathcal{P}\int_0^t \int_0^t \mathcal{A}_\gamma(t_1)\mathcal{A}_\gamma(t_2) dt_1 dt_2\right) T(0) \tag{D.10}$$

with $\mathcal{P}$ is a path ordering operator. By generalizing these to an n-order, we will get

$$T^{(n)}(t) = \frac{1}{n!}\mathcal{P}\int_0^t ... \int_0^t \left(\mathcal{A}_\gamma(t_1)...\mathcal{A}_\gamma(t_n) dt_1 dt_2 ... dt_{n-1} dt_n\right) T(0) \tag{D.11}$$

Hence, for the n-th order, the operator can be simplified into an exponential form

$$T(t) = \mathcal{P}e^{\int_0^t \mathcal{A}_\gamma(t')dt'} = \sum_{n=0} \frac{1}{n!}\mathcal{P}\int_0^t ... \int_0^t \left(\mathcal{A}_\gamma(t_1)...\mathcal{A}_\gamma(t_n)dt_1dt_2...dt_{n-1}dt_n\right)T(0) \quad \text{(D.12)}$$

for which we have set $T(0) = T_{[x,x]} = 1$. We have now identified an object that preserves the gauge invariance of a two-point function in QCD. This object is commonly referred to as a Wilson line or a gauge link and can be expressed in a general form

$$T_{[y,x]} = U_\gamma[y,x] \equiv \mathcal{P}\ \exp\left[\pm ig\int_x^y dz^\mu A_\mu(z)\right]_\gamma. \quad \text{(D.13)}$$

The ± sign in the exponential indicates the charge of the particles involved (quark or antiquark).

D.2 Properties of Wilson lines

1. Hermiticty

   Taking the Hermitian conjugate of a Wilson line will reverse its direction:

   $$\mathcal{U}_{[a,b]} = \mathcal{U}^\dagger_{[b,a]}. \quad \text{(D.14)}$$

2. Decomposability

   A Wilson line can be decomposed into multiple lines:

   $$\mathcal{U}_{[a,c]} = \mathcal{U}_{[a,b]}\mathcal{U}_{[b,c]}. \quad \text{(D.15)}$$

   This decomposition is not unique.

3. Unitarity

   The unitarity property is a consequence of the hermiticity and decomposability properties:

   $$\mathcal{U}^\dagger_{[a,b]}\mathcal{U}_{[a,b]} = \mathcal{U}_{[b,a]}\mathcal{U}_{[a,b]} = 1. \quad \text{(D.16)}$$

Lay summary

It is a well-known fact that any visible matter in our universe is composed of atoms, which consist of electrons orbiting around nuclei comprising protons and neutrons. It is now known that protons and neutrons, examples of hadrons, are not fundamental particles; instead, they are composite particles consisting of quarks and gluons, collectively called partons. At the subatomic level, hadrons are the dominant part, as electrons contribute very little to the overall mass of atoms, being roughly 1800 times lighter than protons. Hence, partons are the fundamental particles that contribute the most to the mass of the atom. This emphasizes the significance of studying partons within hadrons and understanding the strong force that governs their interactions, which can provide profound insights into the nature of matter shaping our observable universe.

To investigate the behavior of partons inside hadrons, particle accelerators are constructed, where fast-moving particles are collided, and detectors are used to detect the outgoing particles that are produced in the collision. By colliding high energetic hadrons with structureless particles, such as electrons and positrons, or other hadrons, researchers can uncover the dynamics of partons and observe their behavior inside hadrons, gaining insights into how they contribute to the properties of hadrons, such as spin and mass. However, the study of high-energy collisions, known as high-energy physics, is both theoretically and experimentally challenging due to many physics and technical aspects that must be considered.

According to the principle of energy and mass conservation, higher energy collisions result in the production of a greater number of particles. Consequently, the collision process appears to be like a catastrophic event, with numerous particles being generated, many of which have very short lifetimes. It becomes crucial to carefully identify the outgoing particles by characterizing their charge, spin, mass, and velocity. The strong force behavior mediated by gluons, which binds quarks inside hadrons, complicates the situation by preventing quarks and gluons from existing as free individual particles. This is called *confinement*, as the quarks and gluons are confined inside hadrons. Fortunately, in high-energy collisions, quarks exhibit *asymptotic freedom*, which dictates that the strong coupling decreases as the energy increases. This allows quarks to be treated as nearly free particles in part of the collision, facilitating a method of expanding in the small coupling ($\alpha_s \ll 1$) in such a way that the third, fourth, and higher power terms can be ignored—these are much smaller compared to the first (leading order, LO) and second terms (next-to-leading order, NLO). This method is called perturbative QCD (pQCD). This method offers significant advantages in simplifying the QCD calculations.

Without this property, we would have to rely only on experimental observations and lattice QCD computation to gain insights into the hadron substructure. Even though the lattice QCD method can be applied in regions of $\alpha_s \gtrsim 1$ where the pQCD method fails, it presents another challenge in terms of requiring extensive computational resources for the analysis of processes at accelerators and for non-static quantities, such as appearing in the description of a collision.

In the case where a proton moves at a very high velocity relative to a probe, the probe will "see" a greater number of partons within the proton. Consequently, the fraction of the proton momentum carried by each parton, denoted by x, becomes much smaller. As confirmed by collinear parton distribution functions (PDFs) studies, when x is moderately small gluons begin to dominate the composition of the proton. As we further decrease x to values below 0.01, known as the small x regime, the phenomenon of saturation, resulting from nonlinear QCD effects, becomes significant. In the large x regime, the proton's content can be described using the one dimensional collinear PDF, but this approach does not apply to the small-x region. Collinear PDF predicts an exponential growth of the partons towards smaller x, which eventually violates the unitarity principle of the cross-section. Therefore, in the small x regime, there should be a framework that controls the growth of the partons. An appropriate framework for this study is the Color Glass Condensate (CGC) description/approach. Within this framework, the high density of partons inside the hadron results in a saturation phenomenon which describes that in the small x regime, the probe is more likely to collide with the high-density gluons that make up the majority of the proton, rather than with a single quark. In this CGC description the transverse momentum and the spatial distribution of partons changes as x changes, requiring going beyond the one dimensional collinear PDFs.

The generalized transverse momentum dependent PDFs (GTMDs), which are the Fourier transform of the Wigner distribution known as the "mother distribution," are higher-dimensional PDFs that can accommodate the saturation phenomenon. Unlike the one-dimensional collinear PDFs that depend only on x, GTMDs can be six-dimensional and depend on a more general correlator that depends on more variables. Studying GTMDs helps us to understand high-energy phenomena and provides a more complete picture of the dynamics of partons within a hadron or a nucleus.

It has been proposed that the cross section of the diffractive dijet production in the high-energy Deep Inelastic Scattering (DIS) is directly proportional to the GTMD. In this high energy (small x) limit, where gluons dominate, the contribution of quarks can be neglected, allowing us to focus solely on the gluon GTMD. In this thesis project we first developed a gluon GTMD model based on the well-established MV (McLerran-Venugopalan) model and incorporated impact parameter dependence. One advantage of the model is that it introduces only two physically motivated free parameters. By fitting these parameters to data of diffractive dijet production at HERA-H1, we observed that the model adequately describes the data for the transverse momentum average of the jet ($K_\perp$) and transverse momentum transfer squared (t). The good agreement of the model with H1 data provides strong support for the GTMD framework utilized in this study. We hope that further validation of this framework will be possible with forthcoming data from experiments at the Large Hadron Collider (LHC) and the Electron-Ion Collider (EIC). These future experiments will allow us to gain more insights into the behavior of partons and the underlying dynamics of high-energy collisions, further refining our understanding of the GTMD and its role in describing diffractive processes.

However, the above model, which is independent of x, does not accurately capture the energy dependence (Q^2) of the data as it only probes the average x of the associated process. To overcome this limitation, an x-dependent model based on the GBW (Golec-Biernat and Wüsthoff) parameterization was introduced. The GBW model is known for its success in describing the cross section of the DIS process, including the diffractive case, at HERA, which motivated us to incorporate this parametrization into our model. By fitting the free parameters of the x-dependent model to the same diffractive dijet data from HERA-H1 in the previous study, we found that the improved model was able to enhance the description of the Q^2 dependence of the data while maintaining a good fit to other variables ($K_\perp$ and t). With the improved model, we provided predictions for the diffractive dijet process at the EIC, serving as a test of the model for future experiments.

Arguing that diffractive J/ψ and dijet production only differ in the final state, we expect that these two processes can be described by the same GTMD framework. The x-dependent model was then further extended to describe exclusive diffractive J/ψ production, with the same parameters employed for both processes. These parameters independently determine various aspects of the cross section: the proton profile width R_p determines the t slope, the parameter λ as the power of x controls the W slope, while $\bar{\chi}$ acts as an overall factor for the saturation scale, determining the cross-section amplitude. For diffractive J/ψ production, we utilized two well-known and simple vector meson wave functions: boosted Gaussian and Gaus-LC. In this study, it is important to note that the primary objective is not to develop a comprehensive model, but rather to investigate whether a generic small-x gluon GTMD model can accurately describe diffractive processes. This five dimensional GTMD description (we assume zero skewness) goes beyond the Generalized Parton Distribution (GPD) description that depends on fewer kinematic variables (x, skewness, and transverse momentum transfer).

Eventually, we found that the x-dependent model fails to accurately describe both processes using the same parameterization, leading to tension in the parameter fits. This raises the question of whether diffractive dijet and J/ψ production should indeed be described by the same GTMD framework. In principle, the tension could arise from multiple sources of uncertainty, such as the vector meson wave functions applied to J/ψ production, the proton profile, corrections (from nonzero skewness and odderon contributions), and even the data from H1 and ZEUS experiments. More specifically, the t slope of the two processes exhibits the same $d\sigma/dt \sim \exp[-bt]$ pattern, but the J/ψ data tends to show a steeper slope, which requires a smaller proton gluonic radius in our model. The discrepancy thus lies in the difference in the t-slope originating from the proton's profile rather than the final state (dijets versus J/ψ production). This suggests that the tension might stem from experimental factors, since the initial proton state should be the same or very similar for the different data sets and processes. Future experimental data will help resolve this issue.

Extending our model to the photonuclear production data at Ultra-Peripheral Collisions (UPC) of Pb nuclei in the LHC as measured by the ALICE collaboration, our study reveals that the A dependence of the saturation scale does not follow the expected form $A^{1/3}$ but instead behaves like $A^{0.27-0.3}$, even though the model does not exclude the former possibility. Also this aspect is dependent on the shape of the proton profile, although not just its width. These findings need further investigations and clarification through additional data at intermediate A values, for instance at RHIC.

Based on the optimized parameter fits obtained, we provided predictions for the corresponding processes expected to take place at the upcoming EIC, as well as UPCs at the LHC and RHIC. Even though the model is generic and not aimed at obtaining the best possible description of the data, it can still validate whether the GTMD formalism can be applied to diffractive processes, and simultaneously aim to provide insights into the sources of tension, specifically concerning the t dependence form. The availability of new data from experiments at the LHC, RHIC, and the future EIC will be important in resolving the tension observed in the t distribution between J/ψ and dijet production. Furthermore, these data will help to elucidate the dependence on the probed skewness in the process and determine the A dependence of the saturation scale for heavy nuclei. It is our hope that these forthcoming experiments will provide the necessary information to address these open questions and refine our understanding of the underlying dynamics.

Leken Samenvatting

Het is een bekend feit dat alle zichtbare materie in ons universum is samengesteld uit atomen, bestaande uit elektronen die rond kernen draaien. De kernen zijn opgebouwd uit protonen en neutronen. Het is bekend dat protonen en neutronen, voorbeelden van hadronen, geen fundamentele deeltjes zijn. In plaats daarvan zijn het samengestelde deeltjes die bestaan uit quarks en gluonen, ook wel gezamenlijk partonen genoemd. Op subatomair niveau zijn hadronen het dominante deel. Elektronen dragen namelijk heel weinig bij aan de totale massa van atomen, omdat ze ongeveer 1800 keer lichter zijn dan protonen. De partonen zijn de fundamentele deeltjes die het meest bijdragen aan de massa van het atoom. Dit benadrukt het belang van het bestuderen van partonen in hadronen en het begrijpen van de sterke kernkracht die hun interacties beschrijft, wat diepgaande inzichten kan verschaffen in de aard van materie die ons waarneembare universum vormgeeft.

Om het gedrag van partonen in hadronen te onderzoeken, worden deeltjesversnellers gebruikt, waar snel bewegende deeltjes botsen, en detectoren de uitgaande deeltjes die bij de botsing worden geproduceerd detecteren. Door hoogenergetische hadronen te laten botsen met structuurloze deeltjes, bijvoorbeeld elektronen en positronen, of andere hadronen, kunnen onderzoekers de dynamica van partonen blootleggen en hun gedrag in hadronen observeren. Dit geeft inzicht in hoe partonen bijdragen aan de eigenschappen van hadronen, zoals de spin en de massa. De studie van hoogenergetische botsingen, bekend als hoge-energiefysica, is echter zowel theoretisch als experimenteel uitdagend vanwege de vele natuurkundige en technische aspecten waarmee rekening moet worden gehouden.

Volgens het principe van energie- en massabehoud resulteren botsingen met hoge energie in de productie van een groot aantal deeltjes. Het botsingsproces lijkt op een catastrofale gebeurtenis, waarbij talloze deeltjes worden gegenereerd, waarvan er vele een zeer korte levensduur hebben. Het is cruciaal om de uitgaande deeltjes zorgvuldig te identificeren door hun lading, spin, massa en snelheid te karakteriseren. De sterke kernkracht, gemedieerd door gluonen, die quarks in hadronen bindt, compliceert de situatie door te voorkomen dat quarks en gluonen bestaan als vrije individuele deeltjes. Dit wordt *confinement* of opsluiting genoemd: de quarks en gluonen zitten opgesloten in hadronen. Gelukkig vertonen quarks bij hoogenergetische botsingen *asymptotische vrijheid*, wat betekent dat de sterke koppeling afneemt naarmate de energie toeneemt. Dit maakt het mogelijk om quarks te behandelen als bijna vrije deeltjes in een deel van de botsing, waardoor de methode om in de kleine koppeling

($\alpha_s \ll 1$) te expanderen wordt vergemakkelijkt doordat de derde, vierde en hogere machtstermen in deze storingsrekening kunnen worden genegeerd - deze zijn veel kleiner in vergelijking met de leidende orde (LO) en de naast-leidende orde (NLO). Deze methode wordt perturbatieve QCD (pQCD) genoemd. pQCD biedt aanzienlijke voordelen bij het vereenvoudigen van de QCD-berekeningen. Zonder deze eigenschap zouden we alleen moeten vertrouwen op experimentele waarnemingen en rooster QCD-berekeningen om inzicht te krijgen in de hadron-substructuur. Hoewel de rooster QCD-methode kan worden toegepast voor $\alpha_s \gtrsim 1$, i.e. waar de pQCD-methode faalt, vormt het een andere uitdaging. Namelijk, het vereist uitgebreide rekenmiddelen voor de analyse van processen bij versnellers en voor niet-statische grootheden, die voorkomen in de beschrijving van een botsing.

In het geval dat een proton met een zeer hoge snelheid beweegt ten opzichte van een ander deeltje, zal dit deeltje een groter aantal partons in het proton 'zien'. Bijgevolg wordt de fractie van het protonmomentum dat door elk parton wordt gedragen, aangeduid met x, veel kleiner. Zoals bevestigd door studies naar collineaire partonverdelingsfuncties (PDF's), wanneer x klein is, zullen gluonen de samenstelling van het proton domineren. Naarmate we x verder verlagen tot waarden onder 0.01, bekend als het kleine x-regime, wordt het fenomeen van verzadiging, als gevolg van niet-lineaire QCD-effecten, significant. In het grote x-regime kan de inhoud van het proton worden beschreven met behulp van de eendimensionale collineaire PDF, maar deze benadering is niet van toepassing op het gebied van kleine x. De collinear PDF voorspelt een exponentiële groei van de partons voor kleinere x, wat uiteindelijk in strijd is met het unitariteitsprincipe van de werkzame doorsnede. Daarom zou er in het regime van kleine x een model moeten zijn dat de groei van de partons beperkt. Een geschikt model hiervoor heet Color Glass Condensate (CGC). Binnen dit model resulteert de hoge dichtheid van partonen in de hadron in een verzadigingsfenomeen dat beschrijft dat in het kleine x-regime een verstrooiend deeltje meer kans heeft om in botsing te komen met de hoge dichtheid van gluonen die het grootste deel van het proton vormen, in plaats van met een enkele quark. In deze CGC-beschrijving verandert het transversale momentum en de ruimtelijke verdeling van partonen naarmate x verandert, waardoor meer nodig is dan de eendimensionale collineaire PDF's.

De gegeneraliseerde transversale impulsafhankelijke PDF's (GTMD's), die de Fouriertransformatie van de Wigner-verdeling zijn, bekend als de 'moederverdeling', zijn hoger-dimensionale PDF's die het verzadigingsfenomeen kunnen accommoderen. In tegenstelling tot de een-dimensionale collineaire PDF's die alleen afhankelijk zijn van x, kunnen GTMD's zes-dimensionaal zijn en afhankelijk van een meer algemene correlator, afhankelijk van meer variabelen. Het bestuderen van GTMD's helpt om hoogenergetische fenomenen te begrijpen en geeft een completer beeld van de dynamiek van partonen in een hadron of een kern.

Het is voorgesteld dat de werkzame doorsnede van de diffractieve dijetproductie in de hoogenergetische Deep Inelastic Scattering (DIS) recht evenredig is met de GTMD. In deze hoge-energielimiet (kleine x), waar gluonen domineren, kan de bijdrage van quarks worden verwaarloosd, waardoor we ons uitsluitend kunnen concentreren op de gluon GTMD. In dit proefschrift ontwikkelen we eerst een gluon GTMD-model op basis van het gevestigde MV (McLerran-Venugopalan) model en integreren we impactparameterafhankelijkheid. Een voordeel van het model is dat het slechts twee fysiek gemotiveerde vrije parameters introduceert. Door deze parameters te bepalen aan de hand van meetgegevens van diffractieve dijetproductie bij HERA-H1, nemen we waar dat het model de metingen voor het transversale momentumgemiddelde van de jet ($K_\perp$) en transversale momentumoverdracht in het kwadraat (t) adequaat beschrijft. De goede overeenkomst van het model met H1-gegevens biedt een sterke ondersteuning voor het GTMD-model dat in deze studie wordt gebruikt. We hopen dat verdere validatie van dit raamwerk mogelijk zal zijn met toekomstige metingen van experimenten bij de Large Hadron Collider (LHC) en de Electron-Ion Collider (EIC). Deze toekomstige experimenten zullen ons in staat stellen meer inzicht te krijgen in het gedrag van partonen en de onderliggende dynamica van hoogenergetische botsingen, waardoor ons begrip van de GTMD en de rol daarvan bij het beschrijven van diffractieve processen verder wordt verfijnd.

Het bovenstaande model, dat onafhankelijk is van x, geeft echter niet nauwkeurig de energieafhankelijkheid (Q^2) van de experimentele data weer, omdat het alleen de gemiddelde x van het bijbehorende proces onderzoekt. Om deze beperking te overwinnen, werd een x-afhankelijk model geïntroduceerd op basis van de GBW-parametrisering (Golec-Biernat en Wüsthoff). Het GBW-model staat bekend voor het succesvol beschrijven van de werkzame doorsnede van het DIS-proces, inclusief het diffractieve geval, bij HERA. Dit motiveert ons om deze parametrisatie in ons model op te nemen. Door de vrije parameters van het x-afhankelijke model te laten bepalen door dezelfde diffractieve dijet meetgegevens van HERA-H1 in de vorige studie, ontdekken we dat het verbeterde model in staat is om de beschrijving van de Q^2-afhankelijkheid van de gegevens te verbeteren en tegelijkertijd een goede fit met andere variabelen ($K_\perp$ en t) te behouden. Met het verbeterde model hebben we voorspellingen gedaan voor het diffractieve dijetproces bij de EIC, die dienen als een test van het model voor toekomstige experimenten.

Met het argument dat diffractieve J/ψ en dijetproductie alleen verschillen in de eindtoestand, verwachten we dat deze twee processen kunnen worden beschreven door hetzelfde GTMD-model. Het x-afhankelijke model is verder uitgebreid om exclusieve diffractieve J/ψ productie te beschrijven, waarbij voor beide processen dezelfde parameters zijn gebruikt. Deze parameters bepalen onafhankelijk verschillende aspecten van de werkzame doorsnede: de breedte van het protonprofiel R_p bepaalt de helling in t, de parameter λ als de macht van x regelt de helling in W, terwijl $\bar{\chi}$ fungeert als een algemene factor voor de verzadigingsschaal en de amplitude van de werkzame doorsnede bepaalt. Voor diffractieve J/ψ productie gebruikten we twee bekende en eenvoudige vectormesongolffuncties: “boosted Gaussian” en “Gaus-LC”. In deze studie is het belangrijk op te merken dat het primaire doel niet is om een alomvattend model te ontwikkelen, maar om te onderzoeken of een generiek klein-x gluon GTMD-model diffractieve processen nauwkeurig kan beschrijven. Deze vijf-dimensionale GTMD-beschrijving (we gaan uit van nul scheefheid) gaat verder dan de beschrijving van de Generalized Parton Distribution (GPD) die afhankelijk is van minder kinematische variabelen (x, scheefheid en transversale momentumoverdracht).

Uiteindelijk ontdekken we dat het x-afhankelijke model er niet in slaagt om beide processen nauwkeurig te beschrijven met dezelfde parametrisering, wat leidt tot afwijkingen in de parameter fits. Dit doet de vraag rijzen of diffractieve dijet en J/ψ productie inderdaad in hetzelfde GTMD-kader moeten worden beschreven. In principe zou de afwijking kunnen voortkomen uit meerdere bronnen van onzekerheid, bijvoorbeeld door de vectormesongolffuncties die worden toegepast op de productie van J/ψ, het protonprofiel, correcties (van niet-nul-scheefheid en odderonbijdragen) en zelfs de meetgegevens van H1- en ZEUS-experimenten. Meer specifiek vertoont de t-helling van de twee processen hetzelfde $d\sigma/dt \sim \exp[-bt]$-patroon, maar de J/ψ-gegevens vertonen veelal een steilere helling, wat een kleinere gluonische straal van het proton in het model vereist. De discrepantie ligt dus in het verschil in de t-helling die voortkomt uit het profiel van het proton in plaats van in de eindtoestand (dijets versus J/ψ productie). Dit suggereert dat de afwijking tussen experiment en model zou kunnen voortkomen uit experimentele factoren, aangezien de initiële protontoestand hetzelfde of zeer vergelijkbaar zou moeten zijn voor de verschillende datasets en processen. Toekomstige experimentele gegevens zullen helpen dit probleem op te lossen.

Als we ons model uitbreiden naar metingen van fotonucleaire productie bij Ultra-Perifere Botsingen (UPC) van Pb-kernen in de LHC zoals gemeten in het ALICE experiment, laat onze studie zien dat de A afhankelijkheid van de verzadigingsschaal niet de verwachte vorm, $A^{1/3}$, volgt, maar zich in plaats daarvan gedraagt als $A^{0.27-0.3}$, ook al sluit het model de eerste mogelijkheid niet uit. Ook dit aspect is afhankelijk van de vorm van het protonprofiel, maar niet alleen van de breedte. Deze bevindingen moeten verder worden onderzocht en verduidelijkt door middel van aanvullende metingen bij tussenliggende A-waarden, bijvoorbeeld bij RHIC.

Op basis van de verkregen geoptimaliseerde parameterfits hebben we voorspellingen gedaan voor de overeenkomstige processen die naar verwachting zullen plaatsvinden bij de toekomstige EIC, evenals voor UPC's bij de LHC en RHIC. Hoewel het model generiek is en niet gericht op het verkrijgen van de best mogelijke beschrijving van de gegevens, kan het nog steeds toetsen of het GTMD-formalisme kan worden toegepast op diffractieve processen, en tegelijkertijd inzicht geven in de reden van de afwijkingen, specifiek met betrekking tot de t afhankelijkheidsvorm. De beschikbaarheid van nieuwe metingen van experimenten in de LHC, RHIC en de toekomstige EIC zal belangrijk zijn voor het oplossen van de afwijking die wordt waargenomen in de t-verdeling tussen J/ψ en dijet-productie. Bovendien zullen deze metingen helpen om de afhankelijkheid van de gemeten scheefheid in het proces op te helderen en de A afhankelijkheid van de verzadigingsschaal voor zware kernen te bepalen. We hopen dat deze toekomstige experimenten de nodige informatie zullen opleveren om deze vragen te beantwoorden en ons begrip van de onderliggende dynamica te verfijnen.

Rangkuman

Merupakan fakta yang secara umum telah diketahui bahwa seluruh materi yang teramati di alam semesta ini tersusun atas atom-atom yang di dalamnya terdapat elektron dan inti. Elektron bergerak mengitari inti atom yang terdiri dari proton dan neutron. Saat ini telah diketahui pula bahwa proton dan neutron, yang merupakan keluarga hadron, bukanlah partikel elementer; sebaliknya, proton dan neutron adalah partikel komposit yang tersusun atas quark dan gluon, secara kolektif disebut sebagai parton. Pada tingkat subatomik, hadron adalah bagian paling dominan dari atom sedangkan elektron berkontribusi sangat sedikit terhadap keseluruhan massa atom, di mana massa elektron 1800 kali lebih ringan dari massa proton. Oleh karena itu, parton merupakan partikel elementer yang berkontribusi paling besar terhadap massa atom. Hal ini memberikan motivasi pentingnya mempelajari parton yang berada di dalam hadron serta memahami gaya kuat (*strong force*) yang mengatur interaksi antar parton. Kedua hal tersebut diharapkan dapat memberi kita informasi mendalam tentang sifat-sifat materi yang membentuk alam semesta ini.

Untuk menyelidiki perilaku parton di dalam hadron, dibangunlah akselerator-akselerator partikel. Di akselerator, partikel-partikel dipercepat hingga memiliki kecepatan tinggi kemudian saling ditabrakkan/dihamburkan. Selanjutnya, digunakan detektor untuk mendeteksi partikel-partikel yang dihasilkan oleh proses hamburan tersebut. Dengan menabrakkan hadron berenergi tinggi dengan partikel elementer lain, seperti elektron dan positron, atau dengan hadron lainnya, para fisikawan dapat mengungkap dinamika parton dan mengamati perilaku parton di dalam hadron. Hal ini bertujuan untuk mendapatkan informasi tentang bagaimana kontribusi parton pada karakter fisis hadron seperti spin dan massa. Namun, studi tentang hamburan partikel energi tinggi, yang dikenal sebagai fisika energi tinggi (*high energy physics*), cukup menantang baik secara teoretis maupun eksperimental karena melibatkan banyak aspek fisika dan teknis yang harus diperhitungkan.

Menurut prinsip kelestarian (*conservation*) energi dan massa, semakin tinggi energi partikel dalam suatu proses hamburan, jumlah partikel yang terproduksi juga akan semakin besar. Akibatnya, proses hamburan partikel energi tinggi akan tampak sebagai peristiwa yang sangat tidak teratur karena banyaknya partikel yang terproduksi. Terlebih lagi, banyak di antara partikel yang dihasilkan tersebut memiliki waktu hidup yang singkat. Oleh karena itu, diperlukan kecermatan yang tinggi untuk mengidentifikasi partikel yang dihasilkan dengan melakukan karakterisasi partikel berdasarkan muatan, spin, massa, dan kecepatannya. Perilaku gaya kuat yang dimediasi oleh gluon yang mengikat quark di dalam hadron membuat proses identifikasi partikel menjadi lebih sulit. Hal ini terjadi karena perilaku gaya kuat membuat quark dan gluon tidak akan muncul sebagai partikel tunggal bebas. Fenomena ini disebut sebagai kungkungan (*confinement*), karena quark dan gluon selalu terkungkung di dalam hadron. Untungnya, dalam hamburan partikel energi tinggi, quark juga mengikuti perilaku kebebasan asimtotik (*asymptotic freedom*) di mana kopling interaksi kuat akan berkurang seiring dengan meningkatnya energi hamburan. Hal ini menjadikan quark dapat diperlakukan sebagai partikel bebas pada sebagian proses hamburan dan memungkinkan untuk diterapkannya metode ekspansi kopling karena kecilnya kopling interaksi kuat pada energi tinggi tersebut ($\alpha_s \ll 1$) sedemikian rupa sehingga suku berpangkat tiga, empat, dan yang lebih tinggi dapat diabaikan. Hal ini dapat dilakukan karena pangkat tinggi untuk suatu nilai kecil bernilai jauh lebih kecil dibandingkan dengan suku pertama (*leading order*, LO) dan suku kedua (*next-to-leading order*, NLO). Metode ini disebut *perturbative* QCD (pQCD). Penerapan metode ini akan menyederhanakan perhitungan QCD secara signifikan. Jika fenomena kebebasan asimtotik ini tidak ada pada QCD, maka dalam QCD, kita hanya akan bergantung pada pengamatan eksperimental dan perhitungan kisi QCD (*lattice* QCD) untuk melakukan analisa substruktur hadron. Akan tetapi, meskipun metode kisi QCD dapat diterapkan untuk nilai $\alpha_s \gtrsim 1$ di mana metode pQCD tidak dapat diterapkan, metode ini memiliki tantangan lain berupa diperlukannya sumber daya komputasi yang sangat besar untuk menyelidiki proses-proses yang terjadi pada akselerator dan menganalisa besaran-besaran non-statis, seperti yang digunakan dalam mendeskripsikan proses hamburan.

Ketika proton bergerak dengan kecepatan yang sangat tinggi relatif terhadap partikel penghambur (*probe*), maka partikel penghambur tersebut akan "melihat" bahwa di dalam proton terdapat banyak sekali parton. Akibatnya, fraksi momentum proton yang dibawa oleh masing-masing parton, dilambangkan dengan x, menjadi sangat kecil. Hal ini telah dikonfirmasi oleh studi fungsi distribusi parton kolinier (*collinear parton distribution functions/collinear PDF*) yang menunjukkan bahwa pada daerah x cukup kecil, gluon akan mendominasi komposisi proton. Ketika nilai x semakin diturunkan ke nilai di bawah 0.01, yang dikenal sebagai daerah x kecil (*small-x regime*), fenomena saturasi (*saturation*) yang dihasilkan dari efek QCD nonlinier menjadi signifikan. Dalam daerah x besar, distribusi parton penyusun proton dapat dijelaskan menggunakan PDF kolinier satu dimensi. Namun, pendekatan ini tidak dapat digunakan untuk daerah x kecil. Hal ini karena PDF kolinier memprediksi bahwa jumlah parton meningkat secara eksponensial ketika x bergerak menuju nilai yang lebih kecil yang akhirnya melanggar prinsip unitaritas tampang lintang (*cross section*). Oleh karena itu, pada daerah x kecil, harus ada suatu kerangka (*framework*) yang dapat mengontrol pertumbuhan parton. Kerangka yang tepat untuk menganalisa parton di daerah ini adalah deskripsi/pendekatan *Color Glass Condensate* (CGC). Dalam kerangka ini, densitas parton yang tinggi di dalam hadron menghasilkan fenomena saturasi. Fenomena ini menggambarkan bahwa pada daerah x kecil, partikel penghambur lebih mungkin bertabrakan dengan gluon daripada dengan quark tunggal, karena gluon memiliki densitas tinggi yang menjadi partikel mayoritas penyusun proton. Dalam deskripsi CGC ini, momentum transversal dan distribusi spasial parton berubah ketika x berubah, sehingga diperlukan fungsi distribusi lain dengan dimensi lebih tinggi dari PDF kolinier satu dimensi.

PDF yang bergantung pada momentum transversal diperumum (*generalized transverse momentum dependent PDFs* /GTMDs), yang merupakan transformasi Fourier dari fungsi distribusi Wigner yang dikenal sebagai *mother distribution*, adalah PDF berdimensi tinggi yang dapat mengakomodasi fenomena saturasi. Berbeda dengan PDF kolinier satu dimensi yang hanya bergantung pada x, GTMD dapat memiliki enam dimensi dan bergantung pada korelator yang lebih umum yang bergantung pada lebih banyak variabel. Mempelajari GTMD membantu kita memahami fenomena hamburan partikel energi tinggi dan memberikan gambaran yang lebih lengkap tentang dinamika parton dalam hadron atau inti atom.

Telah diusulkan bahwa tampang lintang produksi dijet difraktif (*diffractive dijet production*) pada proses hamburan dalam tidak elastik (*Deep Inelastic Scattering*/DIS) energi tinggi akan berbanding lurus dengan GTMD. Dalam hamburan partikel energi tinggi ini (x kecil), di mana partikel penyusun hadron didominasi oleh gluon, kontribusi quark dapat diabaikan, sehingga memungkinkan kita untuk fokus hanya pada GTMD gluon. Dalam penelitian ini untuk pertama kali dikembangkan model GTMD gluon berdasarkan model MV (McLerran-Venugopalan) yang telah mapan dan memasukkan kebergantungan pada *impact parameter*. Salah satu keunggulan dari model ini adalah hanya diperkenalkan dua parameter bebas yang masing-masing memiliki motivasi fisis. Dengan mencocokkan (*fit*) kedua parameter tersebut dengan data produksi dijet difraktif di HERA-H1, diketahui bahwa model tersebut cukup mampu menjelaskan data momentum transversal jet rata-rata ($K_\perp$) dan momentum transversal yang tertransfer kuadrat (t). Kemampuan model tersebut menjelaskan data dari H1 memberikan dukungan kuat untuk menggunakan kerangka GTMD untuk menjelaskan proses-proses difraktif yang didiskusikan dalam penelitian ini. Diharapkan bahwa validasi lebih lanjut dari kerangka GTMD ini akan dapat dilakukan dengan tersedianya data baru dari eksperimen di *Large Hadron Collider* (LHC) dan *Electron-Ion Collider* (EIC). Eksperimen yang diharapkan akan dilakukan di masa mendatang ini memungkinkan kita untuk memahami lebih dalam tentang perilaku parton dan dinamika yang mendasari hamburan partikel energi tinggi, yang selanjutnya dapat menyempurnakan pemahaman kita tentang GTMD dan perannya dalam menjelaskan proses-proses difraktif.

Namun, model yang tidak bergantung pada x di atas tidak secara akurat menjelaskan data kebergantungan pada energi (Q^2) karena model ini hanya mempertimbangkan nilai x rata-rata dari proses terkait. Untuk mengatasi keterbatasan ini, diperkenalkan model baru yang bergantung pada x mengikuti parameterisasi GBW (Golec-Biernat dan Wüsthoff). Model GBW dikenal atas keberhasilannya menjelaskan tampang lintang proses-proses DIS, termasuk proses-proses difraktif di HERA, yang menjadikan motivasi diterapkannya parameterisasi GBW ke dalam model ini. Dengan mencocokkan parameter-parameter bebas dari model baru yang bergantung pada x ini pada data dijet difraktif yang sama dari HERA-H1 yang digunakan dalam analisa sebelumnya, diketahui bahwa model baru ini mampu memberikan deskripsi data kebergantungan Q^2 dengan lebih baik dengan tetap mempertahankan kualitas deskripsi variabel lain ($K_\perp$ dan t).

Dengan model yang diperbarui ini, diberikan prediksi untuk proses dijet difraktif di EIC untuk menguji model ini pada eksperimen-eksperimen berikutnya.

Dengan menggunakan argumen bahwa produksi J/ψ dan produksi dijet difraktif hanya berbeda dalam *final state*, diharapkan bahwa kedua proses ini dapat dijelaskan oleh kerangka GTMD yang sama. Model GTMD yang bergantung pada x kemudian diperluas lebih lanjut untuk menjelaskan produksi J/ψ difraktif eksklusif, dengan menggunakan nilai parameter yang sama untuk kedua proses. Parameter-parameter ini secara independen menentukan berbagai aspek dari tampang lintang: lebar profil proton R_p menentukan kemiringan t, parameter λ sebagai pangkat x mengontrol kemiringan W, sementara $\bar{\chi}$ yang bertindak sebagai faktor untuk mengatur skala saturasi (*saturation scale*) akan menentukan amplitudo tampang lintang. Untuk produksi J/ψ difraktif, digunakan dua fungsi gelombang meson vektor (*vector meson*) yang telah banyak dikenal dan cukup sederhana: boosted Gaussian dan Gaus-LC. Penting untuk dicatat bahwa tujuan utama penelitian ini bukan untuk mengembangkan model yang mampu menjelaskan data secara komprehensif, melainkan lebih menekankan untuk menyelidiki apakah model GTMD gluon x kecil generik dapat secara akurat menggambarkan proses-proses difraksi. Deskripsi GTMD lima dimensi ini (diasumsikan *skewness* bernilai nol) melampaui deskripsi *Generalized Parton Distribution* (GPD) yang bergantung pada lebih sedikit variabel kinematik (x, *skewness*, dan momentum transversal yang tertransfer).

Pada akhirnya, diketahui bahwa model yang bergantung pada x gagal menggambarkan kedua proses tersebut secara akurat menggunakan parameterisasi yang sama, yang menyebabkan ketidaksamaan (*tension*) pada hasil pencocokan parameter untuk kedua proses. Hal ini menimbulkan pertanyaan apakah proses produksi dijet difraktif dan J/ψ memang harus dijelaskan oleh kerangka GTMD yang sama. Pada prinsipnya, ketidaksamaan ini dapat muncul dari berbagai sumber ketidakpastian, seperti fungsi gelombang meson vektor yang diterapkan pada produksi J/ψ, lebar profil proton, koreksi (*skewness* yang tidak nol dan kontribusi odderon), dan bahkan bisa pula data dari data eksperimen H1 dan ZEUS. Lebih khusus lagi, kemiringan t dari kedua proses menunjukkan pola $d\sigma/dt \sim \exp[-bt]$ yang sama, tetapi data J/ψ cenderung menunjukkan kemiringan yang lebih curam yang membutuhkan jari-jari gluonik proton yang lebih kecil dalam model tersebut. Dengan demikian, ketidaksesuaian tersebut terletak pada perbedaan kemiringan t yang berasal dari profil proton dan bukan pada *final state* (dijet versus produksi J/ψ). Hal ini menunjukkan bahwa ketidaksamaan ini bisa jadi berasal dari faktor eksperimental karena keadaan proton awal (*initial proton state*) harus sama atau sangat mirip untuk semua data dan proses-proses yang berbeda. Diharapkan data eksperimen yang lebih banyak di masa mendatang akan membantu menyelesaikan masalah ini.

Dengan memperluas model di atas untuk menjelaskan data produksi fotonuklir pada proses *Ultra-Peripheral Collisions* (UPC) inti Pb pada hasil pengukuran kolaborasi ALICE di LHC, penelitian ini mengungkapkan bahwa kebergantungan skala saturasi pada nomor massa atom A tidak mengikuti pola yang umumnya diharapkan $A^{1/3}$, tetapi lebih mendekati $A^{0.27-0.3}$, meskipun model ini tidak menutup kemungkinan pola $A^{1/3}$ tersebut tetap berlaku di daerah tertentu. Aspek kebergantungan skala saturasi pada A

ini juga dipengaruhi oleh profil proton yang tentu bukan sekedar karena lebar profilnya saja. Temuan ini memerlukan penyelidikan dan klarifikasi lebih lanjut melalui data tambahan untuk inti-inti dengan nilai A menengah, yang misalnya dapat dilakukan di RHIC.

Diberikan prediksi untuk beberapa proses terkait menggunakan hasil pencocokan yang paling optimal antara parameter-parameter model dengan data pada tiap proses. Diharapkan prediksi-prediksi tersebut dapat diuji di akselerator EIC yang sedang dalam proses pembangunan. Diberikan pula prediksi untuk proses UPC yang eksperimennya dapat dilakukan di LHC dan RHIC. Meskipun model ini bersifat generik dan tidak dibangun untuk tujuan utama mendapatkan deskripsi data sebaik mungkin, model ini masih dapat memvalidasi apakah formalisme GTMD dapat diterapkan pada proses difraktif dan secara bersamaan juga dapat untuk memberikan informasi lebih lanjut tentang sumber ketidaksamaan pada parameter yang optimal antara kedua proses, khususnya untuk data tampang lintang sebagai fungsi t. Ketersediaan data tambahan yang dapat diperoleh dari eksperimen di LHC, RHIC, dan EIC di masa depan akan menjadi hal penting untuk dapat mengurai sumber perbedaan yang teramati untuk data distribusi t antara J/ψ dan produksi dijet. Data tersebut juga akan dapat membantu menjelaskan kebergantungan tampang lintang pada parameter *skewness* untuk proses-proses yang telah diteliti dan menentukan kebergantungan skala saturasi pada A untuk inti berat. Diharapkan bahwa eksperimen yang akan dilakukan mendatang ini akan memberikan informasi yang diperlukan untuk menjawab pertanyaan terbuka ini dan meningkatkan pemahaman kita tentang dinamika yang mendasarinya.

Acknowledgments

During my PhD journey, I received a lot of help from people around me and I want to express my gratitude to them.

Let me start by thanking my supervisor, Daniël Boer, for dedicating so much time to guide me. You have assisted me with everything, even before I arrived in Groningen, not only in academic matters but also in helping me adapt to a new culture, language preparation, finding a home, and family matters. As the director of the Van Swinderen Institute (VSI), you are still able to spend time guiding me and addressing my naive questions, even during holidays. TMD is a completely new topic for me, and I had to start from scratch, but you patiently supervised me. Your deep understanding of physics, a structured way of thinking, intuitive explanations, and your approach to supervising students inspire me as I pursue a career in academia. Also, Piet Mulders, you are a very friendly and smart person. Both of you are working together to help me realize my dream of conducting research as a PhD student.

I would also like to express my gratitude to the assessment committee for their time and effort in reading this manuscript and providing valuable feedback to improve my thesis. Additionally, I want to thank the opponents and the defense committee for dedicating their time at the end of the year to make the defense possible.

VSI is not only my office but also a place where I met many inspiring fellow PhD students. We have had so much conversations, spending two weeks in Brazil together, attended seminars, participated in the DRSTP schools, and engaged in many more fun activities. You all have made VSI something beyond Physics. Also, thanks to the VSI office staffs Anneline and Iris, for the assistance with administrative matters.

Thank you very much to Alexander for assisting me with the Dutch part of this thesis. A special thanks to Mas Ali and Fika for being my paranymphs.

Groningen would not feel like home for me and my family without the presence of my Indonesian family in Groningen: deGromiest, PPIG, and all the fellows who will always be a part of my friend list. We have shared so many unforgettable moments, and I will not be able to find other friends who feel like family in quite the same way as you do. Let me mention them one by one: Mas Fajar-Mbak Monik, Mas Ali-Mbak Liany, Mas Joko-Mbak Uci, Mas Latif-Mbak Septi, Mas Azka-Mbak Aidina, Mas Romi-Mbak Arlina, Mbak Nuril, Mas Ega-Mbak Irma, Mas Ivan-Mbak Dita, Mas Khairul-Mbak Retno, Mas Amak-Mbak Putri, Pak Asmoro-Bu Rini, Mas Agung-Mbak Inna, Mas Surya-Mbak Yassaroh, Mas Zaki-Mbak Nadia, Mas Trisno-Mbak Nisa, Mas Azzam-Mbak Gina, Mas

Lana-Mbak Arum, Mbak Zamrotul Izzah, Mbak Fithria Ayu, Mas Naufal-Mbak Moza, Mas Rifqi-Mbak Indri, Mas Angga-Mbak Diah, Mas Akbar-Mbak Andis, Mas Fiki-Mbak Titis, Mas Habibie-Mbak Ma'wa, Mbak Diani, Mas Zainal-Mbak Ayu, Mas Rico-Mbak Sudewi, Mas Deni, and all of my friends who could not be mentioned here, but let me do it in my *du'a*.

To the members of Rumah Tahfidz Kajuit, you are not only my family but also an inseparable part of my life. I have learned so much about life during my 4.5 years with all of you. I hope we have the chance to gather together again someday. I would love to mention each of you individually here, but I apologize if I do not do it properly. Bang Salim-Mbak Atika, Bu Roos, Mas Ristiono-Mbak Afifah, dokter Firas-dokter Sovia, Mas Ardian-Mbak Suvia, Mas Yudi-Mbak Sofa, Pak Yopi-Bu Dewi, Kak Lely-Bang Mirza, Mas Ariadi-Mbak Fitri, Mas Budi-Mbak Nony, Mas Feri-Mbak Inda, Jabar-Fathiya, Ghozi, Arnald, and Ari.

When talking about Indonesian food, I will not forget to mention the Diaspora Indonesia di Groningen and KKKB: Bude Nunung, Bu Elvira, Uwak Asiyah, Mbak Noorna, Bu Aminah, Bu Yayu, Mbak Sindu, and Mbak Amalia. I also learned new things about the Netherlands, the other side of Dutch culture, and how to behave appropriately in Groningen from you.

The people who motivate me the most to return to Indonesia soon are my mother, Giyarti, and my father, Suyadi. The fact that you never ask me about the progress of my PhD does not mean that you ignore me, but rather, it reflects your trust in my efforts to finish this, just as you never inquire about my grades in school. I would also like to express my gratitude for the support from my sisters family Mbak Tiwik-Mas Kardiono and Mbak Nana-Mas Yunus. A warm atmosphere always surrounds me when we gather with my father- and mother-in-law, Pak Sukamto and Bu Sumirah. I am also grateful for the support from Mbak Leny-Mas Nung, Mbak Nita, Mas Nanda, Mbak Andi-Mas Hasan, and Mbak Ratna-Mas Reza.

I am very grateful to have a supportive wife, Jean and cheerful FBI sons who always investigate what "kerja" is like, (Fatih), **F**aza, **B**irru, and **I**lyas. You all make my life more colorful. In the beginning, I felt that it would be hard to balance life between working, research, and family. However, I came to realize in the end that living is not only about working; there are many other sides of the world that wait to be explored together. On many occasions, you all suffered more than I did, as I had to spend more time outside of home, leaving only a little time for all of you.

Thanks to my second home, Department of Physics, Universitas Gadjah Mada, for providing any support I needed during my study. Special thanks to colleagues who continuously bombarded me with questions about when I would finish my PhD and the defense date which always motivated me to wake up and strive to complete my PhD. Thanks also to LPDP for providing support for my entire PhD study.

Finally, thanks to Allah *subhanahu wa ta'ala* who created the universe and allowed me to explore the beauty of Your creation through Physics. I can feel how powerful You are and how small I am. Physics strengthens my faith.

References

[1] M. Gell-Mann, *A Schematic Model of Baryons and Mesons*, Phys. Lett. **8** (1964), 214-215 [*Cited on p. 1*]

[2] G. Zweig, *An SU(3) model for strong interaction symmetry and its breaking. Version 1*, CERN-TH-401. [*Cited on p. 1*]

[3] R. P. Feynman, *The behavior of hadron collisions at extreme energies*, Conf. Proc. C **690905** (1969), 237-258 [*Cited on p. 1*]

[4] H. Fritzsch, M. Gell-Mann and H. Leutwyler, *Advantages of the Color Octet Gluon Picture*, Phys. Lett. B **47** (1973), 365-368 [*Cited on p. 1*]

[5] R. L. Workman *et al.* [Particle Data Group], *Review of Particle Physics*, PTEP **2022** (2022), 083C01 [*Cited on p. 2*]

[6] F. Abe *et al.* [CDF], *Observation of top quark production in $\bar{p}p$ collisions*, Phys. Rev. Lett. **74** (1995), 2626-2631, [arXiv:hep-ex/9503002 [hep-ex]]. [*Cited on p. 2*]

[7] S. Abachi *et al.* [D0], *Observation of the top quark*, Phys. Rev. Lett. **74** (1995), 2632-2637, [arXiv:hep-ex/9503003 [hep-ex]]. [*Cited on p. 2*]

[8] E. D. Bloom, D. H. Coward, H. C. DeStaebler, J. Drees, G. Miller, L. W. Mo, R. E. Taylor, M. Breidenbach, J. I. Friedman and G. C. Hartmann, *et al. High-Energy Inelastic ep Scattering at 6-Degrees and 10-Degrees*, Phys. Rev. Lett. **23** (1969), 930-934 [*Cited on p. 2*]

[9] M. Breidenbach, J. I. Friedman, H. W. Kendall, E. D. Bloom, D. H. Coward, H. C. DeStaebler, J. Drees, L. W. Mo and R. E. Taylor, *Observed behavior of highly inelastic electron-proton scattering*, Phys. Rev. Lett. **23** (1969), 935-939 [*Cited on p. 2*]

[10] R. Brandelik *et al.* [TASSO], *Evidence for Planar Events in e^+e^- Annihilation at High-Energies*, Phys. Lett. B **86** (1979), 243-249 [*Cited on p. 2*]

[11] D. P. Barber, U. Becker, H. Benda, A. Boehm, J. G. Branson, J. Bron, D. Buikman, J. Burger, C. C. Chang and H. S. Chen, *et al. Discovery of Three Jet Events and a Test of Quantum Chromodynamics at PETRA Energies*, Phys. Rev. Lett. **43** (1979), 830 [*Cited on p. 2*]

[12] C. Berger *et al.* [PLUTO], *Evidence for Gluon Bremsstrahlung in e^+e^- Annihilations at High-Energies*, Phys. Lett. B **86** (1979), 418-425 [*Cited on p. 2*]

[13] W. Bartel *et al.* [JADE], *Observation of Planar Three Jet Events in* e^+e^- *Annihilation and Evidence for Gluon Bremsstrahlung*, Phys. Lett. B **91** (1980), 142-147 [*Cited on p. 2*]

[14] G. Aad *et al.* [ATLAS], *Observation of a new particle in the search for the Standard Model Higgs boson with the ATLAS detector at the LHC*, Phys. Lett. B **716** (2012), 1-29, [arXiv:1207.7214 [hep-ex]]. [*Cited on p. 2*]

[15] S. Chatrchyan *et al.* [CMS], *Observation of a New Boson at a Mass of 125 GeV with the CMS Experiment at the LHC*, Phys. Lett. B **716** (2012), 30-61, [arXiv:1207.7235 [hep-ex]]. [*Cited on p. 2*]

[16] A. Accardi, J. L. Albacete, M. Anselmino, N. Armesto, E. C. Aschenauer, A. Bacchetta, D. Boer, W. K. Brooks, T. Burton and N. B. Chang, *et al. Electron Ion Collider: The Next QCD Frontier: Understanding the glue that binds us all*, Eur. Phys. J. A **52** (2016) no.9, 268, [arXiv:1212.1701 [nucl-ex]]. [*Cited on pp. 2 and 76*]

[17] R. Abdul Khalek, A. Accardi, J. Adam, D. Adamiak, W. Akers, M. Albaladejo, A. Al-bataineh, M. G. Alexeev, F. Ameli and P. Antonioli, *et al. Science Requirements and Detector Concepts for the Electron-Ion Collider: EIC Yellow Report*, Nucl. Phys. A **1026** (2022), 122447, [arXiv:2103.05419 [physics.ins-det]]. [*Cited on p. 2*]

[18] K. G. Wilson, *Confinement of Quarks*, Phys. Rev. D **10** (1974), 2445-2459 [*Cited on p. 2*]

[19] D. J. Gross and F. Wilczek, *Ultraviolet Behavior of Nonabelian Gauge Theories*, Phys. Rev. Lett. **30** (1973), 1343-1346 [*Cited on pp. 2 and 8*]

[20] H. D. Politzer, *Reliable Perturbative Results for Strong Interactions?*, Phys. Rev. Lett. **30** (1973), 1346-1349 [*Cited on pp. 2, 7, and 8*]

[21] R. P. Feynman, *Very high-energy collisions of hadrons*, Phys. Rev. Lett. **23** (1969), 1415-1417 [*Cited on pp. 3 and 10*]

[22] E. P. Wigner, *On the quantum correction for thermodynamic equilibrium*, Phys. Rev. **40** (1932), 749-760 [*Cited on p. 3*]

[23] Y. Hatta, B. W. Xiao and F. Yuan, *Probing the Small-*x *Gluon Tomography in Correlated Hard Diffractive Dijet Production in Deep Inelastic Scattering*, Phys. Rev. Lett. **116** (2016) no.20, 202301, [arXiv:1601.01585 [hep-ph]]. [*Cited on pp. 3, 42, 45, 46, 47, 54, and 79*]

[24] L. McLerran, *A Brief Introduction to the Color Glass Condensate and the Glasma*, 38th International Symposium on Multiparticle Dynamics (ISMD 2008, 3-18), [arXiv:0812.4989 [hep-ph]]. [*Cited on p. 4*]

[25] F. Gelis, E. Iancu, J. Jalilian-Marian and R. Venugopalan, *The Color Glass Condensate*, Ann. Rev. Nucl. Part. Sci. **60** (2010), 463-489, [arXiv:1002.0333 [hep-ph]]. [*Cited on pp. 4, 23, 24, and 55*]

[26] K. J. Golec-Biernat and M. Wüsthoff, *Saturation effects in deep inelastic scattering at low* Q^2 *and its implications on diffraction*, Phys. Rev. D **59** (1998), 014017, [arXiv:hep-ph/9807513 [hep-ph]]. [*Cited on pp. 4, 29, 30, 31, 70, and 95*]

[27] K. J. Golec-Biernat and M. Wüsthoff, *Saturation in diffractive deep inelastic scattering*, Phys. Rev. D **60** (1999), 114023, [arXiv:hep-ph/9903358 [hep-ph]]. [*Cited on pp. 4, 29, 70, and 95*]

[28] M. Gell-Mann, *Symmetries of baryons and mesons*, Phys. Rev. **125** (1962), 1067-1084 [*Cited on p. 6*]

[29] D. J. Gross and F. Wilczek, *Asymptotically Free Gauge Theories 1*, Phys. Rev. D **8** (1973), 3633-3652 [*Cited on p. 7*]

[30] D. J. Gross and F. Wilczek, *Asymptotically Free Gauge Theories 2*, Phys. Rev. D **9** (1974), 980-993. [*Cited on p. 7*]

[31] K. G. Wilson, *The Renormalization Group and Strong Interactions*, Phys. Rev. D **3** (1971), 1818 [*Cited on p. 7*]

[32] T. van Ritbergen, J. A. M. Vermaseren and S. A. Larin, *The Four loop beta function in quantum chromodynamics*, Phys. Lett. B **400** (1997), 379-384, [arXiv:hep-ph/9701390 [hep-ph]]. [*Cited on p. 8*]

[33] P. A. Baikov, K. G. Chetyrkin and J. H. Kühn, *Five-Loop Running of the QCD coupling constant*, Phys. Rev. Lett. **118** (2017) no.8, 082002, [arXiv:1606.08659 [hep-ph]]. [*Cited on p. 8*]

[34] F. Herzog, B. Ruijl, T. Ueda, J. A. M. Vermaseren and A. Vogt, *The five-loop beta function of Yang-Mills theory with fermions*, JHEP **02** (2017), 090, [arXiv:1701.01404 [hep-ph]]. [*Cited on p. 8*]

[35] P. A. Zyla *et al.* [Particle Data Group], *Review of Particle Physics*, PTEP **2020** (2020) no.8, 083C01 [*Cited on p. 9*]

[36] A. Deuzeman, M. P. Lombardo and E. Pallante, *Evidence for a conformal phase in SU(N) gauge theories*, Phys. Rev. D **82** (2010), 074503, [arXiv:0904.4662 [hep-ph]]. [*Cited on p. 10*]

[37] A. Deuzeman, M. P. Lombardo and E. Pallante, *The Physics of eight flavours*, Phys. Lett. B **670** (2008), 41-48, [arXiv:0804.2905 [hep-lat]]. [*Cited on p. 10*]

[38] T. M. Yan, *The Parton Model*, Ann. Rev. Nucl. Part. Sci. **26** (1976), 199-238 [*Cited on p. 10*]

[39] J. Collins, *Foundations of perturbative QCD*, Camb. Monogr. Part. Phys. Nucl. Phys. Cosmol. **32** (2011), 1-624 Cambridge University Press, 2013, [*Cited on pp. 14, 37, and 48*]

[40] I. O. Cherednikov, T. Mertens and F. Van der Veken, *Wilson Lines in Quantum Field Theory*, De Gruyter, 2020, [*Cited on pp. 14, 17, 18, 119, and 121*]

[41] V. N. Gribov and L. N. Lipatov, *Deep inelastic ep scattering in perturbation theory*, Sov. J. Nucl. Phys. **15** (1972), 438-450 IPTI-381-71. [*Cited on p. 20*]

[42] Y. L. Dokshitzer, *Calculation of the Structure Functions for Deep Inelastic Scattering and e^+e^- Annihilation by Perturbation Theory in Quantum Chromodynamics.*, Sov. Phys. JETP **46** (1977), 641-653 [*Cited on p. 20*]

[43] G. Altarelli and G. Parisi, *Asymptotic Freedom in Parton Language*, Nucl. Phys. B **126** (1977), 298-318 [*Cited on p. 20*]

[44] R. D. Ball *et al.* [NNPDF], *The path to proton structure at 1% accuracy*, Eur. Phys. J. C **82** (2022) no.5, 428, [arXiv:2109.02653 [hep-ph]]. [*Cited on p. 20*]

[45] S. Dulat, T. J. Hou, J. Gao, M. Guzzi, J. Huston, P. Nadolsky, J. Pumplin, C. Schmidt, D. Stump and C. P. Yuan, *New parton distribution functions from a global analysis of quantum chromodynamics*, Phys. Rev. D **93** (2016) no.3, 033006, [arXiv:1506.07443 [hep-ph]]. [*Cited on p. 20*]

[46] A. D. Martin, W. J. Stirling, R. S. Thorne and G. Watt, *Parton distributions for the LHC*, Eur. Phys. J. C **63** (2009), 189-285, [arXiv:0901.0002 [hep-ph]]. [*Cited on p. 20*]

[47] J. Pumplin, D. R. Stump, J. Huston, H. L. Lai, P. M. Nadolsky and W. K. Tung, *New generation of parton distributions with uncertainties from global QCD analysis*, JHEP **07** (2002), 012, [arXiv:hep-ph/0201195 [hep-ph]]. [*Cited on p. 20*]

[48] H. Abramowicz *et al.* [H1 and ZEUS], *Combination of measurements of inclusive deep inelastic $e^{\pm}p$ scattering cross sections and QCD analysis of HERA data*, Eur. Phys. J. C **75** (2015) no.12, 580, [arXiv:1506.06042 [hep-ex]]. [*Cited on p. 20*]

[49] S. Alekhin, J. Blümlein, S. Moch and R. Placakyte, *Parton distribution functions, α_s, and heavy-quark masses for LHC Run II*, Phys. Rev. D **96** (2017) no.1, 014011, [arXiv:1701.05838 [hep-ph]]. [*Cited on p. 20*]

[50] R. D. Ball *et al.* [NNPDF], *Parton distributions from high-precision collider data*, Eur. Phys. J. C **77** (2017) no.10, 663, [arXiv:1706.00428 [hep-ph]]. [*Cited on p. 21*]

[51] L. N. Lipatov, *Reggeization of the Vector Meson and the Vacuum Singularity in Nonabelian Gauge Theories*, Sov. J. Nucl. Phys. **23** (1976), 338-345 [*Cited on p. 20*]

[52] E. A. Kuraev, L. N. Lipatov and V. S. Fadin, *The Pomeranchuk Singularity in Nonabelian Gauge Theories*, Sov. Phys. JETP **45** (1977), 199-204 [*Cited on p. 20*]

[53] I. I. Balitsky and L. N. Lipatov, *The Pomeranchuk Singularity in Quantum Chromodynamics*, Sov. J. Nucl. Phys. **28** (1978), 822-829 [*Cited on p. 20*]

[54] R. Venugopalan, *The Color glass condensate: An Overview*, Eur. Phys. J. C **43** (2005), 337-344, [arXiv:hep-ph/0502190 [hep-ph]]. [*Cited on p. 23*]

[55] L. D. McLerran and R. Venugopalan, *Computing quark and gluon distribution functions for very large nuclei*, Phys. Rev. D **49** (1994), 2233-2241, [arXiv:hep-ph/9309289 [hep-ph]]. [*Cited on pp. 24, 27, 28, 42, 55, and 71*]

[56] F. Gelis and A. Peshier, *Probing colored glass via q anti-q photoproduction*, Nucl. Phys. A **697** (2002), 879-901, [arXiv:hep-ph/0107142 [hep-ph]]. [*Cited on pp. 24, 27, 28, and 55*]

[57] A. H. Mueller and B. Patel, *Single and double BFKL pomeron exchange and a dipole picture of high-energy hard processes*, Nucl. Phys. B **425** (1994), 471-488. [*Cited on p. 25*]

[58] A. H. Mueller, *Small x Behavior and Parton Saturation: A QCD Model*, Nucl. Phys. B **335** (1990), 115-137 [*Cited on pp. 25 and 55*]

[59] F. E. Low, *A Model of the Bare Pomeron*, Phys. Rev. D **12** (1975), 163-173 [*Cited on p. 25*]

[60] S. Nussinov, *Colored Quark Version of Some Hadronic Puzzles*, Phys. Rev. Lett. **34** (1975), 1286-1289 [*Cited on p. 25*]

[61] M. Wusthoff and A. D. Martin, *The QCD description of diffractive processes*, J. Phys. G **25** (1999), R309-R344, [arXiv:hep-ph/9909362 [hep-ph]]. [*Cited on p. 25*]

[62] G. Beuf, *NLO corrections for the dipole factorization of DIS structure functions at low x*, Phys. Rev. D **85** (2012), 034039, [arXiv:1112.4501 [hep-ph]]. [*Cited on pp. 25, 26, 52, and 58*]

[63] G. Beuf, H. Hänninen, T. Lappi and H. Mäntysaari, *Color Glass Condensate at next-to-leading order meets HERA data*, Phys. Rev. D **102** (2020), 074028, [arXiv:2007.01645 [hep-ph]]. [*Cited on p. 25*]

[64] T. Altinoluk, N. Armesto, G. Beuf and A. H. Rezaeian, *Diffractive Dijet Production in Deep Inelastic Scattering and Photon-Hadron Collisions in the Color Glass Condensate*, Phys. Lett. B **758** (2016), 373-383, [arXiv:1511.07452 [hep-ph]]. [*Cited on pp. 26, 42, 52, 58, 59, 60, and 83*]

[65] H. Hänninen, T. Lappi and R. Paatelainen, *One-loop corrections to light cone wave functions: the dipole picture DIS cross section*, Annals Phys. **393** (2018), 358-412, [arXiv:1711.08207 [hep-ph]]. [*Cited on pp. 26, 52, and 58*]

[66] A. Hebecker, *Diffraction in deep inelastic scattering*, Phys. Rept. **331** (2000), 1-115, [arXiv:hep-ph/9905226 [hep-ph]]. [*Cited on p. 26*]

[67] F. Dominguez, C. Marquet, B. W. Xiao and F. Yuan, *Universality of Unintegrated Gluon Distributions at small x*, Phys. Rev. D **83** (2011), 105005, [arXiv:1101.0715 [hep-ph]]. [*Cited on pp. 26, 40, and 70*]

[68] D. Boer and C. Setyadi, *GTMD model predictions for diffractive dijet production at EIC*, Phys. Rev. D **104** (2021) no.7, 074006, [arXiv:2106.15148 [hep-ph]] [*Cited on pp. 26, 51, and 74*]

[69] A. V. Belitsky, X. Ji and F. Yuan, *Final state interactions and gauge invariant parton distributions*, Nucl. Phys. B **656** (2003), 165-198, [arXiv:hep-ph/0208038 [hep-ph]]. [*Cited on pp. 27 and 37*]

[70] X. d. Ji and F. Yuan, *Parton distributions in light cone gauge: Where are the final state interactions?*, Phys. Lett. B **543** (2002), 66-72, [arXiv:hep-ph/0206057 [hep-ph]]. [*Cited on p. 27*]

[71] D. Boer, P. J. Mulders and F. Pijlman, *Universality of T odd effects in single spin and azimuthal asymmetries*, Nucl. Phys. B **667** (2003), 201-241, [arXiv:hep-ph/0303034 [hep-ph]] [*Cited on pp. 27 and 37*]

[72] D. Boer, T. Van Daal, P. J. Mulders and E. Petreska, *Directed flow from C-odd gluon correlations at small* x, JHEP **07** (2018), 140, [arXiv:1805.05219 [hep-ph]]. [*Cited on pp. 27, 45, 46, 70, and 71*]

[73] L. D. McLerran and R. Venugopalan, *Gluon distribution functions for very large nuclei at small transverse momentum*, Phys. Rev. D **49** (1994), 3352-3355, [arXiv:hep-ph/9311205 [hep-ph]]. [*Cited on pp. 27, 28, 42, 55, and 71*]

[74] L. D. McLerran and R. Venugopalan, *Green's functions in the color field of a large nucleus*, Phys. Rev. D **50** (1994), 2225-2233, [arXiv:hep-ph/9402335 [hep-ph]]. [*Cited on pp. 27, 42, 55, and 71*]

[75] J. Jalilian-Marian, *Limiting fragmentation from the color glass condensate*, Phys. Rev. C **70** (2004), 027902, [arXiv:nucl-th/0212018 [nucl-th]]. [*Cited on p. 29*]

[76] F. Gelis, A. M. Stasto and R. Venugopalan, *Limiting fragmentation in hadron-hadron collisions at high energies*, Eur. Phys. J. C **48** (2006), 489-500, [arXiv:hep-ph/0605087 [hep-ph]]. [*Cited on p. 29*]

[77] H. Kowalski and D. Teaney, *An Impact parameter dipole saturation model*, Phys. Rev. D **68** (2003), 114005, [arXiv:hep-ph/0304189 [hep-ph]]. [*Cited on pp. 29 and 82*]

[78] G. Watt and H. Kowalski, *Impact parameter dependent colour glass condensate dipole model*, Phys. Rev. D **78** (2008), 014016, [arXiv:0712.2670 [hep-ph]]. [*Cited on pp. 29, 81, and 84*]

[79] E. Iancu and A. H. Rezaeian, *Elliptic flow from color-dipole orientation in pp and pA collisions*, Phys. Rev. D **95** (2017) no.9, 094003, [arXiv:1702.03943 [hep-ph]]. [*Cited on pp. 29, 55, 56, and 72*]

[80] S. Aid *et al.* [H1], *A Measurement and QCD analysis of the proton structure function $F_2(x, Q^2)$ at HERA*, Nucl. Phys. B **470** (1996), 3-40, [arXiv:hep-ex/9603004 [hep-ex]]. [*Cited on pp. 30 and 32*]

[81] C. Adloff *et al.* [H1], *A Measurement of the proton structure function $F_2(x, Q^2)$ at low x and low Q^2 at HERA*, Nucl. Phys. B **497** (1997), 3-30, [arXiv:hep-ex/9703012 [hep-ex]]. [*Cited on pp. 30 and 32*]

[82] M. Derrick *et al.* [ZEUS], *Measurement of the proton structure function F_2 at low x and low Q^2 at HERA*, Z. Phys. C **69** (1996), 607-620, [arXiv:hep-ex/9510009 [hep-ex]]. [*Cited on p. 30*]

[83] J. Breitweg *et al.* [ZEUS], *Measurement of the proton structure function F_2 and $\sigma_{tot}^{\gamma^* p}$) at low Q^2 and very low x at HERA*, Phys. Lett. B **407** (1997), 432-448, [arXiv:hep-ex/9707025 [hep-ex]]. [*Cited on p. 30*]

[84] I. Balitsky, *Operator expansion for high-energy scattering*, Nucl. Phys. B **463** (1996), 99-160, [arXiv:hep-ph/9509348 [hep-ph]]. [*Cited on pp. 31 and 95*]

[85] I. Balitsky, *Factorization for high-energy scattering*, Phys. Rev. Lett. **81** (1998), 2024-2027, [arXiv:hep-ph/9807434 [hep-ph]]. [*Cited on p. 31*]

[86] I. Balitsky, *Factorization and high-energy effective action*, Phys. Rev. D **60** (1999), 014020, [arXiv:hep-ph/9812311 [hep-ph]]. [*Cited on p. 31*]

[87] Y. V. Kovchegov, *Small-x F_2 structure function of a nucleus including multiple pomeron exchanges*, Phys. Rev. D **60** (1999), 034008, [arXiv:hep-ph/9901281 [hep-ph]]. [*Cited on pp. 31 and 95*]

[88] J. Jalilian-Marian, A. Kovner, L. D. McLerran and H. Weigert, *The Intrinsic glue distribution at very small x*, Phys. Rev. D **55** (1997), 5414-5428, [arXiv:hep-ph/9606337 [hep-ph]]. [*Cited on pp. 31 and 55*]

[89] J. Jalilian-Marian, A. Kovner and H. Weigert, *The Wilson renormalization group for low x physics: Gluon evolution at finite parton density*, Phys. Rev. D **59** (1998), 014015, [arXiv:hep-ph/9709432 [hep-ph]]. [*Cited on p. 31*]

[90] A. Kovner, J. G. Milhano and H. Weigert, *Relating different approaches to nonlinear QCD evolution at finite gluon density*, Phys. Rev. D **62** (2000), 114005, [arXiv:hep-ph/0004014 [hep-ph]]. [*Cited on p. 31*]

[91] S. Munier and R. B. Peschanski, *Traveling wave fronts and the transition to saturation*, Phys. Rev. D **69** (2004), 034008, [arXiv:hep-ph/0310357 [hep-ph]]. [*Cited on p. 32*]

[92] F. Gelis, R. B. Peschanski, G. Soyez and L. Schoeffel, *Systematics of geometric scaling*, Phys. Lett. B **647** (2007), 376-379, [arXiv:hep-ph/0610435 [hep-ph]]. [*Cited on pp. 32 and 70*]

[93] F. Caola and S. Forte, *Geometric Scaling from GLAP evolution*, Phys. Rev. Lett. **101** (2008), 022001, [arXiv:0802.1878 [hep-ph]]. [*Cited on pp. 32 and 70*]

[94] D. Boer, A. Utermann and E. Wessels, *Geometric Scaling at RHIC and LHC*, Phys. Rev. D **77** (2008), 054014, [arXiv:0711.4312 [hep-ph]]. [*Cited on p. 32*]

[95] E. Wessels, *Signatures of gluon saturation in high energy scattering*, PhD thesis, VU University Amsterdam, 2009. [*Cited on p. 32*]

[96] A. M. Stasto, K. J. Golec-Biernat and J. Kwiecinski, *Geometric scaling for the total $\gamma^* p$ cross section in the low x region*, Phys. Rev. Lett. **86** (2001), 596-599, [arXiv:hep-ph/0007192 [hep-ph]]. [*Cited on pp. 32, 33, and 70*]

[97] J. Breitweg *et al.* [ZEUS], *ZEUS results on the measurement and phenomenology of F_2 at low x and low Q^2*, Eur. Phys. J. C **7** (1999), 609-630, [arXiv:hep-ex/9809005 [hep-ex]]. [*Cited on p. 32*]

[98] J. Breitweg *et al.* [ZEUS], *Measurement of exclusive omega electroproduction at HERA*, Phys. Lett. B **487** (2000), 273-288, [arXiv:hep-ex/0006013 [hep-ex]]. [*Cited on p. 32*]

[99] S. Chekanov *et al.* [ZEUS], *Measurement of the neutral current cross section and F_2 structure function for deep inelastic e^+p scattering at HERA*, Eur. Phys. J. C **21** (2001), 443-471, [arXiv:hep-ex/0105090 [hep-ex]]. [*Cited on p. 32*]

[100] S. Chekanov *et al.* [ZEUS], *High Q^2 neutral current cross sections in e^+p deep inelastic scattering at $\sqrt{s} = 318$ GeV*, Phys. Rev. D **70** (2004), 052001, [arXiv:hep-ex/0401003 [hep-ex]]. [*Cited on p. 32*]

[101] M. Derrick *et al.* [ZEUS], *Measurement of the F_2 structure function in deep inelastic e^+p scattering using 1994 data from the ZEUS detector at HERA*, Z. Phys. C **72** (1996), 399-424, [arXiv:hep-ex/9607002 [hep-ex]]. [*Cited on p. 32*]

[102] M. Arneodo *et al.* [New Muon], *Measurement of the proton and deuteron structure functions, F_2^p and F_2^d, and of the ratio σ_L/σ_T*, Nucl. Phys. B **483** (1997), 3-43, [arXiv:hep-ph/9610231 [hep-ph]]. [*Cited on p. 32*]

[103] M. R. Adams *et al.* [E665], *Proton and deuteron structure functions in muon scattering at 470-GeV*, Phys. Rev. D **54** (1996), 3006-3056 [*Cited on p. 32*]

[104] L. W. Whitlow, E. M. Riordan, S. Dasu, S. Rock and A. Bodek, *Precise measurements of the proton and deuteron structure functions from a global analysis of the SLAC deep inelastic electron scattering cross sections*, Phys. Lett. B **282** (1992), 475-482 [*Cited on p. 32*]

[105] A. C. Benvenuti *et al.* [BCDMS], *A High Statistics Measurement of the Proton Structure Functions $F_2(x, Q^2)$ and R from Deep Inelastic Muon Scattering at High Q^2*, Phys. Lett. B **223** (1989), 485-489 [*Cited on p. 32*]

[106] J. J. Aubert *et al.* [European Muon], *A Detailed Study of the Proton Structure Functions in Deep Inelastic Muon - Proton Scattering*, Nucl. Phys. B **259** (1985), 189 [*Cited on p. 32*]

[107] A. Freund, K. Rummukainen, H. Weigert and A. Schafer, *Geometric scaling in inclusive eA reactions and nonlinear perturbative QCD*, Phys. Rev. Lett. **90** (2003), 222002, [arXiv:hep-ph/0210139 [hep-ph]]. [*Cited on pp. 32 and 70*]

[108] N. Armesto, C. A. Salgado and U. A. Wiedemann, *Relating high-energy lepton-hadron, proton-nucleus and nucleus-nucleus collisions through geometric scaling*, Phys. Rev. Lett. **94** (2005), 022002, [arXiv:hep-ph/0407018 [hep-ph]]. [*Cited on p. 32*]

[109] C. Marquet and L. Schoeffel, *Geometric scaling in diffractive deep inelastic scattering*, Phys. Lett. B **639** (2006), 471-477, [arXiv:hep-ph/0606079 [hep-ph]]. [*Cited on pp. 32 and 70*]

[110] R. D. Ball, V. Bertone, M. Bonvini, S. Marzani, J. Rojo and L. Rottoli, *Parton distributions with small-x resummation: evidence for BFKL dynamics in HERA data*, Eur. Phys. J. C **78** (2018) no.4, 321, [arXiv:1710.05935 [hep-ph]]. [*Cited on p. 32*]

[111] M. Constantinou, A. Courtoy, M. A. Ebert, M. Engelhardt, T. Giani, T. Hobbs, T. J. Hou, A. Kusina, K. Kutak and J. Liang, *et al. Parton distributions and lattice-QCD calculations: Toward 3D structure*, Prog. Part. Nucl. Phys. **121** (2021), 103908, [arXiv:2006.08636 [hep-ph]]. [*Cited on p. 36*]

[112] J. C. He *et al.* [LPC], *Unpolarized Transverse-Momentum-Dependent Parton Distributions of the Nucleon from Lattice QCD*, [arXiv:2211.02340 [hep-lat]]. [*Cited on p. 36*]

[113] A. Bacchetta *et al.* [MAP Collaboration], *Unpolarized transverse momentum distributions from a global fit of Drell-Yan and semi-inclusive deep-inelastic scattering data*, JHEP **10** (2022), 127, [arXiv:2206.07598 [hep-ph]]. [*Cited on p. 37*]

[114] A. Bacchetta, V. Bertone, C. Bissolotti, G. Bozzi, F. Delcarro, F. Piacenza and M. Radici, *Transverse-momentum-dependent parton distributions up to N^{3}LL from*

Drell-Yan data, JHEP **07** (2020), 117, [arXiv:1912.07550 [hep-ph]]. [*Cited on p. 37*]

[115] M. Anselmino, M. Boglione, J. O. Gonzalez Hernandez, S. Melis and A. Prokudin, *Unpolarised Transverse Momentum Dependent Distribution and Fragmentation Functions from SIDIS Multiplicities*, JHEP **04** (2014), 005, [arXiv:1312.6261 [hep-ph]]. [*Cited on p. 37*]

[116] V. Bertone, I. Scimemi and A. Vladimirov, *Extraction of unpolarized quark transverse momentum dependent parton distributions from Drell-Yan/Z-boson production*, JHEP **06** (2019), 028, [arXiv:1902.08474 [hep-ph]]. [*Cited on p. 37*]

[117] J. C. Collins, D. E. Soper and G. F. Sterman, *Factorization of Hard Processes in QCD*, Adv. Ser. Direct. High Energy Phys. **5** (1989), 1-91, [arXiv:hep-ph/0409313 [hep-ph]]. [*Cited on p. 37*]

[118] J. C. Collins, *Proof of factorization for diffractive hard scattering*, Phys. Rev. D **57** (1998), 3051-3056[erratum: Phys. Rev. D **61** (2000), 019902], [arXiv:hep-ph/9709499 [hep-ph]]. [*Cited on p. 37*]

[119] D. Gutierrez-Reyes, S. Leal-Gomez, I. Scimemi and A. Vladimirov, *Linearly polarized gluons at next-to-next-to leading order and the Higgs transverse momentum distribution*, JHEP **11** (2019), 121, [arXiv:1907.03780 [hep-ph]]. [*Cited on p. 37*]

[120] F. Scarpa, D. Boer, M. G. Echevarria, J. P. Lansberg, C. Pisano and M. Schlegel, *Studies of gluon TMDs and their evolution using quarkonium-pair production at the LHC*, Eur. Phys. J. C **80** (2020) no.2, 87, [arXiv:1909.05769 [hep-ph]]. [*Cited on p. 37*]

[121] S. J. Brodsky, D. S. Hwang and I. Schmidt, *Final state interactions and single spin asymmetries in semiinclusive deep inelastic scattering*, Phys. Lett. B **530** (2002), 99-107, [arXiv:hep-ph/0201296 [hep-ph]]. [*Cited on p. 37*]

[122] D. W. Sivers, *Single Spin Production Asymmetries from the Hard Scattering of Point-Like Constituents*, Phys. Rev. D **41** (1990), 83. [*Cited on p. 38*]

[123] J. C. Collins, *Leading twist single transverse-spin asymmetries: Drell-Yan and deep inelastic scattering*, Phys. Lett. B **536** (2002), 43-48, [arXiv:hep-ph/0204004 [hep-ph]]. [*Cited on p. 38*]

[124] A. Bacchetta and P. J. Mulders, *Deep inelastic leptoproduction of spin-one hadrons*, Phys. Rev. D **62** (2000), 114004, [arXiv:hep-ph/0007120 [hep-ph]]. [*Cited on p. 38*]

[125] T. A. A. van Daal, *Mapping the internal structure of hadrons through color and spin effects*, PhD thesis, University of Groningen, 2018 [arXiv:1812.07336 [hep-ph]]. [*Cited on pp. 38 and 40*]

[126] D. W. Sivers, *Hard scattering scaling laws for single spin production asymmetries*, Phys. Rev. D **43** (1991), 261-263 [*Cited on p. 38*]

[127] D. Boer and P. J. Mulders, *Time reversal odd distribution functions in leptoproduction*, Phys. Rev. D **57** (1998), 5780-5786, [arXiv:hep-ph/9711485 [hep-ph]]. [*Cited on p. 38*]

[128] A. M. Kotzinian and P. J. Mulders, *Longitudinal quark polarization in transversely polarized nucleons*, Phys. Rev. D **54** (1996), 1229-1232, [arXiv:hep-ph/9511420 [hep-ph]]. [*Cited on p. 38*]

[129] G. A. Miller, *Densities, Parton Distributions, and Measuring the Non-Spherical Shape of the Nucleon*, Phys. Rev. C **76** (2007), 065209, [arXiv:0708.2297 [nucl-th]]. [*Cited on p. 38*]

[130] A. Airapetian *et al.* [HERMES], *Single-spin asymmetries in semi-inclusive deep-inelastic scattering on a transversely polarized hydrogen target*, Phys. Rev. Lett. **94** (2005), 012002, [arXiv:hep-ex/0408013 [hep-ex]]. [*Cited on p. 38*]

[131] A. Airapetian *et al.* [HERMES], *Observation of a single spin azimuthal asymmetry in semiinclusive pion electro production*, Phys. Rev. Lett. **84** (2000), 4047-4051, [arXiv:hep-ex/9910062 [hep-ex]]. [*Cited on p. 38*]

[132] J. Adams *et al.* [STAR], *cross sections and transverse single spin asymmetries in forward neutral pion production from proton collisions at $\sqrt{s} = 200$ GeV*, Phys. Rev. Lett. **92** (2004), 171801, [arXiv:hep-ex/0310058 [hep-ex]]. [*Cited on p. 38*]

[133] S. Bhattacharya, Z. B. Kang, A. Metz, G. Penn and D. Pitonyak, *First global QCD analysis of the TMD g1T from semi-inclusive DIS data*, Phys. Rev. D **105**, no.3, 034007 (2022). [arXiv:2110.10253 [hep-ph]]. [*Cited on p. 38*]

[134] C. Lefky and A. Prokudin, *Extraction of the distribution function $h_{1T}^{\perp}$ from experimental data*, Phys. Rev. D **91**, no.3, 034010 (2015). [arXiv:1411.0580 [hep-ph]]. [*Cited on p. 38*]

[135] A. Metz and A. Vossen, *Parton Fragmentation Functions*, Prog. Part. Nucl. Phys. **91** (2016), 136-202, [arXiv:1607.02521 [hep-ex]]. [*Cited on p. 39*]

[136] M. G. A. Buffing, A. Mukherjee and P. J. Mulders, *Generalized Universality of Definite Rank Gluon Transverse Momentum Dependent Correlators*, Phys. Rev. D **88** (2013), 054027, [arXiv:1306.5897 [hep-ph]]. [*Cited on p. 40*]

[137] M. Diehl, *Generalized parton distributions*, Phys. Rept. **388** (2003), 41-277 [arXiv:hep-ph/0307382 [hep-ph]]. [*Cited on pp. 40, 41, and 73*]

[138] K. Goeke, M. V. Polyakov and M. Vanderhaeghen, *Hard exclusive reactions and the structure of hadrons*, Prog. Part. Nucl. Phys. **47** (2001), 401-515, [arXiv:hep-ph/0106012 [hep-ph]]. [*Cited on p. 40*]

[139] M. Diehl, *Generalized parton distributions in impact parameter space*, Eur. Phys. J. C **25** (2002), 223-232 [erratum: Eur. Phys. J. C **31** (2003), 277-278], [arXiv:hep-ph/0205208 [hep-ph]]. [*Cited on pp. 40, 43, 44, 55, and 81*]

[140] X. Ji, *Generalized parton distributions*, Ann. Rev. Nucl. Part. Sci. **54** (2004), 413-450 [*Cited on p. 40*]

[141] A. V. Belitsky and A. V. Radyushkin, *Unraveling hadron structure with generalized parton distributions*, Phys. Rept. **418** (2005), 1-387, [arXiv:hep-ph/0504030 [hep-ph]]. [*Cited on p. 40*]

[142] S. Boffi and B. Pasquini, *Generalized parton distributions and the structure of the nucleon*, Riv. Nuovo Cim. **30** (2007) no.9, 387-448, [arXiv:0711.2625 [hep-ph]]. [*Cited on p. 40*]

[143] M. Guidal, H. Moutarde and M. Vanderhaeghen, *Generalized Parton Distributions in the valence region from Deeply Virtual Compton Scattering*, Rept. Prog. Phys. **76** (2013), 066202, [arXiv:1303.6600 [hep-ph]]. [*Cited on p. 40*]

[144] C. Mezrag, *An Introductory Lecture on Generalised Parton Distributions*, Few Body Syst. **63** (2022) no.3, 62, [arXiv:2207.13584 [hep-ph]]. [*Cited on pp. 40 and 42*]

[145] M. Diehl and T. Gousset, *Time ordering in off diagonal parton distributions*, Phys. Lett. B **428** (1998), 359-370, [arXiv:hep-ph/9801233 [hep-ph]]. [*Cited on p. 41*]

[146] G. P. Lepage and S. J. Brodsky, *Exclusive Processes in Perturbative Quantum Chromodynamics*, Phys. Rev. D **22** (1980), 2157 [*Cited on p. 41*]

[147] S. Bhattacharya, C. Cocuzza and A. Metz, *Generalized quasi parton distributions in a diquark spectator model*, Phys. Lett. B **788** (2019), 453-463, [arXiv:1808.01437 [hep-ph]]. [*Cited on p. 41*]

[148] S. Bhattacharya, C. Cocuzza and A. Metz, *Exploring twist-2 GPDs through quasidistributions in a diquark spectator model*, Phys. Rev. D **102** (2020) no.5, 054021, [arXiv:1903.05721 [hep-ph]]. [*Cited on p. 41*]

[149] X. d. Ji, *Viewing the Proton through "Color" Filters*, Phys. Rev. Lett. **91** (2003), 062001, [arXiv:hep-ph/0304037 [hep-ph]]. [*Cited on pp. 42 and 45*]

[150] A. V. Belitsky, X. d. Ji and F. Yuan, *Quark imaging in the proton via quantum phase space distributions*, Phys. Rev. D **69** (2004), 074014, [arXiv:hep-ph/0307383 [hep-ph]]. [*Cited on pp. 42 and 45*]

[151] S. Meissner, A. Metz, M. Schlegel and K. Goeke, *Generalized parton correlation functions for a spin-0 hadron*, JHEP **08** (2008), 038, [arXiv:0805.3165 [hep-ph]]. [*Cited on p. 42*]

[152] S. Meissner, A. Metz and M. Schlegel, *Generalized parton correlation functions for a spin-1/2 hadron*, JHEP **08** (2009), 056, [arXiv:0906.5323 [hep-ph]]. [*Cited on p. 42*]

[153] C. Lorce, B. Pasquini and M. Vanderhaeghen, *Unified framework for generalized and transverse-momentum dependent parton distributions within a 3Q light-cone picture of the nucleon*, JHEP **05** (2011), 041, [arXiv:1102.4704 [hep-ph]]. [*Cited on p. 42*]

[154] M. G. Echevarria, A. Idilbi, K. Kanazawa, C. Lorcé, A. Metz, B. Pasquini and M. Schlegel, *Proper definition and evolution of generalized transverse momentum dependent distributions*, Phys. Lett. B **759** (2016), 336-341, [arXiv:1602.06953 [hep-ph]]. [*Cited on p. 42*]

[155] J. More, A. Mukherjee and S. Nair, *Wigner Distributions For Gluons*, Eur. Phys. J. C **78** (2018) no.5, 389, [arXiv:1709.00943 [hep-ph]]. [*Cited on p. 42*]

[156] C. Lorce and B. Pasquini, *Quark Wigner Distributions and Orbital Angular Momentum*, Phys. Rev. D **84**, 014015 (2011), [arXiv:1106.0139 [hep-ph]]. [*Cited on p. 42*]

[157] C. Lorcé and B. Pasquini, *Structure analysis of the generalized correlator of quark and gluon for a spin-1/2 target*, JHEP **09**, 138 (2013), [arXiv:1307.4497 [hep-ph]]. [*Cited on p. 42*]

[158] V. M. Braun and D. Y. Ivanov, *Exclusive diffractive electroproduction of dijets in collinear factorization*, Phys. Rev. D **72** (2005), 034016, [arXiv:hep-ph/0505263 [hep-ph]]. [*Cited on pp. 42, 51, and 83*]

[159] G. M. Peccini, L. S. Moriggi and M. V. T. Machado, *Investigating the diffractive gluon jet production in lepton-ion collisions*, Phys. Rev. C **102** (2020) no.3, 034903, [arXiv:2003.13882 [hep-ph]]. [*Cited on p. 42*]

[160] N. Kaur and H. Dahiya, *Quark Wigner Distributions and GTMDs of Pion in the Light-Front Holographic Model*, Eur. Phys. J. A **56** (2020) no.6, 172, [arXiv:1909.10146 [hep-ph]]. [*Cited on p. 42*]

[161] X. Luo and H. Sun, *T-odd generalized and quasi transverse momentum dependent parton distribution in a scalar spectator model*, Eur. Phys. J. C **80** (2020) no.9, 828, [arXiv:2005.09832 [hep-ph]]. [*Cited on p. 42*]

[162] J. L. Zhang, Z. F. Cui, J. Ping and C. D. Roberts, *Contact interaction analysis of pion GTMDs*, Eur. Phys. J. C **81** (2021) no.1, 6, [arXiv:2009.11384 [hep-ph]]. [*Cited on p. 42*]

[163] D. E. Soper, *The Parton Model and the Bethe-Salpeter Wave Function*, Phys. Rev. D **15** (1977), 1141 [*Cited on p. 43*]

[164] M. Burkardt, *Impact parameter dependent parton distributions and off forward parton distributions for $\zeta \to 0$*, Phys. Rev. D **62** (2000), 071503 [erratum: Phys. Rev. D **66** (2002), 119903], [arXiv:hep-ph/0005108 [hep-ph]]. [*Cited on pp. 43 and 44*]

[165] M. Burkardt, *Impact parameter space interpretation for generalized parton distributions*, Int. J. Mod. Phys. A **18** (2003), 173-208, [arXiv:hep-ph/0207047 [hep-ph]]. [*Cited on pp. 43, 44, and 55*]

[166] M. Burkardt, *Impact parameter dependent parton distributions and transverse single spin asymmetries*, Phys. Rev. D **66** (2002), 114005, [arXiv:hep-ph/0209179 [hep-ph]]. [*Cited on pp. 43, 44, and 81*]

[167] G. A. Miller, *Defining the proton radius: A unified treatment*, Phys. Rev. C **99** (2019) no.3, 035202, [arXiv:1812.02714 [nucl-th]]. [*Cited on p. 44*]

[168] R. L. Jaffe, *Ambiguities in the definition of local spatial densities in light hadrons*, Phys. Rev. D **103** (2021) no.1, 016017, [arXiv:2010.15887 [hep-ph]]. [*Cited on p. 44*]

[169] D. Boer, *Hadron structure from $\gamma^* p$ scattering: Interpreting hadronic matrix elements*, AIP Conf. Proc. **768** (2005) no.1, 248-252, [arXiv:hep-ph/0409354 [hep-ph]]. [*Cited on p. 45*]

[170] Y. Hatta, B. W. Xiao and F. Yuan, *Gluon Tomography from Deeply Virtual Compton Scattering at Small-x*, Phys. Rev. D **95** (2017) no.11, 114026, [arXiv:1703.02085 [hep-ph]]. [*Cited on pp. 48, 64, 79, 81, and 83*]

[171] V. Bertone, *Matching generalised transverse-momentum-dependent distributions onto generalised parton distributions at one loop*, Eur. Phys. J. C **82** (2022) no.10, 941, [arXiv:2207.09526 [hep-ph]]. [*Cited on p. 49*]

[172] D. Boer and C. Setyadi, *Probing gluon GTMDs through exclusive coherent diffractive processes*, Eur. Phys. J. C **83**, no.10, 890 (2023), [arXiv:2301.07980 [hep-ph]]. [*Cited on pp. 51 and 80*]

[173] J. Zhou, *Elliptic gluon generalized transverse-momentum-dependent distribution inside a large nucleus*, Phys. Rev. D **94** (2016) no.11, 114017, [arXiv:1611.02397 [hep-ph]]. [*Cited on p. 54*]

[174] Y. Hagiwara, Y. Hatta and T. Ueda, *Wigner, Husimi, and generalized transverse momentum dependent distributions in the color glass condensate*, Phys. Rev. D **94** (2016) no.9, 094036, [arXiv:1609.05773 [hep-ph]]. [*Cited on pp. 54, 56, 57, 65, and 71*]

[175] Y. Hagiwara, Y. Hatta, R. Pasechnik, M. Tasevsky and O. Teryaev, *Accessing the gluon Wigner distribution in ultraperipheral pA collisions*, Phys. Rev. D **96** (2017) no.3, 034009, [arXiv:1706.01765 [hep-ph]]. [*Cited on pp. 54, 56, 57, 60, 65, 68, and 71*]

[176] H. Mäntysaari, N. Mueller and B. Schenke, *Diffractive Dijet Production and Wigner Distributions from the Color Glass Condensate*, Phys. Rev. D **99** (2019) no.7, 074004, [arXiv:1902.05087 [hep-ph]]. [*Cited on pp. 54 and 79*]

[177] F. Salazar and B. Schenke, *Diffractive dijet production in impact parameter dependent saturation models*, Phys. Rev. D **100** (2019) no.3, 034007, [arXiv:1905.03763 [hep-ph]]. [*Cited on pp. 54, 56, 71, 72, and 74*]

[178] Y. Hatta, B. W. Xiao, F. Yuan and J. Zhou, *Anisotropy in Dijet Production in Exclusive and Inclusive Processes*, Phys. Rev. Lett. **126** (2021) no.14, 142001, [arXiv:2010.10774 [hep-ph]]. [*Cited on p. 54*]

[179] [CMS], *Angular correlations in exclusive dijet photoproduction in ultra-peripheral PbPb collisions at $\sqrt{s_{NN}} = 5.02~\mathrm{TeV}$*, CMS-PAS-HIN-18-011. [*Cited on p. 54*]

[180] A. H. Mueller, *Parton saturation: An Overview*, [arXiv:hep-ph/0111244 [hep-ph]]. [*Cited on pp. 55 and 113*]

[181] J. Bartels, K. J. Golec-Biernat and K. Peters, *On the dipole picture in the nonforward direction*, Acta Phys. Polon. B **34** (2003), 3051-3068, [arXiv:hep-ph/0301192 [hep-ph]]. [*Cited on pp. 55 and 81*]

[182] K. J. Golec-Biernat and A. M. Stasto, *On solutions of the Balitsky-Kovchegov equation with impact parameter*, Nucl. Phys. B **668** (2003), 345-363, [arXiv:hep-ph/0306279 [hep-ph]]. [*Cited on p. 55*]

[183] K. J. Golec-Biernat and M. Wüsthoff, *Saturation effects in deep inelastic scattering at low Q^2 and its implications on diffraction*, Phys. Rev. D **59** (1998), 014017, [arXiv:hep-ph/9807513 [hep-ph]]. [*Cited on p. 57*]

[184] Y. Hagiwara, *Nucleon tomography with gluon saturation effects*, PhD Thesis, Kyoto University, 2019 [*Cited on p. 57*]

[185] M. Reinke Pelicer, E. Gräve De Oliveira and R. Pasechnik, *Exclusive heavy quark-pair production in ultraperipheral collisions*, Phys. Rev. D **99** (2019) no.3, 034016, [arXiv:1811.12888 [hep-ph]]. [*Cited on p. 60*]

[186] A. Aktas *et al.* [H1], *Dijet Cross Sections and Parton Densities in Diffractive DIS at HERA*, JHEP **10** (2007), 042, [arXiv:0708.3217 [hep-ex]]. [*Cited on pp. 64 and 65*]

[187] F. D. Aaron *et al.* [H1], *Measurement of Dijet Production in Diffractive Deep-Inelastic Scattering with a Leading Proton at HERA*, Eur. Phys. J. C **72** (2012), 1970, [arXiv:1111.0584 [hep-ex]]. [*Cited on pp. 64 and 65*]

[188] H. Abramowicz *et al.* [ZEUS], *Production of exclusive dijets in diffractive deep inelastic scattering at HERA*, Eur. Phys. J. C **76** (2016) no.1, 16, [arXiv:1505.05783 [hep-ex]]. [*Cited on pp. 64 and 73*]

[189] B. Linek, A. Łuszczak, M. Łuszczak, R. Pasechnik, W. Schäfer and A. Szczurek, *Probing proton structure with $c\bar{c}$ correlations in ultraperipheral pA collisions*, [arXiv:2308.00457 [hep-ph]]. [*Cited on p. 65*]

[190] A. Angerami [ATLAS], *Measurements of photo-nuclear jet production in Pb+Pb collisions with ATLAS*, Nucl. Phys. A **967** (2017), 277-280 [*Cited on pp. 68 and 69*]

[191] V. Guzey and M. Klasen, *How large is the diffractive contribution to inclusive dijet photoproduction in ultraperipheral collisions at the LHC?*, Phys. Rev. D **104** (2021) no.11, 114013, [arXiv:2012.13277 [hep-ph]]. [*Cited on p. 68*]

[192] V. Guzey and M. Klasen, *Inclusive dijet photoproduction in ultraperipheral heavy ion collisions at the CERN Large Hadron Collider in next-to-leading order QCD*, Phys. Rev. C **99** (2019) no.6, 065202, [arXiv:1811.10236 [hep-ph]]. [*Cited on p. 68*]

[193] F. Dominguez, B. W. Xiao and F. Yuan, *k_t Factorization for Hard Processes in Nuclei*, Phys. Rev. Lett. **106** (2011), 022301, [arXiv:1009.2141 [hep-ph]]. [*Cited on p. 70*]

[194] D. Boer, M. G. Echevarria, P. Mulders and J. Zhou, *Single spin asymmetries from a single Wilson loop*, Phys. Rev. Lett. **116** (2016) no.12, 122001, [arXiv:1511.03485 [hep-ph]]. [*Cited on p. 70*]

[195] A. H. Mueller, B. W. Xiao and F. Yuan, *Sudakov Resummation in Small-x Saturation Formalism*, Phys. Rev. Lett. **110** (2013) no.8, 082301, [arXiv:1210.5792 [hep-ph]]. [*Cited on p. 70*]

[196] B. W. Xiao, F. Yuan and J. Zhou, *Transverse Momentum Dependent Parton Distributions at Small-x*, Nucl. Phys. B **921** (2017), 104-126, [arXiv:1703.06163 [hep-ph]]. [*Cited on p. 70*]

[197] J. Zhou, *Scale dependence of the small x transverse momentum dependent gluon distribution*, Phys. Rev. D **99** (2019) no.5, 054026, [arXiv:1807.00506 [hep-ph]]. [*Cited on p. 70*]

[198] D. X. Zheng and J. Zhou, *Sudakov suppression of the Balitsky-Kovchegov kernel*, JHEP **11** (2019), 177, [arXiv:1906.06825 [hep-ph]]. [*Cited on p. 70*]

[199] Y. Hatta, E. Iancu, K. Itakura and L. McLerran, *Odderon in the color glass condensate*, Nucl. Phys. A **760** (2005), 172-207, [arXiv:hep-ph/0501171 [hep-ph]]. [*Cited on p. 71*]

[200] H. Mäntysaari, F. Salazar and B. Schenke, *Nuclear geometry at high energy from exclusive vector meson production*, Phys. Rev. D **106** (2022) no.7, 074019, [arXiv:2207.03712 [hep-ph]]. [*Cited on pp. 72, 88, and 95*]

[201] F. D. Aaron *et al.* [H1], *Measurement of Dijet Production in Diffractive Deep-Inelastic Scattering with a Leading Proton at HERA*, Eur. Phys. J. C **72** (2012), 1970, [arXiv:1111.0584 [hep-ex]]. [*Cited on pp. 73, 74, and 86*]

[202] H. Kowalski, L. Motyka and G. Watt, *Exclusive diffractive processes at HERA within the dipole picture*, Phys. Rev. D **74** (2006), 074016, [arXiv:hep-ph/0606272 [hep-ph]]. [*Cited on pp. 79, 81, 82, 83, and 84*]

[203] D. Bendova, J. Cepila and J. G. Contreras, *Dissociative production of vector mesons at electron-ion colliders*, Phys. Rev. D **99** (2019) no.3, 034025, [arXiv:1811.06479 [hep-ph]]. [*Cited on pp. 79 and 84*]

[204] D. Bendova, J. Cepila, J. G. Contreras and M. Matas, *Photonuclear J/ψ production at the LHC: Proton-based versus nuclear dipole scattering amplitudes*, Phys. Lett. B **817** (2021), 136306, [arXiv:2006.12980 [hep-ph]]. [*Cited on pp. 81, 84, and 95*]

[205] J. Nemchik, N. N. Nikolaev and B. G. Zakharov, *Scanning the BFKL pomeron in elastic production of vector mesons at HERA*, Phys. Lett. B **341** (1994), 228-237, [arXiv:hep-ph/9405355 [hep-ph]]. [*Cited on p. 82*]

[206] J. Nemchik, N. N. Nikolaev, E. Predazzi and B. G. Zakharov, *Color dipole phenomenology of diffractive electroproduction of light vector mesons at HERA*, Z. Phys. C **75** (1997), 71-87, [arXiv:hep-ph/9605231 [hep-ph]]. [*Cited on p. 82*]

[207] H. Mäntysaari and P. Zurita, *In depth analysis of the combined HERA data in the dipole models with and without saturation*, Phys. Rev. D **98** (2018), 036002, [arXiv:1804.05311 [hep-ph]]. [*Cited on pp. 82 and 84*]

[208] B. Z. Kopeliovich and B. G. Zakharov, *Quantum effects and color transparency in charmonium photoproduction on nuclei*, Phys. Rev. D **44** (1991), 3466-3472 [*Cited on p. 82*]

[209] E. Eichten, K. Gottfried, T. Kinoshita, K. D. Lane and T. M. Yan, *Charmonium: Comparison with Experiment*, Phys. Rev. D **21** (1980), 203 [*Cited on p. 82*]

[210] E. Eichten, K. Gottfried, T. Kinoshita, K. D. Lane and T. M. Yan, *Charmonium: The Model*, Phys. Rev. D **17** (1978), 3090 [erratum: Phys. Rev. D **21** (1980), 313] [*Cited on p. 82*]

[211] C. Quigg and J. L. Rosner, *Quarkonium Level Spacings*, Phys. Lett. B **71** (1977), 153-157 [*Cited on p. 82*]

[212] J. Cepila, J. Nemchik, M. Krelina and R. Pasechnik, *Theoretical uncertainties in exclusive electroproduction of S-wave heavy quarkonia*, Eur. Phys. J. C **79** (2019) no.6, 495, [arXiv:1901.02664 [hep-ph]]. [*Cited on p. 82*]

[213] N. Barik and S. N. Jena, *Fine - Hyperfine Splittings of Quarkonium Levels in an Effective Power Law Potential*, Phys. Lett. B **97** (1980), 265-268 [*Cited on p. 82*]

[214] W. Buchmuller and S. H. H. Tye, *Quarkonia and Quantum Chromodynamics*, Phys. Rev. D **24** (1981), 132 [*Cited on pp. 82 and 95*]

[215] A. Aktas *et al.* [H1], *Elastic J/ψ production at HERA*, Eur. Phys. J. C **46** (2006), 585-603, [arXiv:hep-ex/0510016 [hep-ex]]. [*Cited on pp. 83, 86, 88, 89, 92, 93, and 94*]

[216] S. Chekanov *et al.* [ZEUS], *Exclusive electroproduction of J/ψ mesons at HERA*, Nucl. Phys. B **695** (2004), 3-37, [arXiv:hep-ex/0404008 [hep-ex]]. [*Cited on pp. 83, 86, 88, 89, 93, and 94*]

[217] A. D. Martin, M. G. Ryskin and T. Teubner, *Q^2 dependence of diffractive vector meson electroproduction*, Phys. Rev. D **62** (2000), 014022, [arXiv:hep-ph/9912551 [hep-ph]]. [*Cited on pp. 84 and 100*]

[218] T. Lappi and H. Mantysaari, *Incoherent diffractive J/ψ production in high energy nuclear DIS*, Phys. Rev. C **83** (2011), 065202, [arXiv:1011.1988 [hep-ph]]. [*Cited on p. 84*]

[219] J. Cepila, J. G. Contreras and M. Krelina, *Coherent and incoherent J/ψ photonuclear production in an energy-dependent hot-spot model*, Phys. Rev. C **97** (2018) no.2, 024901, [arXiv:1711.01855 [hep-ph]]. [*Cited on pp. 84 and 100*]

[220] J. Cepila, J. G. Contreras, M. Krelina and J. D. Tapia Takaki, *Mass dependence of vector meson photoproduction off protons and nuclei within the energy-dependent hot-spot model*, Nucl. Phys. B **934** (2018), 330-340, [arXiv:1804.05508 [hep-ph]]. [*Cited on p. 84*]

[221] V. Guzey and M. Zhalov, *Exclusive J/ψ production in ultraperipheral collisions at the LHC: constrains on the gluon distributions in the proton and nuclei*, JHEP **10** (2013), 207, [arXiv:1307.4526 [hep-ph]]. [*Cited on p. 84*]

[222] V. P. Goncalves, B. D. Moreira and F. S. Navarra, *Investigation of diffractive photoproduction of J/Ψ in hadronic collisions*, Phys. Rev. C **90** (2014) no.1, 015203, [arXiv:1405.6977 [hep-ph]]. [*Cited on p. 84*]

[223] S. Zhang, S. Cai, W. Xiang, Y. Cai and D. Zhou, *Exclusive and dissociative J/ψ production with collinear-improved Balitsky-Kovchegov equation*, Chin. Phys. C **45** (2021) no.7, 073110 [*Cited on p. 84*]

[224] K. J. Eskola, C. A. Flett, V. Guzey, T. Löytäinen and H. Paukkunen, *Exclusive J/ψ photoproduction in ultraperipheral Pb+Pb collisions at the CERN Large Hadron Collider calculated at next-to-leading order perturbative QCD*, Phys. Rev. C **106** (2022) no.3, 035202, [arXiv:2203.11613 [hep-ph]]. [*Cited on p. 84*]

[225] N. Armesto and A. H. Rezaeian, *Exclusive vector meson production at high energies and gluon saturation*, Phys. Rev. D **90** (2014) no.5, 054003, [arXiv:1402.4831 [hep-ph]]. [*Cited on p. 84*]

[226] H. Mäntysaari, *Review of proton and nuclear shape fluctuations at high energy*, Rept. Prog. Phys. **83** (2020) no.8, 082201, [arXiv:2001.10705 [hep-ph]]. [*Cited on p. 84*]

[227] V. N. Gribov and A. A. Migdal, *The Pomeranchuk quasi-stable pole and diffraction scattering at ultrahigh-energy*, Yad. Fiz. **8** (1968), 1213 IPTI-138. [*Cited on p. 84*]

[228] A. G. Shuvaev, K. J. Golec-Biernat, A. D. Martin and M. G. Ryskin, *Off diagonal distributions fixed by diagonal partons at small x and ξ*, Phys. Rev. D **60** (1999), 014015, [arXiv:hep-ph/9902410 [hep-ph]]. [*Cited on p. 84*]

[229] T. Toll and T. Ullrich, *Exclusive diffractive processes in electron-ion collisions*, Phys. Rev. C **87** (2013) no.2, 024913, [arXiv:1211.3048 [hep-ph]]. [*Cited on pp. 84 and 100*]

[230] H. Mäntysaari and B. Schenke, *Revealing proton shape fluctuations with incoherent diffraction at high energy*, Phys. Rev. D **94** (2016) no.3, 034042, [arXiv:1607.01711 [hep-ph]]. [*Cited on pp. 84 and 100*]

[231] C. A. Flett, S. P. Jones, A. D. Martin, M. G. Ryskin and T. Teubner, *How to include exclusive J/ψ production data in global PDF analyses*, Phys. Rev. D **101** (2020) no.9, 094011, [arXiv:1908.08398 [hep-ph]]. [*Cited on p. 84*]

[232] C. Adloff *et al.* [H1], *Charmonium production in deep inelastic scattering at HERA*, Eur. Phys. J. C **10** (1999), 373-393, [arXiv:hep-ex/9903008 [hep-ex]]. [*Cited on p. 86*]

[233] S. Chekanov *et al.* [ZEUS], *Exclusive photoproduction of J/ψ mesons at HERA*, Eur. Phys. J. C **24** (2002), 345-360, [arXiv:hep-ex/0201043 [hep-ex]]. [*Cited on pp. 86, 88, and 89*]

[234] C. Adloff *et al.* [H1], *Elastic photoproduction of J/ψ and Υ mesons at HERA*, Phys. Lett. B **483** (2000), 23-35, [arXiv:hep-ex/0003020 [hep-ex]]. [*Cited on pp. 88 and 89*]

[235] B. Abelev *et al.* [ALICE], *Coherent J/ψ photoproduction in ultra-peripheral Pb-Pb collisions at $\sqrt{s_{NN}} = 2.76$ TeV*, Phys. Lett. B **718** (2013), 1273-1283, [arXiv:1209.3715 [nucl-ex]]. [*Cited on pp. 88 and 89*]

[236] R. Aaij *et al.* [LHCb], *Central exclusive production of J/ψ and $\psi(2S)$ mesons in pp collisions at $\sqrt{s} = 13$ TeV*, JHEP **10** (2018), 167, [arXiv:1806.04079 [hep-ex]]. [*Cited on pp. 88, 89, and 92*]

[237] R. Aaij *et al.* [LHCb], *Updated measurements of exclusive J/ψ and ψ(2S) production cross sections in pp collisions at $\sqrt{s} = 7$ TeV*, J. Phys. G **41** (2014), 055002, [arXiv:1401.3288 [hep-ex]]. [*Cited on pp. 88 and 89*]

[238] S. P. Jones, A. D. Martin, M. G. Ryskin and T. Teubner, *Exclusive J/ψ production at the LHC in the k_T factorization approach*, J. Phys. G **44** (2017) no.3, 03LT01, [arXiv:1611.03711 [hep-ph]]. [*Cited on p. 92*]

[239] S. P. Jones, A. D. Martin, M. G. Ryskin and T. Teubner, *Probes of the small x gluon via exclusive J/ψ and Υ production at HERA and the LHC*, JHEP **11** (2013), 085, [arXiv:1307.7099 [hep-ph]]. [*Cited on pp. 92 and 95*]

[240] C. Alexa *et al.* [H1], *Elastic and Proton-Dissociative Photoproduction of J/ψ Mesons at HERA*, Eur. Phys. J. C **73** (2013) no.6, 2466, [arXiv:1304.5162 [hep-ex]]. [*Cited on p. 92*]

[241] C. Sanchez Gras, *Exceptionally empty charm - Central exclusive production of charmonia at LHCb*, PhD Thesis, Vrije Universiteit Amsterdam, 2022, CERN-THESIS-2022-235. [*Cited on pp. 92 and 95*]

[242] S. Acharya *et al.* [ALICE], *First measurement of the $|t|$-dependence of coherent J/ψ photonuclear production*, Phys. Lett. B **817** (2021), 136280, [arXiv:2101.04623 [nucl-ex]]. [*Cited on pp. 94, 95, and 96*]

[243] S. R. Klein and J. Nystrand, *Interference in exclusive vector meson production in heavy ion collisions*, Phys. Rev. Lett. **84**, 2330-2333 (2000), [arXiv:hep-ph/9909237 [hep-ph]]. [*Cited on p. 94*]

[244] H. Mäntysaari and B. Schenke, *Probing subnucleon scale fluctuations in ultraperipheral heavy ion collisions*, Phys. Lett. B **772** (2017), 832-838, [arXiv:1703.09256 [hep-ph]]. [*Cited on pp. 95 and 100*]

[245] L. Frankfurt, V. Guzey and M. Strikman, *Leading Twist Nuclear Shadowing Phenomena in Hard Processes with Nuclei*, Phys. Rept. **512** (2012), 255-393, [arXiv:1106.2091 [hep-ph]]. [*Cited on p. 95*]

[246] V. Guzey, M. Strikman and M. Zhalov, *Accessing transverse nucleon and gluon distributions in heavy nuclei using coherent vector meson photoproduction at high energies in ion ultraperipheral collisions*, Phys. Rev. C **95** (2017) no.2, 025204, [arXiv:1611.05471 [hep-ph]]. [*Cited on p. 95*]

[247] J. Cepila, J. G. Contreras and M. Matas, *Predictions for nuclear structure functions from the impact-parameter dependent Balitsky-Kovchegov equation*, Phys. Rev. C **102** (2020) no.4, 044318, [arXiv:2002.11056 [hep-ph]]. [*Cited on p. 95*]

[248] D. Bendova, J. Cepila, J. G. Contreras and M. Matas, *Solution to the Balitsky-Kovchegov equation with the collinearly improved kernel including impact-parameter dependence*, Phys. Rev. D **100** (2019) no.5, 054015, [arXiv:1907.12123 [hep-ph]]. [*Cited on p. 95*]

[249] B. Z. Kopeliovich, M. Krelina and J. Nemchik, *Electroproduction of heavy quarkonia: significance of dipole orientation*, Phys. Rev. D **103** (2021) no.9, 094027, [arXiv:2102.06106 [hep-ph]]. [*Cited on p. 95*]

[250] J. Bartels, K. J. Golec-Biernat and H. Kowalski, *A modification of the saturation model: DGLAP evolution*, Phys. Rev. D **66** (2002), 014001, [arXiv:hep-ph/0203258 [hep-ph]]. [*Cited on p. 95*]

[251] B. Z. Kopeliovich, M. Krelina, J. Nemchik and I. K. Potashnikova, *Coherent photoproduction of heavy quarkonia on nuclei*, Phys. Rev. D **105** (2022) no.5, 054023, [arXiv:2201.13021 [hep-ph]]. [*Cited on p. 95*]

[252] J. Adam, *Measurements of quarkonia photoproduction in Ultra-Peripheral Collisions at RHIC*, Quarkonia as Tools 2020 workshop. [*Cited on p. 100*]

[253] M. E. Peskin and D. V. Schroeder, *An Introduction to quantum field theory*, Addison-Wesley, 1995, [*Cited on p. 122*]